

Synthesis and Characterization of Nanoporous Resin Particles for Water Purification

DISSERTATION

zur Erlangung des akademischen Grades
Doctor rerum naturalium
(Dr. rer. nat.)

vorgelegt

dem Bereich Mathematik und Naturwissenschaften
der Technischen Universität Dresden

von

M.Sc. Konstantin B. L. Borchert
geboren am 06. Oktober 1994
in Dresden

Eingereicht am:	22.09.2022
Verteidigt am:	06.12.2022
Gutachter:	Prof. Dr. Andreas Fery Prof. Dr. Jens Weber

Die Dissertation wurde in der Zeit von Dezember 2018 bis September 2022 im Leibniz-Institut für Polymerforschung Dresden e.V. angefertigt.

Table of contents

Abstract	1
Kurzfassung.....	5
List of Publications	9
<i>First-Author Publications</i>	<i>9</i>
<i>Co-Author Publications.....</i>	<i>10</i>
<i>Patent.....</i>	<i>12</i>
<i>Conference Proceedings</i>	<i>12</i>
Oral Presentations	12
Poster	12
List of Figures	13
<i>Mesoporous Poly(Melamine-co-Formaldehyde) Particles for Efficient and Selective Phosphate and Sulfate Removal:.....</i>	<i>14</i>
<i>Tuning the Pore Structure of Templated Mesoporous Poly(melamine-co-formaldehyde) Particles toward Diclofenac Removal:</i>	<i>15</i>
<i>Adsorption vs. Surface Precipitation of Cu²⁺ onto Porous Poly(melamine-co-formaldehyde) Particles:.....</i>	<i>16</i>
<i>SiO₂ Nanospheres as Surfactant and Template in Aqueous Dispersion Polymerizations Yielding Nanoporous Resin Particles:.....</i>	<i>18</i>
<i>Waterborne Phenolic, Triazine-Based Porous Polymer Particles for the Removal of Nickel, Cadmium, and Lead Ions:.....</i>	<i>19</i>
List of Tables	21
<i>Mesoporous Poly(Melamine-co-Formaldehyde) Particles for Efficient and Selective Phosphate and Sulfate Removal:.....</i>	<i>21</i>
<i>Tuning the Pore Structure of Templated Mesoporous Poly(melamine-co-formaldehyde) Particles toward Diclofenac Removal:</i>	<i>21</i>
<i>Adsorption vs. Surface Precipitation of Cu²⁺ onto Porous Poly(melamine-co-formaldehyde) Particles:.....</i>	<i>22</i>
<i>SiO₂ Nanospheres as Surfactant and Template in Aqueous Dispersion Polymerizations Yielding Nanoporous Resin Particles:.....</i>	<i>22</i>

<i>Waterborne Phenolic, Triazine-Based Porous Polymer Particles for the Removal of Nickel, Cadmium, and Lead Ions:</i>	23
Abbreviations	25
Symbols	26
1. Introduction	1
2. Objectives and Experimental Design	5
3. Scientific Background	11
3.1. Poly(melamine-co-formaldehyde)	11
3.1.1. Polymerization Mechanism	11
3.1.2. Synthesis Strategies for the Preparation of Porous PMF Particles.....	13
3.1.3. Fields of Application of PMF	13
3.2. Adsorption	15
3.2.1. Adsorption Isotherms and Mathematical Modeling	16
3.3. Surface Precipitation	20
4. Fundamentals of Instrumental Analytics	23
4.1. Gas Sorption Measurements	23
4.1.1. Determination of Pore Sizes	26
4.1.2. Determination of Specific Surface Area.....	27
4.2. Transmission Electron Microscopy	29
4.3. Inductively Coupled Plasma Optical Emission Spectroscopy	31
Results and Discussion	33
<i>Chapter Overview</i>	33
5. Mesoporous Poly(Melamine-co-Formaldehyde) Particles for Efficient and Selective Phosphate and Sulfate Removal	37
<i>Graphical Abstract</i>	37
<i>Abstract</i>	37
1. Introduction	38
2. Results and Discussion	39
2.1. Synthesis and Characterization of the PMF Particles	40

2.2. Sorption Experiments	47
3. Materials and Methods	54
3.1. Materials	54
3.2. Methods.....	54
3.3. Synthesis of the PMF Particles.....	56
3.4. Water Treatment Experiments	57
4. Conclusions	59
6. Tuning the Pore Structure of Templated Mesoporous Poly(melamine-co-formaldehyde) Particles toward Diclofenac Removal	65
<i>Graphical Abstract</i>	<i>65</i>
<i>Abstract</i>	<i>65</i>
1. Introduction	66
2. Materials	68
3. Methods.....	68
3.1. Synthesis of the PMF particles	70
3.2. Water treatment experiments with diclofenac solution	72
3.3. Theoretical model	72
3. Results and Discussion.....	73
3.1. Synthesis and characterization of the PMF particles.....	74
3.2. Adsorption of Pharmaceuticals.....	80
4. Conclusion.....	84
7. Adsorption vs. Surface Precipitation of Cu²⁺ onto Porous Poly(melamine-co-formaldehyde) Particles	89
<i>Graphical Abstract</i>	<i>89</i>
<i>Abstract</i>	<i>89</i>
1. Introduction	90
2. Materials and methods	91
2.1. Materials.....	91
2.2. Synthesis of the Poly(melamine-co-formaldehyde) particles.....	92
2.3. Methods	93

2.4.	Water treatment experiments	96
3.	<i>Results and discussion</i>	97
3.1.	Synthesis and characterization of the PMF particles	98
3.2.	Cu ²⁺ uptake experiments.....	102
3.3.	Mechanism for Cu ²⁺ and Anion Removal	115
3.4.	Investigation of other heavy metal salts.....	116
4.	<i>Conclusions</i>	117
8.	SiO₂ Nanospheres as Surfactant and Template in Aqueous Dispersion Polymerizations Yielding Nanoporous Resin Particles	121
	<i>Graphical Abstract</i>	121
	<i>Abstract</i>	121
1.	<i>Introduction</i>	122
2.	<i>Materials and methods</i>	123
2.1.	Materials.....	123
2.2.	Methods	124
2.3.	Synthesis of the PMF particles	125
2.4.	Water treatment experiments	128
2.5.	Theoretical model	129
3.	<i>Results and Discussion</i>.....	132
3.1.	PMF-Std	133
3.2.	Influence of the reaction mixture composition	136
3.3.	Variation of the process parameters	140
3.4.	Conclusion on the templating mechanism for PMF-Std	146
3.5.	Acquiring μm-sized porous PMF particles for adsorption application	149
3.6.	Adsorption experiments with K ₂ Cr ₂ O ₇ solution	151
4.	<i>Conclusion</i>.....	155
9.	Waterborne Phenolic, Triazine-Based Porous Polymer Particles for the Removal of Nickel, Cadmium, and Lead Ions	161
	<i>Graphical Abstract</i>	161
	<i>Abstract</i>	161

1. Introduction	162
2. Materials and methods	163
2.1. Materials.....	163
2.2. Synthesis.....	164
2.3. Characterization	166
2.4. Batch adsorption experiments	169
2.5. Calculation and theoretical models	170
3. Results and discussion	172
3.1. Synthesis and characterization of the polymer particles.....	172
3.2. Adsorption experiments with Ni ²⁺ , Cd ²⁺ , and Pb ²⁺ onto P(3PT-F)-3L.....	178
4. Conclusions	184
10. Conclusion and Outlook	191
Contribution to Publications	197
<i>Mesoporous Poly(Melamine-co-Formaldehyde) Particles for Efficient and Selective Phosphate and Sulfate Removal.....</i>	<i>197</i>
<i>Tuning the Pore Structure of Templated Mesoporous Poly(melamine-co-formaldehyde) Particles toward Diclofenac Removal</i>	<i>198</i>
<i>Adsorption vs. Surface Precipitation of Cu²⁺ onto Porous Poly(melamine-co-formaldehyde) Particles</i>	<i>199</i>
<i>SiO₂ Nanospheres as Surfactant and Template in Aqueous Dispersion Polymerizations Yielding Nanoporous Resin Particles.....</i>	<i>200</i>
<i>Waterborne Phenolic, Triazine-Based Porous Polymer Particles for the Removal of Nickel, Cadmium, and Lead Ions.....</i>	<i>201</i>
Danksagung	203
Appendix.....	205
References	207
Eidesstattliche Versicherung	217

Abstract

Through progressive industrialization and the relentless consumption of natural raw materials, man is exerting a negative influence on his habitat. In particular, water as the basis of life and almost all processes of our economy is contaminated by various pollutants due to excessive use and insufficient purification. Here, oxyanions, heavy metal ions and organic pollutants pose a high risk to aquatic habitats and ultimately to humans. Due to insufficient removal, they also contribute to the loss of non-renewable raw materials for industrial cycles. Due to a mostly low effect concentration and potential interactions with diverse living organisms, the removal of many contaminants is extremely important to avoid further altering existing ecosystems.

Adsorption represents an energy-efficient method of removal using adsorbents suitable for this purpose. Highly cross-linked resin polymers such as poly(melamine-co-formaldehyde) (PMF) with its excellent chemical resistance, high number of functional groups and ease of preparation, represent promising starting points for adsorbents.

This dissertation describes the colloidal aqueous synthesis of nanoporous resin particles (e.g. PMF) by templating with SiO₂ nanoparticles (SiO₂ NPs), which are subsequently used to adsorb water pollutants. An overall goal of this work consists of elucidating the mechanism for particle and pore formation by systematically varying various synthesis parameters. Electron microscopy, N₂-sorption and particle size measurement are used to analyze the morphology, size and pore structure of the particles. Comprehensive investigations thus allow to determine the influence of each tested synthesis parameter on these properties.

A very important goal, especially for future large-scale applicability, is the colloidal production of uniform particles, which have both a high ordered porosity and particle diameters in the range of a few micrometers. This enables an application as a fixed-bed adsorber that can be flowed through. This goal is closely linked to the mechanistic elucidation of pore and particle formation in the synthesis.

The prepared nanoporous PMF particles were tested for various adsorption applications after their characterization. In order to obtain a comprehensive picture of the applicability of PMF particles, experiments with oxyanions, with pharmaceuticals as representatives of organic pollutants and with heavy metal ions will be carried out respectively. On the one hand, these experiments will focus on investigating the adsorption performance and mechanism of PMF with the respective pollutant. On the other hand, the influence of the changed porosity on the adsorption mechanism is investigated by using different particles of a varied synthesis parameter.

Sulfate and phosphate ions were investigated in the oxyanion class. Extremely high separation rates were demonstrated for both ions, significantly outperforming previous commercially available materials. In experiments concerning a potential selective adsorption and thus separation of both species, the PMF/SiO₂ hybrid particles, in which the template had not yet been removed, showed a selective sulfate adsorption.

The immobilization of heavy metal ions was analyzed with special focus on the simultaneous separation of the Cu²⁺ ions and respective anions used here. Investigations of the adsorbent after the adsorption experiments by means of electron microscopy, X-ray scattering and electron spin resonance spectroscopy elucidated the adsorption mechanism, which had been insufficiently analyzed so far. Here, adsorption and surface-induced precipitation were identified as partially separate subprocesses, both of which are responsible for the separation of both metal and anions from solution. In adsorption experiments with the monovalent ions nitrate and chloride, a two-step uptake process was identified, which was mathematically described for the first time via a new adsorption isotherm.

In the scope of organic water pollutants, the separation of the pharmaceutical diclofenac is being tested. In particular, the adsorption of pharmaceuticals is an urgent issue due to their low effect concentration and ubiquity in surface and tap waters. Pharmaceutical separation using PMF has hardly been investigated worldwide despite its promising properties. In these experiments, particles templated with SiO₂ NPs of different sizes and stabilized in different ways were tested. This resulted in pore systems that varied from each other especially in their accessibility of the pore system and in the diameter of the connecting channels between the main cavities. These characteristics significantly affected the adsorption capacity and separation rates in low concentration range.

A final goal is to synthesize a resin network that uses an equally highly functional triazine-based monomer instead of melamine. The monomer 2,4,6-tris(2,4,6-trihydroxyphenyl)-1,3,5-triazine (3PT) possesses nine hydroxyl groups each, whereby a polymer based on it should exhibit strongly modified adsorption properties compared to PMF. This monomer was used in an aqueous polymerization analogous to PMF to produce a previously unknown polymer network, which was designated P(3PT-F). Here, templating was omitted because the newly prepared material already exhibited intrinsic nanoporosity due to the size of the 3PT monomer. In subsequent adsorption experiments, very high separation rates were demonstrated for the toxic metal ions Pb²⁺, Cd²⁺ and Ni²⁺. In realistic initial concentrations, the contamination was reduced to drinking water quality in each case. P(3PT-F) also showed highly selective removal of Pb²⁺ over the common ions Ca²⁺, Mg²⁺, K⁺ and Fe²⁺. As fundamental evidence, reusability was also demonstrated by complete desorption with dilute HCl and subsequent re-adsorption without significant reduction in capacity.

Overall, starting from the fundamental study of PMF particle synthesis, a more general understanding of aqueous dispersion polymerization of hydrophobic resins was first derived and templating with hydrophilic SiO₂ NPs was implemented. With the help of understanding the particle growth processes and interactions responsible for templating, the properties of the resulting particles could be controlled. Subsequently, the influence of the changed porosity in particular on the separation performance could be investigated in the adsorption studies. In addition, it was possible to analyze which interactions PMF enters into with the respective pollutant types. By replacing the monomer melamine with a hydroxyl-containing monomer, a novel resin polymer could be produced. With its altered porosity and reactivity, this can now serve as a new starting point for adsorption experiments with strongly altered adsorption performance, e.g. towards heavy metal ions.

Kurzfassung

Durch fortschreitende Industrialisierung und den schonungslosen Verbrauch natürlicher Rohstoffe übt der Mensch negativen Einfluss auf seinen Lebensraum aus. Insbesondere Wasser als Grundlage des Lebens und fast aller Prozesse unserer Wirtschaft wird durch eine übermäßige Nutzung und unzureichende Reinigung mit diversen Schadstoffen kontaminiert. Hierbei stellen Oxyanionen, Schwermetallionen und organische Schadstoffe ein hohes Risiko für aquatische Lebensräume und letztendlich auch den Menschen dar. Durch unzureichende Entfernung tragen sie außerdem zum Verlust nicht-erneuerbarer Rohstoffe für industrielle Kreisläufe bei. Durch eine meist geringe Effektkonzentration und potentielle Wechselwirkungen mit diversen Lebewesen ist die Entfernung vieler Verunreinigungen extrem wichtig, um bestehende Ökosysteme nicht weiter zu verändern.

Adsorption stellt eine energieeffiziente Methode zur Entfernung dieser Schadstoffe durch hierfür geeignete Adsorbentien dar. Hochgradig vernetzte Harzpolymere wie Poly(melamin-co-formaldehyd) (PMF) stellen mit ihrer sehr hohen chemischen Beständigkeit, einer hohen Zahl funktioneller Gruppen und einfachen Herstellbarkeit einen vielversprechenden Ausgangspunkt für Adsorbentien dar.

Diese Dissertation beschreibt die kolloidale, wässrige Synthese nanoporöser Harzpartikel (z. B. PMF) durch eine Templatierung mit SiO_2 Nanopartikeln (SiO_2 NPs), welche anschließend zur Adsorption von Wasserschadstoffen eingesetzt werden. Ein übergeordnetes Ziel dieser Arbeit besteht aus der Aufklärung des Mechanismus zur Partikel- und Porenbildung durch systematische Variation verschiedener Syntheseparameter. Mittels Elektronenmikroskopie, N_2 -Sorption und Partikelgrößenmessung wird die Morphologie, Größe und Porenstruktur der Partikel analysiert. Umfassende Untersuchungen ermöglichen somit, den Einfluss der einzelnen getesteten Syntheseparameter auf diese Eigenschaften zu bestimmen.

Ein sehr wichtiges Ziel, besonders für eine zukünftige großtechnische Anwendbarkeit, ist dabei die kolloidale Herstellung uniformer Partikel, welche sowohl eine hohe geordnete Porosität als auch Partikeldurchmesser im Bereich einiger Mikrometer aufweisen. Dies ermöglicht einen Einsatz als durchströmbaren Festbett-Adsorber. Dieses Ziel ist eng mit der mechanistischen Aufklärung der Poren- und Partikelbildung in der Synthese verknüpft.

Die hergestellten nanoporösen PMF-Partikel wurden nach ihrer Charakterisierung für verschiedene Adsorptionsanwendungen getestet. Um ein umfassendes Bild über die Einsetzbarkeit von PMF-Partikeln zu erhalten, sollen jeweils Versuche mit Oxyanionen, mit Schwermetallionen und mit Pharmazeutika als Vertreter organischer Schadstoffe durchgeführt werden. Bei diesen Versuchen steht zum einen die Untersuchung der Adsorptionsleistung und des Adsorptionsmechanismus des jeweiligen Schadstoffes an PMF im Vordergrund. Zum anderen wird durch die Verwendung verschiedener Partikel, bei welchen

ein einzelner Syntheseparameter variiert wurde, der Einfluss der veränderten Porosität auf den Adsorptionsmechanismus untersucht.

Sulfat- und Phosphationen wurden in der Klasse der Oxyanionen untersucht. Für beide Ionen wurden extrem hohe Abtrennraten nachgewiesen, welche bisherige kommerziell erhältliche Materialien signifikant übertraf. In Versuchen hinsichtlich einer potentiellen selektiven Adsorption und somit Trennung beider Spezies, zeigten die PMF/SiO₂-Hybridpartikel, bei welchen das Templat noch nicht entfernt wurde, eine selektive Sulfatadsorption.

Die Immobilisierung von Schwermetallionen wurde mit besonderem Fokus auf die gleichzeitig auftretende Abtrennung der dafür verwendeten Cu²⁺-Ionen und jeweiliger Anionen analysiert. Durch Untersuchungen des Adsorbens nach den Adsorptionsversuchen mittels Elektronenmikroskopie, Röntgenstreuung und Elektronenspinresonanz-Spektroskopie wurde der bisher unzureichend analysierte Adsorptionsmechanismus aufgeklärt. Hierbei wurden Adsorption und oberflächeninduzierte Fällung als separate Teilprozesse identifiziert, welche beide jeweils für die Abscheidung von sowohl Metall- als auch Anionen aus der Lösung verantwortlich sind. Bei Adsorptionsversuchen mit den einwertigen Ionen Nitrat und Chlorid wurde ein zweistufiger Prozess identifiziert, welcher erstmals über eine neue Adsorptionsisotherme mathematisch beschrieben wurde.

Im Bereich organischer Wasserschadstoffe wird die Abtrennung des Pharmazeutikums Diclofenac getestet. Insbesondere die Adsorption von Pharmazeutika stellt aufgrund von deren geringen Effektkonzentration und Allgegenwärtigkeit in Oberflächen- und Leitungswässern ein dringliches Thema dar. Die Pharmazeutika-Abtrennung mittels PMF wurde trotz seiner vielversprechenden Eigenschaften weltweit bisher kaum untersucht. Im Rahmen dieser Versuche wurden Partikel getestet, welche mit unterschiedlich großen und unterschiedlich stabilisierten SiO₂ NPs templatiert wurden. Dadurch entstanden Porensysteme, die besonders in der Zugänglichkeit ihres Porensystems und in dem Durchmesser der Verbindungskanäle zwischen den Hauptkavitäten voneinander variierten. Diese Eigenschaften wirkten sich signifikant auf die Adsorptionskapazität und die Abtrennraten im niedrigen Konzentrationsbereich aus.

Ein abschließendes Ziel ist die Synthese eines Harznetzwerkes, welches statt Melamin auf einem ebenso hochfunktionellen, triazinbasierten Monomer basiert. Das Monomer 2,4,6-Tris(2,4,6-trihydroxyphenyl)-1,3,5-triazin (3PT) besitzt jeweils neun Hydroxylgruppen, wodurch ein darauf basierendes Polymer stark veränderte Adsorptionseigenschaften gegenüber PMF aufweisen soll. Mit diesem Monomer wurde in einer analog zu PMF durchgeführten wässrigen Polymerisation ein bisher unbekanntes Polymernetzwerk hergestellt, welches als P(3PT-F) bezeichnet wurde. Hierbei wurde auf Templatierung verzichtet, da das neu hergestellte Material bereits intrinsische Nanoporosität durch die

Größe des verwendeten 3PT-Monomers aufwies. In anschließenden Adsorptionsversuchen wurden sehr hohe Abtrennraten für die toxischen Metallionen Pb^{2+} , Cd^{2+} und Ni^{2+} nachgewiesen. In realistischen Ausgangskonzentrationen wurde die Kontamination mit diesen Ionen jeweils auf Trinkwasserqualität reduziert. P(3PT-F) zeigte außerdem eine sehr selektive Abtrennung von Pb^{2+} gegenüber den häufig vorkommenden Ionen Ca^{2+} , Mg^{2+} , K^{+} und Fe^{2+} . Als grundlegender Beweis konnte eine Wiederverwendbarkeit durch die vollständige Desorption mit verdünnter HCl gezeigt werden und eine anschließende erneute Adsorption ohne signifikante Verringerung der Kapazität.

Insgesamt wurde ausgehend von der grundlegenden Untersuchung der PMF-Partikelsynthese erst ein generelleres Verständnis der wässrigen Dispersionspolymerisation hydrophober Harze abgeleitet und die Templatierung mit hydrophilen SiO_2 NPs implementiert. Mithilfe des Verständnisses der Partikelwachstumsprozesse und der Wechselwirkungen, welche für die Templatierung verantwortlich sind, konnten die Eigenschaften der entstehenden Partikel gesteuert werden. Im Rahmen der Adsorptionsuntersuchungen konnte anschließend der Einfluss insbesondere der veränderten Porosität auf die Abtrennleistung untersucht werden. Außerdem konnte analysiert werden, welche Wechselwirkungen PMF mit den jeweiligen Schadstoffarten eingeht. Durch den Austausch des Monomers Melamin gegen das hydroxylhaltige Monomer 3PT konnte ein neuartiges Harzpolymer hergestellt werden. Dieses kann mit seiner veränderten Porosität und Reaktivität nun als neuer Ausgangspunkt für Adsorptionsexperimente mit stark veränderter Adsorptionsleistung z. B. gegenüber Schwermetallionen dienen.

List of Publications

First-Author Publications

1. **A Comparative Study on the Flocculation of Silica and China Clay with Chitosan and Synthetic Polyelectrolytes**
K.B.L. Borchert, C. Steinbach, S. Schwarz, D. Schwarz, *Marine drugs* 19 (2021).
2. **Removal of Lead, Cadmium, and Aluminum Sulfate from Simulated and Real Water with Native and Oxidized Starches**
K.B.L. Borchert*, R. Boughanmi*, B. Reis, P. Zimmermann, C. Steinbach, P. Graichen, A. Svirepa, J. Schwarz, R. Boldt, S. Schwarz, M. Mertig, D. Schwarz, *Polysaccharides* 2 (2021) 429–453. (*contributed equally with R. Boughanmi)
3. **Mesoporous Poly(melamine-co-formaldehyde) Particles for Efficient and Selective Phosphate and Sulfate Removal**
K.B.L. Borchert, C. Steinbach, B. Reis, N. Gerlach, P. Zimmermann, S. Schwarz, D. Schwarz, *Molecules (Basel, Switzerland)* 26 (2021) 6615.
4. **Native and Oxidized Starch for Adsorption of Nickel, Iron, and Manganese Ions from Water**
R. Boughanmi*, K.B.L. Borchert*, C. Steinbach, M. Mayer, S. Schwarz, A. Svirepa, J. Schwarz, M. Mertig, D. Schwarz, *Polysaccharides* 3 (2022) 556–573.
(*contributed equally with R. Boughanmi)
5. **Ecofriendly Removal of Aluminum and Cadmium Sulfate Pollution by Adsorption on Hexanoyl-Modified Chitosan**
B. Reis*, K.B.L. Borchert*, M. Kafetzi, M. Müller, K.H. Carrasco, N. Gerlach, C. Steinbach, S. Schwarz, R. Boldt, S. Pispas, D. Schwarz, *Polysaccharides* 3 (2022) 589–608.
(*contributed equally with B. Reis)
6. **Tuning the Pore Structure of Templated Mesoporous Poly(melamine-co-formaldehyde) Particles for Diclofenac Removal**
K.B.L. Borchert, K.H. Carrasco, C. Steinbach, B. Reis, N. Gerlach, M. Mayer, S. Schwarz, D. Schwarz, *Journal of Environmental Management* 324 (2022) 116221.
7. **Waterborne Phenolic, Triazine-Based Porous Polymer Particles for the Removal of Nickel, Cadmium, and Lead Ions**
K.B.L. Borchert, R. Frenzel, N. Gerlach, B. Reis, C. Steinbach, Benjamin Kohn, Ulrich Scheler, S. Schwarz, D. Schwarz, *JCIS Open* 8 (2022) 100066.
8. **Adsorption vs. Surface Precipitation of Cu²⁺ onto Porous Poly(melamine-co-formaldehyde) Particles**
K.B.L. Borchert, C. Steinbach, B. Reis, U. Lappan, N. Gerlach, S. Schwarz, D. Schwarz, *Microporous and Mesoporous Materials* 348 (2023) 112383.
9. **SiO₂ Nanospheres as Surfactant and Template in Aqueous Dispersion Polymerizations Yielding Nanoporous Resin Particles**
K.B.L. Borchert, N. Gerlach, C. Steinbach, B. Reis, S. Schwarz, D. Schwarz. *Journal of Colloid and Interface Science* 1 (2023) 819.

Co-Author Publications

1. **Porous thiourea-grafted-chitosan hydrogels: Synthesis and sorption of toxic metal ions from contaminated waters**
C.-A. Ghiorghita, K.B.L. Borchert, A.-L. Vasiliu, M.-M. Zaharia, D. Schwarz, M. Mihai, Colloids and Surfaces A: Physicochemical and Engineering Aspects 607 (2020) 125504.
2. **Thermoresponsive PNIPAM-b-PAA block copolymers as “smart” adsorbents of Cu(II) for water restore treatments**
M. Kafetzi, K.B.L. Borchert, C. Steinbach, D. Schwarz, S. Pispas, S. Schwarz, Colloids and Surfaces A: Physicochemical and Engineering Aspects 614 (2021) 126049.
3. **Meso- and macroporous silica-based arsenic adsorbents: effect of pore size, nature of the active phase, and silicon release**
M. Sanna Angotzi, V. Mameli, C. Cara, K.B.L. Borchert, C. Steinbach, R. Boldt, D. Schwarz, C. Cannas, Nanoscale Adv. 3 (2021) 6100–6113.
4. **Cation exchange on colloidal copper selenide nanosheets: a route to two-dimensional metal selenide nanomaterials**
V. Shamraienko, D. Spittel, R. Hübner, M. Samadi Khoshkhoo, N. Weiß, M. Georgi, K.B.L. Borchert, D. Schwarz, V. Lesnyak, A. Eychmüller, J. Mater. Chem. C 306 (2021) 666.
5. **Design of Polymer-Embedded Heterogeneous Fenton Catalysts for the Conversion of Organic Trace Compounds**
Horn, S. Ihmann, F. Müller, D. Pospiech, K.B.L. Borchert, R. Hommel, K. Qin, K. Licha, P.J. Allertz, M. Drache, Processes 9 (2021) 942.
6. **Near-Infrared-Emitting Cd x Hg 1– x Se-Based Core/Shell Nanoplatelets**
Mitrofanov, A. Prudnikau, F. Di Stasio, N. Weiß, R. Hübner, A.M. Dominic, K.B.L. Borchert, V. Lesnyak, A. Eychmüller, Chem. Mater. 33 (2021) 7693–7702.
7. **Size-Dependent Inhibition of Sperm Motility by Copper Particles as a Path toward Male Contraception**
P. Chattopadhyay, V. Magdanz, M. Hernández-Meliá, K.B.L. Borchert, D. Schwarz, J. Simmchen, Advanced NanoBiomed Research 8 (2022) 2100152.
8. **Removal of Iron, Manganese, Cadmium, and Nickel Ions Using Brewers’ Spent Grain**
K.H. Carrasco, E.G. Höfgen, D. Brunner, K.B.L. Borchert, B. Reis, C. Steinbach, M. Mayer, S. Schwarz, K. Glas, D. Schwarz, Polysaccharides 3 (2022) 356–379.
9. **Seed-Mediated Synthesis of Photoluminescent Cu-Zn-In-S Nanoplatelets**
A. Bora, A. Prudnikau, N. Fu, R. Hübner, K.B.L. Borchert, D. Schwarz, N. Gaponik, V. Lesnyak, Chemistry of Materials Chem. Mater. 34 (2022) 9251.
10. **Conjugated Microporous Polymer Hybrid Macroparticles for Enhanced Applicability in Silica-boosted Diclofenac Adsorption**
B. Reis, K. Pfefferkorn, K.B.L. Borchert, P. Zimmermann, C. Steinbach, B.D. Kohn, U. Scheler, U. Reuter, D. Pohl, S. Schwarz, M. Mayer, D. Schwarz, Small Structures (2023) (Accepted).

11. **Bimetallic Pt-Ni Two-Dimensional Interconnected Networks: Developing Self-Assembled Materials for Transparent Electronics**
P. Khavlyuk, A. Mitrofanov, V. Shamraienko, R. Hübner, J. Kresse, K.B.L.Borchert, A. Eychmüller, Chemistry of Materials (submitted December 2022).
12. **Polarity and Functionality Tailored Conjugated Microporous Polymer Coatings on Silica Microspheres for Enhanced Pollutant Adsorption**
B. Reis, K. B.L. Borchert, C. Steinbach, B. D. Kohn, U. Scheler, U. Reuter, N. Gerlach, D. Schwarz, O. Guskova, S. Schwarz, Journal of Colloid and Interface Science (submitted December 2022).

Patent

1. K.B.L. Borchert, S. Schwarz, D. Schwarz, Process for the adsorption of pollutants (*Verfahren zur Adsorption von Schadstoffen*) (DE 10 2022 112 774.5) (Submitted May 2022).

Conference Proceedings

Oral Presentations

1. **4th Freiburger PhD-Conference Sustainability – Your research – our world.**, Technische Universität Bergakademie Freiberg, June 2019, Title: *Synthesis of Mesoporous Resin Particles and Possible Application in Water Purification*. (Participation under former name Konstantin Klein)
2. **Progress in Organic and Macromolecular Compounds Conference 2019 (Macro 2019)**, "Petru Poni" Institute of Macromolecular Chemistry, Iași, Romania, Sep. 2019, Title: *Nanoporous Poly(melamine-co-formaldehyde) Particles for the Adsorption of Micropollutants*. (Participation under former name Konstantin Klein)
3. **Conference of the European Colloid & Interface Society (ECIS 2021)**, Athens, Sep. 2021, Title: *Nanoporous Poly(melamine-co-formaldehyde) Particles for Oxyanion and Heavy Metal Ion Adsorption*.
4. **Interfaces International Conference 2021**, University of Cagliari, Pula, Sep. 2021, Title: *Native and Oxidized Starches as Bioadsorber for Pb²⁺, Cd²⁺, and Al³⁺ from Simulated and Real Waters*.
5. **European Polymer Congress 2022 (EPF 2022)**, European Polymer Federation, Prague, June 2022, Title: *Hard-Templating of Nanoporous Poly(melamine-co-formaldehyde) Particles and Application in Water Treatment*.

Poster

1. **European Polymer Congress 2019 (EPF 2019)**, European Polymer Federation, Heraklion, June 2019, Title: *Nanoporous Poly(melamine-co-formaldehyde) Particles for Water Treatment*. (Participation under former name Konstantin Klein)
2. **4th European Conference on Metal Organic Frameworks and Porous Polymers (EuroMOF 2021)**, Jagiellonian University, Krakow, online, Sep. 2021, Title: *Hard Templating of Poly(melamine-co-formaldehyde) Particles for Tunable Pore Structures for Water Treatment*.

List of Figures

Figure 1. Schematic representation of the synthesis route for the preparation of templated and non-templated PMF particles. The first step shows the prepolymerization of melamine and formaldehyde to the oligomeric prepolymer. Subsequent dispersion polymerization yields templated silica/PMF hybrid particles (H-PMF) with SiO ₂ nanoparticles as template (<i>upper reaction</i>). Subsequent templating/etching with NaOH produces porous PMF particles (P-PMF). Without templating (<i>reaction below</i>), non-templated PMF particles (N-PMF) are obtained. The indicated times (50 min for prepolymerization and 24 h for polymerization) and polymerization temperature (100 °C) are partially varied within the work.	5
Figure 2. Schematic representation of the individual chapter contents of the dissertation on the polymers PMF and P(3PT-F), which are each divided into a synthesis and an application part.	9
Figure 3. Schematic polymerization mechanism for the polycondensation of PMF. a) shows the prepolymerization, which typically takes place at 50 °C, where melamine and formaldehyde first condense to an up to sixfold methylolated (shown here) precursor species, followed by oligomerization to the prepolymer. b) describes the polycondensation at typically 100 °C under base or acid catalysis to an exemplary structure of the crosslinked PMF resin. In c) and d), respectively, the formation of c) methylene bridges and d) ether bridges is visible, which are also highlighted in the exemplary PMF structure in b). e) Elimination reaction of an ether bridge to a methylene bridge with elimination of e.g. formaldehyde or methanol [129,136–138].	12
Figure 4. Schematic representation of adsorption and desorption equilibrium from a fluid phase at adsorption sites of the solid adsorbent.	15
Figure 5. Schematic for the surface mole ratio method, adapted from the graphical abstract of Wei et al. [179].	22
Figure 6. Overview of the classification of pore sizes (according to IUPAC [142]) and suitable gases for analysis with approximate range of applicability. For each gas the respective kinetic diameter d_{kin} [185,186] and the corresponding usual measuring temperature T are given [142].	23
Figure 7. Classification of different isotherms and b) hysteresis loops according to IUPAC. Taken from [142].	25
Figure 8. Classification of different hysteresis loops according to IUPAC, adapted from [142].	26
Figure 9. Structure of a TEM, based on [196]. The beam path of non-scattered electrons is shown in blue, the sample and subsequent intermediate images and the projection on the detector as a red arrow. The beam path of scattered electrons is shown in green and orange. Lenses and apertures are drawn in black.	29
Figure 10. Design of an ICP-OES instrument, based on [201].	31

Mesoporous Poly(Melamine-co-Formaldehyde) Particles for Efficient and Selective Phosphate and Sulfate Removal:

- Figure 5.1.** ATR-FTIR spectra of (a) H-PMF and (b) P-PMF samples. All spectra were normalized to the bending of the triazine ring at 812 cm^{-1} for comparability. The modes marked with a dashed line are 1 NH bending and $\nu\text{ C=N}$; 2 + 3 CH_2 bending; 4 triazine bending; 5 $\nu\text{ Si-O}$ 40
- Figure 5.2.** Thermogravimetric analysis from (a) the H-PMF samples and (b) the P-PMF samples with PMF-66 shown in black, PMF-79 in red, PMF-85 in blue, PMF-88 in green and PMF-89 in orange. 41
- Figure 5.3.** (a) TEM image of H-PMF-66, (f) TEM image of P-PMF-66 and (l) SEM image of P-PMF-66; (b) TEM image of H-PMF-79; (g) TEM image of P-PMF-79 and (m) SEM image of P-PMF-79; (c) TEM image of H-PMF-85; (h) TEM image of P-PMF-85 and (n) SEM image of P-PMF-85; (d) TEM image of H-PMF-88; (i) TEM image of P-PMF-88 and (o) SEM image of P-PMF-88; (e) TEM image of H-PMF-89; (k) TEM image of P-PMF-89 and (p) SEM image of P-PMF-89. 43
- Figure 5.4.** (a) Particle size distributions of the unpurified reaction mixtures of H-PMF samples; (b) particle size distribution of the P-PMF samples and H-PMF-66 after purification. H-PMF-66 is shown in gray, H-PMF-79 in pink, H-PMF-85 in light blue, H-PMF-88 in light green, H-PMF-89 in light orange. P-PMF-66 is shown in black, P-PMF-79 in red, P-PMF-85 in blue, P-PMF-88 in dark green and P-PMF-89 in orange. 43
- Figure 5.5.** (a) Nitrogen (N_2) de-/adsorption isotherms measured at 77 K for H-PMF samples; (b) carbon dioxide (CO_2) de-/adsorption isotherms measured at 273 K for P-PMF samples; (c) nitrogen (N_2) de-/adsorption isotherms measured at 77 K for P-PMF samples. Data points in the adsorption and desorption branch of the isotherms are indicated by filled and empty symbols, respectively. (d) Pore size distribution (PSD) analysis for the adsorption branch was calculated by using QSDFT (quenched solid state density functional theory) model for carbon with slit/cylindrical/sphere pores. H-PMF-66 is shown in gray, H-PMF-79 in pink, H-PMF-85 in light blue, H-PMF-88 in light green, H-PMF-89 in light orange P-PMF-66 is shown in black, P-PMF-79 in red, P-PMF-85 in blue, P-PMF-88 in dark green and P-PMF-89 in orange. 45
- Figure 5.6.** Sorption isotherms for sulfate ions onto H-PMF-66 (gray), P-PMF-66 (black), P-PMF-79 (red), P-PMF-85 (blue), P-PMF-88 (green) and P-PMF-89 (orange) with the corresponding Langmuir fits (solid lines). The corresponding pH values are displayed in Figures S7–S12. The fitting parameters are displayed in Table 5.3. The respective fitting comparison can be seen in Figure S13. 47
- Figure 5.7.** SEM image and SEM-EDX elemental mapping of P-PMF-88 after the adsorption of sulfate with $c_{\text{eq}} = 1502\text{ mg/g SO}_4^{2-}$ with the elements C shown in red, N in yellow and S in dark green.. 49
- Figure 5.8.** Sorption isotherms for phosphate ions onto H-PMF-66 (gray), P-PMF-66 (black), P-PMF-79 (red), P-PMF-85 (blue), P-PMF-88 (green) and P-PMF-89 (orange) with the corresponding Langmuir fits (solid lines). The corresponding pH values are displayed in Figures S7–S12. The fitting parameters are displayed in Table 5.4. The respective fitting comparison can be seen in Figure S14. 50
- Figure 5.9.** SEM image and SEM-EDX elemental mapping of P-PMF-88 after adsorption of phosphate with $c_{\text{eq}} = 1502\text{ mg/g PO}_4^{3-}$ with the elements C shown in red, N in yellow and P in light green. 52

- Figure 5.10.** Percentage adsorption of PO_4^{3-} (solid) and SO_4^{2-} (striped) for H-PMF-66 and the P-PMF samples from a solution containing both 10 mg/L PO_4^{3-} and 10 mg/L SO_4^{2-} , whereby H-PMF-66 is shown in gray, PMF-66 in black, P-PMF-79 in red, P-PMF-85 in blue, P-PMF-88 in green and P-PMF-89 in orange. The respective pH_0 and pH_{eq} values can be seen in Figure S15. 53
- Figure 5.11.** Percentage adsorption of PO_4^{3-} (solid) and SO_4^{2-} (striped) for H-PMF-66 from (a) solutions containing both phosphate (at different concentrations) and 20 mg/L sulfate; (b) solutions of 1:1 ratios of phosphate and sulfate at different concentrations. The respective pH_0 and pH_{eq} values can be seen in Figure S16 and S17. 54

Tuning the Pore Structure of Templated Mesoporous Poly(melamine-co-formaldehyde) Particles toward Diclofenac Removal:

- Figure 6.1.** Structure of diclofenac (DCF) as sodium salt. 68
- Figure 6.2.** Nitrogen (N_2) de-/adsorption isotherms measured at -196°C for H-PMF samples, b) Nitrogen (N_2) de-/adsorption isotherms measured at -196°C for P-PMF samples, c) Carbon dioxide (CO_2) de-/adsorption isotherms measured at 0°C for P-PMF samples, d) Pore size distribution (PSD) analysis for the adsorption branch using QSDFT. d) Carbon dioxide (CO_2) de-/adsorption isotherms measured at 0°C for H-PMF samples are shown in the SI. Data points in the adsorption and desorption branch of the isotherms are indicated by filled and empty symbols, respectively. H-PMF-HS40 is shown in light blue as circles, H-PMF-2HS40 in light green as squares, H-PMF-AS40 in light red as triangles, H-PMF-TMA in light yellow as diamonds, and H-PMF-TM40 in light violet as stars. P-PMF-HS40 is shown in blue as circles, P-PMF-2HS40 in green as squares, P-PMF-AS40 in red as triangles, P-PMF-TMA in yellow as diamonds and P-PMF-TM40 in violet as stars. 76
- Figure 6.3.** Particle size distribution measured by laser diffractometry for a) the H-PMF particles and b) the P-PMF particles. H-PMF-HS40 is shown in light blue (solid), H-PMF-2HS40 in light green (dashed), H-PMF-AS40 in light red (dotted), H-PMF-TMA in light yellow (dash-dot line), and H-PMF-TM40 in light violet (dash-dot-dot line). P-PMF-HS40 is shown in blue (solid), P-PMF-2HS40 in green (dashed), P-PMF-AS40 in red (dotted), P-PMF-TMA in yellow (dash-dot line) and P-PMF-TM40 in violet (dash-dot-dot line). 78
- Figure 6.4.** a) – k) TEM images of a) H-PMF-HS40, b) H-PMF-2HS40, c) H-PMF-AS40, d) H-PMF-TMA, e) H-PMF-TM40, f) P-PMF-HS40, g) P-PMF-2HS40, h) P-PMF-AS40, i) P-PMF-TMA and k) P-PMF-TM40. l) – p) SEM images of l) P-PMF-HS40, m) SEM image of P-PMF-2HS40, n) P-PMF-AS40, o) P-PMF-TMA, and p) of P-PMF-TM40. SEM images of the H-PMF particles are shown in Figure S11 – S15. Enlarged TEM images are shown in Figure S16 – S25. 79
- Figure 6.5.** a) Sorption isotherms for DCF onto P-PMF-HS40 (blue, circles) and P-PMF-2HS40 (green, squares) and P-PMF-AS40 (red, triangles), P-PMF-TMA (yellow, diamonds) and P-PMF-TM40 (violet, stars) with the corresponding Langmuir fits (solid lines). The corresponding pH values are displayed in Figure S31 – S35. A graphical fitting comparison to Dubinin-Radushkevich can be seen in Figure S36. The fitting parameters are displayed in Table 6.4. b) Schematic of the possible interactions for the adsorption of DCF (ocher) with an exemplary structure of PMF

(black). Here, hydrogen bonds are shown in blue, ionic interaction in green and aromatic π - π interaction in red. 81

Adsorption vs. Surface Precipitation of Cu^{2+} onto Porous Poly(melamine-co-formaldehyde) Particles:

Figure 7.1. a) Nitrogen (N_2) de-/adsorption isotherms measured at 77 K for H-PMF and P-PMF samples, b) N_2 de-/adsorption isotherms measured at 77 K for N-PMF samples, c) Pore size distribution (PSD) analysis for the P-PMF samples, calculated from the adsorption branch by using QSDFT (quenched solid-state density functional theory) model for carbon with slit/cylindrical/sphere pores. d) Carbon dioxide (CO_2) de-/adsorption isotherms measured at 273 K for P-PMF and N-PMF samples. Carbon dioxide (CO_2) de-/adsorption isotherms measured at 273 K for H-PMF samples are shown in the SI. Data points in the adsorption and desorption branch of the isotherms are indicated by filled and empty symbols, respectively. P-PMF-0.5 is shown in dark blue with circles, H-PMF-0.5 in light blue with circles, H-PMF-1 in dark green with squares, H-PMF-1 in light green with squares, P-PMF-1.5 in red with triangles, H-PMF-1.5 in pink with triangles, N-PMF-0.5 in yellow with circles, N-PMF-1 in orange with squares, and N-PMF-1.5 in brown with triangles. 99

Figure 7.2. TEM imaging of thin sections of a) H-PMF-0.5, b) H-PMF-1.0, c) H-PMF-1.5, d) P-PMF-0.5, e) P-PMF-1.0, and f) P-PMF-1.5. g) SEM image of P-PMF-0.5, h) SEM image of P-PMF-1.0, and i) SEM image of P-PMF-1.5. Overview images of the H-PMF thin sections are given in Figure S7 – S9. 101

Figure 7.3. a) SEM image of N-PMF-0.5, b) SEM image of N-PMF-1.0, and c) SEM image of N-PMF-1.5. 102

Figure 7.4. a) and b) Adsorption isotherms of a) Cu^{2+} and b) SO_4^{2-} onto P-PMF samples and N-PMF-1.5 from experiments with CuSO_4 solution after 24 h adsorption. c) and d) Adsorption isotherms of c) Cu^{2+} and d) SO_4^{2-} onto P-PMF samples and N-PMF-1.5 from adsorption experiments with CuSO_4 solution after 2 h adsorption. Data points for Cu^{2+} are displayed as filled squares and for SO_4^{2-} as crossed squares. Data points and isotherms for P-PMF-0.5 are shown in blue with circles, for P-PMF-1.0 in green with squares, for P-PMF-1.5 in red with triangles, and for N-PMF-1.5 in brown with triangles. The respective Langmuir isotherm fits are presented as solid lines and the Dubinin-Radushkevich isotherm as dotted lines of the corresponding color. The respective fitting parameters are displayed in Table S2. pH values before and after adsorption are presented in Figure S13. 103

Figure 7.5. a) WAXS diffractogram of P-PMF samples after adsorption experiments with CuSO_4 solution ($c_0 = 15.7 \text{ mmol/L Cu}^{2+}$) and equilibration time of 24 h shown together with the reference reflexes of the identified $\text{Cu}_4(\text{SO}_4)(\text{OH})_6$ species [55]. P-PMF-0.5 is shown in blue, P-PMF-1.0 in green and P-PMF-1.5 in red. b) – k) SEM-EDX images of the P-PMF samples after adsorption (CuSO_4 , $c_0 = 15.7 \text{ mmol/L Cu}^{2+}$) with b) SEM image of P-PMF-0.5 after adsorption with the respective elemental mapping for c) Cu and d) S, e) SEM image of P-PMF-1.0 after adsorption with the respective elemental mapping for f) Cu and g) S, and h) SEM image of P-PMF-1.5 after adsorption with the respective elemental mapping for j) Cu and k) S. 105

- Figure 7.6.** EPR spectra of the PMF samples after adsorption experiments with CuSO_4 solution containing a) 0.16 mmol/L Cu^{2+} and b) 15.7 mmol/L Cu^{2+} . P-PMF-0.5 is shown in blue, P-PMF-1.0 in green, P-PMF-1.5 in red, and N-PMF-1.5 is shown in brown. 107
- Figure 7.7.** a) and b) adsorption isotherms of a) Cu^{2+} and b) NO_3^- onto P-PMF samples and N-PMF-1.5 from experiments with $\text{Cu}(\text{NO}_3)_2$ solution after 24 h adsorption. The inset in a) shows the respective data points for the lower concentration region and the respective Langmuir fitting. In general, data points for Cu^{2+} are displayed as filled symbols, whereas open symbols in the inset represent data points that were not included in the Langmuir fit but shown for clarity. In b), data points for NO_3^- are shown as open symbols, whereas the additionally crossed symbols were used for the Langmuir fitting. The Langmuir isotherms are shown as solid lines for both diagrams. The combined Langmuir/sigmoidal Boltzmann fit is shown as dashed line and all data points were used for this fit in both cases. Data points and isotherms for P-PMF-0.5 are shown in blue with circles, for P-PMF-1.0 in green with squares, for P-PMF-1.5 in red with triangles, and for N-PMF-1.5 in brown with triangles. The respective fitting parameters are displayed in Table 7.3. pH values before and after adsorption are presented in Figure S16..... 108
- Figure 7.8.** a) WAXS diffractogram of P-PMF samples after adsorption experiments with $\text{Cu}(\text{NO}_3)_2$ solution ($c_0 = 15.7$ mmol/L Cu^{2+}) and the reference reflexes of the identified $\text{Cu}_2(\text{NO}_3)(\text{OH})_3$ species [58]. P-PMF-0.5 is shown in blue, P-PMF-1.0 in green and P-PMF-1.5 in red. b) – k) SEM-EDX images of the P-PMF samples after adsorption ($\text{Cu}(\text{NO}_3)_2$, $c_0 = 15.7$ mmol/L Cu^{2+}) with b) SEM image of P-PMF-0.5 after adsorption with the respective elemental mapping for c) Cu and d) N, e) SEM image of P-PMF-1.0 after adsorption with the respective elemental mapping for f) Cu and g) N, and h) SEM image of P-PMF-1.5 after adsorption with the respective elemental mapping for j) Cu and k) N..... 109
- Figure 7.9.** a) WAXS diffractogram of P-PMF-0.5 after adsorption experiments with $\text{Cu}(\text{NO}_3)_2$ solution at different concentrations (equilibration time 24 h) shown together with the reference reflexes of $\text{Cu}_2(\text{NO}_3)(\text{OH})_3$ (black) [58]. The diffractograms are presented in darker colors of blue for higher concentrations of Cu^{2+} . b) EPR spectra of the PMF samples after adsorption experiments with $\text{Cu}(\text{NO}_3)_2$ solution containing 0.16 mmol/L Cu^{2+} . P-PMF-0.5 is shown in blue, P-PMF-1.0 in green, P-PMF-1.5 in red, and N-PMF-1.5 is shown in brown. 110
- Figure 7.10.** a) and b) adsorption isotherms of a) Cu^{2+} and b) Cl^- onto P-PMF samples and N-PMF-1.5 from experiments with CuCl_2 solution after 24 h adsorption. The inset in a) shows the respective data points for the lower concentration region with the respective Langmuir isotherm for these data points. Here, data points for Cu^{2+} are displayed as filled symbols. In b), data points for Cl^- are shown as open symbols, whereas the additionally crossed symbols were used for the Langmuir fitting. The Langmuir isotherms are shown as solid lines for both diagrams. The combined Langmuir/sigmoidal Boltzmann fit is shown as dashed line and all data points were used for this fit. Data points and isotherms for P-PMF-0.5 are shown in blue with circles, for P-PMF-1.0 in green with squares, for P-PMF-1.5 in red with triangles, and for N-PMF-1.5 in brown with triangles. The respective fitting parameters are displayed in Table 7.5. pH values before and after adsorption are presented in Figure S18. 113
- Figure 7.11.** a) SEM image of crystalline $\text{Cu}_4(\text{SO}_4)(\text{OH})_6$ surface precipitate on P-PMF particles and b) Potential equilibria and reactions present in adsorption experiments with dissolved Cu^{2+} and

anions (A^{m-}) which are leading to the removal of the respective ions by either surface precipitation yielding crystalline $[Cu_xA(OH)_y]$ (left-hand side) or adsorption by electrostatic interaction or coordination (right-hand side).....	116
 <i>SiO₂ Nanospheres as Surfactant and Template in Aqueous Dispersion Polymerizations Yielding Nanoporous Resin Particles:</i>	
Figure 8.1. a) Particle size distribution of H-PMF-Std (dashed line) and P-PMF-Std (solid line), b) SEM image of H-PMF-Std, and c) SEM image of P-PMF-Std.....	133
Figure 8.2. TEM images of ultrathin-sections of a) H-PMF-Std, and d) P-PMF-Std; b) TEM image of an ultrathin-section of H-PMF-Std with respective elemental maps for c) nitrogen, e) silicon, and f) oxygen from EFTEM measurements.	135
Figure 8.3. a) Nitrogen (N_2) de-/adsorption isotherm measured at 77 K for P-PMF-Std, b) Pore size distribution (PSD) analysis for the adsorption branch was calculated by using QSDFT (quenched solid-state density functional theory) model for nitrogen on carbon with slit/cylindrical/sphere pores. Data points in the adsorption and desorption branch of the isotherms are indicated by filled and empty symbols, respectively.	136
Figure 8.4. a) Particle size distribution of PMF-Water-2 (dark green), PMF-Water-3 (light green) and PMF-Std (black) with H-PMF samples shown as dashed lines and P-PMF samples as solid lines. b) – c) SEM image of b) H-PMF-Water-2 and c) P-PMF-Water-2. d) – e) TEM images of ultrathin-sections of d) H-PMF-Water-2 and e) P-PMF-Water-2. SEM and TEM images of PMF-Water-3 can be seen in Figure S4 – S9.....	137
Figure 8.5. Particle size distribution of the sample from the a) P-PMF-Cat with P-PMF-Std is shown in black, P-PMF-Cat-43 in dark red, and P-PMF-Cat-11 in light red. b) SEM image of P-PMF-Cat-11, c) SEM image of P-PMF-Cat-43. The corresponding particle size distribution of the hybrid particles with SEM images can be seen in Figure S10.	138
Figure 8.6. Particle size distribution of the sample from the a) P-PMF-SiO ₂ series. P-PMF-Std is shown in black (solid line), P-PMF-SiO ₂ -49 in dark blue (dashed line), P-PMF-SiO ₂ -10 in medium blue (dotted line), and P-PMF-SiO ₂ -0 in light blue (dash-dot line). b) SEM image of P-PMF-SiO ₂ -49, c) SEM image of P-PMF-SiO ₂ -10, and d) SEM image of P-PMF-SiO ₂ -0. The corresponding particle size distribution and SEM images of the H-PMF-SiO ₂ hybrid particles can be seen in Figure S12.	140
Figure 8.7. Particle size distribution of a) the H-PMF samples and b) the P-PMF samples (solid line) from the PMF-Temp series. P-PMF-Std is shown in black (solid line), P-PMF-Temp-90 in red (dashed line), P-PMF-Temp-80 in violet (dotted line), P-PMF-Temp-60 in dark blue (dash-dot line), P-PMF-Temp-40 in medium blue (dash-dot-dot line), and P-PMF-Temp-25 in light blue (short-dashed line). c) – g) SEM images of the P-PMF particles with c) P-PMF-Temp-90, d) P-PMF-Temp-80, e) P-PMF-Temp-60, f) P-PMF-Temp-40, and g) P-PMF-Temp-25.	141
Figure 8.8. a) Nitrogen (N_2) de-/adsorption isotherms measured at 77 K for P-PMF-Temp samples, b) Pore size distribution (PSD) analysis for the adsorption branch was calculated by using QSDFT (quenched solid-state density functional theory) model for nitrogen on carbon with slit/cylindrical/sphere pores. Data points in the adsorption and desorption branch of the	

isotherms are indicated by filled and empty symbols, respectively. P-PMF-Std is shown in black as circles, P-PMF-Temp-90 in red as squares, P-PMF-Temp-80 in violet as upwards triangles, P-PMF-Temp-60 in dark blue as diamonds, P-PMF-Temp-40 in medium blue as stars, and P-PMF-Temp-25 in light blue as downwards triangles.....	142
Figure 8.9. Particle size distribution of a) the H-PMF-Std and the H-PMF-Time samples and b) the respective P-PMF-Time samples after etching with NaOH. PMF-Std is shown in black (solid line), PMF-Time-120 in brown (short-dotted line), PMF-Time-30 in dark violet (dashed line), PMF-Time-20 in rose (dotted line), PMF-Time-10 in light green (dash-dot line), PMF-Time-5 in medium green (dash-dot-dot line) and PMF-Time-0 in dark green (short-dashed line). c) – f) SEM images of c) and d) P-PMF-Time-0, and of e) and f) P-PMF-Time-120. Images of all P-PMF-Time samples are presented in Figure S23.....	144
Figure 8.11. Schematic mechanism for the formation of templated, colloidal H-PMF particles. The oligomeric precursor molecules are shown as yellow stars, the formed PMF resin is shown in white and the SiO ₂ NPs as blue spheres. Here, Step 1 needs sufficient time for the complete conversion of melamine and formaldehyde to the precursor species. Step 4 to 6, which include the interaction with SiO ₂ NPs need ideally a reaction temperature of 100 °C, while decreasing the temperature will lead to a significantly decreased interaction between both.....	148
Figure 8.12. a) Time-dependent adsorption isotherm for $c_0 = 100$ mg/L Cr ₂ O ₇ ²⁻ onto P-PMF-Time-Col with the corresponding Pseudo-first order (solid lines) and pseudo-second order (dashed lines). The corresponding pH values are displayed in Figure S29. The corresponding K ⁺ adsorption is shown in Figure S30. The fitting parameters are displayed in Table S5. b) Sorption isotherm for Cr ₂ O ₇ ²⁻ onto P-PMF-Col after 240 min equilibration time with the corresponding Langmuir (solid line), Sips (dashed line) and Dubinin-Radushkevich (dotted line) fits. The corresponding pH values are displayed in Figure S31 and K ⁺ adsorption is presented in Figure S32. The fitting parameters are displayed in Table 8.5.	151
Figure 8.13. Results for the fixed bed adsorption experiment of Cr ₂ O ₇ ²⁻ ions onto P-PMF-Col from K ₂ Cr ₂ O ₇ solution. The corresponding exponential models (Bohart-Adams, Thomas and Yoon-Nelson) can be seen as solid line, while the Weibull model is shown as dotted line. The corresponding pH values are displayed in Figure S34. The adsorption of K ⁺ is shown in Figure S35.	153

Waterborne Phenolic, Triazine-Based Porous Polymer Particles for the Removal of Nickel, Cadmium, and Lead Ions:

Figure 9.1. Synthesis of the monomer 3PT. [40].....	164
Figure 9.2. a) Reaction scheme of the synthesis of poly(3PT-co-formaldehyde) (P(3PT-F)), b) Image of 3PT powder, and c) image of P(3PT-F)-3L.	166
Figure 9.3. a) Nitrogen (N ₂) sorption isotherms measured at 77 K for the P(3PT-F) samples, b) Pore size distribution (PSD) analysis for the P(3PT-F) samples, calculated from the adsorption branch by using QSDFT (quenched solid-state density functional theory) model for carbon with slit/cylindrical/sphere pores. Data points in the adsorption and desorption branch of the isotherms are indicated by filled and empty symbols, respectively. P(3PT-F)-2 is shown in red,	

List of Figures

P(3PT-F)-3 in dark blue, P(3PT-F)-4 in green, and P(3PT-F)-3L in light blue. Carbon dioxide (CO ₂) sorption isotherms measured at 273 K are shown in Figure S5.	173
Figure 9.4. SEM images of a) and b) P(3PT-F)-2, c) and d) P(3PT-F)-3, e) and f) P(3PT-F)-4, g) and h) P(3PT-F)-3L and i) particle size distribution (volume) for the samples with P(3PT-F)-2 in red, P(3PT-F)-3 in dark blue, P(3PT-F)-4 in green, and P(3PT-F)-3L in light blue.	175
Figure 9.5. a) ¹³ C CP MAS NMR spectra for P(3PT-F)-2 (red line), P(3PT-F)-3 (dark blue line), P(3PT-F)-4 (green line) and P(3PT-F)-3L (light blue line) with peaks 1 – 8, described in detail in Table S1. The peaks are shaded according to the proposed assignments. b) Example chemical substructure of the polymer network. The colored highlights of the peaks 1 – 8 in a) correspond to the similarly highlighted carbon atoms in the chemical structure in b).	176
Figure 9.6. ATR-FTIR spectrum of 3PT (black), P(3PT-F)-2 (red), P(3PT-F)-3 (dark blue), P(3PT-F)-4 (green) and P(3PT-F)-3L (light blue) with the significant mode assignment and normalized to the s-triazine bending at 812 cm ⁻¹ for reasons of comparability.....	177
Figure 9.7. Streaming potential of P(3PT-F)-3L (light blue) over the pH range of 3.5 to 9.0.	178
Figure 9.8. Adsorption isotherm of a) Ni ²⁺ from NiSO ₄ solution and b) Cd ²⁺ from CdSO ₄ solution, and c) b) Pb ²⁺ from Pb(NO ₃) ₂ solution onto P(3PT-F)-3L with the respective fittings for the Sips isotherm model. The pH values before and after adsorption are displayed in Figure S10 – S12. A graphical fitting comparison can be seen in Figure S13 – S15.	179
Figure 9.9. Adsorption capacity of P(3PT-F)-3L from experiments with a Pb(NO ₃) ₂ solution with c ₀ = 100 mg/L Pb ²⁺ at various pH ₀ . The respective pH _{eq} values after adsorption are presented in Figure S22.	182
Figure 9.10. a) Percentage adsorption and b) adsorption capacity of P(3PT-F)-3L from the selectivity experiments with a solution containing 0.5 mmol of Pb ²⁺ (103.6 mg/L), Cu ²⁺ (31.8 mg/L), Fe ²⁺ (27.9 mg/L), Ca ²⁺ (20.0 mg/L), K ⁺ (19.6 mg/L), Mg ²⁺ (12.2 mg/L), and the respective anion Cl ⁻ of all ions with c _{0,Cl-} = 3 mmol/L (212.7 mg/L). The experiment was conducted as triplet with respective standard deviation in both percentage adsorption and capacity shown as vertical bars. The pH ₀ before adsorption was 4.01 and pH _{eq} after adsorption 3.02.	183
Figure 9.11. Adsorbed (orange) and desorbed (green) capacity of Pb ²⁺ from respective adsorption/desorption experiments of P(3PT-F)-3L. The error bars correspond to the standard deviation from duplets. Adsorption was carried out with 30 mL Pb(NO ₃) ₂ solution containing 100 mg/L Pb ²⁺ with an equilibration time of 24 h. Desorption was carried out using 10 mL 0.5 M HCl solution for 3 h equilibration time. The capacity of Pb ²⁺ that was ad-/desorbed, was calculated with respect to the total amount of Pb ²⁺ in the respective 30 mL or 10 mL. The initial pH ₀ of the adsorption experiments was 5.1 and pH _{eq} after adsorption was 3.3 for both times.	183

List of Tables

Mesoporous Poly(Melamine-co-Formaldehyde) Particles for Efficient and Selective Phosphate and Sulfate Removal:

Table 5.1. Results of the elemental analysis (C, H, N) for the different PMF samples. The residue describes the relative mass, which is not attributed to the elements C, H and N. n/n (C/N) is the molar ratio of C atoms/N atoms calculated from elemental analysis.....	42
Table 5.2. Surface area (S_{BET}), pore volume (PV), micro pore volume (MPV) and CO_2 uptake of the H- and P-PMF samples and dried Ludox® HS-40.	45
Table 5.3. Fitting parameters for Langmuir and Dubinin–Radushkevich isotherm models for sulfate adsorption onto H-PMF-66 and P-PMF samples. Q_m thereby is the maximal sorption capacity, K is the equilibrium constant, β_{DR} represents the activity coefficient related to the energy of adsorption E_{Ads} . R^2 (COD) is the coefficient of determination for the respective fit. For all parameters, the corresponding standard error from the fit is given. The respective fitting comparison can be seen in Figure S13.	47
Table 5.4. Fitting parameters for Langmuir and Dubinin–Radushkevich isotherm models for phosphate adsorption onto H-PMF-66 and P-PMF samples. Q_m thereby is the maximal sorption capacity, K is the equilibrium constant, β_{DR} represents the activity coefficient related to the energy of adsorption E_{Ads} . R^2 (COD) is the coefficient of determination for the respective fit. For all parameters, the corresponding standard error from the fit is given. The respective fitting comparison can be seen in Figure S14.	50
Table 5.5. Table of reactants in synthesis (melamine (M), paraformaldehyde (F) and Ludox® HS-40 (HS-40)) for of H-PMF and P-PMF particles with the corresponding sample codes.....	57

Tuning the Pore Structure of Templated Mesoporous Poly(melamine-co-formaldehyde) Particles toward Diclofenac Removal:

Table 6.1. Nominal particle size and stabilizing counter ion of the used silica dispersions, stated by the manufacturer W. R. Grace & Co.-Conn.	70
Table 6.2. Table of reactants (melamine (M), paraformaldehyde (F), and Ludox® HS-40 (for PMF-HS40 and PMF-2HS40), AS-40 (for PMF-AS40), TMA (for PMF-TMA) and TM-40 (for PMF-TM40) of respective H-PMF and P-PMF particles with the corresponding sample codes.....	71
Table 6.3. Surface area (S_{BET}), pore volume (PV), micro pore volume (MPV) and CO_2 uptake of the PMF samples.....	76
Table 6.4. Fitting parameters for Langmuir and Dubinin-Radushkevich isotherm model for DCF adsorption onto the P-PMF samples. Q_m is the maximal sorption capacity, K_L is the Langmuir equilibrium constant, β_{DR} is the activity coefficient for Dubinin-Radushkevich and $E_{\text{Ads,DR}}$ is the mean free energy of adsorption associated with the activity coefficient β_{DR} . The Gibbs energy change ΔG° was calculated from K_L . R^2 (COD) is the coefficient of determination. All parameters are given with their corresponding standard error.....	82

Adsorption vs. Surface Precipitation of Cu^{2+} onto Porous Poly(melamine-co-formaldehyde) Particles:

Table 7.1. Overview of the reactants (melamine (M), paraformaldehyde (F), and Ludox® HS-40 (HS-40)) used for the synthesis with the respective pH values of the reaction mixtures. The synthesis varied in the addition of Ludox® HS-40 as template and the water content. Non-templated samples without the addition of Ludox® HS-40 were labeled as N-PMF. Samples containing Ludox® HS-40 in the reaction mixture were labeled as H-PMF and P-PMF. H-PMF stands for the hybrid (H-) material containing PMF and SiO_2 particles. After the removal of the SiO_2 particles from the hybrid material, the pure PMF polymer (P-PMF) remains.....	92
Table 7.2. Surface area (S_{BET}), pore volume (PV), micro pore volume (MPV) and CO_2 uptake of the PMF samples.....	99
Table 7.3. Fitting parameters for Langmuir (L) isotherm fits for the adsorption of Cu^{2+} and NO_3^- ions from $\text{Cu}(\text{NO}_3)_2$ solution in the low-concentration region after 24 hours equilibrium time (Figure 7.7), respectively. Q_m thereby is the maximum sorption capacity, K_L is the Langmuir equilibrium constant R^2 (COD) is the coefficient of determination for the respective fit. For all parameters, the corresponding standard error from the fit is given.....	109
Table 7.4. Fitting parameters for combined Langmuir and sigmoidal Boltzmann isotherm (L-sB) fits for the adsorption of Cu^{2+} and NO_3^- ions from $\text{Cu}(\text{NO}_3)_2$ solution after 24 hours equilibrium time (Figure 7.7), respectively. Q_m thereby is the maximum sorption capacity from sigmoidal Boltzmann. c_p represents the inflection point of the phase change and dc the slope factor. R^2 (COD) is the coefficient of determination for the respective fit. In the fitting, Langmuir parameters were from the previous fit in low concentrations are used as constants to prevent over-parametrization. For all parameters, the corresponding standard error from the fit is given.	112
Table 7.5. Fitting parameters for Langmuir (L) and combined Langmuir and sigmoidal Boltzmann (L-sB) isotherm fits for the adsorption of Cu^{2+} and Cl^- ions from CuCl_2 solution after 24 hours equilibrium time (Figure 7.10). Q_m thereby is the maximum sorption capacity, K_L is the Langmuir equilibrium constant. c_p represents the medium concentration of the phase change and dc the slope factor, which are both derived from the combined Langmuir and sigmoidal Boltzmann fit. R^2 (COD) is the coefficient of determination for the respective fit. For all parameters, the corresponding standard error from the fit is given.	114

SiO_2 Nanospheres as Surfactant and Template in Aqueous Dispersion Polymerizations Yielding Nanoporous Resin Particles:

Table 8.1. Table of synthesis parameters of respective H-PMF and P-PMF particles with the corresponding sample codes. The used amounts for the reactants are displayed in Table S1. .	127
Table 8.2. Surface area (S_{BET}), pore volume (PV), and micro pore volume (MPV) of the P-PMF-Cat and P-PMF- SiO_2 samples.....	139
Table 8.3. Surface area (S_{BET}), pore volume (PV), and micro pore volume (MPV) of the P-PMF-Temp samples.....	143

Table 8.4. Surface area (S_{BET}), pore volume (PV), and micro pore volume (MPV) of the PMF samples.	145
Table 8.5. Fitting parameters for Langmuir, Sips and Dubinin-Radushkevich isotherm model for $\text{Cr}_2\text{O}_7^{2-}$ adsorption from $\text{K}_2\text{Cr}_2\text{O}_7$ solution onto P-PMF-Col. Q_m thereby is the maximal sorption capacity and K is the Langmuir or Sips equilibrium constant, n is the Sips model exponent, β_{DR} is the activity coefficient for Dubinin-Radushkevich and $E_{\text{Ads,DR}}$ is the mean free energy of adsorption associated with the activity coefficient β_{DR} . For all parameters, the corresponding standard error from the fit is given.	152
Table 8.6. Fitting parameters for the Thomas, Bohart-Adams, Yoon-Nelson and the Weibull model for $\text{Cr}_2\text{O}_7^{2-}$ adsorption onto P-PMF-Col. Q_m thereby is the maximum adsorption capacity and K is the rate constant, N_0 is the saturation concentration per bed volume including bed voidage, $t_{0.5}$ is the breakthrough time of Yoon-Nelson, when half of the contamination is retained. a and b are parameters for the Weibull equation. For all parameters, the corresponding standard error from the fit is given.	154

Waterborne Phenolic, Triazine-Based Porous Polymer Particles for the Removal of Nickel, Cadmium, and Lead Ions:

Table 9.1. Respective masses of the two monomers, 3PT and paraformaldehyde (F), and dispersant volumes used in the synthesis and variation of the equivalents of F for the products P(3PT-F)-2, P(3PT-F)-3, P(3PT-F)-4, and P(3PT-F)-3L.	166
Table 9.2. Surface area (S_{BET}), pore volume (PV), micro pore volume (MPV) and CO_2 uptake of the samples. Carbon dioxide (CO_2) sorption isotherms measured at 273 K are shown in Figure S5.	174
Table 9.3. Fitting parameters for Langmuir, Sips and Dubinin–Radushkevich isotherm models for adsorption of Ni^{2+} and Cd^{2+} onto P(3PT-F)-3L. Q_m thereby is the maximum adsorption capacity, K is the equilibrium constant of Langmuir or Sips, n is the Sips model exponent, and β_{DR} represents the activity coefficient related to the mean free energy of adsorption $E_{\text{Ads,DR}}$. R^2 is the coefficient of determination (COD) for the respective fits. For all parameters, the corresponding standard error given from the fit are displayed. The respective graphical fitting comparison can be seen in Figure S13 – S15. The fitting for Dubinin-Radushkevich was conducted with concentration in mol/L.	180

Abbreviations

3PT	2,4,6-tris(2,4,6-trihydroxyphenyl)-1,3,5-triazine
ATR-FTIR	Attenuated total reflection Fourier-transformed infrared spectroscopy
BET	Brunauer-Emmett-Teller method
DFT	Density functional theory
D-R	Dubinin-Radushkevich isotherm model (abbreviation only used in tables)
EA	Elemental analysis for the determination of the elemental weight fractions of C, H, N and S
EELS	Electron Energy Loss Spectroscopy
EFTEM	Energy-filtered transmission electron microscopy
FK-NMR	Solid-state nuclear magnetic resonance spectroscopy
H-PMF	Templated, non-etched PMF/SiO ₂ hybrid particles
ICP-OES	Inductively coupled Plasma optical emission spectroscopy
IUPAC	International Union of Applied Chemistry
L	Langmuir isotherm model (abbreviation only used in tables)
N-PMF	Non-templated PMF particles
NMR	Nuclear magnetic resonance spectroscopy
P(3PT-F)	Poly(2,4,6-tris(2,4,6-trihydroxyphenyl)-1,3,5-triazine-co-formaldehyde)
PMF	Poly(melamine-co-formaldehyde)
P-PMF	Templated, etched PMF particles
PSD	Pore size distribution
QSDFT	Quenched solid density functional theory
SEM	Scanning electron microscopy
SEM-EDX	Scanning electron microscopy with coupled energy-dispersive X-ray spectroscopy
SiO ₂ NPs	Silica nanoparticles
TEM	Transmission electron microscopy
TGA	Thermogravimetric analysis
UV-VIS	Spectroscopy in the range of ultraviolet and visible light
WAXS	Wide-angle x-ray scattering
WHO	World Health Organization
XRD	X-ray diffractometry

Symbols

a	Weibull model parameter
b	Weibull model exponent
c	Concentration
Index 0	... initial, before the adsorption experiment
Index eq	... in equilibrium, after the adsorption experiment
Index S	... saturation concentration
d	Diameter
d_{kin}	Kinetic diameter of a molecule
d_A	Resolution limit of a microscope
$E(t)$	Exponential term of Thomas/Bohart-Adams/Yoon and Nelson model
$E_{Ads,DR}$	Mean free energy of adsorption calculated by the Dubinin-Radushkevich isotherm model
h	Planck constant ($6.62607015 \cdot 10^{-34} \text{ J} \cdot \text{s}$)
K	Equilibrium or rate constant
Index 1	... of pseudo-first order kinetic model
Index 2	... of pseudo-second order kinetic model
Index A	... of adsorption
Index D	... of desorption
Index F	... of the Freundlich isotherm model
Index L	... of the Langmuir isotherm model
Index S	... of the Sips isotherm model
m	Mass
Index A	... of the adsorbent used
Index e	... of an electron
MPV	Micropore volume
n	Model exponent (of the Freundlich or Sips isotherm model)
N_0	Saturation capacity of Bohart-Adams model
N_A	Avogadro constant
$N_{Ads,eq}$	Number of adsorbate molecules in equilibrium
$N_{Ads,max}$	Maximum number of adsorbate molecules; equal to the number of binding sites
n_a	Adsorbed substance amount in BET equation
n_m	Adsorbed substance amount of a monolayer in BET equation
n_r	Refractive index
p	Pressure
Index 0	Saturation vapor pressure
pH	pH-Wert of a solution
Index 0	... initial, before the adsorption experiment
Index eq	... in equilibrium, after the adsorption experiment
PV	Pore volume
q	Experimental adsorption capacity
Index Des	... respective capacity released by desorption
Index eq	... in equilibrium after adsorption
Index eq,t	... in kinetic equilibrium at time t
Q_m	Maximum adsorption capacity, determined by fitting with an isotherm model
$Q_{m,fit}$	Maximum adsorption capacity, determined by fitting with an isotherm model
$Q_{m,exp}$	Maximum experimentally determined adsorption capacity of an isotherm

Symbols

R	Universal gas constant (8.3145 J/(mol · K))
R^2 (COD)	Coefficient of determination of an isotherm model fit
T	Absolute temperature in K
$t_{0.5}$	break through time by Yoon and Nelson model
t_c	Thickness of adsorbate multilayer in mesopores before pore condensation occurs
u	Superficial velocity
V	Volume of adsorptive solution
v	Volume flow rate
v_e	Velocity of an electron
V_m	Molar volume of the adsorbate
wt. %	Weight percent
X_{red}^2	Mean square weighted deviation of an isotherm model fit
α	Half opening angle of the aperture
β_{DR}	Activity coefficient of the Dubinin-Radushkevich isotherm model
ΔG°	Change in Gibbs free energy
ε	Polanyi potential
Θ	Coverage
λ	Wavelength
σ_m	Average cross-sectional area of a gas molecule
γ	Surface tension

1. Introduction

The increasing industrialization and the simultaneously growing world population increase the negative influence of humanity on its habitat. Water, which is both the basis of all life and the foundation of many industrial processes, is particularly affected by this [1–3]. Although laws to protect the environment and conserve resources, including water, are being incorporated into national legislation worldwide, the pollution of natural surface waters is already very advanced in both emerging and developed countries [1,4,5]. According to the World Health Organization (WHO), about 785 million people are still not sanitized by sufficiently clean water. Of these, about 144 million depend on surface water and its water quality alone [6,7]. In addition to microbiological pollution, chemical pollutants such as toxic heavy metal ions, oxyanions, and persistent organic trace pollutants (also often called emerging pollutants or persistent organic pollutants) [6]. These contaminants harm both the corresponding ecosystems and ultimately humans, who are also exposed to them through bioaccumulation due to their position at the end of the food chain [8–10].

In this context, poly(melamine-co-formaldehyde) (PMF) represents a promising starting material for adsorption processes. PMF is a polymer network that exhibits a number of remarkable properties, such as an extremely high proportion of nitrogen atoms and extreme resistance to acids, bases and organic solvents. In addition to the very high proportion of amino groups, the aromatic *s*-triazine ring can be used to establish strong interactions with pollutants and bind them [11]. Both the separation of hydrophobic pollutants via its aromatic structure and the separation of metal ions via coordinative bonds or anions via ionic interactions with protonated, positively charged amino groups are possible [11]. PMF also has the advantage that it can be prepared from the relatively inexpensive monomers formaldehyde and melamine. It is polymerizable in water, whereby no environmentally harmful organic solvents need to be used [12,13]. Nonetheless, PMF has the crucial disadvantage of lacking intrinsic nanoporosity with pore diameters greater than 1 nm. For adsorption, two important principles for the adsorbents are crucial, namely the accessible number of binding sites and mass transport through the adsorbent. However, in order to provide as many binding sites as possible for the adsorption of contaminants, porosity is crucial to achieve the highest accessible specific surface area. The greatest contribution to an increase in specific surface area is achieved by pores with particularly small diameters. The second point, mass transport, is essential for time-efficient separation. The mass transport is mainly characterized by diffusion, which is enhanced in high pore volumes, thus large pore diameters. These two principles are in conflict with each other, but mesopores with their diameter between 2 nm and 50 nm represent an optimum compromise between the two. They contribute decisively to both increased mass transfer and increased specific surface area. In general, PMF has already been investigated for adsorption of dyes [14–16], sulfate [17] and

heavy metal ions [18,19] from aqueous solutions and CO₂ from gas mixtures [20]. However, syntheses that involved heating melamine and formaldehyde in dimethyl sulfoxide at 170 °C to obtain a pore structure were mainly used for this purpose [14,18,21]. However, this has to be considered critically because the solvent decomposes here and leads to the contamination of the polymer with sulfur [14,21]. This contamination and also the high energy consumption for heating to 170 °C often for mostly 96 h is in strong contradiction to its use as an environmentally friendly adsorbent material. Templating processes, which offer another possibility of pore generation, are usually applied together with the use of organic solvents or surfactants to form a pore structure in PMF [22,23]. Accordingly, an alternative, more environmentally friendly synthesis route for the preparation of highly porous PMF particles is needed, which represents an important further development step for the implementation of PMF as material in water treatment processes.

Heavy anthropogenic contamination with heavy metal ions occurs, for example, through mining activities [7,24–26], smelting and metal processing [7,25,27] as well as through inappropriate disposal of process waste or effluents [25,26,28–30]. In this context, various heavy metal ions have extreme effects on aqueous ecosystems, e.g., metal ions cause gene alterations, liver and kidney damage, and disruption of osmoregulation and hematology in fish, among others [31–36]. For algae and invertebrates, various heavy metal ions are toxic simply because of their acidic nature [34,35]. For humans, the ingestion of heavy metal ions or other metal ions such as Al³⁺ leads to very different pathology, e.g., severe organ damage, damage to the nervous system, reproductive toxicity, and cancer [24,25,31,37–44]. Since the toxicity of these metal ions occurs even at the smallest quantities, the corresponding limit values for drinking water, as specified, for example, by the WHO [45] or the German Drinking Water Ordinance are also very low [46].

The input of oxyanions such as sulfate, nitrate and phosphate to water bodies is strongly influenced by anthropogenic processes in addition to geological processes such as rock weathering. These include mine drainage, coal burning, infiltration of wastewater, use of synthetic detergents, fertilization, soil erosion associated with agricultural activities, and discharge of untreated wastewater into water bodies [47–54]. High sulfate content in water accelerates the corrosion of steel and cement in urban sewers, pipes, and on bridges [55,56]. Sulfate is partially toxic to various aquatic life forms [57,58] and can be microbiologically converted to hydrogen sulfide, resulting in additional pollution [59,60]. Phosphate has drastic effects on the environment as it is the limiting growth factor for most water bodies and is thus crucial for harmful algal blooms and eutrophication [52,53,61–63]. This leads, for example, to oxygen deficiency and foul sludge formation, thus threatening many aquatic life forms [64]. Apart from the ecotoxic and adverse effects of phosphorous on human health, phosphorus extracted from rock resources is finite, while its demand is rapidly increasing with the growing world population [65]. Phosphorus is considered irreplaceable for global agriculture, and it is

expected that the maximum production rate (peak phosphorus) will be reached as early as around 2030 and that rock resources will be exhausted in as little as 50 to 100 years [65,66]. Therefore, more attention must be paid to the recovery of phosphorus from various sources [67–73] as it was tested for recovery from sewage sludge [74–76], metalworking slag [77–81], or municipal waste [82].

Persistent organic pollutants enter the environment in the form of herbicides, dyes, hormones, and pharmaceuticals [83,84]. Pharmaceutical products in particular are of great concern because they have been developed to interfere with biochemical processes of living organisms and are widely used in humans, as well as in cattle and other livestock and pets. In some industrialized countries, more than 100 different pharmaceutical products have been detected in surface, ground or tap water [85]. Some of them are very persistent and can have a half-life of up to several days or even months in freshwater [86]. Diclofenac (DCF), an example of these compounds, is an anti-inflammatory agent used for humans and livestock. Its use for cattle is highly controversial because DCF causes kidney failure in vultures when they eat carcasses of treated deceased animals [87–89]. This has almost led to the extinction of several vulture species in South Asia and Africa, which are now considered critically endangered [90]. In the aquatic environment, DCF has genotoxicity in mussels, causes severe organ damage in fish, and a general decline in macrophyte biovolume [91,92].

The separation of all these pollutant classes from surface waters as well as from contaminated process and waste waters, which are later to be returned to the natural cycle, is imperative.

The current method of separating pollutants currently differs greatly between the different classes of pollutants, as they have both different initial concentrations and exhibit very different potential interactions. The separation of heavy metal ions, for example, is usually realized by flocculation processes with alkaline reagents, coagulation with aluminum or iron salts, or by ion exchange or electrochemical processes [93,94]. However, the disadvantage here is that complete separation is usually not achieved with these processes, or secondary contamination occurs due to the addition of iron or aluminum salts as coagulants [94]. However, heavy metal ions in particular tend to accumulate in sediments, causing long-term contamination of waters and soils [93,94]. Due to their high toxicity, they thus pose a very high potential risk as soon as they are remobilized, such as by the appearance of suitable counter ions, bacteria, dissolved organic matter, natural colloids, or a pH change of the water [95–100].

The removal of oxyanions often takes place by biological processes [101–103]. Biological removal is a lengthy process and can be realized mainly at low concentrations. However, it usually requires good pretreatment and close monitoring of the biotransformation processes taking place to avoid negative side reactions [103]. Especially during the microbiological conversion of sulfate, toxic hydrogen sulfide can be generated [59,60,103].

Organic pollutants are removed to a large extent by oxidation or also by biological processes [104–107]. A disadvantage is that oxidation processes are usually very energy- or material-intensive to ensure continuous conversion. Many organic contaminants can be well degraded by biological processes, but various biocides prevent microbiological conversion [94].

However, all impurities can also be removed by adsorption processes, which is already being implemented on an industrial scale. Adsorption is one of the most energy-efficient methods [108]. With suitable adsorbents, not only selective separation but also the possibility of recovery of the adsorbed raw material can be achieved. The choice of a suitable adsorbent depends on the pollutants contained and on the prevailing properties of the solution to be purified. Surface waters affected by acid mine drainage show an extremely acidic pH, often between 2 – 6 [68,69,109]. Process wastewaters with high heavy metal ion or oxyanion loadings are also often very acidic, such as wastewaters from lithium battery recycling processes after digestion steps with H_2SO_4 and H_2O_2 [110–112]. Accordingly, the adsorbent materials used must be extremely resistant in this corrosive chemical environment. Bio-based adsorbent materials such as chitosan show good adsorption properties [113,114] while being eco-friendly, but unmodified chitosan is not resistant in acidic environments and dissolves [114–116]. Synthetic adsorbent materials are widely used in the form of activated carbon or resins based on styrene and divinylbenzene, which have been modified with ionic groups such as sulfonic acid or ammonium functionalities [101,102,117]. The disadvantage of activated carbon is that it usually does not show good adsorption performance against highly charged pollutants due to its aromatic nature and the absence of functional groups. They are mainly suitable for adsorption of hydrophobic organic contaminants. In contrast, adsorption on commonly available ion exchange resins is based on the opposite ionic charge of the contaminants, and separation is accordingly non-selective. Since the interaction occurs statistically and is influenced maximally by the charge strength of the ions, harmless ions are often adsorbed more strongly when they are present in higher concentrations than the extremely low-concentration impurities.

Due to the many possible interactions that amino groups exhibit with these classes of contaminants, PMF represents an excellent basis for an efficient adsorbent, which will be further explored in this work.

2. Objectives and Experimental Design

This dissertation addresses the synthesis of highly nanoporous resin particles with high density of functional groups and their use for the separation of water pollutants. Specifically, poly(melamine-co-formaldehyde) (PMF) forms the core of this work, as this resin can undergo a variety of physical interactions due to its extraordinary density of nitrogen functionalities in the form of amines and the *s*-triazine ring. These interactions include coordinative, ionic, and dipolar interactions. Thus, PMF represents a very good starting point for the adsorption of diverse pollutants [14–19,118–122].

The overall first goal of this work is the nanostructuring of the intrinsically non-porous PMF resin and the generation of a pore structure with pore diameters in the mesoporous range. So far, mainly syntheses using solvothermal processes or such, which consume large amounts of organic solvents or surfactants have been reported in the literature [14,15,18,21]. In contrast, this work will focus on the preparation of highly porous PMF particles in aqueous dispersion polymerization, which can already be occasionally found in the literature. Here, a pore structure is generated via the use of nanoscopic spherical silica particles (SiO₂ NPs) as a sacrificial matrix in a hard templating process [13]. The use of commercially available SiO₂ NPs has the advantage of future application on a larger scale. The already published synthesis is to be further developed and important properties optimized for later use as an adsorbent by varying various parameters.

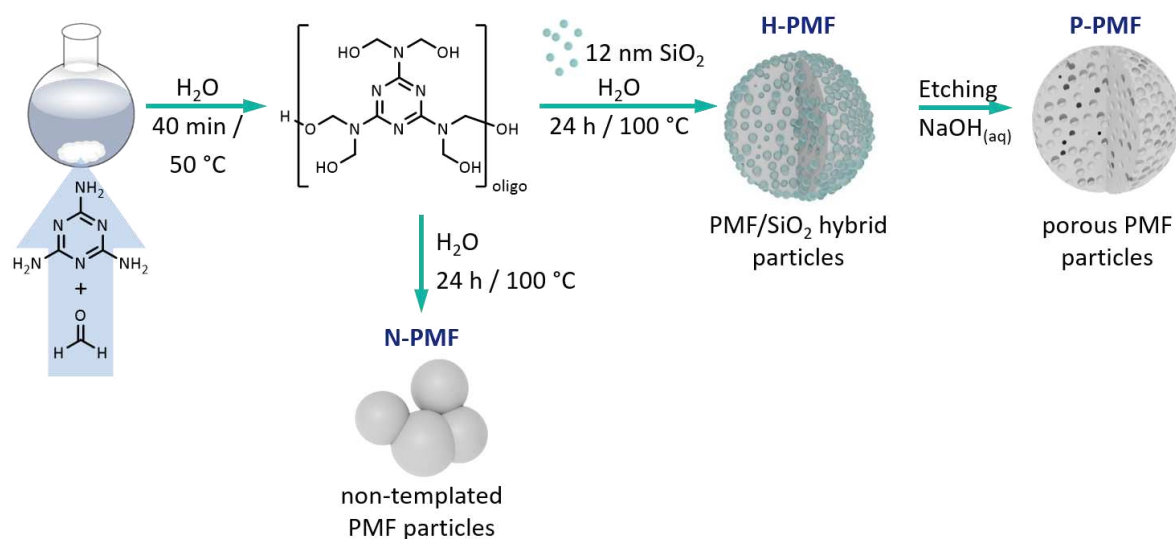


Figure 1. Schematic representation of the synthesis route for the preparation of templated and non-templated PMF particles. The first step shows the prepolymerization of melamine and formaldehyde to the oligomeric prepolymer. Subsequent dispersion polymerization yields templated silica/PMF hybrid particles (H-PMF) with SiO₂ nanoparticles as template (*upper reaction*). Subsequent templating/etching with NaOH produces porous PMF particles (P-PMF). Without templating (*reaction below*), non-templated PMF particles (N-PMF) are obtained. The indicated times (50 min for prepolymerization and 24 h for polymerization) and polymerization temperature (100 °C) are partially varied within the work.

An overview of the synthesis of PMF particles used is shown in Figure 1. The dispersion polymerization consists of two steps. First, a prepolymerization of the monomers melamine and formaldehyde takes place in water at 50 °C, in which both components react to form an oligomeric precursor species. The second step is the actual polymerization, which is started by the addition of oxalic acid as catalyst and takes place at up to 100 °C. By adding the SiO₂ NPs to the precursor solution in the second step, PMF/silica hybrid particles are formed, which are subsequently referred to as H-PMF particles. Etching of these H-PMF particles with aqueous 1 M NaOH solution leads to the removal of the silica particles, yielding porous PMF particles. These will be referred to as P-PMF in the following. Compared to the templated version, PMF particles can also be synthesized using the same methodology without adding silica as a hard template. These non-templated particles are referred to as N-PMF.

Within the framework of this synthesis method, the influence on the resulting particles can be investigated by varying individual synthesis parameters. The morphology of the produced particles will be analyzed by transmission (TEM), scanning electron microscopy (SEM) and particle size measurement (laser diffraction). Elemental analysis (EA), attenuated total reflection Fourier-transformed infrared spectroscopy (ATR-FTIR), energy-filtered TEM (EFTEM), SEM with energy-dispersive X-ray spectroscopy (SEM-EDX), and streaming potential vs. pH measurements will be used to validate the identity and chemical properties of the resin. Thermogravimetric analysis (TGA) will allow quantification of the amount of embedded silica in the H-PMF particles and demonstrate complete removal of the template in the P-PMF particles. Together, the results of these studies will provide information on the influence of individual synthesis parameters on the particle formation and the templating process. The parameters can be distinguished between changed composition of the reaction mixture and changed process parameters. The following parameters were to be investigated for this work:

Composition of the reaction mixture:

- Catalyst concentration
- Amount of dispersant
- Diameter of SiO₂ NPs
- Stabilizer of the template
- Quantity of the template

Process parameters:

- Stirring speed
- Polymerization temperature
- Prepolymerization time

This leads to the investigation of the particle formation mechanism as the second goal of this dissertation. Especially the interaction between the SiO₂ NPs and the different organic species, which occur within the polymerization from the precursor species to the PMF polymer network, have not been sufficiently investigated so far. Basic work on dispersion polymerization with melamine and formaldehyde in water is already available [123], but the multi-component system is incomparably more complex when using SiO₂ NPs together with

melamine, formaldehyde, the resulting oligo- and polymers, the colloidal silica, and water as dispersant. Previous studies on the synthesis of silica-templated PMF particles often only rudimentarily describe the underlying interactions of the reaction components. Comprehensive experiments with varied synthesis parameters and kinetic studies will provide a more comprehensive overall picture. Existing literature describing this system or other resin polymers can be checked for validity and extended if necessary. The results, which can be assigned to this objective, are included in chapters 5 – 8. The influence of the template quantity is presented in more detail in chapter 5. In chapter 6, the influence of different templates with different diameters and different stabilizing counter ions on the resulting pore structure is highlighted. Chapter 7 summarizes the results that can be obtained by using different amounts of dispersant and shows a comparison with non-templated particles of the same synthesis method. Chapter 8 summarizes results on a whole range of parameters, which add to those of the previously mentioned chapters. Especially variation of the catalyst quantity, the influence of the polymerization temperature and the prepolymerization time are also mentioned here and used to propose the underlying mechanism of the PMF synthesis. A short overview about the chapters is given in Figure 2.

In addition to understanding the templating and particle formation process itself, a very important third goal for this work arises: The mechanistic investigation here should lead to the synthesis of uniform PMF particles with a size of several micrometers without significantly reducing the porosity of these particles. In previous literature, only spherical, porous PMF particles with diameters in the range of several hundred nanometers to the maximum of about 1 μm are known, which, however, cannot be used as a flow-through fixed-bed adsorber due to the resulting pressure. To lower the pressure required for flow-through applications, particle diameters in the range of about 10 μm or larger are necessary. The achievement of this goal represents an important step towards the large-scale applicability of these research results. Results working towards this goal can be found in chapter 8.

PMF has been used sporadically in the literature for various adsorption experiments. For example, the adsorption of heavy metals by coordinative bonding to PMF was investigated [19]. However, the PMF prepared in a solvothermal synthesis showed substantial sulfur impurities due to the preparation process, which can significantly affect the adsorption. However, the extent to which this had an influence was not investigated. In the literature, first adsorption experiments on oxyanions can be found very briefly in the sense of a proof of principle [13], in which, however, the maximum adsorption capacity could not be determined. However, this is an important parameter for the performance of adsorbents. Furthermore, there are no publications to date that explicitly investigate the adsorption performance of PMF for both metal ions and anions, although both pollutant classes act competitively in this

regard. While the adsorption of metal ions is based on coordinative interactions, the adsorption of anions requires an ionic interaction with protonated amines, which are thus no longer available for the binding of metal ions.

In the field of organic water pollutants, publications on dyes [15] and nitrobenzene [16] can already be found in the literature. In contrast, adsorption of pharmaceuticals has been performed only in a single study for PMF, although these pollutants are becoming increasingly important due to their persistence, omnipresence and low effect concentration. In this aforementioned study, single experiments were conducted for the removal of ibuprofen, ciprofloxacin, and tetracycline [118]. Accordingly, there is great potential for research in this area in particular.

The adsorption of heavy metal ions, of oxyanions and of organic pollutants, which have hardly been tested so far, can thus be investigated in detail. Specifically, the objective here is to obtain a comprehensive picture of the adsorption mechanism of the different pollutant classes on the highly porous PMF particles. In particular, the relationship between adsorption performance and the pore system of the particles will be established, which will be tested for the respective adsorption application.

In order to investigate the adsorption of oxyanions, sulfate and phosphate ions were selected. Here, a possible separation of both components from a binary system will also be investigated, since the recovery of phosphorus as a limited resource is steadily gaining urgency [65,66,71]. The analysis of the concentrations is performed by optical emission spectroscopy with inductively coupled plasma (ICP-OES). Results on this sub-objective are presented in chapter 5.

Since very little research and publication has been done on the adsorption of pharmaceuticals using PMF, this work will be the first to test the adsorption of diclofenac (DCF), which can be quantified in solution using UV/VIS spectroscopy. Since DCF has a size of about 0.43 nm [124], the size and accessibility of the pores especially in the micro- and mesoporous region can exert considerable influence on the adsorption. Accordingly, the influence of, for example, pore size, diameter of the connecting channels or micropore volume on the adsorption process is to be determined on suitable PMF particles with different pore systems in each case. Results concerning this sub-objective are described in chapter 6.

Cu^{2+} was selected for the heavy metal separation study using PMF particles. Although Cu^{2+} has no particular toxicity, it was chosen for the experiments because it can be analyzed by electron paramagnetic resonance spectroscopy (EPR spectroscopy) to obtain information about the coordination environment. By using different copper(II) salts, we will also test the influence of the anion on the interaction of PMF to Cu^{2+} under competitive conditions. Furthermore, in order to investigate possible cooperative effects such as a joint deposition of these ions on the adsorbent surface, the samples will be investigated after adsorption by wide angle X-ray diffraction (WAXS), energy filtered TEM (EFTEM) and scanning electron

microscopy with coupled energy dispersive X-ray spectroscopy (SEM-EDX). Mathematical modeling of the experiments will be based on the information obtained about the sorption process by the mentioned methods and can be done using known isotherm equations from the literature, if possible. The associated results will be discussed in chapter 7.

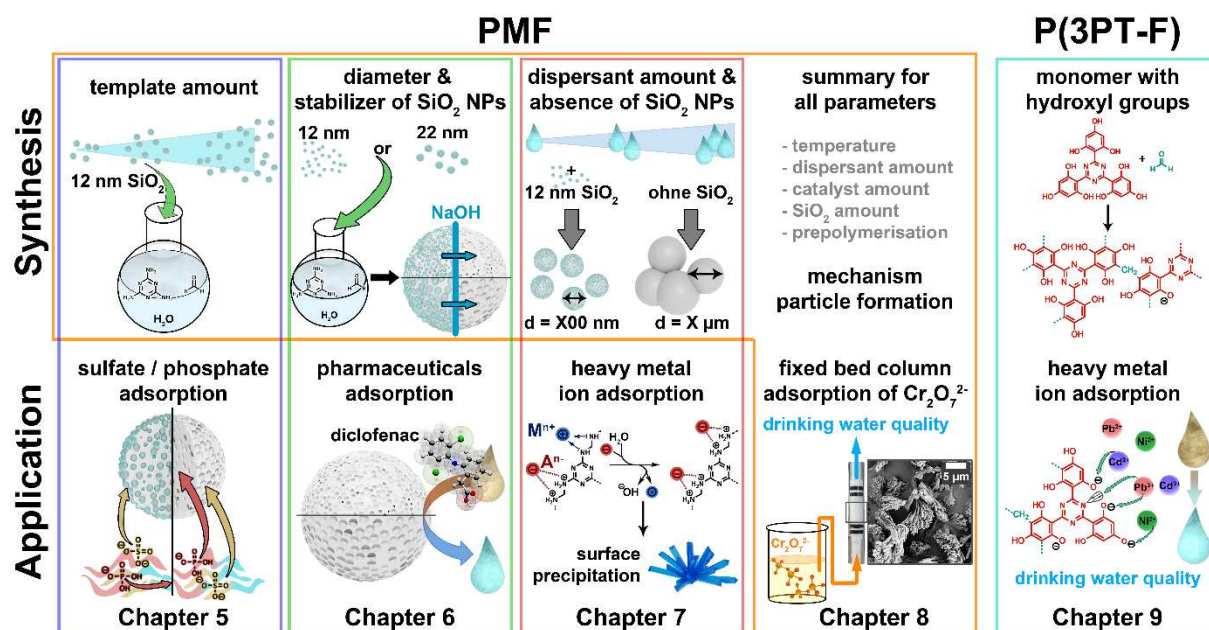


Figure 2. Schematic representation of the individual chapter contents of the dissertation on the polymers PMF and P(3PT-F), which are each divided into a synthesis and an application part.

In order to obtain a modified adsorption performance towards the individual pollutant classes, a modified functionalization of the resin materials can be achieved by exchanging the co-monomer melamine for another monomer. This will be demonstrated using the triazine-based monomer 2,4,6-tris(2,4,6-trihydroxyphenyl)-1,3,5-triazine (3PT) as an example. The monomer synthesis is already known from the literature, and subsequent studies showed that it is capable of expressing strong intramolecular hydrogen bonds between the hydroxyl groups and the s-triazine ring due to its hydroxyl groups and triazine ring [125]. Thus, a resin material containing this monomer is a promising starting point for the adsorption of heavy metal ions via ionic and coordination interactions.

A polymerization of this monomer has already been carried out in the literature with terephthalaldehyde as a solvothermal synthesis at 200 °C for 96 h and this was subsequently tested for proton conductivity [126]. In contrast to this, a polymerization with formaldehyde is to be carried out in the context of this work to produce a previously unpublished polymer. In this case, a less aromatic character of the resulting resin due to the non-aromatic crosslinker formaldehyde would be advantageous for the hydrophilicity of the resulting polymer and thus better accessibility for e.g. heavy metal ions.

For the preparation of these triazine-based resin particles based on the 3PT monomer, dispersion polymerization will be applied analogous to the previously mentioned PMF

particles, using water as an environmentally friendly dispersant. The hitherto unknown polymer network is to be investigated without templating the network formation. Here, as a first parameter, the influence of different amounts of formaldehyde as crosslinker can be tested. The morphological material properties of the produced resin (P(3PT-F)) will be investigated via N₂ sorption, SEM and particle size measurements. Chemically, the novel polymer network is characterized via solid-state nuclear magnetic resonance (FK-NMR) spectroscopy, as well as ATR-FTIR spectroscopy, EA and TGA. Adsorption experiments with various toxic heavy metal ions are performed to fundamentally prove the applicability. Here, the study of the adjusted adsorption equilibrium in solution is also performed by ICP-OES and UV/VIS spectroscopy, and the adsorbent is examined by SEM-EDX analysis after the experiments to gain insight into the mechanism. The synthesis and application of the P(3PT-F) resin is presented in Chapter 9.

3. Scientific Background

3.1. *Poly(melamine-co-formaldehyde)*

Poly(melamine-co-formaldehyde) (PMF) is a copolymer network of melamine and formaldehyde, which has been known since 1936 through its discovery by William F. Talbot [127]. PMF, or melamine resin, quickly gained great commercial importance due to the ease of handling and production of the resin. After its discovery, melamine resin was mainly used as a thermoset for various molded parts, including electronic equipment due to its high thermal resistance and fire retardant properties. It is widely used for the production of various hybrid materials due to its high mechanical and thermal stability, for example, in the gluing of pressed chipboard or as a protective layer on paints [128–130]. Since it is non-toxic under normal use, shatterproof kitchenware is also made from it [128,131]. The basic material melamine was first produced and studied by Justus von Liebig in 1834 [132]. The high economic importance of melamine resin was also due to the fact that melamine could be produced on an industrial scale since the 1930s. Nowadays, it is obtained via the trimerization of urea and belongs to the group of high production volume chemicals (HPVC) [133,134]. It is worth mentioning here that there are already possibilities to synthesize urea from CO₂, so melamine could potentially be obtained in an environmentally friendly way [135].

3.1.1. Polymerization Mechanism

The polymerization of melamine and formaldehyde to PMF occurs in several steps, which are shown in Figure 3. First, the reaction of melamine with several parts of formaldehyde (usually between two and six) already takes place without a catalyst to form methylol melamine precursor [129,136–138]. Here, the amount of formaldehyde used determines the degree of conversion from the primary amino groups to the mono- or di-substituted methylolamines, i.e., to the fully converted hexamethylolmelamine [137,138]. This monomeric precursor species may afterwards partially oligomerize to low molecular weight prepolymers. In this case, the oligomerization and thus increase in molecular weight takes place only slowly without a catalyst and depends strongly on the ambient temperature and correspondingly on the reaction time [128]. In the prepolymer, mainly the expression of reversible ether bridges occurs due to their good cleavability [139,140]. In general, the methylolated precursor species and the oligomeric prepolymer are very hydrophilic due to the high proportion of polar end groups and are highly soluble in water despite the aromatic triazine structure [128].

The actual polymerization takes place via a polycondensation reaction, which can be either acid- or base-catalyzed or conducted without a catalyst by solvothermal synthesis [141]. In this process, two methylolamine groups can react to form a methylene ether bridge or a methylolamine and an amino group can react to form a methylene bridge, in each case with

the elimination of water. Under basic conditions, the reaction favors ether bridges, while acid catalysis leads to a higher number of methylene bridges [20]. Furthermore, it is possible to eliminate one molecule of formaldehyde or methanol from methylene ether bridges, which also leads to the formation of a methylene bridge [129,137,138,140]. This is known as curing of the resin. The resulting non-crystalline network structure is characterized by a high density of three-dimensional crosslinks, which give PMF its high thermal and mechanical stability. The polymerization rapidly decreases the number of hydrophobic end groups and simultaneously increases the degree of crosslinking of the polymer, which enhances the aromatic character of the polymer and therefore increases the hydrophobicity of PMF sharply [128]. The spatially very dense network structure of PMF also leads to very small pore diameters (d) in the ultramicroporosity range ($d < 0.7$ nm) [142]. Here, the pore diameters achieved are in some cases so small that they are already below the kinetic radius of CO_2 molecules and are accordingly not accessible neither by N_2 nor CO_2 sorption measurements [121].

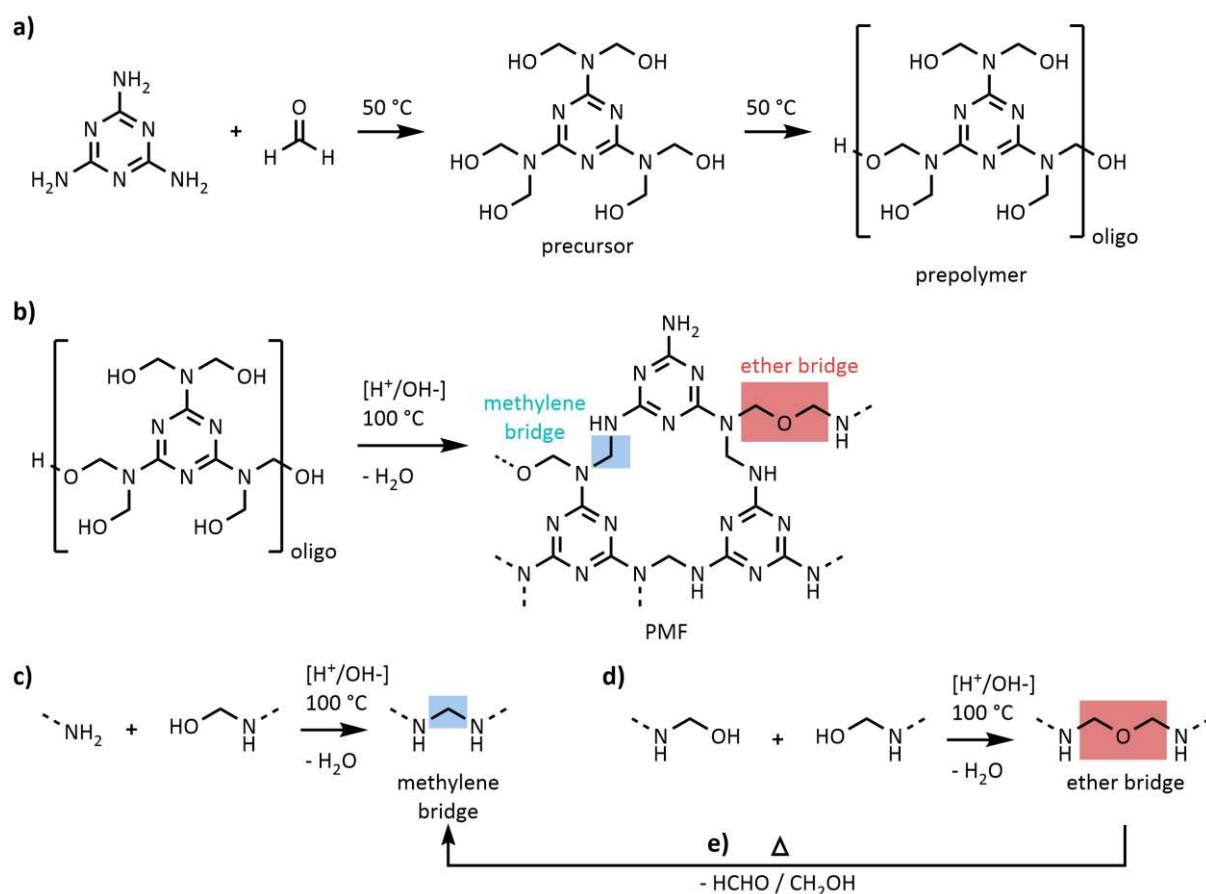


Figure 3. Schematic polymerization mechanism for the polycondensation of PMF. a) shows the prepolymerization, which typically takes place at 50 °C, where melamine and formaldehyde first condense to an up to sixfold methylolated (shown here) precursor species, followed by oligomerization to the prepolymer. b) describes the polycondensation at typically 100 °C under base or acid catalysis to an exemplary structure of the crosslinked PMF resin. In c) and d), respectively, the formation of c) methylene bridges and d) ether bridges is visible, which are also highlighted in the exemplary PMF structure in b). e) Elimination reaction of an ether bridge to a methylene bridge with elimination of e.g. formaldehyde or methanol [129,136–138].

3.1.2. Synthesis Strategies for the Preparation of Porous PMF Particles.

Since the PMF resin has no porosity apart from ultramicropores, the functional groups of the resin are quasi inaccessible and potential mass transport of liquids through the polymer via diffusion is negligible. This greatly reduces its applicability for e.g. separation processes, since only an extremely limited amount of functional groups is thus available [119]. Therefore, in order for PMF to develop its full efficiency, it is necessary to increase its specific surface area so that as many functional groups as possible are available for adsorption application. To date, PMF is usually solvothermally synthesized to increase its specific surface area by polymerization at 170 °C in dimethyl sulfoxide for 96 h [14,18,21]. However, it is known that these temperatures lead to thermal decomposition of the solvent and thus to significant sulfur contamination of the obtained PMF [14,21]. Moreover, the consumption of organic solvent as well as the high energy required for heating reduces the usability of the adsorbent for environmental applications. Hard templating, i.e., the use of a solid as a structuring matrix, represents another, less frequently used method for generating a pore structure. For example, silica nanoparticles (SiO₂ NPs) can be used to create PMF-SiO₂ hybrid materials. Subsequent dissolution of the SiO₂ NPs with, for example, NaOH solution then leaves a pore structure with pore diameters the size of the template used [15,17,143]. Here, the use of water as a 'green', environmentally friendly solvent and the use of non-toxic and commercially available silica as a template is a key advantage.

3.1.3. Fields of Application of PMF

PMF has a very high proportion of nitrogen functionalities (mostly around 50 wt.%) due to its *s*-triazine ring and its three amino groups per melamine unit, as well as the small molecular size of formaldehyde as crosslinker. This leads to PMF forming potential starting points for use as a catalyst [144-148], for energy storage applications [149,150] gas separation or storage [119-121], or for the production of nitrogen-doped carbon [151,152]. More rarely, the application of PMF as an adsorbent for various pollutants is being investigated. There are already some studies on the adsorption of dyes [15] or other organic contaminants such as nitrobenzene [16]. However, for the adsorption of pharmaceuticals on PMF, there is only one study so far, in which single experiments were performed for the separation of ibuprofen, ciprofloxacin and tetracycline [118]. Accordingly, there is a very high research potential in this area. In the category of heavy metal ions, only Pb²⁺ has been studied in detail [18,19], and other studies show only basic single experiments for the separation of other heavy metal ions [15]. Here, the question arises as to the underlying adsorption mechanism, especially since simultaneous to the heavy metal ion separation, the interaction with the respective anions was not investigated, which, however, can most likely have a major influence due to their negative charge. Non-metallic oxyanions such as sulfate, nitrate and phosphate were separated in individual experiments as proof of concept. Here, for example, no adsorption

capacity for the adsorption was given or potential separation of multiple ions tested. Especially in the field of oxyanions and heavy metal ions, there is thus a great potential to investigate removal rates, adsorption capacity and also potential cooperative or competitive uptake of both pollutant classes. Furthermore, especially the separation of pharmaceuticals is promising, since PMF with its aromatic structure shows a very good potential for this and pharmaceuticals are also in the focus of worldwide research due to their low effect concentrations.

3.2. Adsorption

Adsorption refers to the accumulation of a substance from a fluid phase at the interface to a solid phase. Adsorption is a subtype of sorption processes in general and is distinguished from absorption, in which a substance enters the interior of a solid phase and accumulates there (Figure 4). The accumulating substance in its fluid phase is called adsorptive, while the boundary phase that forms is called adsorbate. The phase on which adsorption takes place is called adsorbent. The reverse of the process is called desorption and is in constant equilibrium with adsorption [153]. The first scientific publication describing a sorption process was made as early as 1777 by Carl Wilhelm Scheele [154].

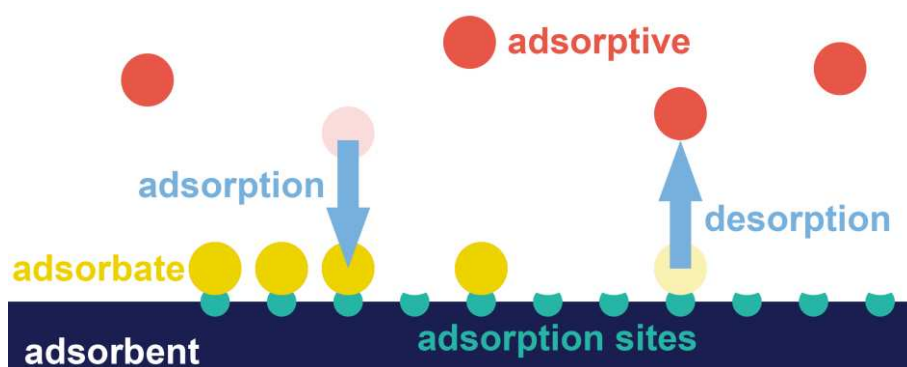


Figure 4. Schematic representation of adsorption and desorption equilibrium from a fluid phase at adsorption sites of the solid adsorbent.

Adsorption often refers to physical adsorption (physisorption), in which the interactions between adsorptive and adsorbent are characterized by non-covalent interactions (hydrogen bonding, ionic interaction, dipolar interaction, and hydrophobic interaction). In contrast, chemical adsorption (chemisorption) describes the formation of chemical bonds between adsorptive and adsorbent, thus leading to electron transfer between the adsorptives and the substrate. This usually makes physisorption a reversible process, whereas chemisorption is much more difficult to reverse. In the following, adsorption refers to physisorption.

Although only non-covalent interactions are used, the uptake of a substance by binding to an adsorbent resembles a chemical reaction and is characterized by substance-specific kinetics and thermodynamics and by an equilibrium between adsorption and desorption [155]. These processes are mainly determined by the time to reach equilibrium, the temperature, and the concentration of the adsorbent in the fluid phase, in addition to the kind of adsorptive and adsorbent itself. To measure adsorption in a system, in most cases the initial concentration and the equilibrium concentration of the adsorbent in the fluid phase are measured. Spectroscopic methods are often used for this purpose. Another possible method is gravimetric determination using the weight of the adsorbent. The adsorption capacity or loading q_{eq} of a substance corresponds to the mass or amount of substance of the adsorbate

per mass of adsorbent. For adsorption experiments from the liquid phase, it is calculated via the following equation:

$$q_{eq} = \frac{(c_0 - c_{eq}) \cdot V}{m_A} \quad (1)$$

c_0 and c_{eq} correspond to the initial and equilibrium concentration of the adsorbent in the volume V of the liquid phase, respectively. m_A represents the mass of the adsorbent used in the test.

In most cases, an adsorbent is characterized by a finite number of adsorption sites at which adsorptive can be bound. The relative surface coverage Θ can be characterized by this. It describes the ratio of the amount of substance of the bound adsorbate $N_{Ads,eq}$ and the number of binding sites $N_{Ads,max}$ and also corresponds to the ratio of equilibrium loading q_{eq} and maximum adsorption capacity Q_m (see equation (2)).

$$\Theta = \frac{N_{Ads,eq}}{N_{Ads,max}} = \frac{q_{eq}}{Q_m} \quad (2)$$

3.2.1. Adsorption Isotherms and Mathematical Modeling

Adsorption isotherms are recorded to represent the equilibrium of adsorption and desorption at a certain temperature. For this purpose, the ratio of adsorptive to adsorbent is varied at constant temperature, which often results in characteristic curves for the amount of adsorbate. For this purpose, either the mass of the adsorbent can be changed with a constant initial concentration or the initial concentrations can be varied with a constant adsorbent mass. The recorded values can be represented as adsorption isotherm in a $q_{eq}(c_{eq})$ diagram.

In order to describe the adsorption process mathematically and to derive physical quantities such as the equilibrium constant of the sorption process, the maximum loading or the adsorption energy, various isotherm models have been developed. These will be discussed in more detail below. Often adsorption models were first defined for adsorption of gases on solids and only later adapted for application to adsorption from liquids. This was done by using the equilibrium concentration c_{eq} instead of the partial pressure.

Since the present work focuses on the separation of pollutants from solutions, the following will mainly deal with the corresponding formula for adsorption from a solution. In the following, K represents the corresponding equilibrium constant, Q_m the maximum adsorption capacity and n a model exponent.

Henry Isotherm Model

The simplest model represents the linear adsorption isotherm, which is based on Henry's law for the solubility of gases in liquids (see equation (3)) [156]. Here, the adsorption capacity is assumed to increase directly proportional to the equilibrium concentration. This model is

mainly used for adsorption at extreme dilutions, very high temperatures or very low surface occupancies, in which the adsorption process can still be assumed to be linear, since no linear relationship applies outside these applications.

$$q_{eq} = K_H \cdot c_{eq} \quad (3)$$

Freundlich Isotherm Model

The first mathematical equation for an adsorption isotherm was published by Herbert Freundlich [157,158]. The Freundlich isotherm model (equation (4)) originally describes the adsorption of a gas on a surface in relation to its partial pressure. The starting point here is an energetically heterogeneous surface on which adsorption becomes energetically less favorable with increasing loading. The relationship between loading and equilibrium concentration is purely empirical in this model. Thus, when correlating the experimental data and the mathematical representation via the Freundlich isotherm, it cannot be assumed that the surface is actually energetically heterogeneous. In addition, the isotherm does not exhibit saturation loading especially at high concentrations and does not follow the correlation of Henry's law at low concentrations. As this is not true for any real surface, the use of the Freundlich isotherm is also controversial [153].

$$q_{eq} = K_F \cdot c_{eq}^n \quad (4)$$

Langmuir Isotherm Model

The Langmuir isotherm, on the other hand, is not empirical, but is based on the mathematical description of an ideal system. The adsorbent has a certain number of adsorption sites, each of which is energetically equivalent. One adsorptive particle can be bound to each of these, which leads to the formation of a monolayer on the adsorbent when completely covered. In general, it is assumed that there is no interaction between adsorptive particles, so no change in the heat of adsorption occurs with increased coverage of the surface and no formation of multilayer adsorption can occur [159]. Adsorption is proportional to the prevailing concentration in the fluid phase, expressed by the adsorption equilibrium constant K_A . Desorption is correspondingly expressed by its own equilibrium constant K_D . Once the equilibrium between adsorption and desorption is reached, it can be expressed by the following equation [160]:

$$K_A \cdot c_{eq} \cdot (1 - \Theta) = K_D \cdot \Theta \quad (5)$$

By replacing the coverage Θ with the q_{eq}/Q_m term from equation (6), the Langmuir isotherm equation can be obtained in its nonlinear form, where the Langmuir equilibrium constant K_L is the ratio of K_A/K_D :

$$q_{eq} = \frac{Q_m \cdot K_L \cdot c_{eq}}{1 + K_L \cdot c_{eq}} \quad (6)$$

It should be noted that real experiments usually deviate from at least one of the assumptions made by the Langmuir model. In particular, interactions between adsorptive species often occur or the surface of the adsorbent has heterogeneous sites with deviating surface potential [160]. Nevertheless, the Langmuir model can provide a sufficient description of the achievable maximum adsorption capacity Q_m as well as a description of the average equilibrium constant, which is why it is very often used. Moreover, the Langmuir model forms the basis for a whole series of more complex adsorption models, which partially implement the real conditions mentioned above.

Sips Isotherm Model

In order to better describe heterogeneous surfaces in particular, Robert Sips published an adsorption isotherm in 1948, which was also intended to make the statistical distribution of the adsorption energy of different adsorption sites accessible [161]. Specifically, it combines the Langmuir and Freundlich equations. In doing so, it retains a maximum saturation capacity expressed by the structure of the Langmuir equation and extends it to include the statistical energy distribution of heterogeneous adsorption sites around a mean value with the model exponent n (see equation (7)). The energy distribution here strongly resembles a Gaussian distribution in the adsorption energies calculated from it [161]. For $n = 1$, the Sips isotherm equation simplifies again to the Langmuir model.

$$q_{eq} = \frac{Q_m \cdot K_S \cdot c_{eq}^n}{1 + K_S \cdot c_{eq}^n} \quad (7)$$

Although the model exponent is also empirical in nature, the Sips model adjusts the Langmuir model for energetic heterogeneity of binding sites. However, a potential interaction between adsorptive species is still not considered.

Dubinin-Radushkevich Isotherm Model

The Dubinin-Radushkevich isotherm model is also based on the assumption of an energetic Gaussian distribution over adsorption sites of a heterogeneous surface through its consideration of the Polanyi potential ϵ of surfaces [162], which has its foundations in the Van der Waals forces [163,164]. The nonlinear form is shown in equation (8). Here, β_{DR} represents the activity coefficient of the model.

$$q_{eq} = Q_m \cdot \exp(-\beta_{DR} \cdot \epsilon^2) \quad (8)$$

The Polanyi potential ϵ can be replaced here by the following term, which includes the universal gas constant R , to show a dependence of the acting attractive forces on the temperature T , and the ratio of equilibrium concentration c_{eq} and saturation concentration c_s :

$$\varepsilon = RT \cdot \ln \left(\frac{c_s}{c_{eq}} \right) \quad (9)$$

Here, however, the saturation concentration is not well determinable empirically, since it is not identical to the solubility of the adsorptive. Therefore, another numerically identical solution is necessary. Subject to two necessary conditions, c_s/c_{eq} can be exchanged for $1 + 1/c_{eq}$. First, this requires the equilibrium concentration to be several orders of magnitude smaller than c_s , and second, the fitting must be done using mol/L as the unit for the concentration [165].

Thus, by substituting the term into equation (9), we obtain the following expression for the Polanyi potential:

$$\varepsilon = RT \cdot \ln \left(1 + \frac{1}{c_{eq}} \right) \quad (10)$$

The following equation is obtained by substituting equation (10) in (8) for the Dubinin-Radushkevich model, which can then be used for fitting:

$$q_{eq} = Q_m \cdot \exp \left(-\beta_{DR} \cdot \left(RT \cdot \ln \left(1 + \frac{1}{c_{eq}} \right) \right)^2 \right) \quad (11)$$

The Dubinin-Radushkevich model has the advantage of providing the mean free energy of adsorption $E_{Ads,DR}$ via the activity coefficient β_{DR} . The relationship is shown in equation (12).

$$E_{ads,DR} = \frac{1}{\sqrt{2 \cdot \beta_{DR}}} \quad (12)$$

Although the Dubinin-Radushkevich model was originally developed only for adsorption on microporous surfaces, it has been demonstrated that it is equally suitable for the description of macro-, meso- and nonporous systems [166]. However, since it does not follow the Henry model in low ranges of coverages and concentration ranges, it should be used mainly for the description in the range of intermediate surface coverages [167,168].

3.3. *Surface Precipitation*

The process of surface precipitation describes a special case in the separation of molecules or ions from an aqueous system. Strictly speaking, it is to be distinguished from adsorption, although it can occur simultaneously or adsorption can also be the trigger of this process.

In surface precipitation, one or more adsorptives are removed from a solution by the formation of a new solid phase close to the surface of the adsorbent. This consists of a molecular unit or complex repeating in three spatial dimensions, but not necessarily crystalline [169]. Here, the precipitation process is initiated by homogeneous or heterogeneous nucleation and leads to the inclusion or co-precipitation of the adsorptive species. These three-dimensional character of the new phase distinguishes surface precipitation from adsorption, which is mainly considered as a two-dimensional arrangement of adsorbed species on a surface, although possibly with multiple layers. A mechanistic discussion of surface precipitation took place as early as the early 1970s [169–173].

A prerequisite for the process of surface precipitation is a large potential difference between the boundary phase and the bulk phase of the solution. This means, for example, that the pH or the electrochemical potential at the adsorbent/solution boundary phase is higher or lower than in the liquid phase of the system [170]. The crucial differences between boundary phase and liquid phase, which can be found for different systems from the literature, are often highly debated and rarely clearly provable.

A whole range of interfacial phenomena can be considered as possible driving forces near the adsorbent interface (compared to the solution) for a deposition of ions or molecules. For example, a change in pH [170], a change in streaming potential due to previously adsorbed ions, or a dissociation of surface functionalities or ions. An example of the latter would be a dissociation of hydroxide ions from a metal hydroxide interface [174]. Last, there also exists the possibility of a constant equilibrium between dissociation and reattachment of metal ions from the adsorbent material itself near its boundary phase [175]. These and other effects are usually discussed controversially in the literature, since they are also inextricably linked and often two or more effects occur simultaneously. A clear proof of these effects is hardly possible so far, because the investigation of the nanoscopic, local boundary phase separated from the surrounding solution is not possible yet. For an investigation of the process in solution, i.e. in situ, zetapotential measurements, X-ray diffraction and some spectroscopic methods such as ATR-FTIR spectroscopy are partially suitable. However, in the case of zetapotential, porous systems in particular are difficult to determine, due to the very slow equilibration during their titration by limited diffusion into the pores especially for macromolecules. In X-ray diffraction, the usually large scattering reflex of water significantly reduces the accuracy of the measurement. Spectroscopic methods such as FTIR spectroscopy and electron spin resonance spectroscopy (for suitable elements) still show the greatest

potential for studying the native boundary phase of solution/precipitate/adsorbent. Analysis of the dried samples after the precipitated phase has formed allows the solid part of the sample to be studied by spectroscopic methods, X-ray diffraction, or electron microscopy. This can be done usually without interference, but neglects the influence of potentially necessary drying of the sample.

Surface precipitation has often been studied for the separation of various inorganic ions using inorganic sorbents such as metal oxides [174], minerals or soil samples [176,177] or other materials such as sulfides [175]. Crystalline precipitates often also occur at the interface [176–178]. In some cases, activated carbon [179] and, much less frequently, organic materials [180–183] are also investigated for surface precipitation. Here, the formation of precisely ordered, crystalline species is only rarely documented [181,182]. Especially for organic adsorbents, the loaded surface is not sufficiently investigated to differentiate between surface precipitation and adsorption, and in even fewer cases it is also correctly assigned to surface precipitation, although crystalline species are visible, for example [114].

In order to mathematically model surface precipitation, various approaches have been presented in the literature. According to Sposito, the simplest and universally applicable method is the summation of different known adsorption isotherms under the assumption that the species to be separated are always the same form in solution and in the separated state [169]:

$$q_{eq} = \sum_{i=1} \frac{Q_{m,i} \cdot K_i \cdot c_{eq,i}^{n_i}}{1 + K_i \cdot c_{eq,i}^{n_i}} \quad (13)$$

Here, however, the inconsistency of different adsorption isotherms at negative values for the concentration is a hindrance, which, however, occurs when the term of an isotherm is shifted along the concentration axis by subtraction, e.g. using the variable c_P as starting point for a second uptake step. Here, the term $c_{eq} - c_P$ leads to a definition gap and an inconsistency for values of c_{eq} below c_P . Accordingly, conventional adsorption isotherms are only useful if both adsorption and surface precipitation have the same starting point and occur in the same concentration range. In that case, however, it is questionable how the capacity increase due to adsorption and surface precipitation can be distinguished from each other in order to describe both processes mathematically separately.

For binary systems where, for example, both an anion and a cation are precipitated simultaneously, the surface mole ratio method was proposed to use [179]. Here, the ratio of separated anion and separated cation is plotted against the equilibrium concentration of one of the two substances. This should result in a graph with two linear sections of different slope in the publications. These two sections indicate the respective range in which the loading is caused by adsorption or surface precipitation. This is shown as an example in Figure 5.

Plot of the Surface Mole Ratio method

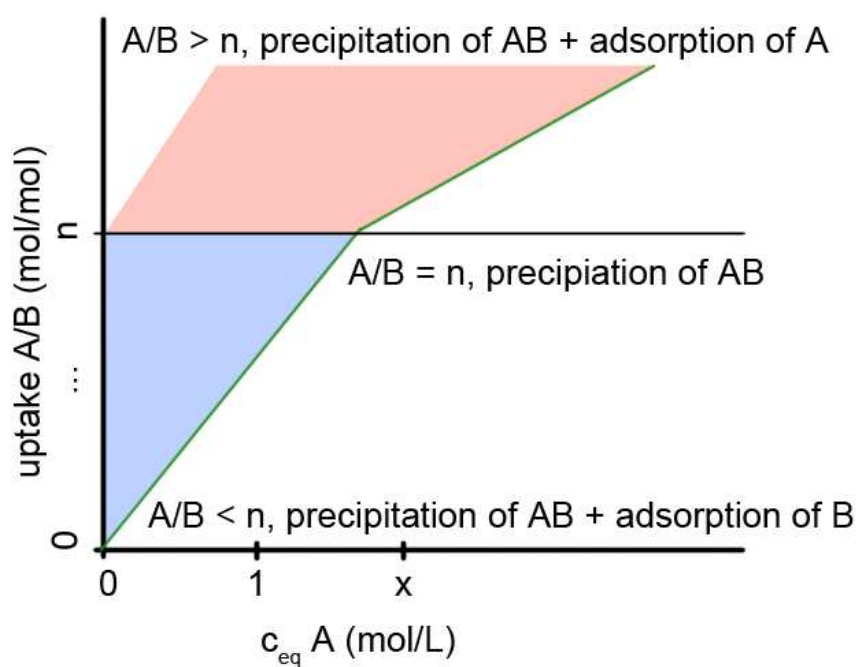


Figure 5. Schematic for the surface mole ratio method, adapted from the graphical abstract of Wei et al. [179].

4. Fundamentals of Instrumental Analytics

4.1. Gas Sorption Measurements

Sorption measurements with different gases are nowadays used as standard, both for the investigation of pore structures and determination of the specific surface area of solid materials and for the investigation of gas storage processes. The adsorption of a gas on a solid is measured as a function of the relative pressure p/p_0 in equilibrium. Here, p_0 represents the saturation vapor pressure of the adsorbent. The volume of gas added and adsorbed is usually measured volumetrically, but can also be determined gravimetrically. Physical interactions such as dipole interactions or dispersion forces are usually responsible for the interaction between the gas molecule and the sample. The measurement of chemisorption of different gases is also possible, depending on the measurement method aimed at [184]. In sorption measurements, the binding strength of the adsorbent correlates with the measured equilibrium pressure p during adsorption or desorption. While only a monolayer of the adsorbent can be bound on planar surfaces, curved surfaces allow a stronger interaction between adsorbent and adsorbent. By recording the gas uptake at certain equilibrium pressures, the curvature, or pore diameter d , of the sample can thus be determined. A distinction is made between micropores ($d < 2$ nm), mesopores ($2 \text{ nm} < d < 50$ nm) and macropores ($50 \text{ nm} < d$). A further distinction is made in the area of micropores: they can be divided into supermicropores ($2 \text{ nm} < d < 0.7$ nm), ultramicropores ($0.7 \text{ nm} < d < 0.4$ nm) and submicropores ($0.4 \text{ nm} < d$) [142] (see Figure 6).

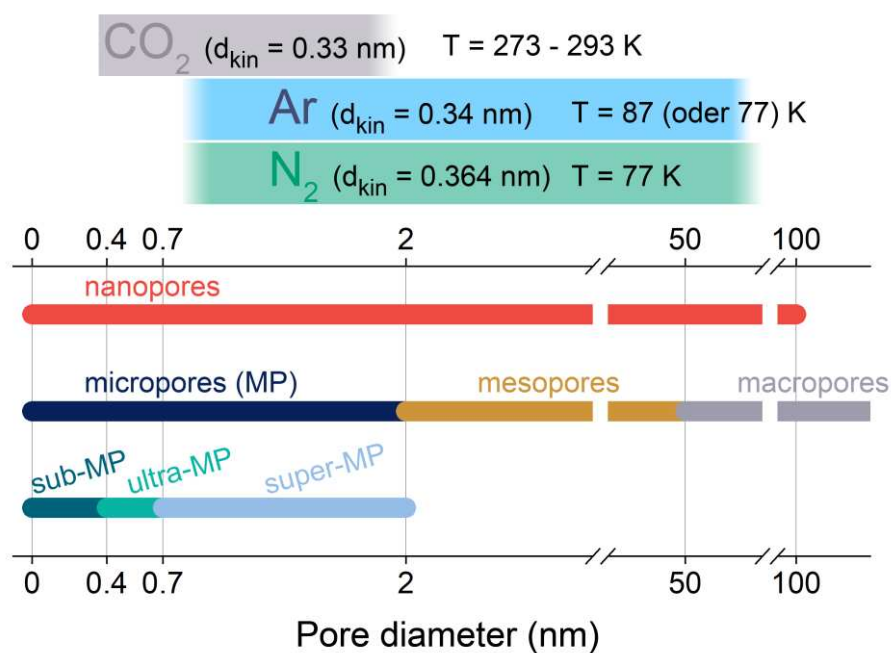


Figure 6. Overview of the classification of pore sizes (according to IUPAC [142]) and suitable gases for analysis with approximate range of applicability. For each gas the respective kinetic diameter d_{kin} [185,186] and the corresponding usual measuring temperature T are given [142].

The gases used for sorption are e.g. N₂, CO₂, Ar and water vapor, which are measured in relative pressures in the interval $0 < p/p_0 < 1$ or absolute pressures up to often 1 bar [142]. N₂ isotherms at a temperature of $-196\text{ }^{\circ}\text{C}$ (77 K) often serves as the standard here due to its ease of use and good availability. Due to its non-ideal behavior and the linear molecular shape of N₂, Ar sorption measurements are of increasing interest, either at 77 K or 87 K [187]. Here, the measurement at 87 K shows the advantage of faster equilibration compared to nitrogen since the micropore uptake step occurs at higher relative pressures [142]. However, both N₂ and Ar have the disadvantage that particularly small micropores are not accessible at cryogenic temperatures (77 K / 87 K) due to kinetic inhibition of the adsorbent. CO₂ measurements are used for this purpose, which show sufficiently high adsorption at 273 K [142]. Measurements at 293 K or 283 K are also often used in the literature, especially when investigating whether the material is suitable for CO₂ storage.

The adsorption and desorption isotherms are plotted against the relative pressure measured to represent the sorption process. If the adsorption and desorption isotherms differ, this is referred to as a hysteresis loop. According to IUPAC, 6 different types of adsorption isotherms are distinguished (see Figure 7) [142,184]. Type I isotherms are characteristic of microporous samples. At very low relative pressures, a very steep gas uptake is recognizable. In this case, the micropores allow the adsorbent to bind strongly by interacting with a very large area of the same pore due to its small diameter. Type II isotherms are typical of nonporous materials with mainly macroporous character. In the first slight increase at low p/p_0 values, the uptake of a monolayer of the gas up to point B is evident. With increasing pressure, the uptake increases due to adsorption of further adsorbate layers. In type III, no monolayer adsorption occurs, but direct multilayer adsorption is seen in higher pressure ranges, often due to interactions of the adsorptive molecules with each other. Type IV isotherms are usually characterized by an occurring hysteresis loop (type IVa) and are typical for mesoporous substances. In mesopores, so-called capillary condensation occurs, in which molecules from the gas phase condense below their saturation vapor pressure to form a liquid-like phase. Any hysteresis that occurs is triggered by delayed desorption. Above a critical pore diameter, the condensed phase is metastable after adsorption. The renewed transition of the molecules into the gas phase accordingly requires a lower relative pressure, which leads to the formation of the hysteresis loop. The critical pore diameter depends on temperature and adsorptive (for N₂ at 77K, for example, about 4 nm) [142]. If no hysteresis occurs, a type IVb isotherm is reached, which accordingly has mesopores with sizes below the critical pore diameter.

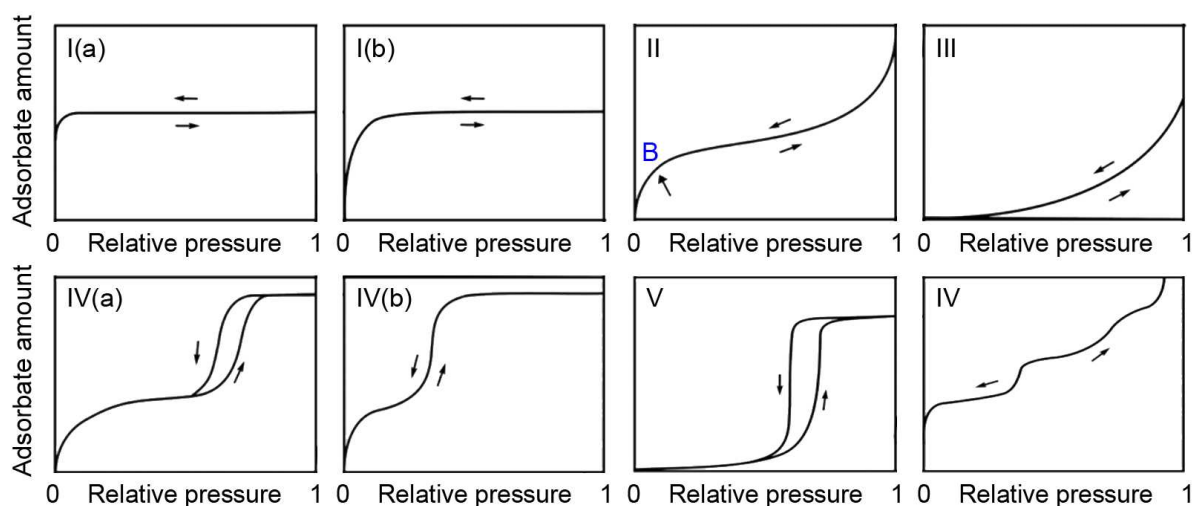


Figure 7. Classification of different isotherms and b) hysteresis loops according to IUPAC. Taken from [142].

For pore systems, not only the diameters of the pores themselves, i.e. the larger cavities, are decisive, but also their connecting channels to each other or to the outside. Especially in the area of mesopores, these connecting channels cause the occurrence of deviating adsorption and desorption processes, i.e. hysteresis loops. While the adsorption branch reflects the corresponding diameters of the pore cavities, the desorption branch reflects the respective diameters of the connecting channels due to the transfer of nitrogen from the condensed to the gas phase. In case the diameter of these connecting channels is too small, pore blocking may occur. In this case, condensed nitrogen remains in pores whose diameter theoretically exceeds the critical value for evaporation, but which are only connected to the external system via a very narrow throat. As a result, the condensate remains as such in the pore until a relative pressure is reached which is sufficient to evaporate the nitrogen in the narrow connecting channel, thus releasing all the pore condensate at this relative pressure. This links the shape of the respective hysteresis loops very closely to the formed pore structure and allows a classification into five classes (Figure 8). For this work, the types H1 and H2 are of importance. Type H1 hysteresis loops, with their steep and parallel adsorption and desorption branches, indicate a very uniform mesopore structure with little fluctuation, such as found in templated silica. The steep slope here implies that both the pores themselves and their connecting channels have the same diameter. The hysteresis type H2 results from a more complex pore structure, which is strongly influenced by specific network effects. As an example of these effects, the steep desorption step of H2(a) indicates pore blockage or percolation caused by very narrow connecting channels or bottlenecks between pores, while the less steep adsorption curve indicates a broader distribution of cavity diameters. In contrast, H2(b) results from a very narrowly distributed pore size distribution in the cavities, causing the adsorption curve to be quite steep. Desorption indicates a wider pore size

distribution in the diameter of the connection channels, which can also lead to pore blockage [188].

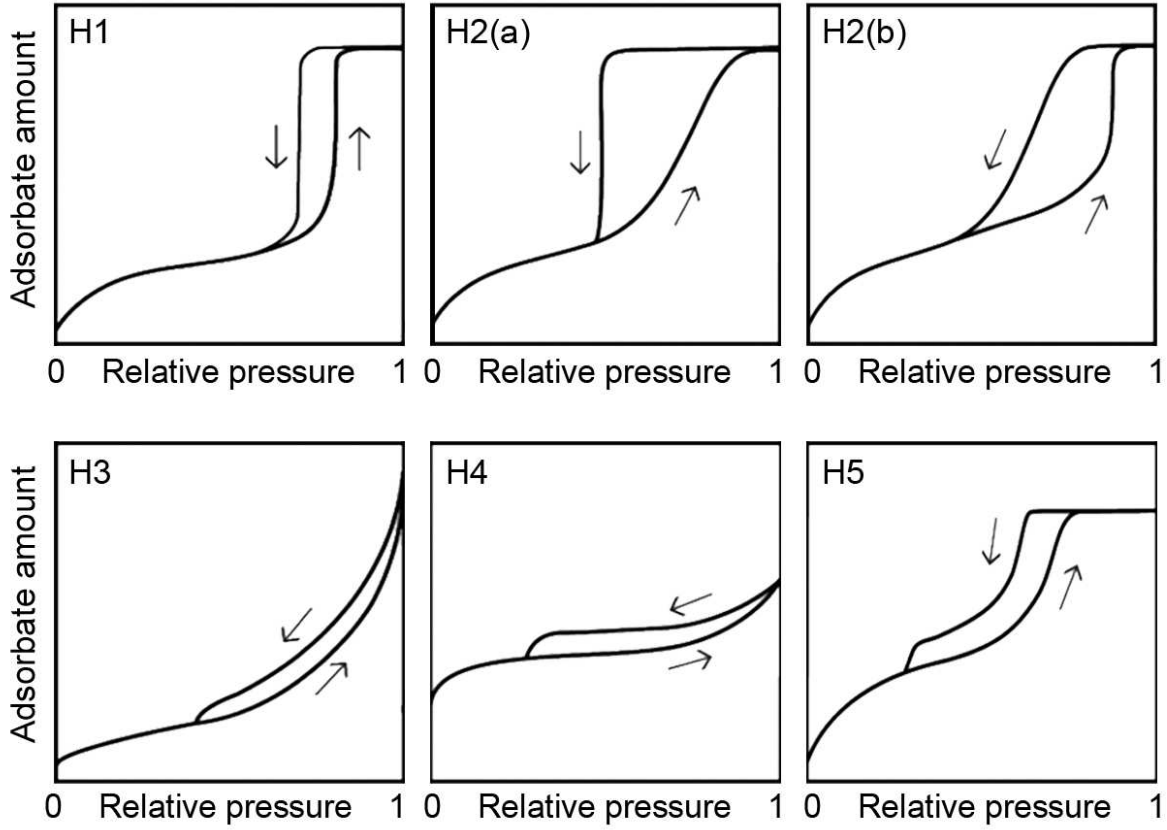


Figure 8. Classification of different hysteresis loops according to IUPAC, adapted from [142].

4.1.1. Determination of Pore Sizes

Conclusions about the pore diameter can be drawn via the respective relative pressure at which adsorption takes place. The pore condensation in the area of the mesopores can be described by the Kelvin equation, which can calculate the respective pore diameter via the meniscus of the pore condensate (equation (14)). Here, γ stands for the surface tension of the liquid, V_m is the molar volume, r_p is the pore diameter, and t_c is the film thickness before pore condensation. [142]

$$\ln(p/p_0) = \frac{-2\gamma \cdot V_m}{(r_p - t_c) \cdot R \cdot T} \quad (14)$$

A standard isotherm (t-curve) is used to calculate the multilayer thickness before pore condensation. Particularly in the area of small mesopores, the deviation of the idealized system from the real pore diameters is considerable, which is why various density functional theory (DFT) models are increasingly being used [142]. These better represent reality and thus achieve better modeling to reach accurate conclusions especially for more complex hysteresis loops with delayed adsorption or desorption as found in types H2 – H5 [189,190].

4.1.2. Determination of Specific Surface Area

The determination of the specific surface area is usually performed using N₂ adsorption data and is based on the Brunauer-Emmet-Teller equation (BET equation), which is given in equation (15) [191].

$$\frac{p/p_0}{n_a \cdot (1 - p/p_0)} = \frac{1}{n_m \cdot C} + \frac{C - 1}{n_m \cdot C} (p/p_0) \quad (15)$$

Here, n_a and n_m stand for the adsorbed total amount of substance and the amount of substance of a monolayer, respectively. C represents a model constant which is closely related to the adsorption energy of the monolayer. The BET equation is based on the Langmuir equation mentioned in section 3.2.1 extended to include multilayer adsorption. Here, the adsorption of further layers requires the same adsorption energy in each case, which, however, is different from the energy of the first adsorption layer.

When plotting the measured data according to the BET plot as $(p/p_0) \cdot n_a \cdot (1 - p/p_0)$ against the relative pressure p/p_0 , the amount of substance of a monolayer is obtained. Here, the linear part of the plot is used with values in the typical range of $0.05 \leq p/p_0 \leq 0.30$. Thereby, the monolayer capacity indicates the number of N₂ molecules in a monolayer via the Avogadro constant (N_A). Using the mean cross-sectional area of the molecule (σ_m), the occupied area and thus the specific surface area S_{BET} can then be calculated. This is summarized in equation (16). [142,184]

$$S_{BET} = \frac{n_m \cdot N_A \cdot \sigma_m}{m_{ads}} \quad (16)$$

It is worth mentioning with this method that these are strongly idealized assumptions. Especially for super-microporous systems ($2 \text{ nm} > d > 0.7 \text{ nm}$) there are stronger deviations due to pore condensation simultaneously to monolayer adsorption, which cannot be distinguished here.

4.2. Transmission Electron Microscopy

The optical investigation of structures has a very large share in the analysis of functional surfaces. Light microscopy, despite modern improvement of its resolution in the context of STED (stimulated emission depletion) microscopy, does not have the resolution necessary to image structures in the range of a few nanometers [192,193]. A transmission electron microscope (TEM), on the other hand, is able to achieve a very low resolution limit d_A due to the small wavelength λ of a generated electron beam, which can be calculated by the Abbe equation (equation (17)) [194,195]. Here, n_r stands for the refractive index of the medium and α for half the aperture angle of the objective.

$$d_A = \frac{\lambda}{2 \cdot n_r \cdot \sin \alpha} \quad (17)$$

The wavelength of electrons is accessible via the DeBroglie equation with the Planck constant h , the mass m_e and velocity of the electron v_e :

$$\lambda = \frac{h}{m_e \cdot v_e} \quad (18)$$

For TEM, accelerating voltages between 100 and 300 keV are typically used. A voltage of 200 keV, for example, results in a wavelength of 2.51 nm.

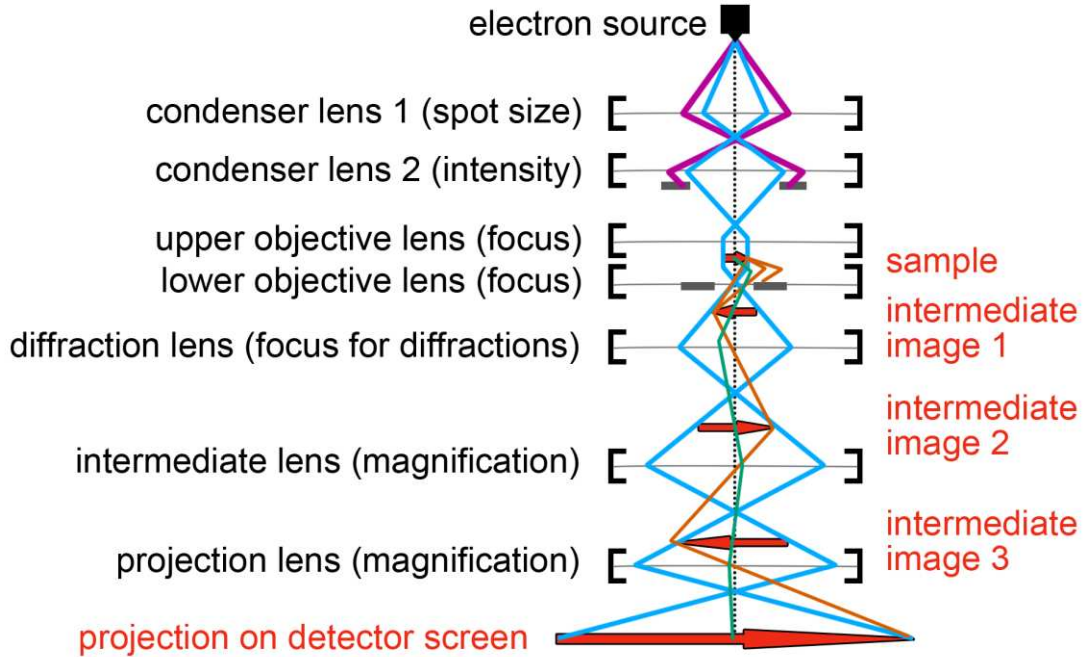


Figure 9. Structure of a TEM, based on [196]. The beam path of non-scattered electrons is shown in blue, the sample and subsequent intermediate images and the projection on the detector as a red arrow. The beam path of scattered electrons is shown in green and orange. Lenses and apertures are drawn in black.

For the investigation by means of TEM, a sufficiently thin sample, usually with thicknesses up to about 100 nm, is irradiated while passing electrons are detected. The transmissivity of

the sample and thus its maximum possible thickness depends strongly on the quantity and velocity of the electrons as well as on the composition of the investigated material itself. A general setup of a TEM is shown in Figure 9.

In general, the electron beam path must be evacuated, since remaining air molecules otherwise lead to strong scattering of the electrons. After the electron beam is generated by a W or a LaB6 filament, the electron beam is directed through several electromagnetic lenses onto the sample. As the electrons pass through the sample, they interact with and are scattered by the atoms of the sample (Rutherford scattering) [197]. Accordingly, the atomic mass in the material, the density, and the thickness of the material contribute to the imaging. Elastically scattered electrons can be blocked via a contrast aperture and thus it is possible to only use the pure transmission of the sample for imaging. [196,198]

Inelastic scattering of electrons by passing through the sample causes them to lose velocity. This effect is used for imaging by partial blocking the electrons with an energy filter aperture based on their kinetic energy. This allows only electrons of a certain energy loss to pass through the spectrometer and subsequently contribute to imaging. In the case of inner shell ionization, the energy loss values are element specific. This allows the use in Electron Energy Loss Spectroscopy (EELS) to detect specific elements and to map their distribution graphically. For this purpose, several images are acquired, usually some each below the specific ionization energy of the element under investigation for the determination of the background intensity and one above the ionization energy. From the intensity differences, an image can be created which has a higher brightness at the locations containing the element under investigation [199]. This technique is often also referred to as energy-filtered TEM (EFTEM).

For this technique, sufficient transmittance of the sample is particularly necessary, since the largest number of electrons pass without elastic or inelastic scattering. For this purpose, thin sections often have to be prepared. Therefore a sample is usually embedded in an epoxy resin and the resin monolith is then cut with a diamond knife on an ultramicrotome. Typically, this results in thin section samples with typical thicknesses around 50 nm to 100 nm nanometers or slightly above.

4.3. Inductively Coupled Plasma Optical Emission Spectroscopy

Inductively coupled plasma optical emission spectroscopy (ICP-OES) is used for the quantitative analysis of various elements of a solution or, more rarely, of solid samples. The measurement method is based on the ionization of atoms by an inductively coupled plasma in order to subsequently detect and quantify the element-specific emitted photons [200].

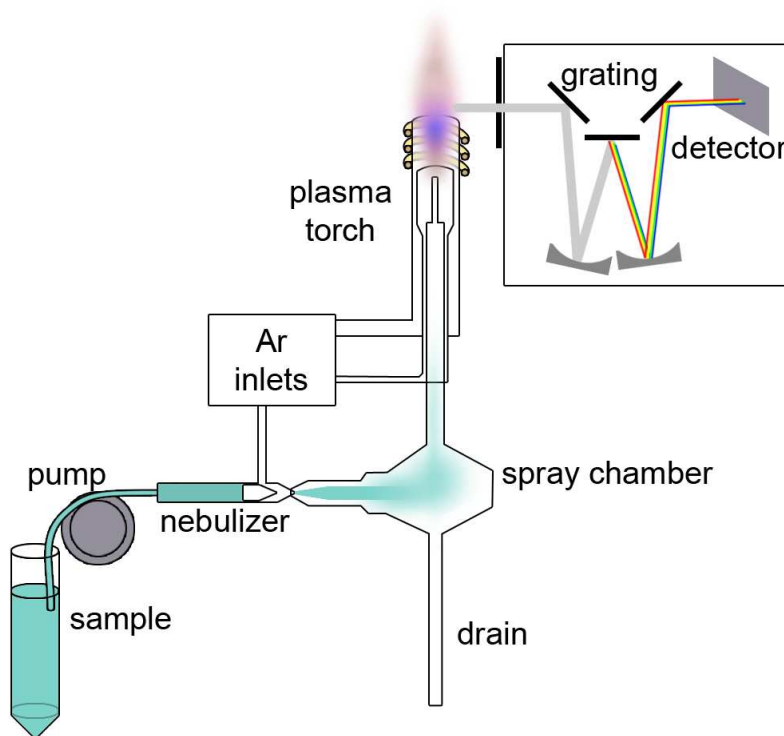


Figure 10. Design of an ICP-OES instrument, based on [201].

The structure of an ICP-OES consists of two parts: First, the corresponding inductively coupled plasma for excitation of the atoms, and second, the optical spectrometer for detection of emitted photons [202]. A schematic setup is shown in Figure 10. In most cases, the sample feed is in liquid form and is fed to the plasma chamber as an aerosol after nebulizing. Argon is predominantly used for the plasma, which is initiated by a Tesla spark and then ionized and held in the radio frequency electromagnetic field of a coil. Typically, this plasma has a temperature of 8000 – 10000 K. The sample is atomized and ionized in the plasma by collisions with ions and electrons. The transitions of excited electrons to lower energy levels emit photons of specific wavelengths, which correlate in energy to specific electron transitions. The emitted light is split by wavelength using a spectrometer and, in modern instruments, detected using semiconductor photodetectors. Photons of specific wavelengths can thus specifically detect elements and quantify them via the intensity of the emission. In order to correlate a detected intensity with a concentration in the original solution, a calibration with internal or external standard of known concentration must be performed.

Results and Discussion

Chapter Overview

The results of the present work are divided into the work with the two polymers PMF and P(3PT-F). The contents of the following chapters are briefly summarized here as an overview. Here, each chapter is based on one publication and covers both the synthesis of the respective resin particles and an application of the particles as an adsorbent for a specific pollutant class.

5. Mesoporous Poly(Melamine-co-Formaldehyde) Particles for Efficient and Selective Phosphate and Sulfate Removal: In this chapter, the synthesis of mesoporous PMF particles using different amounts of template is presented. This variation results in significant differences in the pore diameter obtained and the diameter of the connection channels between pores, even though the same template diameter was used. The used amount of SiO₂ NP also strongly influences the obtained particle diameter. The obtained porous PMF particles and one PMF/SiO₂ hybrid sample are then investigated for an application to adsorb sulfate and phosphate ions from acidic solutions. Furthermore, a possible selectivity of the particles was investigated to allow separation of both ions from mixed solutions.

6. Tuning the Pore Structure of Templated Mesoporous Poly(melamine-co-formaldehyde) Particles toward Diclofenac Removal: The results in this section show a synthesis of mesoporous PMF particles in which both the diameter of the SiO₂ NPs was varied (12 nm and 22 nm) and the stabilizing counter ions in the Ludox® dispersion (Na⁺, NH₄⁺, none). The investigation showed that the obtained pore diameter after template removal is adjustable by the template size. The different stabilizing counter ions mainly lead to strong changes in the diameter of the connecting channels between the pores. Thus, more open, well-connected pore structures, as well as pore systems with limited permeability due to narrower connecting channels, can be generated. The PMF particles were subsequently tested for the separation of DCF as a representative of persistent organic contaminants. Experiments showed that PMF is efficiently able to adsorb DCF. In particular, at low concentrations, it can be completely removed from water, which is important because the real-world concentrations are in the low µg/L range. In particular, the results of this chapter show that PMF has great potential to separate other pharmaceutical trace compounds due to its multiple interactions.

7. Adsorption vs. Surface Precipitation of Cu²⁺ onto Porous Poly(melamine-co-formaldehyde) Particles: Chapter 7 deals with the interaction of PMF particles with metal ions when anions are present and the influence of porosity on the system. For this purpose, both porous PMF particles were prepared by the known hard-templating method and PMF particles to which no SiO₂ NPs were added as template and which accordingly did not form any

mesopores. In addition, the amount of water as dispersant in the reaction solution was varied. It was found that the amount of water had a strong influence on the particle diameter and also the internal morphology of the particles. An increased amount of water decreased the particle diameter. At a very low dispersant amount, the formation of three compartments in the particle structure occurred, which allows first few conclusions about the stabilization of the particles in their formation.

In a complex study with several Cu(II) salt solutions, the uptake of Cu^{2+} and of the respective anion was then tested. Here, the non-templated particles showed little adsorption of metal ions, with these being displaced from the adsorption sites by the respective anion as the concentration increased.

In contrast, a combination of adsorption and surface precipitation was found in the porous particles, producing an insoluble crystalline precipitate containing both Cu^{2+} and the respective anion. In the case of sulfate as a divalent anion, the two processes overlapped, so that no separate mathematical modelling of both processes was possible, while two distinct uptake steps were observed for monovalent ions. By introducing a new adsorption isotherm combining the Langmuir isotherm and a sigmoidal Boltzmann equation, both processes could be modeled. However, these very fundamental results provide insight into the fundamental and complex interactions of amines, metal ions and anions and also pave the way for the synthesis of new hybrid materials, for example as a combination of amino-containing polymers and crystalline inorganic species.

8. SiO₂ Nanospheres as Surfactant and Template in Aqueous Dispersion Polymerizations Yielding Nanoporous Resin Particles: This chapter presents the results of a comprehensive study on the fundamentals of PMF particle formation and templating. In this study, six different parameters were individually varied to analyze their influence on the interaction of silica with the hydrophilic PMF precursor species and PMF prepolymer as well as with the hydrophobic PMF resin polymer. Especially through varying the amount of catalyst, polymerization temperature and prepolymerization time, it was possible to postulate a comprehensive mechanism describing the interaction of silica with the different PMF polymerization stages. In this work, it was also possible for the first time to prepare particles suitable for the use as column material by an environmentally friendly colloidal polymerization in water. These particles have a size of about 10 μm and exhibit a high specific surface area. In a first pilot test they could be used as fixed bed adsorbents for the separation of toxic dichromate ions.

9. Waterborne Phenolic, Triazine-Based Porous Polymer Particles for the Removal of Nickel, Cadmium, and Lead Ions: In a further study, melamine was substituted for a trihydroxyphenyl-functionalized triazine-based monomer in syntheses with formaldehyde to

produce a novel resin polymer with outstanding amount of phenolic groups. This polymer has intrinsic microporosity, which results in high specific surface areas. To investigate the influence of formaldehyde as a crosslinker, its amount was varied. The most suitable polymer was then prepared in a larger batch to show that it can be synthesized in upscaled amounts. In subsequent experiments on separation with toxic or carcinogenic heavy metal ions Cd^{2+} , Pb^{2+} and Ni^{2+} , the polymer showed high separation rates at low concentrations and also high adsorption capacities, making it a good starting point for exploring further triazine-based resin polymers as highly functional materials. It was proven that the adsorbent it exhibited selectivity for the adsorption of Pb^{2+} over more commonly occurring but non-toxic metal ions such as Fe^{2+} , Ca^{2+} , Mg^{2+} , and K^+ . Furthermore, reusability of the material was demonstrated by facile, quantitative desorption of adsorbed Pb^{2+} with a small amount of diluted HCl, circumventing organic chelators such as ethylenediaminetetraacetic acid. Subsequently, adsorption was carried out without decrease in adsorption performance.

5. Mesoporous Poly(Melamine-co-Formaldehyde) Particles for Efficient and Selective Phosphate and Sulfate Removal

This chapter is based on the publication in *Molecules* **2021**, *26*, 6615.

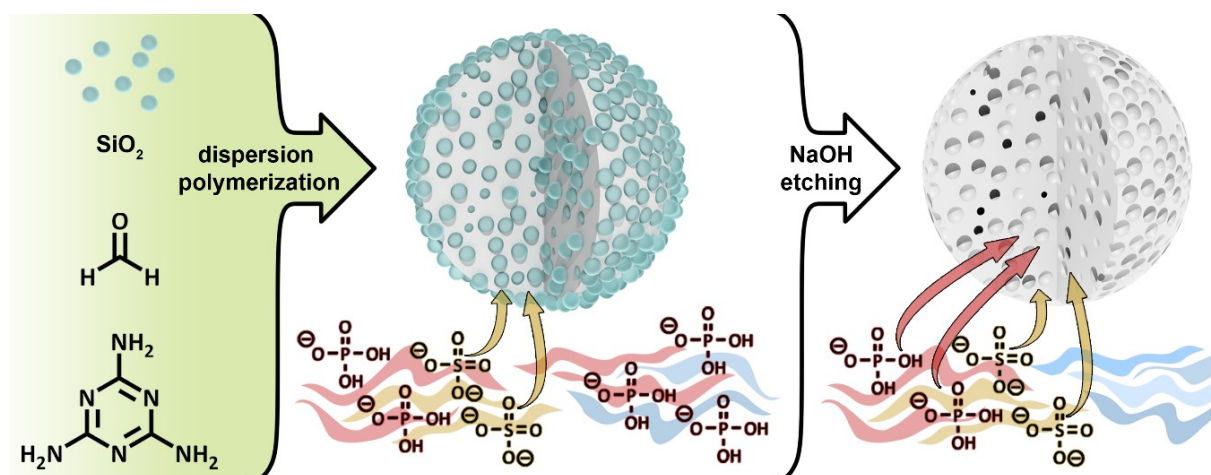
(DOI: 10.3390/molecules26216615)

By Konstantin B. L. Borchert, Christine Steinbach, Berthold Reis, Niklas Gerlach, Philipp Zimmermann, Simona Schwarz and Dana Schwarz*

Leibniz-Institut für Polymerforschung Dresden e.V., Hohe Str. 6, 01069 Dresden, Germany;

* Corresponding authors

Graphical Abstract



Abstract

Due to the existence-threatening risk to aquatic life and entire ecosystems, the removal of oxyanions such as sulfate and phosphate from anthropogenic wastewaters, such as municipal effluents and acid mine drainage, is inevitable. Furthermore, phosphorus is an indispensable resource for worldwide plant fertilization, which cannot be replaced by any other substance. This raises phosphate to one of the most important mineral resources worldwide. Thus, efficient recovery of phosphate is essential for ecosystems and the economy. To face the harsh acidic conditions, such as for acid mine drainage, an adsorber material with a high chemical resistivity is beneficial. Poly(melamine-co-formaldehyde) (PMF) sustains these conditions whilst its very high amount of nitrogen functionalities (up to 53.7 wt.%) act as efficient adsorption sites. To increase adsorption capacities, PMF was synthesized in the form of mesoporous particles using a hard-templating approach yielding specific surface areas up to 409 m²/g. Different amounts of silica nanospheres were utilized as template and evaluated for the adsorption of sulfate and phosphate ions. The adsorption isotherms were validated by the Langmuir model. Due to their properties, the PMF particles possessed

outperforming maximum adsorption capacities of 341 and 251 mg/g for phosphate and sulfate, respectively. Furthermore, selective adsorption of sulfate from mixed solutions of phosphate and sulfate was found for silica/PMF hybrid particles.

1. Introduction

Oxyanions such as sulfate and phosphate are one of the most frequently occurring pollutants in natural water bodies. High levels of sulfate in water cause corrosion of steel and cement in urban sewers, pipes and bridges [1,2]. Sulfate is toxic for various aquatic lifeforms [3,4] and can be microbiologically converted to hydrogen sulfide, leading to additional contamination [5,6]. Sulfate pollution is naturally caused by weathering of minerals or volcanic activity, but the anthropogenic share of pollution by, e.g., mining drainage, coal combustion, sewage infiltration and synthetic detergents increases with progressing industrialization [7–10]. Phosphate has a drastic effect on the environment, as it represents the growth-limiting factor for most water bodies and is therefore decisive for harmful algal blooms and eutrophication [11–16]. This leads, e.g., to oxygen deficiency and fouling mud formation, threatening many aquatic lifeforms [17]. Anthropogenic phosphate pollution is mainly caused by fertilization and soil erosion connected to farming activities as well as wastewater discharge [11,16,18].

Furthermore, phosphorus from rock resources is finite while its demand is increasing rapidly [19] with the growing world population. Therefore, more attention needs to be paid to the recovery of phosphorous from various sources [20–26] such as sewage sludge [27–29], metalworking slag [30–33] or municipal waste [34]. One of the most promising solutions is the adsorption from aqueous media such as effluents from leaching processes or from mine drainage [21,22]. However, the low pH values of these solutions, which lead to a corrosive environment, are suggested unsuitable for different types of adsorber materials such as, e.g., various unmodified metal oxides [35–37] or biobased adsorbents as unmodified chitosan [38]. For example, different iron oxide and hydroxide species were investigated for the adsorption of phosphate, mainly from solutions with $\text{pH} \geq 2$ [39–41] or even buffered to $\text{pH} = 7$ [42]. When pH is lowered further below a pH of 2.0, the adsorbent is dissolving. Non-modified chitosan as another example is known to be soluble in highly acidic media, making it unsuitable for the adsorbent in acid wastewaters. Poly(melamine-co-formaldehyde) (PMF) is a chemically extremely resistant polymer resin with a high amount of nitrogen functionalities, which makes the material a suitable adsorbent at all pH values. Thus, in the last decade various synthetic concepts were developed to obtain a highly nanoporous material with a moderate monodisperse particle size. One of the approaches comprises heating of the reaction solution in DMSO in closed vessels up to 180 °C yielding in DMSO decomposition and sulfur residuals in the polymer [43–45]. Another concept to obtain spherical nanoporous PMF particles

involves emulsion polymerization in Span® 80 and n-dodecane [46]. The efficient adsorption of heavy metal ions such as Pb^{2+} , methylene blue and sulfate on PMF has already been reported [45–49]. To the best of our knowledge, the adsorption properties of PMF toward sulfate and phosphate have not been investigated, with the exception of our author team [47]. The adsorption capacities from phosphate and sulfate were not yet specified by application of isotherm models. Furthermore, recycling of lithium-based batteries often only aims for the recovery of Li and other metals, while phosphate from, e.g., lithium iron phosphate or LiPF_6 batteries is of lesser interest. In the recycling processes, hydrometallurgical processes are often applied. This includes oxidation with, e.g., H_2SO_4 and H_2O_2 or $\text{Na}_2\text{S}_2\text{O}_8$ and acid leaching of the components, or extraction with phosphoric acid [50–52], which leads to highly acidic and phosphorous rich waste streams often also containing high levels of sulfate. Here, a feasible P-recovery procedure could be a selective separation achieved by an adsorption process.

Here, we present a simple and purely water-based green concept for the synthesis of mesoporous PMF particles, using silica nanoparticles (SiO_2 NPs) as a hard template. We investigated the impact of the SiO_2 NPs (66 to 89 wt.%) as a hard template for monodisperse mesopores and on the particle formation acting as Pickering emulsion. Hence, we characterized the particles with both scanning and transmission electron microscopy, laser diffractometry and nitrogen sorption to determine the particle size distribution and pore size distribution (PSD), respectively. These results were used to gain insights into the pore and particle formation mechanism. Further, the chemical structure was investigated using ATR-FTIR spectroscopy and elemental analysis to examine the differences in chemical composition. Finally, the characterized particles were used in adsorption experiments with sulfuric and phosphoric acid. The obtained isotherms were validated by Langmuir and Dubinin–Radushkevich isotherm models. Furthermore, the PMF particles were investigated for selective sulfate and phosphate adsorption.

2. Results and Discussion

A hard templating approach with monodisperse SiO_2 NPs (12 nm in diameter) was applied for the synthesis of mesoporous PMF particles. To investigate the influence of the SiO_2 NPs on the particle and pore formation, the amount of template (66 to 89 wt.%) for the PMF particle synthesis was varied. Hence, the labeling of the samples includes a suffix referring to the theoretical initial silica content in wt.% in the hybrid material. The prefix H- corresponds to the silica hybrid particles without removal of the template and the prefix P- corresponds to the pure PMF particles after removal of the template.

2.1. Synthesis and Characterization of the PMF Particles

The chemical structure of the PMF particles was analyzed by ATR-FTIR, EA and TGA. ATR-FTIR measurements featured a broad band between 3280 cm^{-1} and 3500 cm^{-1} originating from various valence modes of secondary amines (Figures S1 and S2). The more discrete band at 2956 cm^{-1} was attributed to methylene stretching. Together with the bands at 1487 and 1350 cm^{-1} assigned to CH_2 bending, these bands confirmed the formation of methylene bridges. The rather prominent band at 1550 cm^{-1} was attributable to both NH bending and $\text{C}=\text{N}$ valence modes. The less prominent band at around 1000 cm^{-1} originated from the $\text{C}-\text{O}-\text{C}$ ether bridges. Further, the band at 812 cm^{-1} was assigned to the bending of the triazine ring. Since this mode should be constant throughout all samples, it was used for normalization. Every sample spectrum exhibited these characteristic bands matching the literature [53–55] and confirming the formation of the melamine resin matrix in all cases.

Additionally, all H-PMF spectra showed a prominent band at approximately 1100 cm^{-1} , which was attributed to the Si–O stretching mode (Figure 5.1, Si–O mode indicated through bold line). This verified the efficient integration of the silica template into the resin. Further, the absence of this band in the P-PMF spectra proved the thorough removal of the template (compare Figure 5.1a).

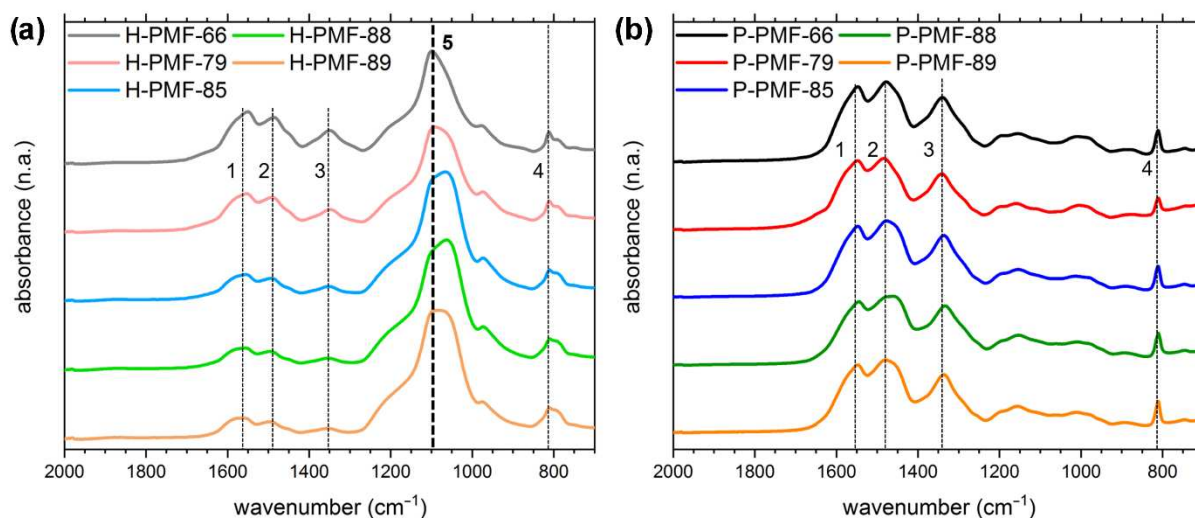


Figure 5.1. ATR-FTIR spectra of (a) H-PMF and (b) P-PMF samples. All spectra were normalized to the bending of the triazine ring at 812 cm^{-1} for comparability. The modes marked with a dashed line are 1 NH bending and $\nu\text{ C}=\text{N}$; 2 + 3 CH_2 bending; 4 triazine bending; 5 $\nu\text{ Si}-\text{O}$.

To investigate the successful templating of the PMF particles and the subsequent removal of the silica template in detail, thermogravimetric analysis was conducted. The different ratios of added template to the PMF synthesis can be seen in Figure 5.2a. At $1000\text{ }^{\circ}\text{C}$, the hybrid PMF samples exhibited residual masses of 55, 62, 72, 77 and 81 wt.% for H-PMF-66, H-PMF-79, H-PMF-85, H-PMF-88 and H-PMF-89, respectively. As expected, the residual mass increased with the increasing amount of silica added the synthesis. In Figure 5.2b, no residual mass is

presented at 1000 °C, showing the absence of silica. Thus, these results are in agreement with the ATR-FTIR spectra.

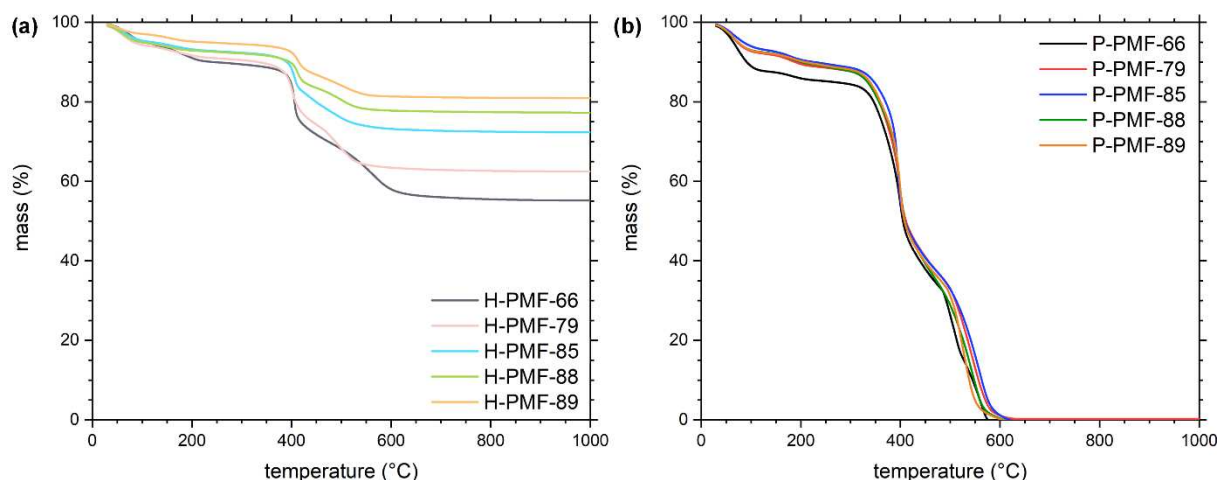


Figure 5.2. Thermogravimetric analysis from (a) the H-PMF samples and (b) the P-PMF samples with PMF-66 shown in black, PMF-79 in red, PMF-85 in blue, PMF-88 in green and PMF-89 in orange.

The PMF samples exhibited the typical decomposition steps, which are also described in the literature [56–58]. Although temperature ranges vary between different publications, the main mass losses are agreed on. First, mainly physical dehydration up to 150 °C can be observed. Second, from 100 to 180 °C, elimination of formaldehyde from free methylolamine groups as well as the condensation of methylolamine groups with each other or amine groups is possible, whereby formaldehyde and water are released. Around 180 to 350 °C, chemical degradation of ether bridges occurred, releasing formaldehyde as a curing process. Starting around 350 °C, methylene bridges degraded and from 390 °C degradation of the triazine ring occurred [56–58].

From the TGA results, it can be observed that among all P-PMF samples a very similar decomposition can be found, both in the temperatures of the decomposition steps and also in the mass loss of each step. This indicates a similar chemical structure of the P-PMF samples.

During the polycondensation reaction between melamine and formaldehyde, different reaction steps occur. The resulting PMF resin can feature different amounts of methylene and ether bridges between the triazine units. For a statistical evaluation of the bridging of the PMF resin, the molar ratio of C to N atoms can be discussed (see Table 5.1). For all PMF samples, the H-PMF materials exhibited higher relative C/N ratios in comparison to the P-PMF samples, since the oxalic acid or oxalate can interact with the silica surface and is therefore still present in the hybrid samples and removed with the template in the P-PMF. Alternatively, the methylol amine functionalities could participate in the resin/silica interaction. These groups will not be converted into ether or methylene bridges and are subsequently hydrolyzed in the washing steps by 1M NaOH solution as methylol amines are prone to hydrolysis in strong basic

Mesoporous Poly(Melamine-co-Formaldehyde) Particles for Efficient and Selective Phosphate and Sulfate Removal

or acidic media [59,60]. Therefore, it can be concluded that in the prepared hybrid materials, either oxalic acid species or methylol amine groups participate in the PMF/silica interaction, which are then removed during the NaOH washing procedure. Furthermore, it can be seen that all P-PMF samples comprised a very similar C/N ratio.

Table 5.1. Results of the elemental analysis (C, H, N) for the different PMF samples. The residue describes the relative mass, which is not attributed to the elements C, H and N. n/n (C/N) is the molar ratio of C atoms/N atoms calculated from elemental analysis.

Sample	C (wt.%)	H (wt.%)	N (wt.%)	Residue (wt.%)	n/n (C/N)
H-PMF-66	14.6	2.4	19.5	63.5	0.87
P-PMF-66	33.5	4.9	49.4	12.1	0.79
H-PMF-79	11.9	2.2	16.8	69.1	0.82
P-PMF-79	35.6	4.8	52.4	7.1	0.79
H-PMF-85	7.3	1.6	9.9	81.2	0.85
P-PMF-85	35.6	4.8	53.5	6.0	0.78
H-PMF-88	5.7	1.4	7.7	85.3	0.87
P-PMF-88	35.5	4.8	53.7	6.1	0.77
H-PMF-89	5.4	1.2	7.1	86.3	0.89
P-PMF-89	35.3	4.7	53.7	6.2	0.77

To evaluate the morphology and template inclusion of the H- and P-PMF samples, SEM and TEM investigations were carried out (see Figure 5.3) as well as particle size measurements (Figure 5.4). In the last row of Figure 5.3, the SEM images of the P-PMF samples are presented. For all P-PMF samples, aggregates of spherical primary particles are visible with diameters in the range of hundreds of nanometers. The TEM images of the H-PMF samples display the incorporation of the template (i.e., SiO₂ NPs) in the PMF resin, which can be seen on the edges of the larger hybrid particles. Additionally, H-PMF-88 and H-PMF-89 shows comparably large amounts of SiO₂ NPs around the hybrid particles. These silica particles were not noticeably integrated in the PMF resin but instead loose surrounded the H-PMF hybrid particles (especially, e.g., H-PMF-89) due to a poor interaction with PMF resin during hybrid particle synthesis. Two main assumptions can be derived: first, this decreased interaction could be due to the differing pH in the reaction mixtures as presented in Table 5.1. The increasing amount of alkaline Ludox® HS-40 from PMF-66 to PMF-89 led to an increased pH value of the reaction solution. Thus, the polymerization reaction as well as the interaction between the SiO₂ NPs and the substrates in the reaction were highly pH sensitive. The isoelectric point (IEP) of the silica NPs was around a pH value of 1.6 [61]. Less surface charge on the SiO₂ NPs increased aggregation but also the potential to interact with the hydrophobic PMF surface, leading to increased incorporation. Secondly, with the increasing amount of silica, there was potentially not enough PMF in the synthesis to incorporate all SiO₂ NPs.

Mesoporous Poly(Melamine-co-Formaldehyde) Particles for Efficient and Selective Phosphate and Sulfate Removal

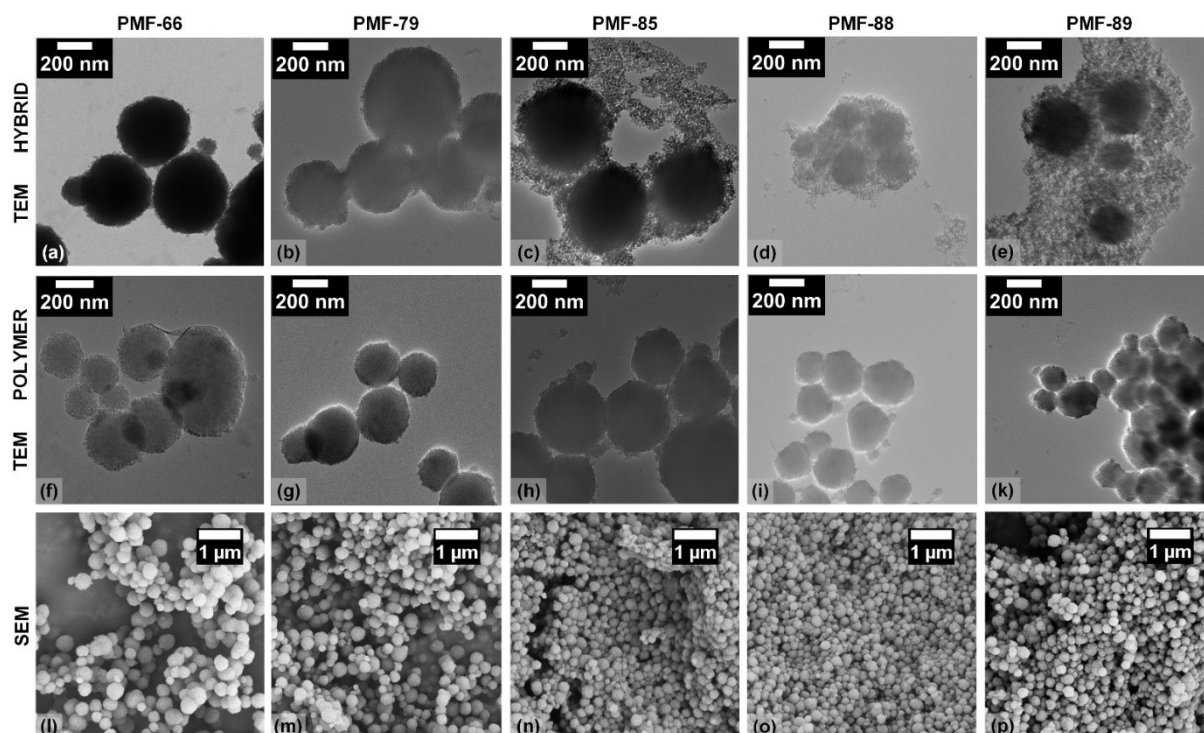


Figure 5.3. (a) TEM image of H-PMF-66, (f) TEM image of P-PMF-66 and (l) SEM image of P-PMF-66; (b) TEM image of H-PMF-79; (g) TEM image of P-PMF-79 and (m) SEM image of P-PMF-79; (c) TEM image of H-PMF-85; (h) TEM image of P-PMF-85 and (n) SEM image of P-PMF-85; (d) TEM image of H-PMF-88; (i) TEM image of P-PMF-88 and (o) SEM image of P-PMF-88; (e) TEM image of H-PMF-89; (k) TEM image of P-PMF-89 and (p) SEM image of P-PMF-89.

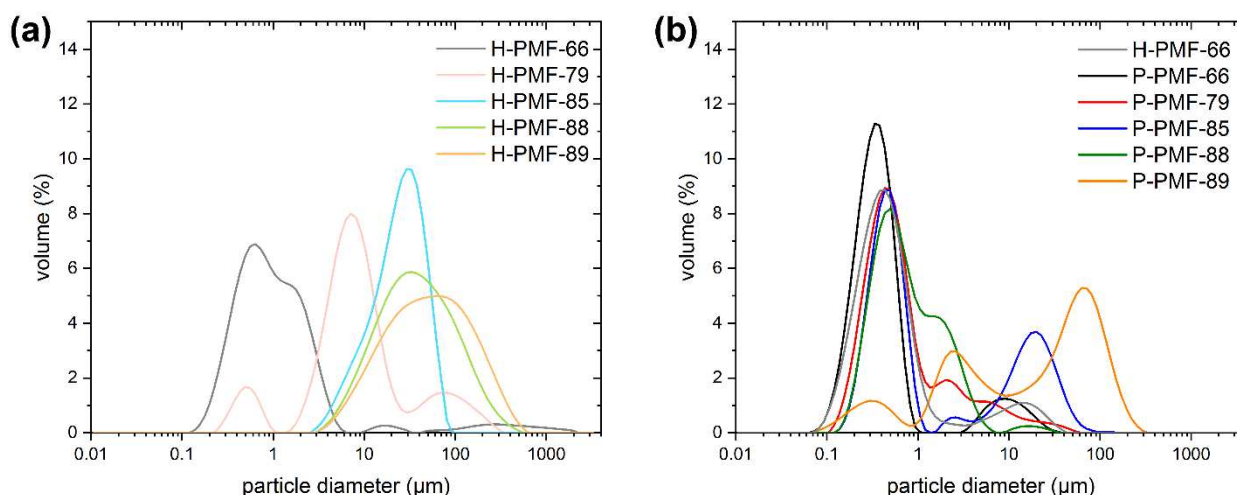


Figure 5.4. (a) Particle size distributions of the unpurified reaction mixtures of H-PMF samples; (b) particle size distribution of the P-PMF samples and H-PMF-66 after purification. H-PMF-66 is shown in gray, H-PMF-79 in pink, H-PMF-85 in light blue, H-PMF-88 in light green, H-PMF-89 in light orange. P-PMF-66 is shown in black, P-PMF-79 in red, P-PMF-85 in blue, P-PMF-88 in dark green and P-PMF-89 in orange.

In the TEM images of all P-PMF samples, a complete removal of the silica template can be observed. Furthermore, the remaining pore structure is visible for all samples, leading to a porous particle network and a successful templating approach.

In addition to the electron microscopy images, the particle size distribution curves were determined by dynamic light scattering for the H-PMF reaction mixtures and the purified P-PMF and H-PMF-66 particles (Figure 5.4). From Figure 5.4a, it is visible that the reaction mixture of H-PMF-66 and partially H-PMF-79 contained sub-micrometer particles. These can be attributed to smaller silica NP aggregates as well as non-aggregated PMF particles. In contrast, the particle size distribution of H-PMF-85 ranged from 2 to 100 μm and the one of H-PMF-88 and H-PMF-89 only featured a peak between 2 and 600 μm . Therefore, formation of very large aggregates consisting of silica and PMF can be derived, as can also be seen from TEM imaging (Figure 5.3d,e) and SEM imaging (Figure S3).

All P-PMF samples possessed bi- or multimodal size distribution with the main peak between 300 and 500 nm except for P-PMF-89 (see Figure 5.4b). For P-PMF-79 and P-PMF-88 this main peak is relatively broad, featuring a shoulder at larger diameters. P-PMF-89 features three broad peaks at approximately 500 nm, 1.5 μm and the largest at around 70 μm . Comparing the purified H-PMF-66 with P-PMF-66, a minor shift in the particle diameter is visible. This is in agreement with the theory that the outer silica layer is removed by etching with NaOH. In addition, aggregates of hybrid particles that are held together by silica particles are separated in the etching process.

All samples featured at least one minor peak at larger particle sizes in the μm range, which can be explained by aggregates of the sub-particles. This is also the explanation for the particle size distribution of P-PMF-89: the particle sizes of the spherical sub-particles displayed in Figure 5.3 are in the range of hundreds of nanometers but large aggregates of them can be seen. The main particle sizes of the other P-PMF particles measured with DLS are in very good agreement with the SEM and TEM images.

To analyze the impact of the SiO_2 NPs on the porosity of the PMF particles, both materials (hybrid (H) and polymer (P)) were investigated by N_2 sorption isotherms at 77 K (see Figure 5.5). The results for the specific surface area, total and micropore volume and CO_2 uptake are stated in Table 5.2. The impact of the amount of silica particles can already be seen from the N_2 sorption isotherms for the hybrid particles (Figure 5.5a). H-PMF-66 shows a type II isotherm, which is typical for non-porous materials. The other H-PMF samples with higher silica contents featured an isotherm of type IV (H1) character, indicative of large mesopores [62,63]. Furthermore, with an increasing amount of silica particles, the hysteresis is more pronounced yielding higher specific surface areas. Pure spherical silica particles of Ludox[®] HS-40, washed with EtOH and subsequently dried, exhibited a specific surface area of 185 m^2/g (see isotherm and PSD in Figures S4 and S5; S_{BET} in agreement with the literature [64,65]). The observations of the PDSs are well in line with previous results obtained by PMF–silica mixtures [46,47].

Mesoporous Poly(Melamine-co-Formaldehyde) Particles for Efficient and Selective Phosphate and Sulfate Removal

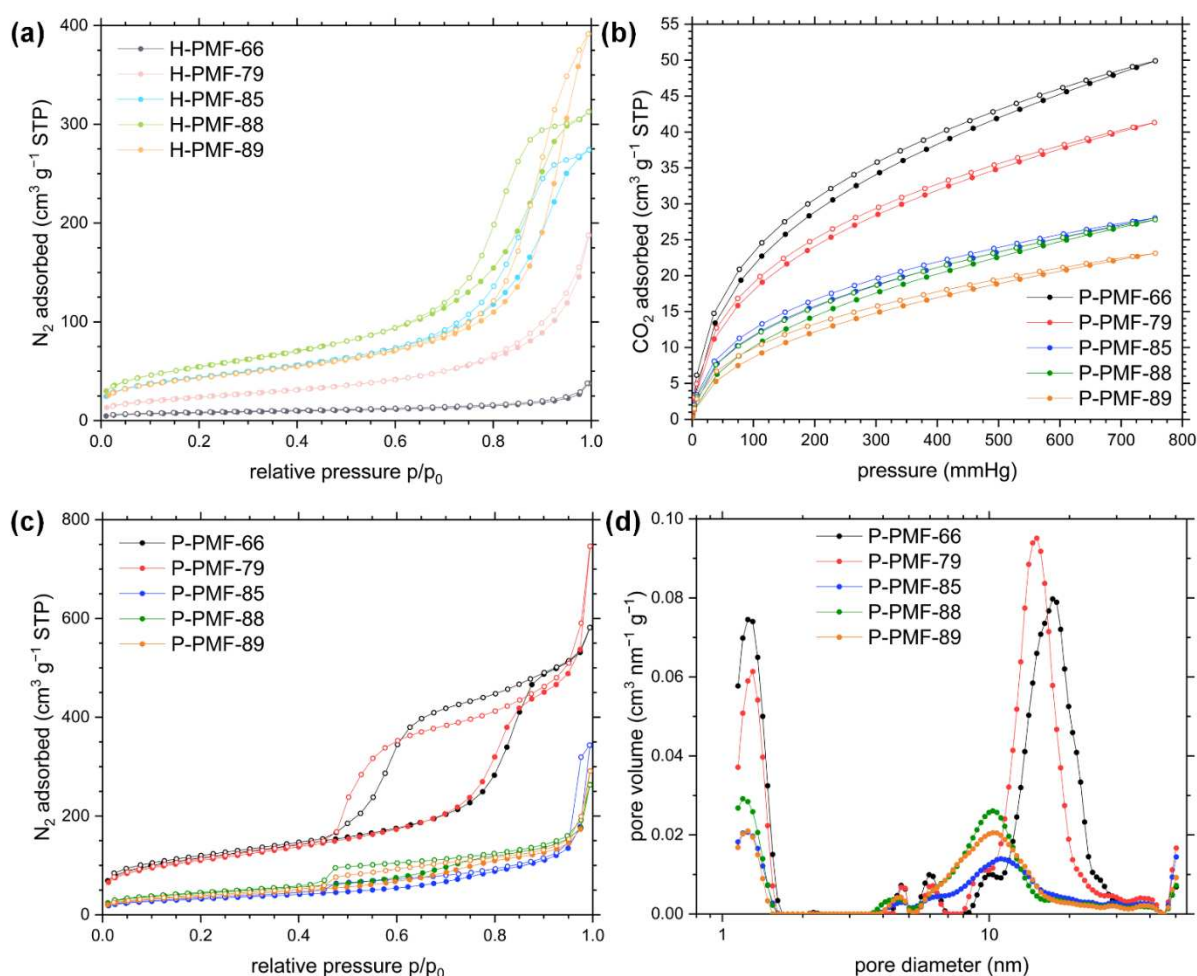


Figure 5.5. (a) Nitrogen (N₂) de-/adsorption isotherms measured at 77 K for H-PMF samples; (b) carbon dioxide (CO₂) de-/adsorption isotherms measured at 273 K for P-PMF samples; (c) nitrogen (N₂) de-/adsorption isotherms measured at 77 K for P-PMF samples. Data points in the adsorption and desorption branch of the isotherms are indicated by filled and empty symbols, respectively. (d) Pore size distribution (PSD) analysis for the adsorption branch was calculated by using QSDFT (quenched solid state density functional theory) model for carbon with slit/cylindrical/sphere pores. H-PMF-66 is shown in gray, H-PMF-79 in pink, H-PMF-85 in light blue, H-PMF-88 in light green, H-PMF-89 in light orange P-PMF-66 is shown in black, P-PMF-79 in red, P-PMF-85 in blue, P-PMF-88 in dark green and P-PMF-89 in orange.

Table 5.2. Surface area (S_{BET}), pore volume (PV), micro pore volume (MPV) and CO₂ uptake of the H- and P-PMF samples and dried Ludox[®] HS-40.

Sample Code	S_{BET} (m ² g ⁻¹) ^a	PV (cm ³ g ⁻¹) ^b	MPV (cm ³ g ⁻¹) ^c	CO ₂ Uptake (mmol g ⁻¹) ^d
H-PMF-66	28	n.a.	n.a.	n.a.
P-PMF-66	409	0.78	0.15	2.23
H-PMF-79	87	0.19	n.a.	n.a.
P-PMF-79	393	0.76	0.15	1.84
H-PMF-85	159	0.39	0.06	n.a.
P-PMF-85	116	0.23	0.04	1.25
H-PMF-88	198	0.45	0.07	n.a.
P-PMF-88	156	0.24	0.06	1.24

Mesoporous Poly(Melamine-co-Formaldehyde) Particles for Efficient and Selective Phosphate and Sulfate Removal

H-PMF-89	155	0.50	0.06	n.a.
P-PMF-89	136	0.23	0.05	1.03
Ludox® HS-40^e	185	0.71	0.07	n.a.

^a Surface area calculated from N₂ adsorption isotherm using BET equation; ^b pore volume (PV) calculated from N₂ uptake at p/p₀ = 0.95; ^c micro pore volume (MPV) calculated from N₂ uptake at p/p₀ = 0.10; ^d CO₂ uptake calculated for 273 K and 1 bar. ^e For Ludox® HS-40 particles precipitated with ethanol and subsequently dried.

The P-PMF samples exhibited type IV isotherms with type H1 hysteresis loops starting at p/p₀ ~ 0.42. For type H1 isotherms, adsorption and desorption isotherms are parallel to each other due to an accessible and well-connected pore system. Hence, the P-PMF samples featured ordered mesopores due to the successful implementation of the silica template to the resin. The specific surface area of the P-PMF series had its maximum value at 409 m²/g with a silica template content of 66 wt.% (i.e., P-PMF-79, see Table 5.2, Figure 5.5c). P-PMF-85 featured the lowest specific surface area with 116 m²/g. The PSDs of P-PMF-66 and P-PMF-79 were very similar with pore sizes of around 15 nm in diameter, indicating a well-implemented templating process. P-PMF-85 featured a smaller amount of mesopores yielding in a decrease in surface area. Overall, the peaks of the PSD of P-PMF-85, P-PMF-88 and P-PMF-89 exhibited a generally broader PSD in comparison to P-PMF-79 and P-PMF-66. As already shown in Figure 5.3, a template amount ≥ 85 wt.% leads to a partial incorporation of SiO₂ NPs into the polymer network because the ratio of SiO₂ NPs in comparison to the available amount of PMF is too high. Thus, the broad and smaller PSD of P-PMF-85, P-PMF-88 and P-PMF-89 can be explained by a partial pore collapse in the PMF particles due to the lack of PMF during the synthesis. The network is not as crosslinked and stable as for the samples P-PMF-79 and P-PMF-66. This results in a great variance in pore sizes and a decrease in surface area.

The CO₂ sorption experiments and the calculated CO₂ uptake follows the trend shown by the N₂ sorption experiments (Table 5.2, Figure 5.5d). The relatively high CO₂ uptake of up to 2.23 mmol/g for P-PMF-66 and the course of the curve indicates a combination of micro- and mesopores in the PMF structure. Furthermore, all samples exhibited hysteresis loops in the adsorption/desorption curve at 273 K.

To further analyze the potential adsorption properties resulting from the chemical structure, streaming potential vs. pH curves were determined for all H- and P-PMF samples, as presented in Figure S6. While the H-PMF samples exhibited an isoelectric point (IEP) between pH 3.7 and 4.8, the IEP of the P-PMF samples featured IEP above pH 6. The positive charge of all PMF samples was due to their abundant amino functionalities, which are partially positively charged in dependence of the pH value. SiO₂ NPs are negatively charged with an IEP often below a pH of 3.0 [65,66]. Thus, this led to a significant decrease in the IEP values of the H-PMF particles in comparison to the P-PMF particles.

2.2. Sorption Experiments

To investigate the adsorption of oxyanions onto the PMF resins in dependency of the silica content in the materials synthesis, adsorption isotherms of all P-PMF samples with sulfuric acid and phosphoric acid were determined. For comparison, the adsorption isotherm of the hybrid material H-PMF-66 was investigated as well. Furthermore, the isotherms were validated with the Langmuir and Dubinin–Radushkevich model (Figure 5.6). A fitting comparison is shown in Figure S13.

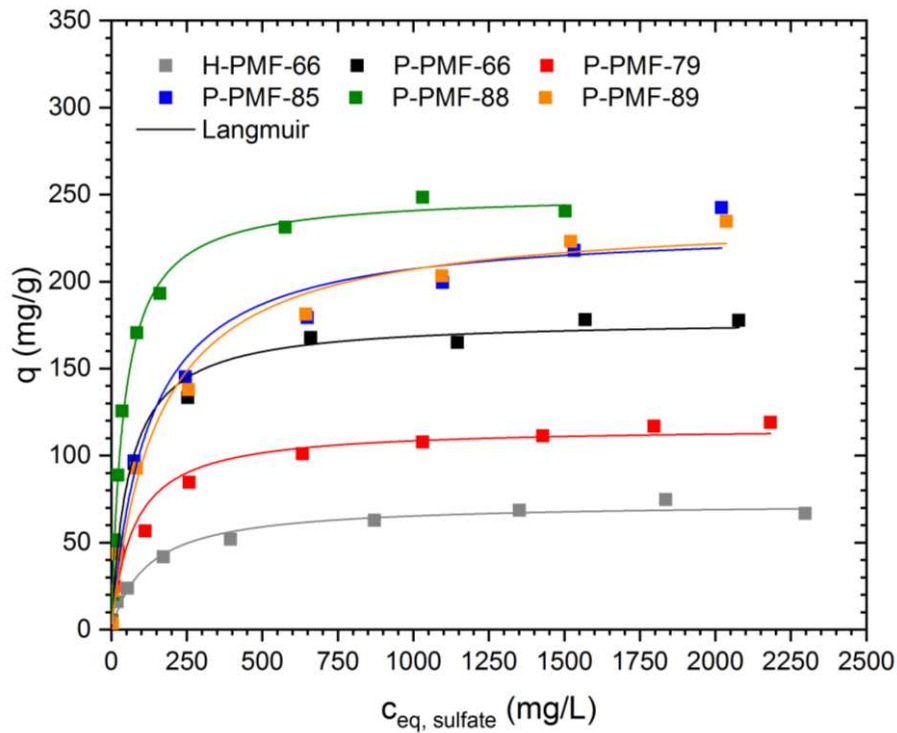


Figure 5.6. Sorption isotherms for sulfate ions onto H-PMF-66 (gray), P-PMF-66 (black), P-PMF-79 (red), P-PMF-85 (blue), P-PMF-88 (green) and P-PMF-89 (orange) with the corresponding Langmuir fits (solid lines). The corresponding pH values are displayed in Figures S7–S12. The fitting parameters are displayed in Table 5.3. The respective fitting comparison can be seen in Figure S13.

Table 5.3. Fitting parameters for Langmuir and Dubinin–Radushkevich isotherm models for sulfate adsorption onto H-PMF-66 and P-PMF samples. Q_m thereby is the maximal sorption capacity, K is the equilibrium constant, β_{DR} represents the activity coefficient related to the energy of adsorption E_{Ads} , R^2 (COD) is the coefficient of determination for the respective fit. For all parameters, the corresponding standard error from the fit is given. The respective fitting comparison can be seen in Figure S13.

Sample	Model	Q_m mg/g	K L/mg	β_{DR} $10^{-7} \text{ mol}^2/\text{J}^2$	$E_{ads,DR}$ kJ/mol	R^2 (COD)
H-PMF-66	Langmuir	73.0 ± 2.4	8.46 ± 1.39	--	--	0.987
	Dubinin–Radushkevich	64.1 ± 3.5	--	1.56 ± 0.47	1.79 ± 0.27	0.934
P-PMF-66	Langmuir	178.4 ± 4.2	17.15 ± 2.47	--	--	0.992
	Dubinin–Radushkevich	162.2 ± 7.3	--	0.61 ± 0.16	2.86 ± 0.36	0.957
P-PMF-79	Langmuir	116.4 ± 4.8	13.67 ± 3.44	--	--	0.968

Mesoporous Poly(Melamine-co-Formaldehyde) Particles for Efficient and Selective Phosphate and Sulfate Removal

	Dubinin–Radushkevich	103.22 ± 5.7	--	0.56 ± 0.17	2.99 ± 0.45	0.917
P-PMF-85	Langmuir	232.4 ± 10.8	8.3 ± 1.96	--	--	0.979
	Dubinin–Radushkevich	205.0 ± 12.4	--	1.96 ± 0.68	1.59 ± 0.27	0.934
P-PMF-88	Langmuir	250.7 ± 4.5	24.25 ± 1.84	--	--	0.995
	Dubinin–Radushkevich	230.3 ± 6.1	--	0.56 ± 0.05	2.99 ± 0.14	0.985
P-PMF-89	Langmuir	238.4 ± 8.8	6.61 ± 1.16	--	--	0.987
	Dubinin–Radushkevich	206.5 ± 12.0	--	2.59 ± 0.84	1.38 ± 0.22	0.940

The adsorption capacity of sulfate ions was determined by increasing the amount of sulfuric acid in solution (i.e., c_0 increases). Thus, since the pH was not adjusted, the pH decreased with the increasing concentration of sulfate ions. Among all P-PMF samples, P-PMF-88 exhibited the largest experimental adsorption capacity for sulfate with 250 mg/g. The other P-PMF samples showed respective adsorption capacities around 230 mg/g (P-PMF-85 and P-PMF-89), 150 mg/g (P-PMF-66) and 100 mg/g (P-PMF-79). Although P-PMF-66 and P-PMF-79 featured the highest surface areas, both samples possessed the lowest adsorption capacities. P-PMF-88, P-PMF-89 and P-PMF-85 shared relatively similar PSDs with a broad peak between approximately 6 and 14 nm in diameter (Figure 5.5d), which is beneficial for the adsorption of sulfate ions. In contrast, P-PMF-66 and P-PMF-79 exhibited a monodisperse pore size with diameters around 15 and 17 nm, respectively. The maximum experimental adsorption capacity of the hybrid H-PMF-66 sample was 75 mg/g, which can be explained by the absence of pores and therefore the significantly smaller surface area of the sample. Furthermore, the adsorption capacity for H-PMF-66 was calculated to the total mass of the particles including the 55 wt.% of silica. The Langmuir fits describe the corresponding adsorption isotherms successfully (R^2 values ranging from 0.979 to 0.995) (see Table 5.3). Thus, the removal of sulfate ions occurs as monolayer adsorption process on an energetically homogeneous surface. From these results, two main points can be deduced for the adsorption of sulfate: first, the calculated values for the specific surface area by BET from N_2 sorption measurements do not correlate with the sulfate adsorption capacities for P-PMF. Second, the broad pore size distributions featuring in total smaller pore sizes have a positive effect on the adsorption performance for P-PMF-88, P-PMF-85 and P-PMF-89 (Figure 5.5d). P-PMF-66 and especially P-PMF-79 featured a very homogenous pore size of approximately 15 nm and significantly lower adsorption capacities. The fitting with Dubinin–Radushkevich showed high R^2 values, which were below the ones from Langmuir fitting in all cases. Nonetheless, the calculated energy of adsorption values E_{Ads} ranging from 2.99 to 1.38 conclude a physisorption process. Additionally, a strong interaction toward sulfate ions can be deduced from the steep slope of the isotherms at low c_{eq} values and E_{Ads} , especially for P-PMF-88, P-PMF-79 and P-PMF-66.

The pH_0 and pH_{eq} values of the adsorption experiments are shown in Figures S7–S12. For the adsorption mechanism, the pH of the solution is an important parameter. The pH increases through the adsorption process, which can be explained by the protonation of different

nitrogen functionalities within the PMF particles enabling ionic interactions to the sulfate ions. Above a pH of 2.0, sulfate is almost to 100% present in its divalent SO_4^{2-} form. At lower pH values, it shifts to the protonated HSO_4^- form, which is in equimolar share at approximately $\text{pH} = 1.75$ [67].

P-PMF-88 with $c_{\text{eq}} = 1502 \text{ mg/L SO}_4^{2-}$ was further investigated after the adsorption process by SEM-EDX. Figure 5.7 features a homogeneous distribution of sulfur (i.e., sulfate) on the sample. Thus, the adsorption process occurred on a homogenous surface.

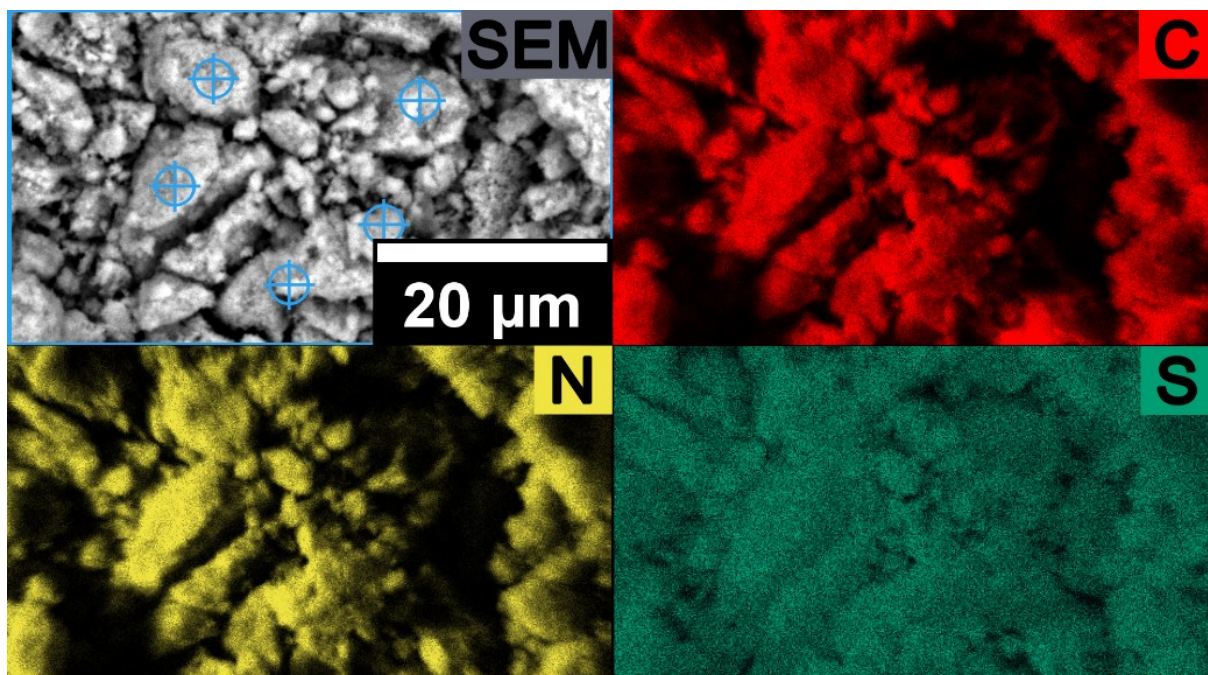


Figure 5.7. SEM image and SEM-EDX elemental mapping of P-PMF-88 after the adsorption of sulfate with $c_{\text{eq}} = 1502 \text{ mg/g SO}_4^{2-}$ with the elements C shown in red, N in yellow and S in dark green.

Additionally, the adsorption of phosphate ions was investigated in the same concentration range as for sulfate ions (Figure 5.8 and Table 5.4). Similar to the experiments with sulfate, P-PMF-88 showed the highest adsorption capacity with 297 mg phosphate/g. The second-highest adsorption capacity was achieved for P-PMF-85 (241 mg/g), followed by P-PMF-66 (191 mg/g), P-PMF-89 (151 mg/g) and P-PMF-79 (144 mg/g). Comparing the H-PMF-66 hybrid sample with the corresponding P-PMF-66, the drastic decrease in the adsorption capacity to approximately 45 mg/g is obvious. This effect can be explained by the significantly lower surface area. The trend for the adsorption capacities for phosphate is relatively similar to sulfate except for P-PMF-89.

Mesoporous Poly(Melamine-co-Formaldehyde) Particles for Efficient and Selective Phosphate and Sulfate Removal

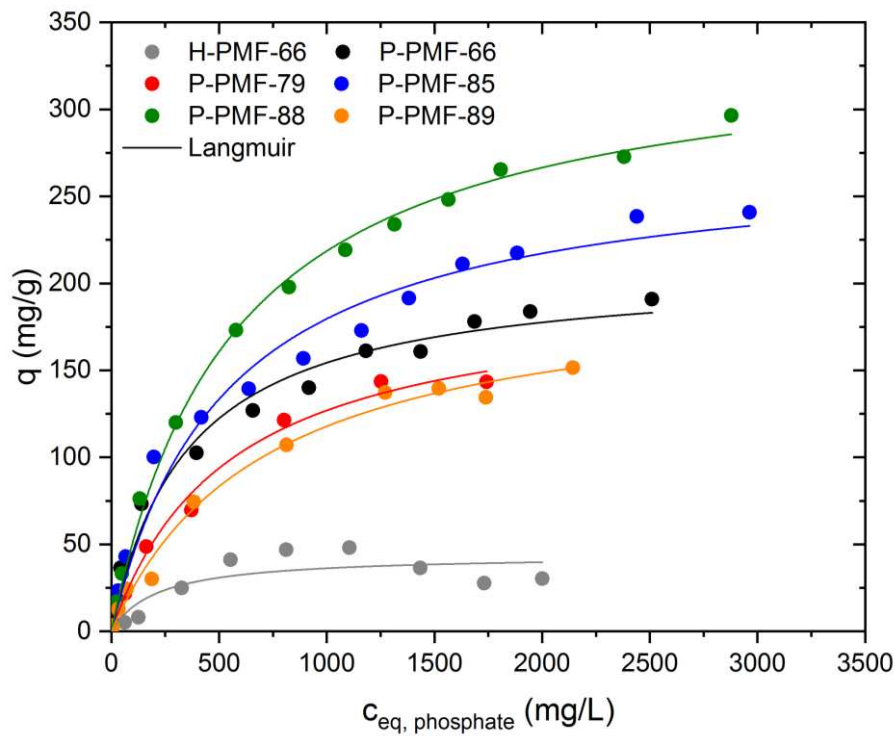


Figure 5.8. Sorption isotherms for phosphate ions onto H-PMF-66 (gray), P-PMF-66 (black), P-PMF-79 (red), P-PMF-85 (blue), P-PMF-88 (green) and P-PMF-89 (orange) with the corresponding Langmuir fits (solid lines). The corresponding pH values are displayed in Figures S7–S12. The fitting parameters are displayed in Table 5.4. The respective fitting comparison can be seen in Figure S14.

Table 5.4. Fitting parameters for Langmuir and Dubinin–Radushkevich isotherm models for phosphate adsorption onto H-PMF-66 and P-PMF samples. Q_m thereby is the maximal sorption capacity, K is the equilibrium constant, β_{DR} represents the activity coefficient related to the energy of adsorption E_{Ads} , R^2 (COD) is the coefficient of determination for the respective fit. For all parameters, the corresponding standard error from the fit is given. The respective fitting comparison can be seen in Figure S14.

Sample	Model	Q_m mg/g	K L/mg	β_{DR} $10^{-7} \text{ mol}^2/\text{J}^2$	$E_{ads,DR}$ kJ/mol	R^2 (COD)
H-PMF-66	Langmuir	43.9 ± 7.6	4.72 ± 3.51	--	--	0.748
	Dubinin–Radushkevich	39.0 ± 3.8	--	7.13 ± 3.58	0.83 ± 0.21	0.825
P-PMF-66	Langmuir	208.9 ± 9.5	2.83 ± 0.50	--	--	0.984
	Dubinin–Radushkevich	164.2 ± 8.9	--	6.47 ± 2.36	0.88 ± 0.16	0.907
P-PMF-79	Langmuir	196.4 ± 11.2	1.83 ± 0.28	--	--	0.993
	Dubinin–Radushkevich	138.0 ± 9.7	--	1.16 ± 3.42	0.66 ± 0.10	0.942
P-PMF-85	Langmuir	274.6 ± 14.4	1.89 ± 0.33	--	--	0.978
	Dubinin–Radushkevich	204.5 ± 12.2	--	11.9 ± 4.42	0.65 ± 0.12	0.867
P-PMF-88	Langmuir	341.4 ± 7.3	1.78 ± 0.12	--	--	0.997
	Dubinin–Radushkevich	256.4 ± 12.4	--	16.0 ± 4.64	0.56 ± 0.08	0.935
P-PMF-89	Langmuir	201.3 ± 12.4	1.41 ± 0.23	--	--	0.990
	Dubinin–Radushkevich	142.6 ± 6.4	--	1.96 ± 0.43	0.50 ± 0.05	0.964

Comparing the adsorption of sulfate and phosphate, phosphate possessed a significantly higher adsorption capacity despite the higher valency of the phosphate species at low pH

values [67–69]. In the adsorption experiments, pH_{eq} values between 2.0 and 3.0 were measured for higher phosphate concentrations (see Figures S7–S12). In this pH range, phosphate is present either as monovalent H_2PO_4^- or uncharged H_3PO_4 , whereas the concentration of HPO_4^{2-} or PO_4^{3-} is negligible. In general, phosphoric acids are less acidic than sulfuric acid, which can alter the adsorption behavior of the samples in terms of ionic interactions due to protonated nitrogen functionalities. Furthermore, phosphate ions and their protonated species are more likely to form hydrogen bonds as its P–O or P=O bonds exhibit a greater dipole moment than the S–O or S=O bonds of sulfate, respectively. Thus, the higher adsorption capacity of phosphate can be explained by the formation of hydrogen bonds between, e.g., N–H and the oxygen of phosphate or an unprotonated nitrogen atom with an O–H group of the phosphate species. In addition, the undissociated H_3PO_4 molecule can interact by hydrogen bonding with the PMF polymer. Additionally, the monovalent phosphate species can adsorb by ionic interactions with the PMF particles. Thereby, only one amino group would be needed for this binding motive, leading to higher adsorption capacities. Additionally, as seen in literature for ion exchange materials, a possible process is multiple bound molecules of higher charge sharing binding sites with species of lower charge in order to equalize the charge of both molecules [70]. This would lead to an overall higher adsorption, supporting our findings. The Langmuir and Dubinin–Radushkevich fittings are displayed in Figure S14. Except from H-PMF-66, the Langmuir isotherm model comprised a more valid fitting for the given isotherms with regard to R^2 values (see Table 5.4). However, the obtained adsorption capacities from Langmuir showed values around the highest experimental values. The fitting parameters support the outstanding adsorption capacity of P-PMF-88 for phosphate with $Q_m = 341 \text{ mg/g}$, followed by P-PMF-85 with 275 mg/g .

The E_{Ads} values for the phosphate adsorption from Dubinin–Radushkevich are in the range of 0.89 to 0.50 kJ/mol. When comparing these with the ones obtained in the adsorption experiments with sulfate, a significantly stronger adsorption interaction for sulfate can be seen which can be, e.g., due to the lower valence of phosphate in this pH region.

After the adsorption experiment of the H-PMF-88 sample with phosphate solution ($c_{\text{eq}} = 2879 \text{ mg/L}$), SEM-EDX analysis for an elemental mapping was carried out (see Figure 5.9). Similar to sulfate, phosphate is homogeneously distributed over the sample surface which supports the suggestion of a homogenous adsorption process.

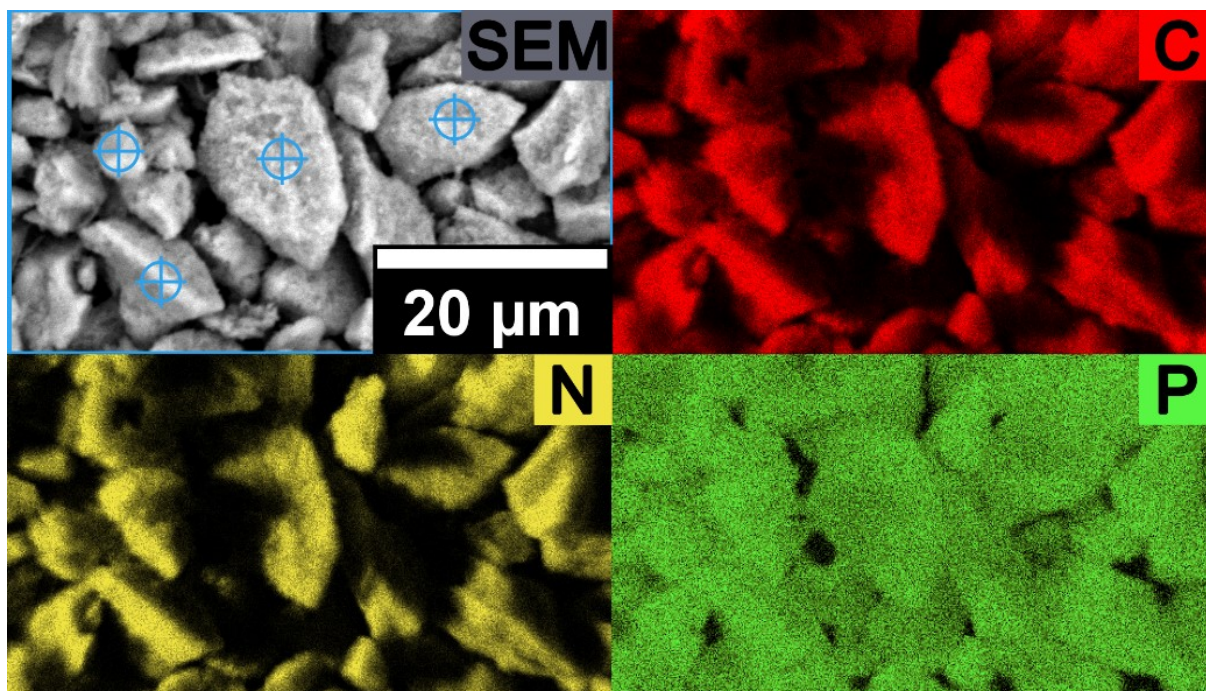


Figure 5.9. SEM image and SEM-EDX elemental mapping of P-PMF-88 after adsorption of phosphate with $c_{eq} = 1502 \text{ mg/g PO}_4^{3-}$ with the elements C shown in red, N in yellow and P in light green.

The obtained adsorption capacities for phosphate and sulfate outperform different commercially available ion exchange resins which are applied in industrial scale for water treatment applications (see Tables S1 and S2) by far. E.g., Amberlite IRA-900 or Lewatit K6362 as anion exchange resins featured adsorption capacities of 57 and 167 mg sulfate/g, respectively [71,72]. The adsorption capacity of P-PMF was as high as 251 mg/g. For phosphate, adsorption capacities between 24 to 147 mg/g were found for commercially available anion exchange resins [73–75]. P-PMF samples here reached outstanding 341 mg/g as adsorption capacities.

To investigate the adsorption affinity of sulfate in competition with phosphate, adsorption experiments with a solution containing both 10 mg/L sulfate and 10 mg/L phosphate were carried out. The results can be seen in Figure 5.10 and the corresponding pH values are presented in Figure S15.

In general, all samples featured a higher adsorption of sulfate than phosphate. The P-PMF samples successfully removed nearly all sulfate ions in the solution (95 to 100%). The simultaneous adsorption of phosphate ions yielded in broad distribution ranging from 16 to 58% of adsorption. Thus, the ratio of adsorbed sulfate per adsorbed phosphate ranged from 1.7 to 5.7 among the P-PMF samples. P-PMF-89 featured the highest adsorption of phosphate with 58%, while at the same time 100% of sulfate was adsorbed as well. This is in agreement with the significantly lower E_{Ads} values for phosphate compared to sulfate, as was shown by the Dubinin–Radushkevich isotherm fitting.

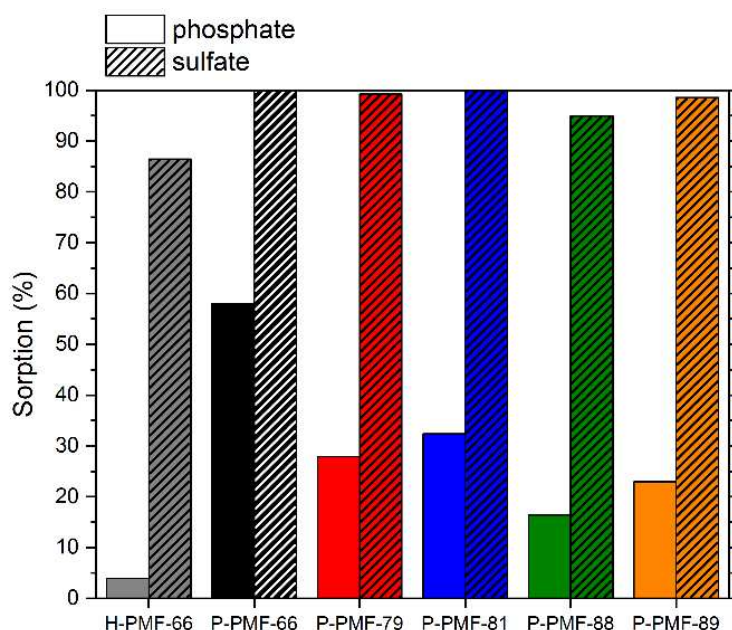


Figure 5.10. Percentage adsorption of PO_4^{3-} (solid) and SO_4^{2-} (striped) for H-PMF-66 and the P-PMF samples from a solution containing both 10 mg/L PO_4^{3-} and 10 mg/L SO_4^{2-} , whereby H-PMF-66 is shown in gray, PMF-66 in black, P-PMF-79 in red, P-PMF-85 in blue, P-PMF-88 in green and P-PMF-89 in orange. The respective pH_0 and pH_{eq} values can be seen in Figure S15.

In comparison to the P-PMF samples, H-PMF-66 featured 87% adsorption of sulfate and 4% adsorption for phosphate due to the extremely low surface area. However, the different adsorption process on the surface of the particle led to a ratio of adsorbed sulfate to adsorbed phosphate of approximately 21.6:1, which indicates an exceptional preferable adsorption of sulfate ions. In contrast, the adsorption of phosphate onto the P-PMF samples was significantly higher with a ratio of only 1.7 $\text{SO}_4^{2-}:\text{PO}_4^{3-}$.

As H-PMF-66 showed an outstanding selectivity for sulfate adsorption, we additionally investigated its adsorption behavior for various other phosphate/sulfate ratios and concentrations (Figure 5.11). The results show a clear selectivity towards the adsorption of sulfate and only minor adsorption of phosphate even in a 40:20 ratio of phosphate to sulfate of the initial solution. Hereby, sulfate ions were adsorbed via ionic interaction on the outer surface of the hybrid particles. Probably, as hydrogen bonds in confined pores could be decisive for phosphate adsorption, the absence of a viable pore structure and the lower strength of hydrogen bonds vs. ionic interactions hindered its adsorption. When increasing the overall concentration while maintaining the 1:1 ratio (Figure 5.11b), sulfate was still strongly favored by the H-PMF-66 sample, decreasing overall adsorption of both sulfate and phosphate in most cases. As the synthesis of H-PMF-66 is simple, it represents a viable separator for wastewaters contaminated with mixtures of sulfate and phosphate.

Mesoporous Poly(Melamine-co-Formaldehyde) Particles for Efficient and Selective Phosphate and Sulfate Removal

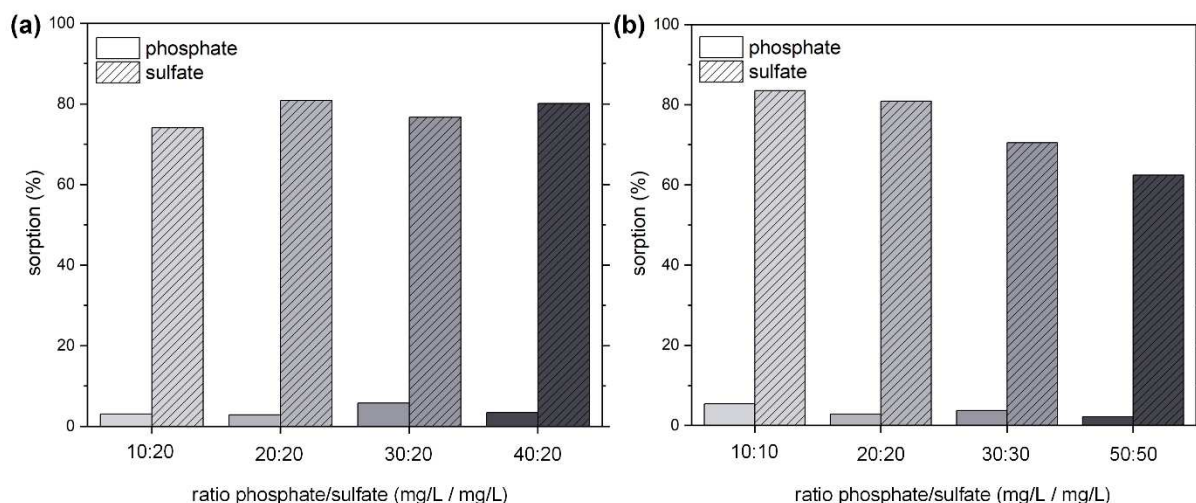


Figure 5.11. Percentage adsorption of PO_4^{3-} (solid) and SO_4^{2-} (striped) for H-PMF-66 from (a) solutions containing both phosphate (at different concentrations) and 20 mg/L sulfate; (b) solutions of 1:1 ratios of phosphate and sulfate at different concentrations. The respective pH_0 and pH_{eq} values can be seen in Figure S16 and S17.

3. Materials and Methods

3.1. Materials

3.1.1. PMF Particles

For the synthesis of the PMF particles, melamine (Sigma-Aldrich, München, Germany, 99%), paraformaldehyde (Sigma-Aldrich, München, Germany, 95%), oxalic acid (Sigma-Aldrich, München, Germany, 99%), NaOH (Honeywell, Offenbach, Germany, $\geq 98\%$) and Ludox[®] HS-40 (Sigma-Aldrich, München, Germany, 40 wt.% in H_2O) were used as received without further purification. The synthesis was carried out in ultrapure water purified by a Milli-Q Advantage A10[®] system (Millipore, Darmstadt, Germany) (total organic carbon = 5 ppb, resistivity of 18.2 $\text{M}\Omega\cdot\text{cm}$ at 25 °C).

3.1.2. Oxyanions

For the adsorption experiments, H_2SO_4 (Acros, 96% in H_2O) and H_3PO_4 (Sigma-Aldrich, München, Germany, 85% in H_2O) were used as received without further purification.

3.1.3. Ultrapure Water

For all experiments, ultrapure water purified by a Milli-Q Advantage A10[®] system (Millipore, Darmstadt, Germany) (total organic carbon = 5 ppb, resistivity of 18.2 $\text{M}\Omega\cdot\text{cm}$) was used.

3.1.4. ICP-OES Standard Solutions

For the ICP-OES measurements 10,000 mg/L P (Bernd Kraft, Duisburg, Germany) and 9998 mg/L S (Sigma-Aldrich, München, Germany) were used as standard solutions.

3.2. Methods

Thermogravimetric analysis (TGA) was performed by using the device 1 Star System from Mettler Toledo, Gießen, Germany. The measurements were carried out with approximately 5 to 8 mg of the sample in a platinum crucible. The investigated temperature range was from 25 to 1000 °C with a heating rate of 10 °C/min, under air atmosphere at a flow rate of 40 mL/min.

Scanning electron microscopy (SEM) was carried out using a SEM Ultra Plus from Carl Zeiss Microscopy GmbH, Oberkochen, Germany. For this purpose, the samples were fixed with double-sided adhesive carbon tape on an aluminum pin sample tray and afterwards streamed with N₂ to obtain only a thin layer of particles. The samples were then sputtered with 3 nm of platinum using a Sputter Coater SCD050 from Leica Microsystems, Wetzlar, Germany before the investigation started. The measurements were carried out with an acceleration voltage of 3 keV at different magnifications.

Transmission electron microscopy (TEM) was carried out using a Libra 120 device from Carl Zeiss Microscopy GmbH, Oberkochen, Germany. The acceleration voltage was 120 keV. The studied particles were dispersed in ultrapure water and dropped onto a carbon-coated Cu mesh.

Particles sizes of both, the purified particles and the unpurified reaction mixtures after synthesis were analyzed using a Zetasizer Nano ZS (Malvern, Kassel, Germany). Therefore, the reaction mixture was prepared as stated in Section 3.3 for each sample. After the synthesis, the dispersion was stirred for 15 min before measurement. Data were evaluated using Particle RI: 1.5, Abs.: 0.1000 and Dispersant RI: 1.3300.

Nitrogen and CO₂ sorption measurements were performed using the Autosorb iQ MP from Quantachrome Instruments, Boynton Beach, USA. Samples of 100 mg were activated by degassing in vacuum (5×10^{-10} mbar) at 110 °C for 24 h. The nitrogen sorption measurements were performed at 77 K. The surface area was calculated in the relative pressure (p/p_0) range from 0.07 to 0.22 by BET method [76]. The pore size distribution (PSD) was determined by a QSDFT (quenched solid density functional theory) model fit of the nitrogen adsorption isotherm, including spherical, cylindrical and slit pores of carbon materials. CO₂ sorption measurements were performed at 273 K.

Attenuated total reflection infrared spectroscopy (ATR-FTIR) measurements were performed using a Tensor 27 device equipped with a Platinum ATR module both from Bruker Corporation, Billerica, MA, USA. All samples were measured in dry state with a resolution of 2 cm⁻¹ and with 100 scans. The acquired spectra were subjected to atmospheric compensation to remove the rotation bands of water. Further, all spectra were normalized using the triazine ring-bending band at 812 cm⁻¹.

Inductively coupled plasma optical emission spectrometry (ICP-OES) (iCAP 7400 from Thermo Scientific) was used to determine the sulfate and phosphate ion concentrations in

simulated water. Thus, four standards were used (Standard 1: S (3000 mg/L), P (3000 mg/L) in 4 wt.% HNO₃; Standard 2: S (1000 mg/L), P (1000 mg/L) in 4 wt.% HNO₃; Standard 3: S (500 mg/L), P (500 mg/L) in 4 wt.% HNO₃; Standard 4: S (100 mg/L), P (100 mg/L) in 4 wt.% HNO₃). To each sample (8 mL) 2 mL 20% nitric acid was added prior to analysis. Each concentration was determined from threefold measurement.

Streaming potential vs. pH curves were measured to determine the surface charge of the particles in dependence of the pH value. The particles were characterized by titration to either pH 3 or 9 from the initial pH with the particle charge detector Müttek PCD-04 from the company BTG Instruments GmbH, Wessling, Germany with 0.1 M HCl or 0.1 M NaOH, respectively. For this purpose, 0.16 g particles were added to 100 mL of ultrapure water. The dispersion was homogenized with an ultrasonic bath for 2 h.

Scanning electron microscope with energy-dispersive X-ray spectroscopy (SEM-EDX): The elemental mapping of the samples after adsorption was carried out using a Phenom XL Workstation from Thermo Scientific (Waltham, MA, USA) with an energy-dispersive X-ray spectroscopy detector (Silicon Drift Detector SDD, thermoelectrically cooled (LN₂free), 25 mm² detector active area). The samples were fixed on double-sided adhesive carbon tape on an aluminum pin sample tray. The measurements were carried out in high vacuum mode ($p = 0.1$ Pa) with an acceleration voltage of 10 keV at different magnifications.

pH measurement: The measurement of pH was carried out with the device SevenExcellence from Mettler Toledo (Gießen, Germany) at r.t..

Centrifugation: The adsorber materials were separated from the supernatant by centrifugation with the device 5804 from Eppendorf (Leipzig, Germany) at r.t. and 10,000 rpm.

Elemental analysis was carried out using a vario MICRO cube from the company Elementar, Langenselbold, Germany.

3.3. Synthesis of the PMF Particles

3.3.1. Synthesis of PMF-66

The PMF-66 particles were synthesized as recently published [47] with minor modifications by first dispersing 9.1 g (72.2 mmol) melamine (M) and 12.95 g (431.2 mmol) paraformaldehyde (F) in 175 mL ultrapure water in a 1 L round bottom flask. The dispersion was stirred at 50 °C for 40 min under reflux. A solution of 525 mL ultrapure water with 1.4 g (15.5 mmol) oxalic acid and 42.0 g Ludox[®] HS-40 was prepared and then added to the reaction mixture. The resulting mixture was stirred for 24 h at 100 °C under reflux.

3.3.2. Synthesis of PMF-79, PMF-85, PMF-88 and PMF-89 Particles

The synthesis of PMF-79, PMF-85, PMF-88 and PMF-89 was modified by increasing the amount of Ludox[®] HS-40 (see Table 5.5). PMF particles containing silica particles are called

Mesoporous Poly(Melamine-co-Formaldehyde) Particles for Efficient and Selective Phosphate and Sulfate Removal

hybrid (H-). After the removal of the silica particles by treatment of the hybrid particles with NaOH, nanoporous PMF-particles (P-) were obtained.

Table 5.5. Table of reactants in synthesis (melamine (M), paraformaldehyde (F) and Ludox® HS-40 (HS-40)) for of H-PMF and P-PMF particles with the corresponding sample codes.

Sample	m (M)	m (F)	m (HS-40)	Ratio (M-F-HS-40) ^a	pH (HS-40) ^b	pH ^c	pH ^d
PMF-66	9.1 g	12.95 g	42 g	66%	9.8	2.14	3.52
PMF-79	9.1 g	12.95 g	84 g	79%	9.8	2.44	3.89
PMF-85	9.1 g	12.95 g	126 g	85%	9.8	3.27	4.32
PMF-88	9.1 g	12.95 g	168 g	88%	9.8	4.07	5.01
PMF-89	9.1 g	12.95 g	182 g	89%	9.8	4.15	5.15

^a Mass ratio of Ludox® HS-40/(melamine + paraformaldehyde + Ludox® HS-40) in reaction mixture; ^b pH of the pure Ludox® HS-40 dispersion; ^c pH of the dispersion containing ultrapure water, oxalic acid and Ludox® HS-40 solution; ^d pH of the final reaction mixture after 24 h at 100 °C under reflux.

Purification of H-PMF samples: The sediment was transferred into a 1 L vessel with ultrapure water. The particles were washed in ultrapure water three times. Meanwhile, the vessel with the dispersion was placed on a shaker for 24 h at r.t.. Subsequently, the sedimented particles were freeze-dried. As these particles still contained the SiO₂ NPs, these samples are called hybrid PMF (H-PMF) samples.

Purification of P-PMF samples: To obtain the pure PMF particles, the sediment of the reaction mixture was transferred into a 1 L vessel and filled with 1 M NaOH solution to remove the SiO₂ NPs. The solution was placed on a shaker for 24 h. The washing procedure with 1 M NaOH was repeated two more times. The particles were then transferred to a Spectra/Por™ 2 dialysis bag (Spectrum Chemical Mfg. Corp., New Brunswick, USA) and dialyzed with ultrapure water. The resulting particles were freeze-dried.

3.4. Water Treatment Experiments

3.4.1. Adsorption Experiments with Sulfuric and Phosphoric Acid

Next, 50 mg of each adsorber material was placed into a 50 mL centrifuge tube. Subsequently, 30 mL of the adsorptive solution was added to every sample. The pH of the samples was not adjusted. The samples were then magnetically stirred for 24 h at r.t. Afterwards, the samples were centrifuged for 12 min at 10,000 rpm. The supernatant of the samples after the adsorption and the initial concentrations of the adsorptive solutions were analyzed by ICP-OES. The pH of the solutions were determined.

3.4.2. Theoretical Model

To determine the sorption efficiency of the PMF samples, the concentrations of the adsorbed oxyanions in equilibrium were detected by ICP-OES. In Equation (5.1), these concentrations were used for the calculation of the adsorption in percent. Thereby, c_0 is the

Mesoporous Poly(Melamine-co-Formaldehyde) Particles for Efficient and Selective Phosphate and Sulfate Removal

concentration of the respective ion in the initial solution and c_{eq} is the concentration after reaching equilibrium.

$$\text{adsorption} = 100\% \cdot \frac{c_0 - c_{eq}}{c_0} \quad (5.1)$$

The respective sorption capacity q_{eq} in equilibrium was calculated as follows:

$$q_{eq} = \frac{(c_0 - c_{eq}) \cdot V_L}{m_A} \quad (5.2)$$

With V_L referring to the given volume of the adsorptive solution and m_A to the mass of the sorbent material used in the experiment.

To model the sorption process, Langmuir (Equation (5.3)) [77] and Dubinin–Radushkevich [78] (Equations (5.4)–(5.7)) isotherm models were chosen.

$$q_{eq} = \frac{Q_m \cdot K_L \cdot c_{eq}}{1 + K_L \cdot c_{eq}} \quad (5.3)$$

K_L thereby represents the Langmuir equilibrium constant and Q_m the maximum adsorption capacity [79,80].

The non-linear equation for the Dubinin–Radushkevich isotherm model is the following [56,57]:

$$q_{eq} = Q_m \cdot \exp(-\beta_{DR} \cdot \varepsilon^2) \quad (5.4)$$

Q_m again represents the maximum adsorption capacity, β_{DR} the activity coefficient which is related via Equation (5.7) to the mean free energy of adsorption $E_{ads,DR}$ and ε corresponds to the Polanyi potential, which can also be expressed by Equation (5.5).

$$\varepsilon = RT \cdot \ln\left(\frac{c_s}{c_{eq}}\right) \quad (5.5)$$

c_s hereby represents the solubility of the adsorbate. The term inside the logarithm $\frac{c_s}{c_{eq}}$ can be exchanged for $1 + \frac{1}{c_{eq}}$ according to Zhou, leading to the same numerical solution with two requirements: First, this is only possible for values of $c_{eq} \ll c_s$. Second, it is important to use molar concentrations for the fitting [81]. We have implemented both as suggested. This leads to the following term for the Polanyi potential:

$$\varepsilon = RT \cdot \ln\left(1 + \frac{1}{c_{eq}}\right) \quad (5.6)$$

$$E_{ads,DR} = \frac{1}{\sqrt{2 \cdot \beta_{DR}}} \quad (5.7)$$

4. Conclusions

We successfully prepared highly functional PMF samples for use in oxyanion adsorption from simulated wastewater by a facile hard templating method with SiO₂ NPs. We thoroughly characterized both the hybrid silica/resin samples and the purified samples after template removal. Here, we showed that the preparation of samples with different pore size distributions and different specific surface areas between 136 and 409 m²/g is possible. The pore system exhibited a significant influence on the adsorption behavior, whereas the specific surface area did not affect the adsorption capacity as much as expected. P-PMF represent excellent adsorbers for oxyanions with outstanding adsorption capacities of 341 mg PO₄³⁻/g and 251 mg SO₄²⁻/g modeled with Langmuir and Dubinin–Radushkevich isotherm model. These adsorption capacities surpass industrially available ion exchange materials by two to five times in terms of adsorption capacity, while at the same time synthesis is possible with very convenient raw materials. The hybrid silica/resin material presents selective adsorption of sulfate, enabling a simple separation technique for wastewaters containing both sulfate and phosphate ions. E.g., in the battery production, wastewaters could first be treated with hybrid silica/PMF particles to adsorb sulfate selectively, and afterwards, separate phosphate with the porous P-PMF particles for phosphate recovery.

Author Contributions

Conceptualization, K.B.L.B.; **methodology**, C.S., K.B.L.B.; **validation**, K.B.L.B.; **formal analysis**, B.R., C.S., K.B.L.B.; **investigation**, B.R., P.Z., N.G., C.S., K.B.L.B.; **resources**, S.S.; **data curation**, K.B.L.B., D.S.; **writing—original draft preparation**, K.B.L.B.; **writing—review and editing**, B.R., P.Z., C.S., K.B.L.B., D.S., S.S.; **visualization**, C.S., K.B.L.B., D.S.; **supervision**, D.S.; **project administration**, S.S.; **funding acquisition**, S.S. All authors have read and agreed to the published version of the manuscript.

Funding

This research was funded by Bundesministerium für Bildung und Forschung, grant number 01DJ18010.

Acknowledgments

The authors thank Eileen Schierz and Roland Schulze for conduction of the elemental analysis and Marina Oelmann for the measurement of zeta potential vs. pH curves.

References

1. Fatima, T.; Muntean, A. Sulfate attack in sewer pipes: Derivation of a concrete corrosion model via two-scale convergence. *Nonlinear Anal. Real World Appl.* **2014**, *15*, 326–344, doi:10.1016/j.nonrwa.2012.01.019.

Mesoporous Poly(Melamine-co-Formaldehyde) Particles for Efficient and Selective Phosphate and Sulfate Removal

2. Katayev, E.A.; Ustynyuk, Y.A.; Sessler, J.L. Receptors for tetrahedral oxyanions. *Coord. Chem. Rev.* **2006**, *250*, 3004–3037, doi:10.1016/j.ccr.2006.04.013.
3. Elphick, J.R.; Davies, M.; Gilron, G.; Canaria, E.C.; Lo, B.; Bailey, H.C. An aquatic toxicological evaluation of sulfate: The case for considering hardness as a modifying factor in setting water quality guidelines. *Environ. Toxicol. Chem.* **2010**, *30*, 247–253, doi:10.1002/etc.363.
4. Soucek, D.J.; Kennedy, A.J. Effects of hardness, chloride, and acclimation on the acute toxicity of sulfate to freshwater invertebrates. *Environ. Toxicol. Chem.* **2005**, *24*, 1204–1210, doi:10.1897/04-142.1.
5. Austigard, Å.D.; Svendsen, K.; Heldal, K.K. Hydrogen sulphide exposure in waste water treatment. *J. Occup. Med. Toxicol.* **2018**, *13*, 1–10, doi:10.1186/s12995-018-0191-z.
6. Lamers, L.P.M.; Govers, L.L.; Janssen, I.C.J.M.; Geurts, J.J.M.; Van Der Welle, M.E.W.; Van Katwijk, M.M.; Van Der Heide, T.; Roelofs, J.G.M.; Smolders, A.J.P. Sulfide as a soil phytotoxin—a review. *Front. Plant Sci.* **2013**, *4*, 268, doi:10.3389/fpls.2013.00268.
7. Wang, H.; Zhang, Q. Research Advances in Identifying Sulfate Contamination Sources of Water Environment by Using Stable Isotopes. *Int. J. Environ. Res. Public Heal.* **2019**, *16*, 1914, doi:10.3390/ijerph16111914.
8. Liu, C.-Q.; Lang, Y.-C.; Satake, H.; Wu, J.; Li, S.-L. Identification of Anthropogenic and Natural Inputs of Sulfate and Chloride into the Karstic Ground Water of Guiyang, SW China: Combined $\delta^{37}\text{Cl}$ and $\delta^{34}\text{S}$ Approach. *Environ. Sci. Technol.* **2008**, *42*, 5421–5427, doi:10.1021/es800380w.
9. Man, K.; Ma, Z.M.; Xu, X.J. Research on the Mechanism of Sulfate Pollution of Groundwater in Jiaozuo Area. *Appl. Mech. Mater.* **2014**, *665*, 436–439, doi:10.4028/www.scientific.net/amm.665.436.
10. Miao, Z.; Carroll, K.; Brusseau, M.L. Characterization and quantification of groundwater sulfate sources at a mining site in an arid climate: The Monument Valley site in Arizona, USA. *J. Hydrol.* **2013**, *504*, 207–215, doi:10.1016/j.jhydrol.2013.09.030.
11. Mekonnen, M.M.; Hoekstra, A.Y. Global Anthropogenic Phosphorus Loads to Freshwater and Associated Grey Water Footprints and Water Pollution Levels: A High-Resolution Global Study. *Water Resour. Res.* **2018**, *54*, 345–358, doi:10.1002/2017wr020448.
12. Schindler, D.W.; Carpenter, S.; Chapra, S.C.; Hecky, R.E.; Orihel, D. Reducing Phosphorus to Curb Lake Eutrophication is a Success. *Environ. Sci. Technol.* **2016**, *50*, 8923–8929, doi:10.1021/acs.est.6b02204.
13. Schindler, D.W.; Vallentyne, J.R. *The algal Bowl: Overfertilization of the World's Freshwaters and Estuaries*; University of Alberta Press: Edmonton, AB, Canada, 2008; ISBN 9780888644848.
14. Sylvan, J.B.; Dortch, Q.; Nelson, D.M.; Brown, A.F.M.; Morrison, W.; Ammerman, J.W. Phosphorus Limits Phytoplankton Growth on the Louisiana Shelf During the Period of Hypoxia Formation. *Environ. Sci. Technol.* **2006**, *40*, 7548–7553, doi:10.1021/es061417t.
15. Seitzinger, S.P.; Harrison, J.; Dumont, E.; Beusen, A.; Bouwman, L. Sources and delivery of carbon, nitrogen, and phosphorus to the coastal zone: An overview of Global Nutrient Export from Watersheds (NEWS) models and their application. *Glob. Biogeochem. Cycles* **2005**, *19*, 1–11, doi:10.1029/2005gb002606.
16. Farmer, A.M. Phosphate pollution: A global overview of the problem. In *Phosphorus: Polluter and Resource of the Future—Removal and Recovery from Wastewater*; Schaum, C., Ed.; IWA Publishing: London, United Kingdom, 2018; pp 35–55; ISBN 9781780408361.
17. Horrigan, L.; Lawrence, R.S.; Walker, P. How sustainable agriculture can address the environmental and human health harms of industrial agriculture. *Environ. Health Perspect.* **2002**, *110*, 445–456, doi:10.1289/ehp.02110445.
18. Alewell, C.; Ringeval, B.; Ballabio, C.; Robinson, D.A.; Panagos, P.; Borrelli, P. Global phosphorus shortage will be aggravated by soil erosion. *Nat. Commun.* **2020**, *11*, 4546, doi:10.1038/s41467-020-18326-7.
19. Summaries, M.C. *Mineral Commodity Summaries*; U. S. Government Publishing Office: Washington, DC, USA, 2021; p. 200; doi:10.3133/mcs2021.
20. Chrispim, M.C.; Scholz, M.; Nolasco, M.A. Phosphorus recovery from municipal wastewater treatment: Critical review of challenges and opportunities for developing countries. *J. Environ. Manag.* **2019**, *248*, 109268, doi:10.1016/j.jenvman.2019.109268.
21. Petzet, S.; Peplinski, B.; Cornel, P. On wet chemical phosphorus recovery from sewage sludge ash by acidic or alkaline leaching and an optimized combination of both. *Water Res.* **2012**, *46*, 3769–3780, doi:10.1016/j.watres.2012.03.068.
22. Remmen, K.; Müller, B.; Köser, J.; Wessling, M.; Wintgens, T. Phosphorus recovery in an acidic environment using layer-by-layer modified membranes. *J. Membr. Sci.* **2019**, *582*, 254–263, doi:10.1016/j.memsci.2019.03.023.
23. Roy, E. Phosphorus recovery and recycling with ecological engineering: A review. *Ecol. Eng.* **2017**, *98*, 213–227, doi:10.1016/j.ecoleng.2016.10.076.
24. Jupp, A.R.; Beijer, S.; Narain, G.C.; Schipper, W.; Sloopweg, J.C. Phosphorus recovery and recycling—closing the loop. *Chem. Soc. Rev.* **2020**, *50*, 87–101, doi:10.1039/d0cs01150a.

Mesoporous Poly(Melamine-co-Formaldehyde) Particles for Efficient and Selective Phosphate and Sulfate Removal

25. Kong, L.; Hu, X.; Xie, Z.; Ren, X.; Long, J.; Su, M.; Diao, Z.-H.; Chen, D.; Shih, K.; Hou, L. Accelerated phosphorus recovery from aqueous solution onto decorated sewage sludge carbon. *Sci. Rep.* **2018**, *8*, 1–8, doi:10.1038/s41598-018-31750-6.
26. Tonini, D.; Saveyn, H.G.M.; Huygens, D. Environmental and health co-benefits for advanced phosphorus recovery. *Nat. Sustain.* **2019**, *2*, 1051–1061, doi:10.1038/s41893-019-0416-x.
27. Atienza-Martínez, M.; Gea, G.; Arauzo, J.; Kersten, S.R.; Kootstra, A.M.J. Phosphorus recovery from sewage sludge char ash. *Biomass Bioenergy* **2014**, *65*, 42–50, doi:10.1016/j.biombioe.2014.03.058.
28. Meng, X.; Huang, Q.; Xu, J.; Gao, H.; Yan, J. A review of phosphorus recovery from different thermal treatment products of sewage sludge. *Waste Dispos. Sustain. Energy* **2019**, *1*, 99–115, doi:10.1007/s42768-019-00007-x.
29. Monea, M.C.; Meyer, C.; Steinmetz, H.; Schönberger, H.; Drenkova-Tuhtan, A. Phosphorus recovery from sewage sludge—phosphorus leaching behavior from aluminum-containing tertiary and anaerobically digested sludge. *Water Sci. Technol.* **2020**, *82*, 1509–1522, doi:10.2166/wst.2020.414.
30. Ohtake, H.; Tsuneda, S. *Phosphorus Recovery and Recycling*, Springer: Singapore, Singapore, 2019; ISBN 978-981-10-8030-2.
31. Du, C.-M.; Gao, X.; Ueda, S.; Kitamura, S.-Y. Separation and recovery of phosphorus from steelmaking slag via a selective leaching–chemical precipitation process. *Hydrometallurgy* **2019**, *189*, 105–109, doi:10.1016/j.hydromet.2019.105109.
32. Lv, N.-N.; Du, C.-M.; Kong, H.; Yu, Y.-H. Leaching of Phosphorus from Quenched Steelmaking Slags with Different Composition. *Metals* **2021**, *11*, 1026, doi:10.3390/met11071026.
33. Lin, L.; Bao, Y.; Wang, M.; Jiang, W.; Zhou, H. Separation and Recovery of Phosphorus from P-bearing Steelmaking Slag. *Journal of Iron and Steel Research International* **2014**, *21*, 496–502.
34. Kalmykova, Y.; Fedje, K.K. Phosphorus recovery from municipal solid waste incineration fly ash. *Waste Manag.* **2013**, *33*, 1403–1410, doi:10.1016/j.wasman.2013.01.040.
35. Schwertmann, U. Solubility and dissolution of iron oxides. *Plant Soil* **1991**, *130*, 1–25, doi:10.1007/bf00011851.
36. Han, J.; Kim, M.; Ro, H.-M. Factors modifying the structural configuration of oxyanions and organic acids adsorbed on iron (hydr)oxides in soils. A review. *Environ. Chem. Lett.* **2020**, *18*, 631–662, doi:10.1007/s10311-020-00964-4.
37. Wang, D.; Guan, K.; Bai, Z.; Liu, F. Facile preparation of acid-resistant magnetite particles for removal of Sb(III) from strong acidic solution. *Sci. Technol. Adv. Mater.* **2016**, *17*, 80–88, doi:10.1080/14686996.2016.1145530.
38. Reis, B.; Gerlach, N.; Steinbach, C.; Carrasco, K.H.; Oelmann, M.; Schwarz, S.; Müller, M.; Schwarz, D. A Complementary and Revised View on the N-Acylation of Chitosan with Hexanoyl Chloride. *Mar. Drugs* **2021**, *19*, 385, doi:10.3390/md19070385.
39. Li, M.; Liu, J.; Xu, Y.; Qian, G. Phosphate adsorption on metal oxides and metal hydroxides: A comparative review. *Environ. Rev.* **2016**, *24*, 319–332, doi:10.1139/er-2015-0080.
40. Ajmal, Z.; Muhmood, A.; Usman, M.; Kizito, S.; Lu, J.; Dong, R.; Wu, S. Phosphate removal from aqueous solution using iron oxides: Adsorption, desorption and regeneration characteristics. *J. Colloid Interface Sci.* **2018**, *528*, 145–155, doi:10.1016/j.jcis.2018.05.084.
41. Siwek, H.; Bartkowiak, A.; Włodarczyk, M. Adsorption of Phosphates from Aqueous Solutions on Alginate/Goethite Hydrogel Composite. *Water* **2019**, *11*, 633, doi:10.3390/w11040633.
42. Lalley, J.; Han, C.; Li, X.; Dionysiou, D.D.; Nadagouda, M.N. Phosphate adsorption using modified iron oxide-based sorbents in lake water: Kinetics, equilibrium, and column tests. *Chem. Eng. J.* **2015**, *284*, 1386–1396, doi:10.1016/j.cej.2015.08.114.
43. Song, Y.; Ma, R.; Jiao, C.; Hao, L.; Wang, C.; Wu, Q.; Wang, Z. Magnetic mesoporous polymelamine-formaldehyde resin as an adsorbent for endocrine disrupting chemicals. *Microchim. Acta.* **2017**, *185*, 19, doi:10.1007/s00604-017-2593-5.
44. Yin, J.; Zhang, T.; Schulman, E.; Liu, D.; Meng, J. Hierarchical porous metallized poly-melamine-formaldehyde (PMF) as a low-cost and high-efficiency catalyst for cyclic carbonate synthesis from CO₂ and epoxides. *J. Mater. Chem. A* **2018**, *6*, 8441–8448, doi:10.1039/c8ta00625c.
45. Tan, M.X.; Sum, Y.N.; Ying, J.Y.; Zhang, Y. A mesoporous poly-melamine-formaldehyde polymer as a solid sorbent for toxic metal removal. *Energy Environ. Sci.* **2013**, *6*, 3254–3259, doi:10.1039/c3ee42216j.
46. Schwarz, D.; Weber, J. Synthesis of mesoporous poly(melamine-formaldehyde) particles by inverse emulsion polymerization. *J. Colloid Interface Sci.* **2017**, *498*, 335–342, doi:10.1016/j.jcis.2017.03.064.
47. Schwarz, D.; Weber, J. Organic-solvent free synthesis of mesoporous and narrow-dispersed melamine resin particles for water treatment applications. *Polymer* **2018**, *155*, 83–88, doi:10.1016/j.polymer.2018.09.028.

Mesoporous Poly(Melamine-co-Formaldehyde) Particles for Efficient and Selective Phosphate and Sulfate Removal

48. Ming, G.; Duan, H.; Meng, X.; Sun, G.; Sun, W.; Liu, Y.; Lucia, L. A novel fabrication of monodisperse melamine–formaldehyde resin microspheres to adsorb lead (II). *Chem. Eng. J.* **2016**, *288*, 745–757, doi:10.1016/j.cej.2015.12.007.
49. Wang, Y.; Xie, Y.; Zhang, Y.; Tang, S.; Guo, C.; Wu, J.; Lau, R. Anionic and cationic dyes adsorption on porous poly-melamine-formaldehyde polymer. *Chem. Eng. Res. Des.* **2016**, *114*, 258–267, doi:10.1016/j.cherd.2016.08.027.
50. Zeng, X.; Li, J.; Singh, N. Recycling of Spent Lithium-Ion Battery: A Critical Review. *Crit. Rev. Environ. Sci. Technol.* **2014**, *44*, 1129–1165, doi:10.1080/10643389.2013.763578.
51. Huang, B.; Pan, Z.; Su, X.; An, L. Recycling of lithium-ion batteries: Recent advances and perspectives. *J. Power Sources* **2018**, *399*, 274–286, doi:10.1016/j.jpowsour.2018.07.116.
52. Wang, Y.; An, N.; Wen, L.; Wang, L.; Jiang, X.; Hou, F.; Yin, Y.; Liang, J. Recent progress on the recycling technology of Li-ion batteries. *J. Energy Chem.* **2020**, *55*, 391–419, doi:10.1016/j.jechem.2020.05.008.
53. Schwarz, D.; Weber, J. Waterborne Colloidal Polymer/Silica Hybrid Dispersions and Their Assembly into Mesoporous Poly(melamine-formaldehyde) Xerogels. *Langmuir* **2015**, *31*, 8436–8445, doi:10.1021/acs.langmuir.5b00990.
54. Schwarz, D.; Weber, J. Nanoporous Poly(Melamine Formaldehyde) Networks by Aqueous Dispersion Polycondensation-Synthesis and Adsorption Properties. *Macromol. Mater. Eng.* **2015**, *300*, 531–541, doi:10.1002/mame.201400330.
55. Socrates, G. *Infrared and Raman Characteristic Group Frequencies: Tables and Charts*, 3rd ed.; John Wiley and Sons, Ltd.: Chichester, UK, 2004; Volume 35; ISBN 978-0-470-09307-8.
56. Merline, D.J.; Vukusic, S.; Abdala, A. Melamine formaldehyde: Curing studies and reaction mechanism. *Polym. J.* **2012**, *45*, 413–419, doi:10.1038/pj.2012.162.
57. Ullah, S.; Bustam, M.A.; Nadeem, M.; Naz, M.Y.; Tan, W.L.; Shariff, A.M. Synthesis and Thermal Degradation Studies of Melamine Formaldehyde Resins. *Sci. World J.* **2014**, *2014*, 1–6, doi:10.1155/2014/940502.
58. Devallencourt, C.; Saiter, J.; Fafet, A.; Ubrich, E. Thermogravimetry/Fourier transform infrared coupling investigations to study the thermal stability of melamine formaldehyde resin. *Thermochim. Acta.* **1995**, *259*, 143–151, doi:10.1016/0040-6031(95)02262-z.
59. Bentley, J. *Organic film formers. Paint and Surface Coatings*; Elsevier: Amsterdam, The Netherlands, 1999; pp 19–90; ISBN 9781855733480.
60. Herlinger, H.; Hoffmann, M.; Husemann, E.; Istel, E.; Kern, W.; Krimm, H.; Müller, E.; Rinke, H.; Schmitz-Josten, R.; Schneider, P. (Eds.). Polyadditions-bzw. Polykondensationsprodukten von Carbonyl- und Thiocarbonylverbindungen (X). In *Makromolekulare Stoffe*; Georg Thieme Verlag: Stuttgart, Germany, 1963; ISBN 9783131972743.
61. Allen, L.H.; Matijević, E. Stability of colloidal silica. *J. Colloid Interface Sci.* **1969**, *31*, 287–296, doi:10.1016/0021-9797(69)90172-6.
62. Thommes, M.; Kaneko, K.; Neimark, A.V.; Olivier, J.P.; Rodriguez-Reinoso, F.; Rouquerol, J.; Sing, K.S. Physisorption of gases, with special reference to the evaluation of surface area and pore size distribution (IUPAC Technical Report). *Pure Appl. Chem.* **2015**, *87*, 1051–1069, doi:10.1515/pac-2014-1117.
63. Sing, K.S.W. Reporting physisorption data for gas/solid systems with special reference to the determination of surface area and porosity (Provisional). *Pure Appl. Chem.* **1982**, *54*, 2201–2218, doi:10.1351/pac198254112201.
64. Rahman, I.A.; Vejayakumaran, P.; Sipaut, C.S.; Ismail, J.; Chee, C.K. Size-dependent physicochemical and optical properties of silica nanoparticles. *Mater. Chem. Phys.* **2009**, *114*, 328–332, doi:10.1016/j.matchemphys.2008.09.068.
65. Kosmulski, M. *Surface Charging and Points of Zero Charge*; CRC Press: New York, NY, USA, 2009; ISBN 9780429093395.
66. Ortelli, S.; Costa, A.L.; Matteucci, P.; Miller, M.R.; Blois, M.; Gardini, D.; Tofail, S.A.M.; Tran, L.; Tonelli, D.; Poland, C.A. Silica modification of titania nanoparticles enhances photocatalytic production of reactive oxygen species without increasing toxicity potential in vitro. *RSC Adv.* **2018**, *8*, 40369–40377, doi:10.1039/c8ra07374k.
67. Casas, J.; Alvarez, F.; Cifuentes, L. Aqueous speciation of sulfuric acid–cupric sulfate solutions. *Chem. Eng. Sci.* **2000**, *55*, 6223–6234, doi:10.1016/s0009-2509(00)00421-8.
68. Campbell, N.A.; Reece, J.B. *Biology; Recording for the Blind & Dyslexic*: Princeton, NJ, USA, 2005; ISBN 0-8053-7171-0.
69. Powell, K.J.; Brown, P.L.; Byrne, R.H.; Gajda, T.; Hefter, G.; Sjöberg, S.; Wanner, H. Chemical speciation of environmentally significant heavy metals with inorganic ligands. Part 1: The Hg²⁺–Cl[–], OH[–], CO₃^{2–}, SO₄^{2–}, and PO₄^{3–} aqueous systems (IUPAC Technical Report). *Pure Appl. Chem.* **2005**, *77*, 739–800, doi:10.1351/pac200577040739.

Mesoporous Poly(Melamine-co-Formaldehyde) Particles for Efficient and Selective Phosphate and Sulfate Removal

70. Helfferich, F.G. *Ion Exchange*; Dover ed.; Dover Publications: New York, NY, USA, 1995; ISBN 0-486-68784-8.
71. Tan, L.C.; Calix, E.M.; Rene, E.R.; Nanchaiah, Y.V.; Van Hullebusch, E.D.; Lens, P.N.L. Amberlite IRA-900 Ion Exchange Resin for the Sorption of Selenate and Sulfate: Equilibrium, Kinetic, and Regeneration Studies. *J. Environ. Eng.* **2018**, *144*, 04018110-1–04018110-12, doi:10.1061/(asce)ee.1943-7870.0001453.
72. Haghsheno, R.; Mohebbi, A.; Hashemipour, H.; Sarrafi, A. Study of kinetic and fixed bed operation of removal of sulfate anions from an industrial wastewater by an anion exchange resin. *J. Hazard. Mater.* **2009**, *166*, 961–966, doi:10.1016/j.jhazmat.2008.12.009.
73. Li, Z.; Xu, S.; Li, Y.; Arai, Y. Novel Application of Hybrid Anion Exchange Resin for Phosphate Desorption Kinetics in Soils: Minimizing Re-Adsorption of Desorbed Ions. *Soil Syst.* **2020**, *4*, 36, doi:10.3390/soilsystems4020036.
74. Nur, T.; Johir, M.; Loganathan, P.; Nguyen, T.; Vigneswaran, S.; Kandasamy, J. Phosphate removal from water using an iron oxide impregnated strong base anion exchange resin. *J. Ind. Eng. Chem.* **2013**, *20*, 1301–1307, doi:10.1016/j.jiec.2013.07.009.
75. Sowmya, A.; Meenakshi, S. Removal of nitrate and phosphate anions from aqueous solutions using strong base anion exchange resin. *Desalination Water Treat.* **2013**, *51*, 7145–7156, doi:10.1080/19443994.2013.771286.
76. Brunauer, S.; Emmett, P.H.; Teller, E. Adsorption of Gases in Multimolecular Layers. *J. Am. Chem. Soc.* **1938**, *60*, 309–319, doi:10.1021/ja01269a023.
77. Langmuir, I. The constitution and fundamental properties of solids and liquids. part i. solids. *J. Am. Chem. Soc.* **1916**, *38*, 2221–2295, doi:10.1021/ja02268a002.
78. Dubinin, M.M. The Equation of the Characteristic Curve of Activated Charcoal. *Proc. USSR Acad. Sci.* **1947**, *55*, 327–329.
79. Foo, K.Y.; Hameed, B.H. Insights into the modeling of adsorption isotherm systems. *Chem. Eng. J.* **2010**, *156*, 2–10, doi:10.1016/j.cej.2009.09.013.
80. Kamga, F.T. Modeling adsorption mechanism of paraquat onto Ayous (*Triplochiton scleroxylon*) wood sawdust. *Appl. Water Sci.* **2018**, *9*, 1–14, doi:10.1007/s13201-018-0879-3.
81. Zhou, X. Correction to the calculation of Polanyi potential from Dubinnin-Rudushkevich equation. *J. Hazard. Mater.* **2019**, *384*, 121101, doi:10.1016/j.jhazmat.2019.121101.

6. Tuning the Pore Structure of Templated Mesoporous Poly(melamine-co-formaldehyde) Particles toward Diclofenac Removal

This chapter is based on the publication in *Journal of Environmental Management* **2022**, 324, 116221.

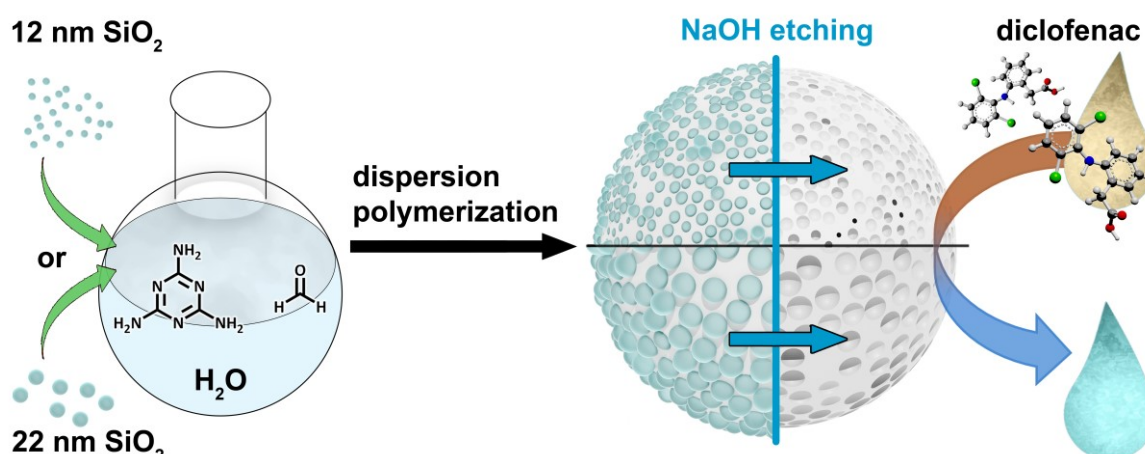
(DOI: 10.1016/j.jenvman.2022.116221)

By Konstantin B. L. Borchert, Karina Haro Carrasco, Christine Steinbach, Berthold Reis, Niklas Gerlach, Martin Mayer*, Simona Schwarz* and Dana Schwarz*

Leibniz-Institut für Polymerforschung Dresden e.V., Hohe Str. 6, 01069 Dresden, Germany;

* Corresponding authors

Graphical Abstract



Abstract

The increasing demand and implementation of pharmaceuticals poses severe risk to different aquatic species as detectable contaminant in almost every surface water worldwide. Diclofenac (DCF) as one of the most common used analgesics was investigated as contaminant to be removed by adsorption onto nanoporous poly(melamine-co-formaldehyde) (PMF) particles featuring a very high amount of nitrogen functionalities. To achieve a high specific surface area (up to 416 m²/g) and a tunable pore system by hard templating, four different SiO₂ nanoparticles were used as template. Differences in the pore formation and achieved pore structure were elucidated. For the first time, the adsorption of DCF onto PMF was tested. In batch adsorption experiments, impactful adsorption capacities as high as 76 μmol/g were achieved and complete removal at initial concentrations of 2 mg/L DCF. Differences in the connectivity and the micropore structure were decisive for uptake in low concentrations and the achieved adsorption capacity, respectively. As the presented PMF particles can be easily synthesized with the monomers formaldehyde and melamine combined with colloidal silica

as sacrificial template and water as green solvent, this material presents a viable adsorbent for the removal of DCF at a larger scale. Our study further indicates a high potential for the removal of other pharmaceuticals.

1. *Introduction*

Environmental pollution by pharmaceutical products and drugs is pervasive and imminent, (Nguyen et al., 2020; Rath et al., 2021) as they are very persistent in the environment (Gworek et al., 2019). Furthermore, pharmaceutical products and drugs are designed to interfere with biochemical processes of living organisms and applied widespread for humans, cattle, and other animals. Explicitly severe are the effects of diclofenac (DCF) for vultures, which are eating carcasses of treated, deceased animals, since DCF is causing renal failure (Bamford et al., 2009; Oaks et al., 2004; Swan et al., 2006). This almost caused the extinction of different vulture species of south-Asia and Africa, which are now critically endangered (Naidoo et al., 2009). Furthermore, DCF poses fatal harm to the aquatic environment, causing genotoxicity to mussels, organ damage to fish, and general decline in macrophyte biovolume (Joachim et al., 2021).

Consequently, removal of DCF, amongst the other over 100 pharmaceutical products detectable in surface, ground, or tap water is the only way to protect the environment (Beek et al., 2016). The European Union included DCF into the first Watch List of the Water Framework Directive, expressing the need for continuous monitoring of DCF levels in surface water (Simon et al., 2022). Most commonly, photocatalytic degradation is used for removal (Andreozzi et al., 2003; Radke et al., 2010; Tixier et al., 2003). However, sufficient removal of DCF is not ensured by current technology owing to the relatively low DCF concentration in the range of several $\mu\text{g/L}$. With only around 20% mean removal efficiency downstream of wastewater treatment plants (Johnson et al., 2013), DCF is one of the most commonly detected pharmaceuticals in the effluents (Verlicchi et al., 2012). Hereby, the concentration often exceeds surface water quality standards as such set by the EU (Carere et al., 2016; Johnson et al., 2013). Current research focuses on either oxidation processes (Beltrán et al., 2009; Pérez-Estrada et al., 2005; Song et al., 2017; Xian et al., 2019), adsorption by charcoal (Genç et al., 2021; Tomul et al., 2019), or metal oxide particles (Leone et al., 2018; Liang et al., 2019). The latter are often performed at pH values, where DCF is insoluble (Cuccarese et al., 2021; Larous and Meniai, 2016), which increases adsorption capacities by precipitation effects of DCF (Skube et al., 2004). Furthermore, pH values below 5 do not correspond to native pH values for municipal wastewaters usually being around 6 – 8 (Odjadjare and Okoh, 2010).

Poly(melamine-co-formaldehyde) (PMF) is a thermally and chemically stable adsorbent material with high versatility due to its high amount of different N-functionalities. Porous PMF enables the adsorption of various pollutants like heavy metal ions via coordinative bonds (Tan

et al., 2013), anionic pollutants via electrostatic interaction (Borchert et al., 2021; Schwarz and Weber, 2018), and organic pollutants such as dyes via electrostatic, hydrophobic and π - π interaction (Schwarz and Weber, 2017; Wang et al., 2016) and the adsorption of CO₂ (Schwarz and Weber, 2015). PMF is presenting a great material, as melamine and formaldehyde are commercially available and relatively inexpensive due to their high production volume when compared to other functional materials as ion exchange resins or metal organic frameworks. The monomers formaldehyde and melamine can be synthesized from CO₂, which enables future synthesis via a green preparation method (Rauch et al., 2019; Wang et al., 2018). Moreover, PMF is extremely stable and thus, it firstly is a non-hazard material (World Health Organization, 2009), and secondly, poses the potential to be reusable. The excellent stability enables applications even under harsh chemical conditions. Owing to the aromatic character and the high nitrogen amount for ionic interactions and hydrogen bonds, PMF is predestinated to absorb aromatic organic contaminants. Interestingly, PMF has only been tested for the removal of pharmaceuticals once, where only ibuprofen, ciprofloxacin and tetracycline were tested with few experiments (Zhang and Chen, 2016). As the efficient removal of pharmaceutical contaminants is a pressing topic, one objective of this study is to prove a potential applicability of PMF in this matter.

Here, DCF was chosen to act as exemplary pharmaceutical in this study because of its omnipresence in natural surface waters worldwide, its persistence and furthermore its drastic environmental influence. Thus, even more importantly, we focus on the adsorption investigations in the challenging neutral pH range of 6 – 8, which are typical for municipal wastewaters proving the applicability in real-world municipal wastewaters (Odjadjare and Okoh, 2010).

To date, porous PMF is mostly synthesized solvothermal under harsh chemical conditions, consuming solvents like dimethyl sulfoxide (DMSO) at 170 °C and above for 3 d. This yields in thermal decomposition of DMSO and unwanted incorporation of sulfur in the PMF structure (Tan et al., 2013; Wang et al., 2016; Yang et al., 2010).

Here, we present a truly green approach to the synthesis of mesoporous PMF particles. We use a dispersion polymerization of melamine and paraformaldehyde in water and a hard-templating approach with silica nanoparticles (SiO₂ NPs) partially investigated before by our author team (Borchert et al., 2021; Schwarz and Weber, 2018). Our first objective was to investigate the influence of using different commercially available SiO₂ NPs as template. Therefore, we added 12 nm and 22 nm SiO₂ NPs to the polymerization reaction, respectively, to investigate the influence of the template diameter on the pore size. Additionally, the commercially available SiO₂ NPs dispersions were stabilized with diverse counter ions, to test the potential influence on the templating or polymerization reaction (i.e., particle formation and porosity) as well. We have thoroughly analyzed the obtained particles by N₂ and CO₂

sorption and transmission and scanning electron microscopy to evaluate the pore structure and morphology. For chemical characterization, ATR-FTIR spectroscopy, thermogravimetric analysis, and elemental analysis have been used. Our second objective was the subsequent application of the particles for the adsorption of DCF from water with special focus on alterations caused by differences in the pore system. With this, we are the first to report the adsorption of DCF onto PMF and the second for adsorption of pharmaceuticals by PMF in general. Hereby, we highlighted the differing adsorption behavior caused by the respective exhibited pore structures. We elucidated the underlying mechanism caused by more open or closed pore systems, respectively.

2. Materials

Melamine (99%), paraformaldehyde (95%), oxalic acid (99% and 98%), Ludox[®] HS-40 (40 wt.% in H₂O), Ludox[®] AS-40 (40 wt.% in H₂O), Ludox[®] TMA (34 wt.% in H₂O), Ludox[®] TM-40 (40 wt.% in H₂O), and diclofenac sodium salt (Sigma, >98%, chemical structure in Figure 6.1) were purchased from Sigma-Aldrich (München, Germany). NaOH (≥ 98%) was purchased from Honeywell (Offenbach, Germany). All chemicals were used as received without further purification. For all experiments and syntheses, ultrapure water purified by a Milli-Q Advantage A10[®] system (Millipore, Darmstadt, Germany) (total organic carbon = 5 ppb, resistivity of 18.2 MΩ·cm) was used.

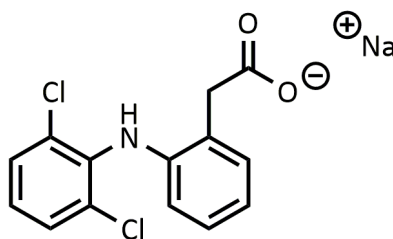


Figure 6.1. Structure of diclofenac (DCF) as sodium salt.

3. Methods

Thermogravimetric analysis (TGA) was performed using the device 1 Star System (Mettler Toledo, Gießen, Germany). The measurements were carried out with approximately 5 to 8 mg of the sample in a platinum crucible. The investigated temperature range was from 30 °C to 1000 °C with a heating rate of 10 °C/min, under air atmosphere at a flow rate of 40 mL/min.

Scanning electron microscopy (SEM) was carried out using a SEM Ultra Plus (Carl Zeiss Microscopy GmbH, Oberkochen, Germany). The samples were fixed with double-sided adhesive carbon tape on an aluminum pin sample tray and afterwards streamed with N₂ to obtain a thin layer of particles. The samples were sputtered with 3 nm of platinum using a Sputter Coater SCD050 (Leica Microsystems, Wetzlar, Germany) before the investigation. The measurements were carried out with an acceleration voltage of 3 keV.

Transmission electron microscopy (TEM) was carried out using a Libra 200 device (Carl Zeiss Microscopy GmbH, Oberkochen, Germany). The acceleration voltage was 200 keV. The studied particles were dispersed in ultrapure water and dripped onto a carbon coated Cu mesh.

Particles sizes of the purified particles were analyzed using a Mastersizer 3000 (Malvern, Kassel, Germany). For redispersion, 0.1 g was dispersed with ultrasonication in 15 mL ultrapure water and afterwards added dropwise to the measurement cell until the detector obscuration was between 13 to 20%. The data was evaluated using the model “Polydisperse”, a particle refractive index (RI) of 1.5, absorbance of 0.1000 and a dispersant RI: 1.3300.

Nitrogen and CO₂ sorption measurements were performed using the Autosorb iQ MP (Quantachrome Instruments, Boynton Beach, USA). Samples were degassed in vacuum (5×10^{-10} mbar) at 110 °C for 24 hours. The nitrogen sorption measurements were performed at -196 °C. The surface area was calculated in the relative pressure (p/p_0) range from 0.07 to 0.22 by BET method (Brunauer et al., 1938). The pore size distribution was derived by a QSDFT fit of the adsorption branch considering spherical, cylindrical and slit pores calculated with ASiQWin software (Quantachrome Instruments, Boynton Beach, USA). The pore volume (PV) and micropore volume (MPV) of the samples was converted using the N₂ uptake at $p/p_0 = 0.95$ and 0.1, respectively. Pore size distribution for the connection channels was calculated using the Barrett-Joyner-Halenda method (BJH) (Barrett et al., 1951) and the desorption curve. CO₂ sorption measurements were performed at 0 °C. The derived micropore size distribution was calculated using a NLDFT method calculated with ASiQWin software (Quantachrome Instruments, Boynton Beach, USA).

Attenuated total reflection infrared spectroscopy (ATR-FTIR) measurements were performed using a Tensor 27 device equipped with a Platinum ATR module (Bruker Corporation, Billerica, USA). All samples were measured in dry state with a resolution of 2 cm⁻¹ and 100 scans. The acquired spectra were subjected to manually performed atmospheric compensation removing the rotation bands of water and afterwards normalized using the triazine ring-bending band at 812 cm⁻¹.

pH measurement: The pH was measured with the device SevenExcellence (Mettler Toledo, Gießen, Germany) at r.t.

Centrifugation: The adsorbents were centrifuged with the device Sigma 3-18KS (Sigma Laborzentrifugen GmbH, Osterode, Germany) at r.t.

CHNS elemental analysis (EA) was carried out using a vario MICRO cube (Elementar, Langenselbold, Germany).

UV-Vis spectra for the isotherms were measured with a Cary 5000 (Agilent, USA) in 1 cm quartz cuvettes. In order to resolve small concentration changes, the spectral range from 200 to 400 nm was measured at a data interval of 0.333 nm with a scan rate of 20 nm/min. For the

Tuning the Pore Structure of Templated Mesoporous Poly(melamine-co-formaldehyde) Particles toward Diclofenac Removal

determination of the drug concentrations, a calibration was conducted from known concentrations (see Supporting Information Figure S1) and all measurements were background corrected against ultrapure water in the same cuvette used for the actual measurement. The diclofenac concentration was determined at the peak at 276 nm via Gaussian fitting to extract exact peak positions and intensities (see example in Figure S2). For measurements of the time-dependent adsorption, see section 1.3.1 in the SI.

3.1. Synthesis of the PMF particles

Five different PMF particles were synthesized either with different commercially available silica nanoparticles (SiO_2 NPs) as template or using a doubled amount of template. The template hereby differs in diameter as well as in its stabilizing counter ion. The nominal properties of the SiO_2 NPs are displayed in Table 6.1. The obtained PMF particles are named in their suffix after the commercial silica name codes for easier differentiation. Furthermore, as the PMF particles can either be the SiO_2 /PMF hybrid particles or the etched, pure PMF particles after template removal, the respective prefixes H- for hybrid and P- for the purified, porous materials were chosen.

Table 6.1. Nominal particle size and stabilizing counter ion of the used silica dispersions, stated by the manufacturer W. R. Grace & Co.-Conn.

Ludox® dispersion	Particle size (nm)	Counter ion	SiO_2 content (wt.%)	pH	Obtained PMF particles
Ludox® HS-40	12	Na^+	40	9.5 – 10.3	PMF-HS40 and PMF-2HS40
Ludox® AS-40	22	NH_4^+	40	9.0 – 10.0	PMF-AS40
Ludox® TMA	22	none	34	3.5 – 7.0	PMF-TMA
Ludox® TM-40	22	Na^+	40	9.0 – 10.5	PMF-TM40

3.1.1. Synthesis of PMF-HS40

The PMF-HS40 particles were synthesized as recently published (Borchert et al., 2021; Schwarz and Weber, 2018) with minor modifications. 9.1 g (72.2 mmol) melamine (M) and 12.95 g (431.2 mmol) paraformaldehyde (F) were dispersed in 175 mL ultrapure water in a 1 L round bottom flask. The dispersion was stirred at 50 °C for 40 min. A solution of 525 mL ultrapure water with 1.4 g (15.5 mmol) oxalic acid and 42.0 g Ludox® HS-40 (Table 6.1) was prepared and then added to the reaction mixture. This mixture was stirred for 24 h at 100 °C under reflux.

3.1.2. Synthesis of PMF-2HS40

The PMF-2HS40 particles were synthesized as stated in Section 2.3.1 but the doubled amount (84.0 g) of Ludox® HS-40 was used.

Tuning the Pore Structure of Templated Mesoporous Poly(melamine-co-formaldehyde) Particles toward Diclofenac Removal

3.1.3. Synthesis of PMF-AS40, PMF-TMA, and PMF-TM40 particles

Additionally, to the commonly used Ludox[®] HS-40 dispersion, three similar Ludox[®] dispersions with 22 nm SiO₂ NPs in diameter were used as template particles in the synthesis for comparison (see Table 6.1).

PMF-AS40, PMF-TMA, and PMF-TM40 were synthesized by respective modifications to the PMF-HS40 synthesis: Instead of Ludox[®] HS-40, Ludox[®] AS-40, Ludox[®] TMA or Ludox[®] TM40 were used, respectively. The amounts of the respective dispersions added are given in Table 6.2. The amount of silica in the dispersion was equal to the amount of Ludox[®] HS-40 in the synthesis of PMF-HS40. To account for lower wt.% of silica in Ludox[®] TMA, only 67.6 mL water were added in the second step for the dispersion of oxalic acid and Ludox[®] TMA (see Table 6.2).

Table 6.2. Table of reactants (melamine (M), paraformaldehyde (F), and Ludox[®] HS-40 (for PMF-HS40 and PMF-2HS40), AS-40 (for PMF-AS40), TMA (for PMF-TMA) and TM-40 (for PMF-TM40) of respective H-PMF and P-PMF particles with the corresponding sample codes.

Sample	m (M) (g)	m (F) (g)	m _{Ludox[®]} (g)	m _{SiO₂} (g)	V (water) (mL)	pH _{Template} ^a	pH ^b	pH ^c
PMF-HS40	9.1	12.95	42	16.8 g	25 + 75	9.5 – 10.3	2.14	3.52
PMF-2HS40	9.1	12.95	84	16.8 g	25 + 75	9.5 – 10.3	2.44	3.89
PMF-AS40	9.1	12.95	42	16.8 g	25 + 75	9.0 – 10	1.96	3.38
PMF-TMA	9.1	12.95	49	16.8 g	25 + 68	3.5 – 7	1.84	3.21
PMF-TM40	9.1	12.95	42	16.8 g	25 + 75	9.0 – 10.5	1.88	3.28

^apH of the pure Ludox[®] solution at 25 °C.; ^bpH of the dispersion with ultrapure water, oxalic acid and Ludox[®] solution. ^cpH of the final reaction mixture after 24 hours at 100 °C under reflux.

Purification of H-PMF samples: The sediment was transferred into a 1 L vessel with ultrapure water. For three times, this vessel was filled to a total volume of 1 L with ultrapure water and shaken for 24 hours at room temperature. Subsequently, the particles sedimented, decanted and freeze-dried. As these particles still contain the SiO₂ NPs, these samples are called hybrid PMF (H-PMF) samples.

Purification of P-PMF samples: To obtain the pure PMF particles, the sediment of the reaction mixture was transferred into a 1 L vessel and filled with 1 M NaOH solution to remove the silica particles. The solution was shaken for 24 hours, then sedimented and decanted. The washing procedure with 1 M NaOH was repeated two more times. In the case of P-PMF-TMA, one more washing step was needed for the complete removal of the template. The particles were then transferred to a Spectra/Por[™] 2 dialysis bag (Spectrum Chemical Mfg. Corp., New Brunswick, USA) and dialyzed with ultrapure water and subsequently freeze-dried.

3.2. Water treatment experiments with diclofenac solution

0.1 g of each adsorbent was placed into a 50 mL centrifuge tube. Subsequently, 30 mL of the adsorptive solution was added to every sample. The pH of the samples was not adjusted. The samples were then magnetically stirred for 24 hours at 25 °C. Afterwards, the samples were centrifuged for 60 min at 11000 rpm (corresponding to a relative centrifugal field of $12716 \times g$). The supernatant of the samples after the adsorption and the initial concentrations of the adsorptive solutions were analyzed by UV-Vis. The pH of the solutions was determined.

3.3. Theoretical model

The determined DCF concentrations were used for the calculation of the adsorption in percent in equation (6.1). Thereby, c_0 is the concentration of the respective ion in the initial solution and c_{eq} is the concentration after reaching equilibrium.

$$\text{adsorption in \%} = 100\% \times \frac{c_0 - c_{eq}}{c_0} \quad (6.1)$$

The respective sorption capacity q_{eq} in equilibrium was calculated as follows:

$$q_{eq} = \frac{(c_0 - c_{eq}) \times V_L}{m_A} \quad (6.2)$$

V_L refers to the adsorptive volume and m_A to the adsorbent mass used.

To model the adsorption, the Langmuir (Eq. 6.3) (Langmuir, 1916) and Dubinin-Radushkevich (Eq. 6.8) (Dubinin, 1947) isotherm model were chosen in non-linear form, which is preferable to linear fitting, because dependent and independent variables are not changed by linearization and therefore potential errors are not transformed by the logarithm in an unpredictable way (Osmari et al., 2013; Subramanyam and Das, 2014; Wang and Guo, 2020). Here, the non-linear form of the Langmuir isotherm model is presented with K_L being the Langmuir equilibrium constant and Q_m the maximum adsorption capacity (Foo and Hameed, 2010; Togue Kamga, 2019). This equation was directly used in the fitting procedure.

$$q_{eq} = \frac{Q_m \times K_L \times c_{eq}}{1 + K_L \times c_{eq}} \quad (6.3)$$

The Dubinin-Radushkevich model in non-linear form is depicted in Eq. 6.4.

$$q_{eq} = Q_m \times \exp(-\beta_{DR} \times \varepsilon^2) \quad (6.4)$$

Hereby, the Polanyi potential ε can be exchanged by the following:

$$\varepsilon = RT \times \ln \left(\frac{c_s}{c_{eq}} \right) \quad (6.5)$$

c_s hereby represents the solubility of the adsorbate, which is not easily accessible in the adsorbent-adsorptive system empirically. The term inside the logarithm $\frac{c_s}{c_{eq}}$ can be exchanged

for $1 + \frac{1}{c_{eq}}$ according to Zhou, leading to the same numerical solution with two requirements: First, this is only possible for values of $c_{eq} \ll c_s$. In the adsorption experiments, the used concentrations of diclofenac sodium are below their maximum solubility in ultrapure water by three orders of magnitude (Skube et al., 2004). The alkaline character of the adsorbent here should add towards even higher c_s values. Second, the use mol/L concentrations for the fitting is mandatory (Zhou, 2020), which we applied accordingly. This leads to the following term for ε :

$$\varepsilon = RT \times \ln \left(1 + \frac{1}{c_{eq}} \right) \quad (6-6)$$

The activity coefficient β_{DR} is related via Eq. 6.7 to the mean free energy of adsorption $E_{ads,DR}$. (Foo and Hameed, 2010; Togue Kamga, 2019)

$$E_{ads,DR} = \frac{1}{\sqrt{2 \times \beta_{DR}}} \quad (6.7)$$

In Eq. 6.8, the final non-linear form of Dubinin-Radushkevich is shown, which was used for the fitting procedure.

$$q_{eq} = Q_m \times \exp \left(-\beta_{DR} \times \left(RT \times \ln \left(1 + \frac{1}{c_{eq}} \right) \right)^2 \right) \quad (6.8)$$

Calculation of isotherm model fitting was performed in Origin 2018 by non-linear fitting with Levenberg-Marquardt algorithm until $\chi \leq 10^{-9}$ or χ no longer changed.

When evaluating the adsorption thermodynamics, the change in free Gibbs energy ΔG° can be calculated from the Langmuir isotherm constant K_L , given in L/mol. The mismatch between K_L in L/mol and the dimensionless activity coefficient K_a is deliberately ignored, as it allows reasonably approximation for weakly charged substrates (Liu, 2009).

$$\Delta G^\circ = -RT \times \ln(K_a) \quad (6.9)$$

3. Results and Discussion

Porous PMF particles were synthesized in a dispersion polymerization from melamine and formaldehyde under acidic conditions. Water was used as green solvent and commercially available, monodisperse SiO_2 NP as hard templates. As the PMF exhibits a nonporous structure itself (Schwarz and Weber, 2018), hard templating was implemented to the polymerization reaction yielding mesopores after template removal. Mesopores are decisive for the mass transport in the adsorption processes. To investigate the influence of monodisperse SiO_2 NPs in detail, four different dispersions with varying particle diameters (i.e. 12 nm and 22 nm), stabilizing counter ions, as well as pH value (see Table 6.1) were added to each polymerization. These parameters impact the specific surface area and pore size as well as the morphology of

the PMF particles. The labeling of the obtained PMF samples utilizes a suffix referring to the respective name of the commercially available silica dispersion. The prefix H- or P- corresponds to the silica/PMF hybrid materials before template removal or the pure PMF particles after removal with NaOH, respectively. Acidic catalysis was chosen, as this is known to facilitate the formation of methylene bridges in comparison to dimethylene ether bridges favored in alkaline conditions (Binder and Dunky, 2002). Methylene bridges are preferable in terms of stability of the material under harsh conditions as well as showing less polar behavior potentially facilitating later adsorption of organic pollutants.

3.1. Synthesis and characterization of the PMF particles

The formation of the PMF structure, the exclusion of possible side reactions, and the purity of the final product is crucial for the application as adsorbent. Therefore, thorough structural analysis was performed for both the H-PMF (Figure S3) and the P-PMF (Figure S4) samples via ATR-FTIR measurements. An indicator is the band at 812 cm^{-1} related to the triazine ring-bending of the incorporated melamine, which was also used for referencing (Baraka et al., 2007; Schwarz and Weber, 2015; Socrates, 2015). Further, the bands at 1348 cm^{-1} and 1490 cm^{-1} ($\delta(\text{CH}_2)$) and at 2956 cm^{-1} ($\nu(\text{CH}_2)$, weak) indicate the formation of methylene bridges. At $3280 - 3500\text{ cm}^{-1}$ ($\nu(\text{NH}_2)$) and 1550 cm^{-1} ($\delta(\text{NH})$), the amino functionalities are visible in all spectra. For P-PMF a band at $\approx 1000\text{ cm}^{-1}$ ($\nu(\text{COC})$) indicates a partial formation of ether bridges. For H-PMF samples, this region is superimposed by the dominant Si-O stretching mode at 1100 cm^{-1} associated with the silica template. The absence of this band within the P-PMF spectra confirms the sufficient removal of the template through NaOH.

Further information about the network structure is derived from EA (see Table S1) with a statistical assertion about the network structure via the relative C/N molar ratio. When comparing the H-PMF to the respective P-PMF samples, a higher relative C/N molar ratio is observed. Here, oxalate species may still be present in the samples, but are removed in the etching process. In addition, methylolamine functionalities can be present in H-PMF samples, which are hydrolysable in NaOH and therefore eliminated in the etching step (Bentley, 1999; Herlinger et al., 1963). The high residual mass of the H-PMF samples is attributed to the remaining silica, while in P-PMF samples this mass represents oxygen from water, methylolamine, or ether groups.

In particular, TGA measurements show the incorporation of SiO_2 NPs into the resin structure and subsequent removal, besides showing the typical decomposition steps, which are described in literature (see Figure S5 – S8) (Devallencourt et al., 1995; Merline et al., 2013; Ullah et al., 2014). Here, the residual masses at $1000\text{ }^\circ\text{C}$ for almost all H-PMF samples, excluding H-PMF-2HS40, are between 55 wt.% to 56 wt.% referring to the incorporated silica

mass. This indicates that both, the particle diameter and the stabilizing counter ion of the silica showed no influence on the incorporation of the template. H-PMF-2HS40 as only exception showed 61 wt.% silica as residual mass at 1000 °C, owing to the doubled amount of SiO₂ NPs added to the reaction mixture. Here, the final silica uptake is not linearly related to the amount used in synthesis. For the etched P-PMF samples, the SiO₂ NPs were completely removed for P-PMF-AS40, P-PMF-TM40, P-PMF-HS40 and even P-PMF-2HS40 with the doubled amount by washing with 1 M NaOH for 3 d. In contrast, templating with Ludox[®] TMA yielded in a residual mass of approximately 5 wt.% after three washing steps. This cannot be attributed to the particle size of 22 nm alone because the template removal of P-PMF-AS40 and P-PMF-TM40 was successful. When washing four times with 1 M NaOH, the template of P-PMF-TMA is removed completely (see Figure S7). This behavior indicates a less ordered and less interconnected pore structure. Differences in the derived weight loss (DTG) from hybrid to respective etched samples are showing a general shift in their decomposition steps to higher temperatures after etching. This is indicating that etching is partially also curing the resin, thus enhancing thermal stability.

The porosity as well as the particles external morphology are crucial parameters for the adsorption, as they define the accessibility of functional groups and the available surface area. Hence, porosity and morphology were evaluated using N₂ and CO₂ sorption measurements (see Figure 6.2 and Table 6.3) as well as SEM and TEM imaging (Figure 6.4). In the nitrogen sorption experiments with the H-PMF samples (see Figure 6.2a), type II isotherms are seen (Sing, 1982; Thommes et al., 2015), indicating a non-porous structure with the entrapped template in the particle structure. In vast contrast, the P-PMF samples (see Figure 6.2b) possess a type IV isotherm corresponding to a significant amount of mesopores. All samples except P-PMF-TMA exhibited a H1 hysteresis loop, distinguished by a parallel path of adsorption branch to desorption branch. This shape indicates a very well connected and ordered pore system (Schlumberger and Thommes, 2021; Thommes et al., 2015). For P-PMF-HS40 and P-PMF-2HS40, the hysteresis loop closed at a relative pressure $p/p_0 = 0.45$ and at around $p/p_0 = 0.60$ to 0.65 for P-PMF-TM40 and P-PMF-AS40. The relative pressure of $p/p_0 = 0.45$ thereby indicates small mesopores partially limiting desorption and therefore is shifted to lower p/p_0 values. The onset of the hysteresis loops around $p/p_0 = 0.60$ to 0.65 indicates wider connection channels, starting desorption at higher relative pressures. This is in accordance with the pore size distribution (PSD) (see Figure 6.2d). Hence, the achieved pore structure of all of these samples is comparatively monodisperse and ordered. In contrast, the sample P-PMF-TMA featured a H2(b) type hysteresis loop, indicating a complex and less ordered connection system of homogenous mesopores also including ink-bottle effects seen from the delayed desorption in the interval $0.45 < p/p_0 < 0.70$ (Schlumberger and Thommes, 2021; Thommes et al., 2015). Hence, this explains the additionally required washing step in

Tuning the Pore Structure of Templated Mesoporous Poly(melamine-co-formaldehyde) Particles toward Diclofenac Removal

the template removal. Potentially, the absence of counter ions in the TMA silica dispersion leads to the incorporation of single silica particles with less and more chaotic connection channels.

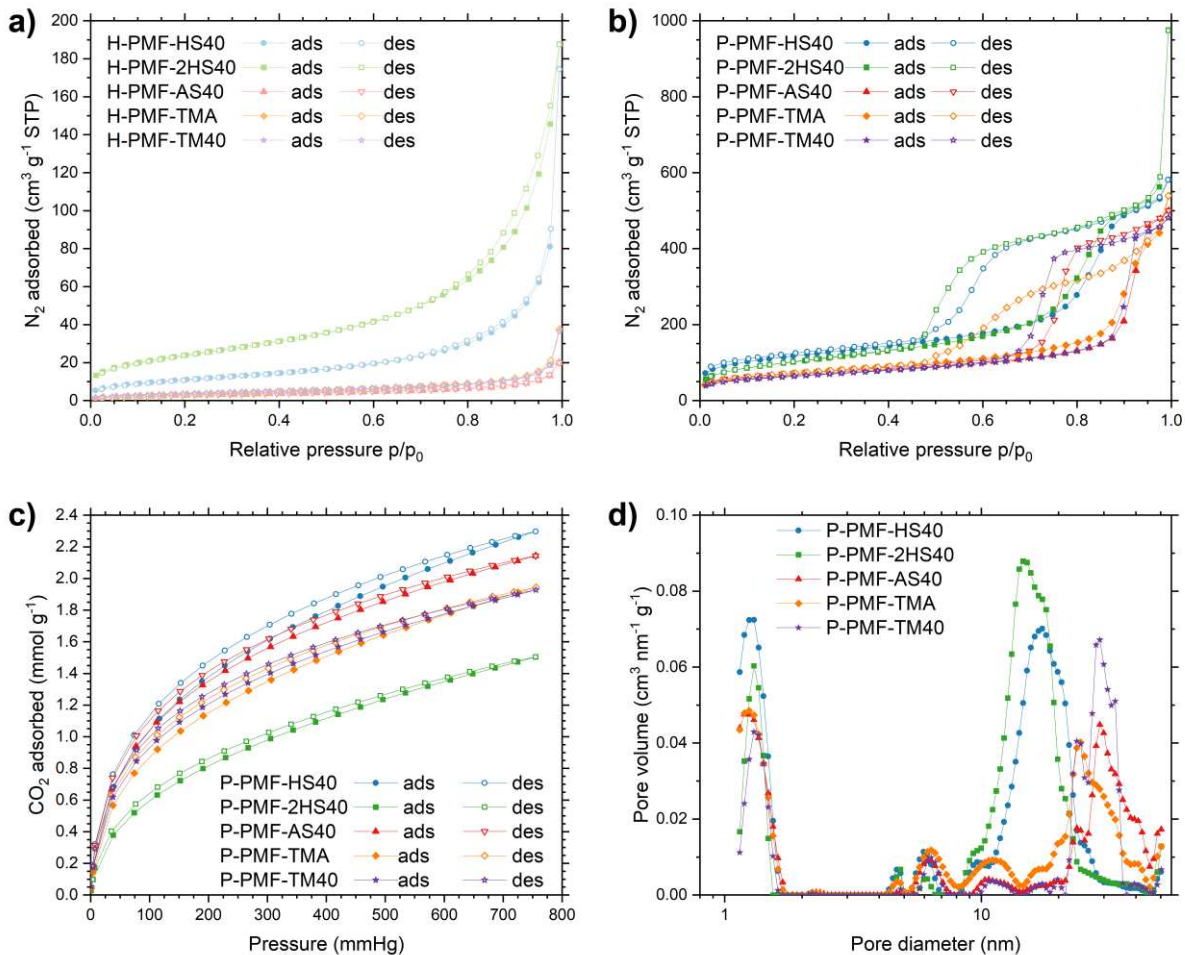


Figure 6.2. Nitrogen (N_2) de-/adsorption isotherms measured at -196°C for H-PMF samples, b) Nitrogen (N_2) de-/adsorption isotherms measured at -196°C for P-PMF samples, c) Carbon dioxide (CO_2) de-/adsorption isotherms measured at 0°C for P-PMF samples, d) Pore size distribution (PSD) analysis for the adsorption branch using QSDFT. d) Carbon dioxide (CO_2) de-/adsorption isotherms measured at 0°C for H-PMF samples are shown in the SI. Data points in the adsorption and desorption branch of the isotherms are indicated by filled and empty symbols, respectively. H-PMF-HS40 is shown in light blue as circles, H-PMF-2HS40 in light green as squares, H-PMF-AS40 in light red as triangles, H-PMF-TMA in light yellow as diamonds, and H-PMF-TM40 in light violet as stars. P-PMF-HS40 is shown in blue as circles, P-PMF-2HS40 in green as squares, P-PMF-AS40 in red as triangles, P-PMF-TMA in yellow as diamonds and P-PMF-TM40 in violet as stars.

As overview from the PSD (see Figure 6.2d), it is noticeable that by the use of two different template diameters (12 nm and 22 nm) and varying the amount of silica or the respective counter ion, five different pore structures were obtained. All samples are showing a peak in their PSD closely to the diameter of their respective template with variance in the peak width. Hence, the hard templating approach was successful. From the Barrett-Joyner-Halenda method (BJH) (Barrett et al., 1951) and the desorption curve, the PSD of the connection

Tuning the Pore Structure of Templated Mesoporous Poly(melamine-co-formaldehyde) Particles toward Diclofenac Removal

channels in the mesoporous regime can be derived (Thommes et al., 2015). The obtained PSD in Figure S9 is supporting the finding that especially P-PMF-TMA is exhibiting a less ordered, thus broader distribution in size as well as less pores and thus a more blocked pore system. The other samples are showing either wider channel diameters (for P-PMF-AS40 and P-PMF-TM40) or significantly more channels (for P-PMF-HS40 and P-PMF-2HS40), thus a more accessible pore system in the mesoporous region.

Table 6.3. Surface area (S_{BET}), pore volume (PV), micro pore volume (MPV) and CO_2 uptake of the PMF samples.

Sample code	S_{BET} ($\text{m}^2 \text{g}^{-1}$) ^a	PV ($\text{cm}^3 \text{g}^{-1}$) ^b	MPV ($\text{cm}^3 \text{g}^{-1}$) ^c	CO_2 uptake (mmol g^{-1}) ^d
H-PMF-HS40	41	n.a.	n.a.	n.a.
P-PMF-HS40	416	0.78	0.16	2.29
H-PMF-2HS40	92	0.20	n.a.	n.a.
P-PMF-2HS40	370	0.82	0.13	1.50
H-PMF-AS40	10	n.a.	n.a.	n.a.
P-PMF-AS40	241	0.71	0.09	2.14
H-PMF-TMA	13	0.02	n.a.	n.a.
P-PMF-TMA	256	0.64	0.10	1.94
H-PMF-TM40	13	n.a.	n.a.	n.a.
P-PMF-TM40	228	0.68	0.08	1.93

^aSurface area calculated from N_2 adsorption isotherm using BET equation. ^bPore volume (PV) calculated from N_2 uptake at $p/p_0 = 0.95$. ^cMicro pore volume (MPV) calculated from N_2 uptake at $p/p_0 = 0.10$. ^d CO_2 uptake calculated for 0 °C and 1 bar.

The sorption isotherms with CO_2 at 0 °C (see Figure 6.2c and Table 6.3) for the P-PMF particles do not exhibit related trends to the obtained N_2 sorption isotherms, especially for the comparison of P-PMF-HS40 and P-PMF-2HS40. This leads to the assumption of additional effects such as micropores only accessible for CO_2 . The interaction with polar groups on the pore wall might have an impact as well. The high CO_2 uptake of P-PMF-HS40 with 2.29 mmol/g in comparison to P-PMF-2HS40 with a similar specific surface area calculated from the N_2 isotherm can be attributed to additional CO_2 -accessible small and narrow micropores (< 1.5 nm). However, these narrow micropores can have an impact on the adsorption performance for small molecules such as DCF. Although the calculated specific surface area of P-PMF-AS40, P-PMF-TMA and P-PMF-TM40 is smaller due to the larger mesopores, their CO_2 uptake is higher in comparison to P-PMF-2HS40. Thus, the general higher amount of SiO_2 NPs in P-PMF-2HS40 seems to have a strong influence on the accessibility of micropores by diffusion. As mesopores and their higher surface volume increases diffusion, the higher mass transfer through the particle structure does allow for a higher throughput in the surrounding micropores, where diffusion is inhibited. Especially P-PMF-AS40 is showing a high difference in the low calculated micropore volume from N_2 sorption vs. the high uptake of CO_2 . This can

be due to limited mobility of N₂ at cryogenic temperatures, occurring for very fine micropores (Thommes et al., 2015), indicating lower accessibility of these pores for less mobile adsorptives. From NLDFT fitting derived from CO₂ sorption, the micropore structure can be derived (Dassanayake et al., 2016; Wickramaratne and Jaroniec, 2013). However, the P-PMF samples all show similar pore sizes (Figure S10) and possessed a small hysteresis loop with a bent curve progression.

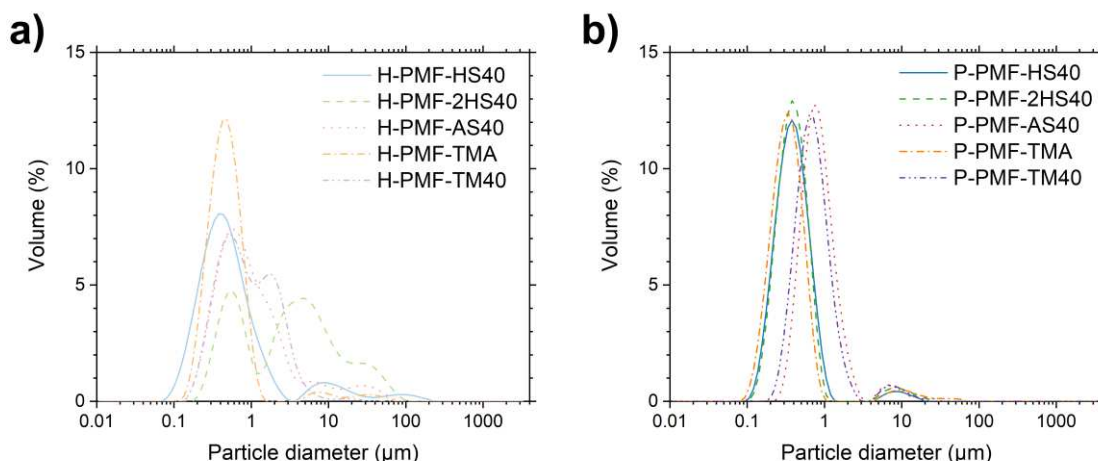


Figure 6.3. Particle size distribution measured by laser diffractometry for a) the H-PMF particles and b) the P-PMF particles. H-PMF-HS40 is shown in light blue (solid), H-PMF-2HS40 in light green (dashed), H-PMF-AS40 in light red (dotted), H-PMF-TMA in light yellow (dash-dot line), and H-PMF-TM40 in light violet (dash-dot-dot line). P-PMF-HS40 is shown in blue (solid), P-PMF-2HS40 in green (dashed), P-PMF-AS40 in red (dotted), P-PMF-TMA in yellow (dash-dot line) and P-PMF-TM40 in violet (dash-dot-dot line).

According to the particle size distribution measurements (see Figure 6.3 and Table S2), the hybrid particles formed aggregates of various sizes leading to a broad size distribution with multiple peaks in most cases (SEM images in Figure S3 – S7). Herein, H-PMF-TMA is an exception with a single peak at 330 nm. As the silica particles of Ludox[®] TMA are not stabilized by counter ions and feature a pH below 7, this leads to higher colloidal stability of the hybrid particles in dispersion, preventing the formation of very large aggregates as seen by the rest of the H-PMF particles. Especially H-PMF-2HS40 with the doubled amount of silica in the reaction mixture exhibited large aggregates and a broad particle size distribution. In contrast, the diameters of the different P-PMF particles are uniform and homogenous. Here, it is visible that the particle sizes are influenced by the type of template used in synthesis. P-PMF-HS40 and P-PMF-2HS40, which are both synthesized with 12 nm in diameter SiO₂ NPs, exhibited similar particle diameters with their maxima being around 380 nm. The particle diameter of P-PMF-AS40 and P-PMF-TM40, both using 22 nm in diameter SiO₂ NPs, are also similar in their peak maxima with values around 720 nm and 630 nm, respectively. P-PMF-TMA represents again an exception to this and its particle diameter of approximately 330 nm is closer to the diameters of particles with 12 nm template. When comparing the P-PMF samples with their

hybrid particles, the particle sizes are reduced slightly, as expected from the etching procedure to remove the SiO₂ NPs. Especially H-PMF-2HS40 is showing much larger diameters than its P-PMF counterpart, as the silica is facilitating aggregation. This leads to two main peaks in the particle size distribution of H-PMF-2HS40 with maxima around 560 nm and 4.5 μm. The dependence of the particle size of the used template can be explained by a Pickering-like stabilization effect that the SiO₂ NPs have on the nascent PMF particles in synthesis. Consequently, larger SiO₂ NPs lead to the formation of larger hybrid particles.

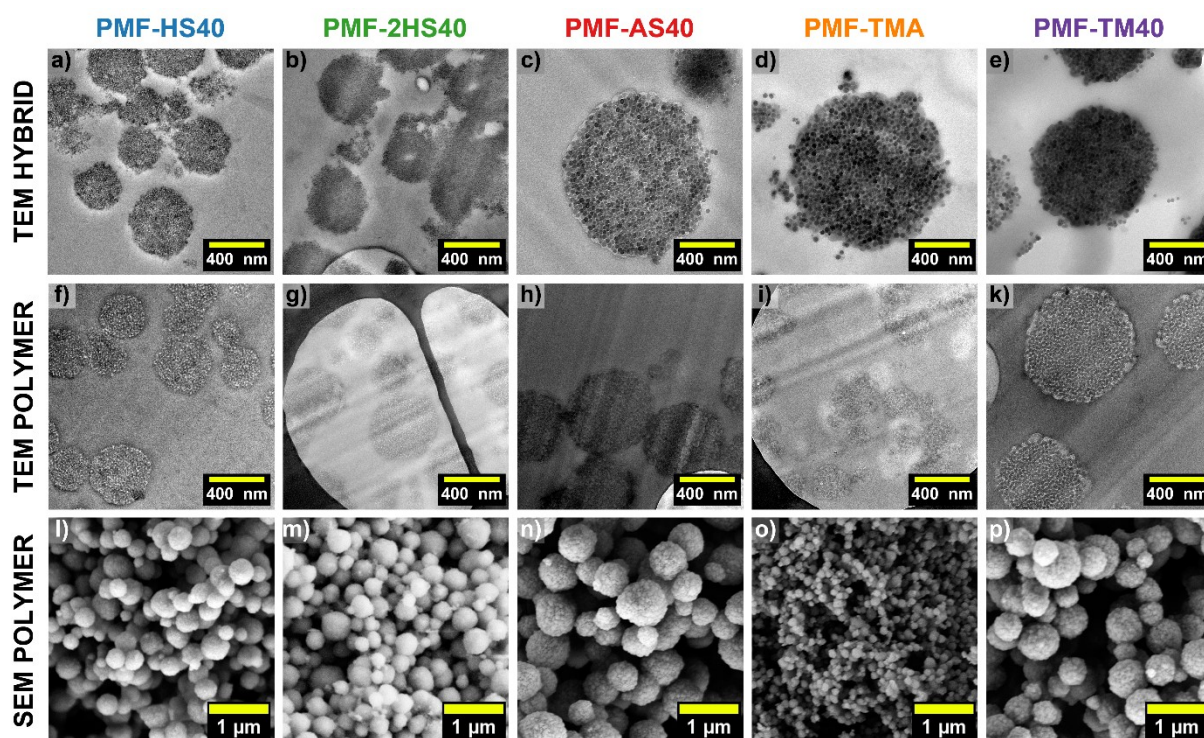


Figure 6.4. a) – k) TEM images of a) H-PMF-HS40, b) H-PMF-2HS40, c) H-PMF-AS40, d) H-PMF-TMA, e) H-PMF-TM40, f) P-PMF-HS40, g) P-PMF-2HS40, h) P-PMF-AS40, i) P-PMF-TMA and k) P-PMF-TM40. l) – p) SEM images of l) P-PMF-HS40, m) SEM image of P-PMF-2HS40, n) P-PMF-AS40, o) P-PMF-TMA, and p) of P-PMF-TM40. SEM images of the H-PMF particles are shown in Figure S11 – S15. Enlarged TEM images are shown in Figure S16 – S25.

From TEM imaging of thin-sections of embedded H-PMF and P-PMF particles (Figure 6.4 a – k), we can optically assess the inclusion of the SiO₂ NPs into the resin structure. Larger images with higher resolution are presented in Figure S16 – S25. It is visible that the pore size of the templated, etched P-PMF particles matches the SiO₂/hybrid particles very well. Therefore, no shrinkage occurs after template removal. Comparing especially the three P-PMF particles with the 22 nm templates, significant differences in the interconnection of the pore system are visible (Figure S23 – S25): P-PMF-AS40 and P-PMF-TM40 show very thin pore walls between the main cavities. Furthermore, a high number of connection channels to the surrounding cavities can be found, visible by the altered brightness of the walls around the pore cavities, when walls are discontinued. In sharp contrast, P-PMF-TMA shows thicker pore

walls, which are also enclosing the pore cavities almost completely in every instance. This is in good agreement with the results from N₂ sorption measurements, especially the BJH analysis. For P-PMF-HS40 and P-PMF-2HS40 a well-connected pore system similar to P-PMF-AS-40 and P-PMF-TM40 can be seen.

Consequently, the required porosity and chemical structure of the samples was validated. Further, we showed that changing the diameter of templating SiO₂ NPs and especially changing the respective stabilizing ion indeed allows tuning of the pore size. Here, the stabilizing charge impacts especially the interconnectivity in the pore structure making it an ideal test system for the following adsorption of pharmaceuticals.

3.2. Adsorption of Pharmaceuticals

To investigate the adsorption of the different mesoporous PMF particles towards DCF, isotherms of all P-PMF samples with solutions of DCF were determined. The isotherms were subsequently evaluated with the Langmuir isotherm model to get a more detailed information of the sorption process. We used batch experiments with initial DCF concentrations between 1.5 and 1000 µmol/L. For that, DCF-Na salt was dissolved in ultrapure water and diluted to the required concentration. The initial and equilibrium concentrations and the pH of the solutions before and after the adsorption process were measured.

To determine the equilibrium time for the study, preliminary kinetic experiments were conducted, which are presented in section 1.3.1 of the SI. From the results, an equilibration time of 24 h was chosen as the plateau is reached at this time.

In adsorption experiments with DCF, different problems can occur, which are drastically influencing the achieved adsorption. Due to the low solubility of DCF at low pH (Skube et al., 2004), the pH of the solution has to be monitored closely. For example, dissolving the DCF-Na salt in ultrapure water is increasing the pH₀ of the solution as result of the carboxylate group being protonated again and therefore shifting to an uncharged species, which will precipitate in higher concentrations due to hydrophobic interactions. When an adsorbent is added to the solution, which itself is releasing protons from its surface, more DCF is protonated subsequently leading to precipitation of the uncharged species (Moral-Rodríguez et al., 2019). This is causing an apparent drop of the equilibrium concentration resulting in an increased DCF adsorption. However, as the goal of the investigation is to determine the adsorption capacity with regard to a later application for real wastewater treatment, this apparent removal of DCF by precipitation is not even close to the application needed. In real wastewater treatment applications, DCF will always be in extremely low concentrations, which cannot precipitate by pH although DCF will be uncharged due to protonation (Skube et al., 2004). Therefore, it can be concluded that adsorbents, which are leading to a precipitating of DCF by

lowering the pH of the batch experiments will be of no use for remediation of low DCF concentration although showing a very high apparent adsorption capacity.

This effect is seen when applying for example the hybrid H-PMF-HS40 particles to DCF-Na solutions (see Figure S28). As the surface is composed of silica to a great amount, a drastic decrease from pH_0 to pH_{eq} is seen over the adsorption process (see Figure S29), also visible in ultrapure water (see Figure S30). H-PMF-HS40 exhibited an extremely high adsorption of up to 87% at 1000 $\mu\text{mol/L}$ DCF caused by precipitation of DCF in acidic environment. The achieved isotherm was not showing any plateau up to the tested concentrations and cannot be modeled reasonably. Only higher concentrations of DCF are prone to precipitation by pH changes, as also seen in the ‘adsorption’ isotherm of H-PMF-HS40, which exemplarily visualizes the general issue of DCF.

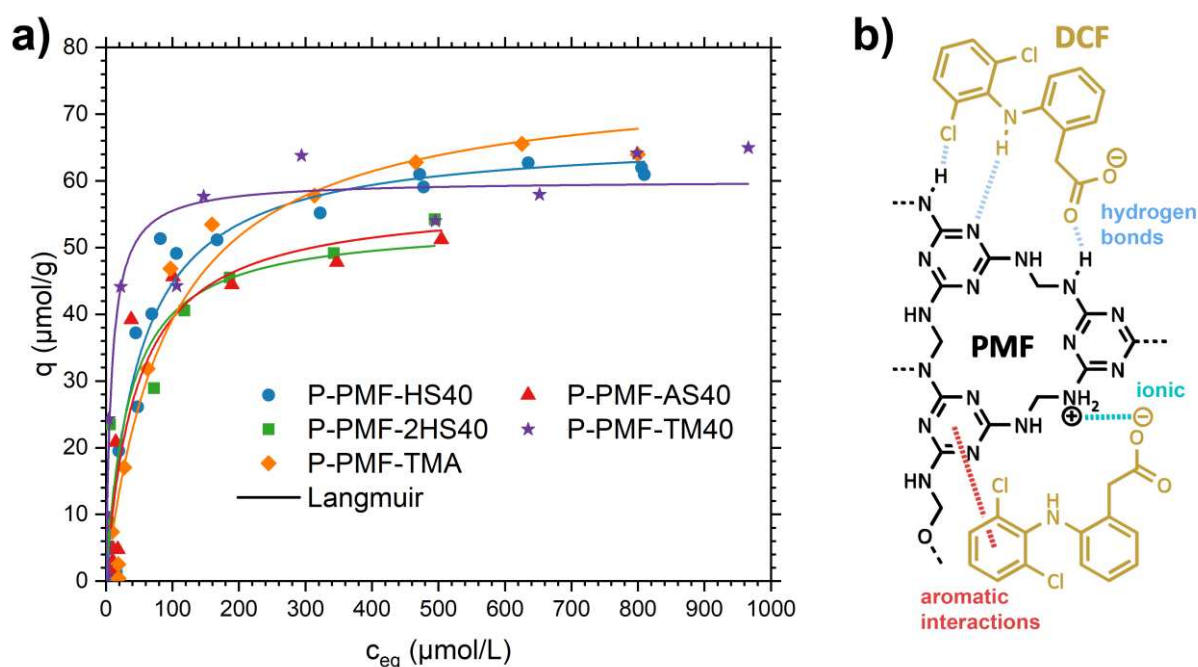


Figure 6.5. a) Sorption isotherms for DCF onto P-PMF-HS40 (blue, circles) and P-PMF-2HS40 (green, squares) and P-PMF-AS40 (red, triangles), P-PMF-TMA (yellow, diamonds) and P-PMF-TM40 (violet, stars) with the corresponding Langmuir fits (solid lines). The corresponding pH values are displayed in Figure S31 – S35. A graphical fitting comparison to Dubinin-Radushkevich can be seen in Figure S36. The fitting parameters are displayed in Table 6.4. b) Schematic of the possible interactions for the adsorption of DCF (ocher) with an exemplary structure of PMF (black). Here, hydrogen bonds are shown in blue, ionic interaction in green and aromatic π - π interaction in red.

In contrast, the porous P-PMF samples consisted of a very high amount of accessible aromatic triazine rings and amino and imine functionalities due to the porosity. Thus, the P-PMF samples act as buffer to the DCF solutions even in ultrapure water (see Figure S30). Therefore, achieved adsorption capacities presented here (see Figure 6.5a) can be attributed to interactions of the positively charged amino groups of the P-PMF with the negatively charged DCF or various interactions with the triazine rings (π - π interactions, dipole

Tuning the Pore Structure of Templated Mesoporous Poly(melamine-co-formaldehyde) Particles toward Diclofenac Removal

interactions, hydrogen bonds, ionic interaction) with DCF (Figure 6.5b). Precipitation can be ruled out with the achieved pH_{eq} values (see Figure S31 – S35).

The P-PMF samples reached plateaus between 40 $\mu\text{mol/g}$ and 70 $\mu\text{mol/g}$. The Langmuir isotherm fitting is well representative for the experiments (see Figure 6.5a and Table 6.4), which indicates a homogeneous monolayer adsorption for the DCF removal. In case of P-PMF-2HS40, the Dubinin-Radushkevich fit is insignificantly better in terms of R^2 . In general, the Dubinin-Radushkevich fitting overestimates the maximum adsorption capacity Q_m , whereas the Langmuir fit seem to be more reasonable, being closer the maximum experimental values $Q_{m,exp}$.

Table 6.4. Fitting parameters for Langmuir and Dubinin-Radushkevich isotherm model for DCF adsorption onto the P-PMF samples. Q_m is the maximal sorption capacity, K_L is the Langmuir equilibrium constant, β_{DR} is the activity coefficient for Dubinin-Radushkevich and $E_{Ads,DR}$ is the mean free energy of adsorption associated with the activity coefficient β_{DR} . The Gibbs energy change ΔG° was calculated from K_L . R^2 (COD) is the coefficient of determination. All parameters are given with their corresponding standard error.

Sample	$Q_{m,exp}^*$ ($\mu\text{mol/g}$)	Model	Q_m ($\mu\text{mol/g}$)	$\frac{Q_{m,fit}}{Q_{m,exp}}$ (%)	K_L (L/mmol)	β_{DR} (10^{-9} mol^2/J^2)	$E_{Ads,DR}$ (kJ/mol)	ΔG° (kJ/mol)	R^2 (COD)
P-PMF-HS40	62.7	L	66.7 ± 2.9	106.4	20.2 ± 3.7	--	--	-9.30	0.955
		D-R	161.3 ± 24.8	257.3	--	2.76 ± 0.36	13.5 ± 0.9	--	0.894
P-PMF-2HS40	54.2	L	53.7 ± 5.4	99.1	29.2 ± 13.6	--	--	-9.64	0.911
		D-R	174.1 ± 38.1	321.2	--	3.14 ± 0.47	12.6 ± 1.0	--	0.919
P-PMF-AS40	51.2	L	57.3 ± 7.0	111.9	22.0 ± 9.0	--	--	-9.37	0.869
		D-R	186.8 ± 72.7	364.8	--	3.33 ± 0.83	12.3 ± 1.5	--	0.778
P-PMF-TMA	65.6	L	75.7 ± 5.7	115.4	10.8 ± 2.8	--	--	-8.70	0.946
		D-R	232.7 ± 63.6	354.7	--	3.69 ± 0.68	11.7 ± 1.1	--	0.869
P-PMF-TM40	65.0	L	60.1 ± 2.2	92.5	122.2 ± 34.1	--	--	-10.98	0.963
		D-R	118.0 ± 13.2	181.5	--	1.87 ± 0.25	16.3 ± 1.1	--	0.933

* maximum experimental adsorption capacity of the isotherm

The change in Gibbs free energy, ΔG° , can be derived from the Langmuir isotherm constant K_L . As ΔG° gives negative values for all samples, this means that the adsorption process is exergonic and therefore occurring spontaneous.

The equilibrium constant K_L itself clearly indicates differing affinities of the samples toward DCF. P-PMF-TMA exhibited the lowest calculated K_L (10.7 L/mmol) due to the demanding pore system. Lacking well-defined connection channels, diffusion into the pores is limited. In contrast, P-PMF-TM40 featured an extremely high K_L with 122 L/mmol showing

strongly favored adsorption also in low concentration regions. The high capacity at $c_0 = 200 \mu\text{mol/L}$ DCF can be explained by the well-connected pore system with wide pore diameters.

In general, the adsorption of DCF into the pore system, especially as charged ion, is adding towards an energetic barrier for other accessing DCF species. Thus, wider pore systems with larger pore volumes would enable for easier penetration and higher mass transfer. Although narrow pores allow strong interactions with the DCF ion (estimated to be 0.43 nm (Maitani et al., 1993)), narrow pores can be blocked for other DCF species, which then cannot pass by. This lowers overall affinity and slope in DCF uptake.

Directly comparing P-PMF-HS40 with P-PMF-2HS40, the achieved adsorption capacities follow the trend of the CO_2 sorption (Figure 6.2), although both samples exhibited similar high specific surface areas by N_2 sorption and similar pore diameters of 12 nm. However, P-PMF-HS40 featured a much higher CO_2 uptake due to a better accessible pore system and a higher amount of small micropores. Although P-PMF-AS40 showed a high CO_2 uptake, it was proven that it exhibited lower accessibility of the micropores as the N_2 micropore volume significantly differed from the CO_2 uptake. Here, less mobile adsorptives as N_2 at cryogenic temperatures as well as the large DCF molecule are kinetically hindered. Thus, even in this prospect, the accessibility of the pores is crucial for the uptake of DCF.

Besides porosity, other parameters as the different particle diameters or the different nitrogen content (seen by low C/N molar ratios) do not exhibit a visible influence. The greatest correlation can be seen first for the micropore volume, as micropores are enabling for strong interaction with the DCF, therefore leading to higher adsorption capacities. However, small connection channels especially in the mesoporous regime are inhibiting the adsorption as already adsorbed DCF is strongly hindering further uptake. Thus, the micropore structure is decisive for the final 'storage' of the DCF in the adsorbent structure, but large mesopores are needed to allow the transport within the particles to reach the micropores in the first place contributing to the steep uptake in low-concentrations.

The isotherm fit with the Dubinin-Radushkevich model is useful to calculate the mean free energy of adsorption from the activity coefficient β_{DR} (Eq. 6.7). As this parameter is mostly dependent on the slope of the isotherm, the adsorption energy $E_{\text{Ads,DR}}$ can be reliably determined from the fit although Q_m differs from the experimental results. The derived energy of adsorption of P-PMF-TM40 with 16.3 kJ/mol implies a very strong interaction of the DCF molecules with the sample's surface, supporting also the derived assertion of the Langmuir equilibrium constant. Although the adsorption energies of DCF towards the other samples are lower, they are still representing very strong interactions between DCF and PMF in general.

A comparison of the adsorption capacities with literature is presented with discussion in the SI (Section 2). Unfortunately, the sole comparison of adsorption capacities cannot estimate the efficiency of the respective material in low concentrations. DCF is posing severe

environmental harm even at concentrations of several $\mu\text{g/L}$, thus complete removal is needed at these concentrations. Here, the removal efficiency at low concentrations needs to be compared. P-PMF-TM40 is achieving a percentage removal of 97% of DCF at $6.8 \mu\text{mol/L}$ (4 mg/L) and even complete removal at $3.4 \mu\text{mol/L}$ (2 mg/L), thus showing the extremely crucial removal efficiency that is needed. Realistic concentrations of e.g. $1 \mu\text{g/L}$ can therefore easily be remediated. Here, a volume over 19000 L at $1 \mu\text{g/L}$ would contain the mass of DCF of what is equivalent to the achieved adsorption capacity of 1 g P-PMF-TM40. Therefore, PMF presents a viable alternative for the removal of DCF.

4. Conclusion

In summary, we successfully synthesized highly nanoporous PMF samples with varying pore diameters for the efficient removal of diclofenac. Different colloidal SiO_2 NPs were used as sacrificial template with differing particle sizes (12 nm and 22 nm) and stabilizing counter ions (Na^+ , NH_3^+ , or none). The morphology and constitution of these particles was analyzed in-depth and potential influences of the template on the particle formation and templating process were highlighted. We showed that the template diameter is well represented by the pore size of the etched particles. The stabilizing counter ion shows a critical influence on the interconnectivity of the pore system in terms of the size and number of the connecting channels. We showed that the synthesized particles are reliable adsorbents for diclofenac. Influences of the pore structure onto the adsorption process were highlighted and attention paid to pH, so that the uptake of DCF is solely due to adsorption and not due to acidic precipitation. We found that efficient adsorption in low concentrations is increased by the mesoporous connection channels between the main pore cavities as they are crucial for the transport into the particle. Low-diameter connection channels are blocked by adsorbate molecules and therefore hinder access of further adsorptive. The adsorption capacity is decided by the available micropores. Especially for larger adsorptives such as DCF, the accessibility of these fine micropores is critical. From differences in CO_2 uptake vs. microporosity determined by N_2 , kinetic hindrance for sterically challenging adsorptives can be seen. We showed that reliable adsorption capacities of up to $76 \mu\text{mol/g}$ are achieved with P-PMF-TMA. P-PMF-TM40 showed an outstandingly steep uptake in very dilute DCF solutions with high mean free energy of adsorption and good adsorption capacities. Especially the uptake in low-concentration regions is decisive for the applicability for real wastewater treatment. As DCF is a critical and persistent pollutant, present in almost every municipal wastewater and surface water worldwide, templated PMF particles as cost-efficient material could be a key for the removal of this contaminant at a larger scale. It is posing a low-cost alternative to equally functional materials as styrene- or phenolic-based resins and metal organic frameworks. Furthermore, as DCF is well established as a model contaminant, highly

porous PMF particles are a promising adsorbent for other organics, which pose high risk to health or environment.

Acknowledgements

This research was funded by the German Federal Ministry of Education and Research, grant number 01DJ18010. The authors thank Eileen Schierz for conduction of elemental analysis measurements and Uta Reuter for the preparation of the thin sections used for TEM imaging. We furthermore want to thank all eight reviewers for their constructive criticism to improve this publication.

References

- Andreozzi, R., Raffaele, M., Nicklas, P., 2003. Pharmaceuticals in STP effluents and their solar photodegradation in aquatic environment. *Chemosphere* 50 (10), 1319–1330.
- Bamford, A.J., Monadjem, A., Anderson, M.D., Anthony, A., Borello, W.D., Bridgeford, M., Bridgeford, P., Hancock, P., Howells, B., Wakelin, J., Hardy, I.C.W., 2009. Trade-offs between specificity and regional generality in habitat association models: a case study of two species of African vulture. *Journal of Applied Ecology* 46, 852–860. <https://doi.org/10.1111/j.1365-2664.2009.01669.x>.
- Baraka, A., Hall, P.J., Heslop, M.J., 2007. Preparation and characterization of melamine–formaldehyde–DTPA chelating resin and its use as an adsorbent for heavy metals removal from wastewater. *Reactive and Functional Polymers* 67, 585–600. <https://doi.org/10.1016/j.reactfunctpolym.2007.01.015>.
- Barrett, E. P., Joyner, L. G., Halenda, P. P., 1951. The Determination of Pore Volume and Area Distributions in Porous Substances. I. Computations from Nitrogen Isotherms. *J. Am. Chem. Soc.* 73 (1), 373–380. doi:10.1021/ja01145a126.
- Beek, T. aus der, Weber, F.-A., Bergmann, A., Hickmann, S., Ebert, I., Hein, A., Küster, A., 2016. Pharmaceuticals in the environment—Global occurrences and perspectives. *Environmental toxicology and chemistry* 35, 823–835. <https://doi.org/10.1002/etc.3339>.
- Beltrán, F.J., Pocostales, P., Alvarez, P., Oropesa, A., 2009. Diclofenac removal from water with ozone and activated carbon. *Journal of hazardous materials* 163, 768–776. <https://doi.org/10.1016/j.jhazmat.2008.07.033>.
- Bentley, J., 1999. Organic film formers, in: *Paint and Surface Coatings*, 7 volumes. Elsevier, pp. 19–90.
- Binder, W.H., Dunky, M., 2002. Melamine-Formaldehyde Resins, in: *Encyclopedia of Polymer Science and Technology*, vol. 74. John Wiley & Sons, Inc, Hoboken, NJ, USA, p. 978.
- Borchert, K.B.L., Steinbach, C., Reis, B., Gerlach, N., Zimmermann, P., Schwarz, S., Schwarz, D., 2021. Mesoporous Poly(melamine-co-formaldehyde) Particles for Efficient and Selective Phosphate and Sulfate Removal. *Molecules* (Basel, Switzerland) 26. <https://doi.org/10.3390/molecules26216615>.
- Brunauer, S., Emmett, P.H., Teller, E., 1938. Adsorption of Gases in Multimolecular Layers. *J. Am. Chem. Soc.* 60, 309–319. <https://doi.org/10.1021/ja01269a023>.
- Carere, M., Polesello, S., Kase, R., Gawlik, B. M., 2015. The Emerging Contaminants in the Context of the EU Water Framework Directive. *Emerging Contaminants in River Ecosystems. The Handbook of Environmental Chemistry.*, 46. Springer, Cham, pp. 197–215.
- Cuccarese, M., Brutti, S., Bonis, A. de, Teghil, R., Mancini, I.M., Masi, S., Caniani, D., 2021. Removal of diclofenac from aqueous solutions by adsorption on thermo-plasma expanded graphite. *Scientific reports* 11, 3427. <https://doi.org/10.1038/s41598-021-83117-z>.
- Dassanayake, R.S., Gunathilake, C., Jackson, T., Jaroniec, M., Abidi, N., 2016. Preparation and adsorption properties of aerocellulose-derived activated carbon monoliths. *Cellulose* 23, 1363–1374. <https://doi.org/10.1007/s10570-016-0886-1>.
- Devallencourt, C., Saiter, J.M., Fafet, A., Ubrich, E., 1995. Thermogravimetry/Fourier transform infrared coupling investigations to study the thermal stability of melamine formaldehyde resin. *Thermochimica Acta* 259, 143–151. [https://doi.org/10.1016/0040-6031\(95\)02262-Z](https://doi.org/10.1016/0040-6031(95)02262-Z).
- Dubin, M.M., 1947. The Equation of the Characteristic Curve of Activated Charcoal. *Proceedings of the USSR Academy of Sciences* 55, 327–329.
- Foo, K.Y., Hameed, B.H., 2010. Insights into the modeling of adsorption isotherm systems. *Chemical Engineering Journal* 156, 2–10. <https://doi.org/10.1016/j.cej.2009.09.013>.

Tuning the Pore Structure of Templated Mesoporous Poly(melamine-co-formaldehyde) Particles toward Diclofenac Removal

- Genç, N., Durna, E., Erkişi, E., 2021. Optimization of the adsorption of diclofenac by activated carbon and the acidic regeneration of spent activated carbon. *Water science and technology : a journal of the International Association on Water Pollution Research* 83, 396–408. <https://doi.org/10.2166/wst.2020.577>.
- Gworek, B., Kijeńska, M., Zaborowska, M., Wrzosek, J., Tokarz, L., Chmielewski, J., 2019. Pharmaceuticals in aquatic environment. Fate and behaviour, ecotoxicology and risk assessment – A review. *Acta Poloniae Pharmaceutica - Drug Research* 76, 397–407. <https://doi.org/10.32383/appdr/103368>.
- Herlinger, Hoffmann, Husemann, Istel, Kern, Krimm, Müller, Rinke, Schmitz-Josten, Schneider, Schulz, Spielberger, Wegler, Werner (Eds.), 1963. *Makromolekulare Stoffe*. Georg Thieme Verlag, Stuttgart.
- Joachim, S., Beaudouin, R., Daniele, G., Geffard, A., Bado-Nilles, A., Tebby, C., Palluel, O., Dedourge-Geffard, O., Fieu, M., Bonnard, M., Palos-Ladeiro, M., Turiès, C., Vulliet, E., David, V., Baudoin, P., James, A., Andres, S., Porcher, J.M., 2021. Effects of diclofenac on sentinel species and aquatic communities in semi-natural conditions. *Ecotoxicology and environmental safety* 211, 111812. <https://doi.org/10.1016/j.ecoenv.2020.111812>.
- Johnson, A. C., Dumont, E., Williams, R. J., Oldenkamp, R., Cisowska, I., Sumpter, J. P., 2013. Do concentrations of ethinylestradiol, estradiol, and diclofenac in European rivers exceed proposed EU environmental quality standards? *Environmental science & technology* 47 (21), 12297–12304. doi:10.1021/es4030035.
- Langmuir, I., 1916. The Constitution and Fundamental Properties of Solids and Liquids. Part I. Solids. *J. Am. Chem. Soc.* 38, 2221–2295. <https://doi.org/10.1021/ja02268a002>.
- Larous, S., Meniai, A.-H., 2016. Adsorption of Diclofenac from aqueous solution using activated carbon prepared from olive stones. *International Journal of Hydrogen Energy* 41, 10380–10390. <https://doi.org/10.1016/j.ijhydene.2016.01.096>.
- Leone, V.O., Pereira, M.C., Aquino, S.F., Oliveira, L.C.A., Correa, S., Ramalho, T.C., Gurgel, L.V.A., Silva, A.C., 2018. Adsorption of diclofenac on a magnetic adsorbent based on maghemite: experimental and theoretical studies. *New J. Chem.* 42, 437–449. <https://doi.org/10.1039/C7NJ03214E>.
- Liang, X.X., Omer, A.M., Hu, Z.-H., Wang, Y.-G., Di Yu, Ouyang, X.-K., 2019. Efficient adsorption of diclofenac sodium from aqueous solutions using magnetic amine-functionalized chitosan. *Chemosphere* 217, 270–278. <https://doi.org/10.1016/j.chemosphere.2018.11.023>.
- Liu, Y., 2009. Is the Free Energy Change of Adsorption Correctly Calculated? *J. Chem. Eng. Data* 54, 1981–1985. <https://doi.org/10.1021/je800661q>.
- Maitani, Y., Kugo, M., Nakagaki, M., Nagai, T., 1993. Ionic size and behavior of diclofenac salts in water and ethanol/water mixtures by conductivity at 25 degrees C. *Journal of pharmaceutical sciences* 82, 1245–1249. <https://doi.org/10.1002/jps.2600821212>.
- Merline, D.J., Vukusic, S., Abdala, A.A., 2013. Melamine formaldehyde: curing studies and reaction mechanism. *Polym J* 45, 413–419. <https://doi.org/10.1038/pj.2012.162>.
- Moral-Rodríguez, A.I., Leyva-Ramos, R., Ania, C.O., Ocampo-Pérez, R., Isaacs-Páez, E.D., Carrales-Alvarado, D.H., Parra, J.B., 2019. Tailoring the textural properties of an activated carbon for enhancing its adsorption capacity towards diclofenac from aqueous solution. *Environmental science and pollution research international* 26, 6141–6152. <https://doi.org/10.1007/s11356-018-3991-x>.
- Naidoo, V., Wolter, K., Cuthbert, R., Duncan, N., 2009. Veterinary diclofenac threatens Africa's endangered vulture species. *Regulatory toxicology and pharmacology : RTP* 53, 205–208. <https://doi.org/10.1016/j.yrtph.2009.01.010>.
- Nguyen, V.-H., Smith, S.M., Wantala, K., Kajitvichyanukul, P., 2020. Photocatalytic remediation of persistent organic pollutants (POPs): A review. *Arabian Journal of Chemistry* 13, 8309–8337. <https://doi.org/10.1016/j.arabjc.2020.04.028>.
- Oaks, J.L., Gilbert, M., Virani, M.Z., Watson, R.T., Meteyer, C.U., Rideout, B.A., Shivaprasad, H.L., Ahmed, S., Chaudhry, M.J.I., Arshad, M., Mahmood, S., Ali, A., Khan, A.A., 2004. Diclofenac residues as the cause of vulture population decline in Pakistan. *Nature* 427, 630–633. <https://doi.org/10.1038/nature02317>.
- Odjadjare, E.E.O., Okoh, A.I., 2010. Physicochemical quality of an urban municipal wastewater effluent and its impact on the receiving environment. *Environmental monitoring and assessment* 170, 383–394. <https://doi.org/10.1007/s10661-009-1240-y>.
- Osmari, T.A., Gallon, R., Schwaab, M., Barbosa-Coutinho, E., Severo, J.B., Pinto, J.C., 2013. Statistical Analysis of Linear and Non-Linear Regression for the Estimation of Adsorption Isotherm Parameters. *Adsorption Science & Technology* 31, 433–458. <https://doi.org/10.1260/0263-6174.31.5.433>.
- Pérez-Estrada, L.A., Malato, S., Gernjak, W., Agüera, A., Thurman, E.M., Ferrer, I., Fernández-Alba, A.R., 2005. Photo-fenton degradation of diclofenac: identification of main intermediates and degradation pathway. *Environmental science & technology* 39, 8300–8306. <https://doi.org/10.1021/es050794n>.
- Radke, Michael, Ulrich, Hanna, Wurm, Carolin, Kunkel, Uwe, 2010. Dynamics and attenuation of acidic pharmaceuticals along a river stretch. *Environmental science & technology* 44 (8), 2968–2974. doi:10.1021/es903091z.

Tuning the Pore Structure of Templated Mesoporous Poly(melamine-co-formaldehyde) Particles toward Diclofenac Removal

- Rathi, B.S., Kumar, P.S., Vo, D.-V.N., 2021. Critical review on hazardous pollutants in water environment: Occurrence, monitoring, fate, removal technologies and risk assessment. *The Science of the total environment* 797, 149134. <https://doi.org/10.1016/j.scitotenv.2021.149134>.
- Rauch, M., Strater, Z., Parkin, G., 2019. Selective Conversion of Carbon Dioxide to Formaldehyde via a Bis(silyl)acetal: Incorporation of Isotopically Labeled C1 Moieties Derived from Carbon Dioxide into Organic Molecules. *J. Am. Chem. Soc.* 141, 17754–17762. <https://doi.org/10.1021/jacs.9b08342>.
- Schlumberger, C., Thommes, M., 2021. Characterization of Hierarchically Ordered Porous Materials by Physisorption and Mercury Porosimetry—A Tutorial Review. *Adv. Mater. Interfaces* 8, 2002181. <https://doi.org/10.1002/admi.202002181>.
- Schwarz, D., Weber, J., 2015. Nanoporous Poly(Melamine Formaldehyde) Networks by Aqueous Dispersion Polycondensation-Synthesis and Adsorption Properties. *Macromol. Mater. Eng.* 300, 531–541. <https://doi.org/10.1002/mame.201400330>.
- Schwarz, D., Weber, J., 2017. Synthesis of mesoporous poly(melamine-formaldehyde) particles by inverse emulsion polymerization. *Journal of colloid and interface science* 498, 335–342. <https://doi.org/10.1016/j.jcis.2017.03.064>.
- Schwarz, D., Weber, J., 2018. Organic-solvent free synthesis of mesoporous and narrow-dispersed melamine resin particles for water treatment applications. *Polymer* 155, 83–88. <https://doi.org/10.1016/j.polymer.2018.09.028>.
- Simon, E., Duffek, A., Stahl, C., Frey, M., Scheurer, M., Tuerk, J., Gehrmann, L., Könemann, S., Swart, K., Behnisch, P., Olbrich, D., Brion, F., Aït-Aïssa, S., Pasanen-Kase, R., Werner, I., Vermeirssen, E.L.M., 2022. Biological effect and chemical monitoring of Watch List substances in European surface waters: Steroidal estrogens and diclofenac - Effect-based methods for monitoring frameworks. *Environment international* 159, 107033. <https://doi.org/10.1016/j.envint.2021.107033>.
- Sing, K.S.W., 1982. Reporting physisorption data for gas/solid systems: With special reference to the determination of surface area and porosity. *Pure & Applied Chemistry* 54, 2201–2218.
- Skube, M.K.; Meleh, M.; Veber, M.; Vrecer, F. Study of physicochemical parameters affecting the release of diclofenac sodium from lipophilic matrix tablets. *Acta chimica slovenica* **2004**, 409–425.
- Socrates, G., 2015. Infrared and Raman characteristic group frequencies: Tables and charts, 3rd ed. John Wiley & Sons LTD, Chichester [etc.], Skoroszyt.
- Song, S., Su, Y., Adeleye, A.S., Zhang, Y., Zhou, X., 2017. Optimal design and characterization of sulfide-modified nanoscale zerovalent iron for diclofenac removal. *Applied Catalysis B: Environmental* 201, 211–220. <https://doi.org/10.1016/j.apcatb.2016.07.055>.
- Subramanyam, B., Das, A., 2014. Linearised and non-linearised isotherm models optimization analysis by error functions and statistical means. *Journal of environmental health science & engineering* 12, 92. <https://doi.org/10.1186/2052-336X-12-92>.
- Swan, G.E., Cuthbert, R., Quevedo, M., Green, R.E., Pain, D.J., Bartels, P., Cunningham, A.A., Duncan, N., Meharg, A.A., Oaks, J.L., Parry-Jones, J., Shultz, S., Taggart, M.A., Verdoorn, G., Wolter, K., 2006. Toxicity of diclofenac to Gyps vultures. *Biology letters* 2, 279–282. <https://doi.org/10.1098/rsbl.2005.0425>.
- Tan, M.X., Sum, Y.N., Ying, J.Y., Zhang, Y., 2013. A mesoporous poly-melamine-formaldehyde polymer as a solid sorbent for toxic metal removal. *Energy Environ. Sci.* 6, 3254. <https://doi.org/10.1039/C3EE42216J>.
- Thommes, M., Kaneko, K., Neimark, A.V., Olivier, J.P., Rodriguez-Reinoso, F., Rouquerol, J., Sing, K.S.W., 2015. Physisorption of gases, with special reference to the evaluation of surface area and pore size distribution (IUPAC Technical Report). *Pure and Applied Chemistry* 87, 1051–1069. <https://doi.org/10.1515/pac-2014-1117>.
- Tixier, Céline, Singer, Heinz P., Oellers, Sjef, Müller, Stephan R., 2003. Occurrence and fate of carbamazepine, clofibric acid, diclofenac, ibuprofen, ketoprofen, and naproxen in surface waters. *Environmental science & technology* 37 (6), 1061–1068. doi:10.1021/es025834r.
- Togue Kamga, F., 2019. Modeling adsorption mechanism of paraquat onto Ayous (Triplochiton scleroxylon) wood sawdust. *Appl Water Sci* 9, 456. <https://doi.org/10.1007/s13201-018-0879-3>.
- Tomul, F., Arslan, Y., Başoğlu, F.T., Babuçuoğlu, Y., Tran, H.N., 2019. Efficient removal of anti-inflammatory from solution by Fe-containing activated carbon: Adsorption kinetics, isotherms, and thermodynamics. *Journal of environmental management* 238, 296–306. <https://doi.org/10.1016/j.jenvman.2019.02.088>.
- Ullah, S., Bustam, M.A., Nadeem, M., Naz, M.Y., Tan, W.L., Shariff, A.M., 2014. Synthesis and Thermal Degradation Studies of Melamine Formaldehyde Resins. *The Scientific World Journal* 2014, 1–6. <https://doi.org/10.1155/2014/940502>.
- Verlicchi, P., Al Aukidy, M., Zambello, E., 2012. Occurrence of pharmaceutical compounds in urban wastewater: removal, mass load and environmental risk after a secondary treatment—a review. *The Science of the total environment* 429, 123–155. <https://doi.org/10.1016/j.scitotenv.2012.04.028>.

Tuning the Pore Structure of Templated Mesoporous Poly(melamine-co-formaldehyde) Particles toward Diclofenac Removal

- Wang, H., Xin, Z., Li, Y., 2018. Synthesis of Ureas from CO₂, in: Wu, X.-F., Beller, M. (Eds.), Chemical Transformations of Carbon Dioxide. Springer International Publishing, Cham, pp. 177–202.
- Wang, J., Guo, X., 2020. Adsorption isotherm models: Classification, physical meaning, application and solving method. *Chemosphere* 258, 127279. <https://doi.org/10.1016/j.chemosphere.2020.127279>.
- Wang, Y., Xie, Y., Zhang, Y., Tang, S., Guo, C., Wu, J., Lau, R., 2016. Anionic and cationic dyes adsorption on porous poly-melamine-formaldehyde polymer. *Chemical Engineering Research and Design* 114, 258–267. <https://doi.org/10.1016/j.cherd.2016.08.027>.
- Wickramaratne, N.P., Jaroniec, M., 2013. Activated carbon spheres for CO₂ adsorption. *ACS applied materials & interfaces* 5, 1849–1855. <https://doi.org/10.1021/am400112m>.
- World Health Organization, Food, Agriculture Organization of the United Nations, 2009. Toxicological and health aspects of melamine and cyanuric acid : report of a WHO expert meeting in collaboration with FAO, supported by Health Canada, Ottawa, Canada, 1-4 December 2008. World Health Organization, 66 p.
- Xian, G., Zhang, G., Chang, H., Zhang, Y., Zou, Z., Li, X., 2019. Heterogeneous activation of persulfate by Co₃O₄-CeO₂ catalyst for diclofenac removal. *Journal of environmental management* 234, 265–272. <https://doi.org/10.1016/j.jenvman.2019.01.013>.
- Yang, G., Han, H., Du, C., Luo, Z., Wang, Y., 2010. Facile synthesis of melamine-based porous polymer networks and their application for removal of aqueous mercury ions. *Polymer* 51, 6193–6202. [doi:10.1016/j.polymer.2010.10.052](https://doi.org/10.1016/j.polymer.2010.10.052).
- Zhang, X., Chen, F., 2016. Facile Synthesis of Mesoporous Poly(melamine–formaldehyde) Solid Adsorbent in Ethylene Glycol. *Chemistry Letters* 45 (4), 412–414. [doi:10.1246/cl.151202](https://doi.org/10.1246/cl.151202).
- Zhou, X., 2020. Correction to the calculation of Polanyi potential from Dubinnin-Rudushkevich equation. *Journal of hazardous materials* 384, 121101. <https://doi.org/10.1016/j.jhazmat.2019.121101>.

7. Adsorption vs. Surface Precipitation of Cu^{2+} onto Porous Poly(melamine-co-formaldehyde) Particles

This chapter is based on the publication in *Microporous and Mesoporous Materials* **2023**, 348, 112383.

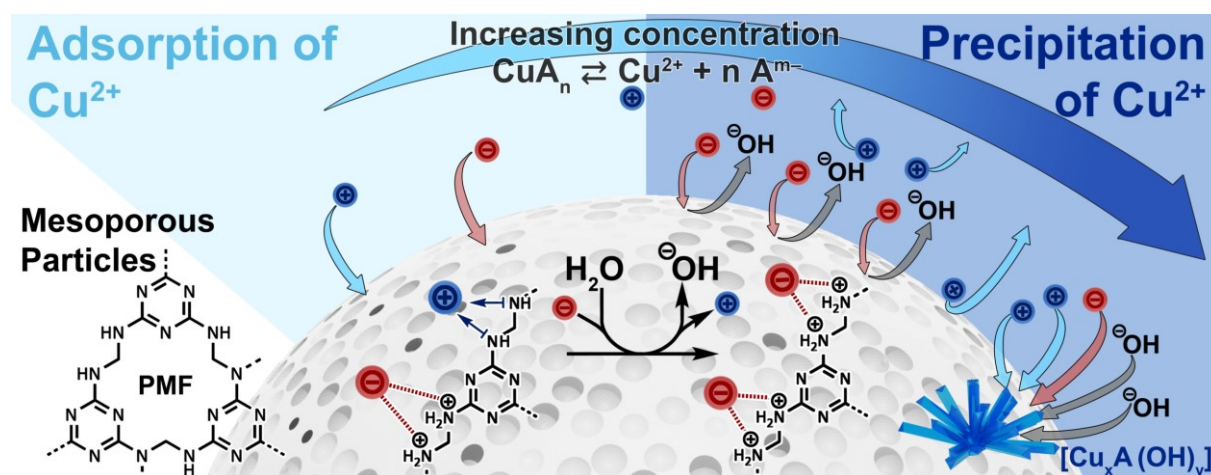
(DOI: 10.1016/j.micromeso.2022.112383).

By Konstantin B. L. Borchert, Christine Steinbach, Berthold Reis, Uwe Lappan, Niklas Gerlach, Martin Mayer, Simona Schwarz* and Dana Schwarz*

Leibniz-Institut für Polymerforschung Dresden e.V., Hohe Str. 6, 01069 Dresden, Germany;

* Corresponding authors

Graphical Abstract



Abstract

The application of multi-functional materials like Poly(melamine-co-formaldehyde) (PMF) for water purification pose the advantage that differing pollutants can be separated. The high nitrogen content of PMF enables potential chelation of heavy metal ions as well as electrostatic interactions with anions after protonation. Furthermore, amines can induce surface precipitation of heavy metal ions. For these reasons, it is important to investigate the complex interplay of adsorption and surface precipitation when regarding the uptake of both the metal ion as well as the anion. To investigate these processes, we synthesized mesoporous PMF particles with high specific surface areas up to $421 \text{ m}^2/\text{g}$ by dispersion polymerization in water using SiO_2 nanoparticles as hard template. Subsequent adsorption experiments with these porous PMF particles and different Cu(II) salts (CuSO_4 , $\text{Cu(NO}_2)_3$, CuCl_2), we investigated the occurrence of surface precipitation and adsorption both as superimposition and as two distinct uptake steps. The surface precipitate was identified as $\text{Cu}_x\text{A(OH)}_y$ hydroxide species with the respective anion A. Investigations with WAXS, SEM-EDX and EPR spectroscopy showed the regions for adsorption and surface precipitation. With this knowledge, we were

able to model the uptake with a new adsorption isotherm by combination of the Langmuir and sigmoidal Boltzmann equation.

1. *Introduction*

Synthetic materials like various resins have been continuously investigated for energy-efficient adsorption of contaminants from water or gas phases. Recent investigations showed that especially Poly(melamine-co-formaldehyde) (PMF) can be an extremely efficient adsorbent material for removal of e.g. carbon dioxide from gas mixtures [1] or organic pollutants [2–4], oxyanions [5,6] and toxic heavy metal ions [7,8] from contaminated water. PMF is offering very great advantages with its simple synthesis procedures, low material prizes and high adsorption capacities in combination with high resistance against acids, bases, organic solvents and high temperatures. Furthermore it can be polymerized in water avoiding toxic solvents [1,2,5,6,9]. As part of our author team showed, the surface area of PMF particles can be significantly increased using an environmentally friendly hard templating method with colloidal silica nanoparticles overcoming PMFs disadvantage of forming compact resin structures [10]. However, the synthesis of PMF particles can still be optimized by variation of different synthesis parameters, also contributing to a greater comprehension of the particle formation seen in the complex water-PMF-silica system. We already showed, that the pore structure has significant influence on the adsorption behavior towards oxyanions [6]. This is why it is all the more important to fully understand the underlying mechanism for separation applications. Until now, the separation mechanism of different pollutants such as heavy metal ions is not well investigated, especially when considering the influence of respective anions. Our author team recently analyzed the heavy metal ion removal with respect to the present anion in solution, whereas significant differences were determinable [11,12]. As PMF is able to adsorb both, anions by electrostatic interactions and metal ions by chelation, the underlying system of adsorption potentially consists of various dependent equilibria adding to a great complexity of the topic. Furthermore, an interaction between anions and cations during adsorption cannot be ruled out by publications right now. Furthermore, the process of surface precipitation can also be adding to the removal of heavy metal ions as well as anions [13–15], which increases the separation efficiency for two applications. Although surface precipitation is commonly investigated for the removal of hydrolysable heavy metal ions by inorganic metal oxide materials [16–21] and soils [22–25], the process is extremely seldom analyzed or tested for organic materials [26–29]. For these reasons, understanding the complex interplay of these processes is necessary to apply PMF and other adsorbents to its full potential. Furthermore, understanding this mechanism enables the preparation of new inorganic-polymeric hybrid materials, which are recently investigated for different prestigious applications such as catalysis [30,31].

Herein, we present a study on the synthesis of various PMF particles, differing by either applying a hard templating method with silica nanospheres for high specific surface areas or without templating for direct comparison. These potential adsorbents were comprehensively

characterized using electron microscopy, nitrogen and carbon dioxide sorption, FTIR spectroscopy, and elemental analysis. Subsequently, the particles were applied in adsorption experiments with solutions of different copper(II) salts (CuCl_2 , $\text{Cu}(\text{NO}_3)_2$, and CuSO_4) as Cu^{2+} ions can be analyzed especially by electron paramagnetic resonance spectroscopy (EPR), resolving the nature of adsorptive-adsorbent interaction. We analyzed the adsorption process by ICP-OES spectroscopy and afterwards studied the samples using EPR spectroscopy, wide-angle XRD, FTIR and SEM-EDX measurements to clarify the structure of the adsorbed phases and propose an adsorption mechanism. We are the first to analyze a two-step uptake of Cu^{2+} , caused by both adsorption and surface precipitation with a detailed insight into the partaking equilibria. On this basis, we proposed an adsorption mechanism, pointing out the influence of mono- and bivalent anions as well as the adsorbents porosity on the process. From these in-depth analyses, we are able to propose a new combination of adsorption isotherm for the modeling of the two-step uptake with meaningful insights into the two processes.

2. *Materials and methods*

2.1. *Materials*

2.1.1. *PMF particles*

For the synthesis of the PMF particles, melamine (Sigma-Aldrich, München, Germany, 99%), paraformaldehyde (Sigma-Aldrich, München, Germany, 95%), oxalic acid (Sigma-Aldrich, München, Germany, 99%), NaOH (Honeywell, Offenbach, Germany, $\geq 98\%$) and Ludox® HS-40 (Sigma-Aldrich, München, Germany, 40 wt.% in H_2O) were used as received without further purification. The synthesis was carried out in ultrapure water (see section 2.1.4).

2.1.2. *Metal salts*

For the adsorption experiments, CuSO_4 (anhydrous, p.a., $\geq 99.0\%$), CuCl_2 (dihydrate, reagent grade), and $\text{Cu}(\text{NO}_3)_2$ (trihydrate, p.a., $\geq 99.0\%$) were purchased from Sigma-Aldrich (Munich, Germany) and used as received without further purification.

2.1.3. *ICP-OES standard solutions*

For the ICP-OES measurements, the following standards were used: 10,000 mg/L P in H_2O (Bernd Kraft, Duisburg, Germany), 10,000 mg/L Cu in 2 mol/L HNO_3 (Bernd Kraft, Duisburg, Germany) and 9,998 mg/L S in H_2O (Sigma-Aldrich, Munich, Germany). $\text{HNO}_{3(\text{aq})}$ (65%, p.a.) was purchased from VWR (Darmstadt, Germany).

2.1.4. *Ultrapure water*

For all experiments, ultrapure water purified by a Milli-Q Advantage A10® system (Millipore, Darmstadt, Germany) (total organic carbon = 5 ppb, resistivity of 18.2 $\text{M}\Omega\cdot\text{cm}$ at 25 °C) was used.

2.2. Synthesis of the Poly(melamine-co-formaldehyde) particles

Different particles were synthesized either without hard templating (non-templated, N-PMF samples) or with a hard-templating approach, where H-PMF samples represent the obtained silica/PMF hybrid particles and P-PMF samples refer to the pure polymer PMF particles after template removal. Furthermore, the amount of water added to the reaction mixture was varied yielding in the numbers -0.5, -1.0 and -1.5 in the sample names. Here, the Suffix -1.0 corresponds to 500 mL (100%) water in the synthesis. From this, the volume of water as dispersant was varied by multiplication with the factor 0.5 or 1.5 for the PMF-0.5 and PMF-1.5 samples, respectively. The used reactants and volumes can also be seen in Table 7.1. The synthesis with the hard templating approach thereby was carried out as recently published [5,6] with minor modifications.

Table 7.1. Overview of the reactants (melamine (M), paraformaldehyde (F), and Ludox® HS-40 (HS-40)) used for the synthesis with the respective pH values of the reaction mixtures. The synthesis varied in the addition of Ludox® HS-40 as template and the water content. Non-templated samples without the addition of Ludox® HS-40 were labeled as N-PMF. Samples containing Ludox® HS-40 in the reaction mixture were labeled as H-PMF and P-PMF. H-PMF stands for the hybrid (H-) material containing PMF and SiO₂ particles. After the removal of the SiO₂ particles from the hybrid material, the pure PMF polymer (P-PMF) remains.

Sample	m (M)	m (F)	m (HS-40)	V (water)	pH (HS-40) ^a	pH ^b	pH ^c
N-PMF-0.5	6.5 g	9.25 g	0 g	62.5 + 187.5 mL	--	1.48	2.93
N-PMF-1	6.5 g	9.25 g	0 g	125.0 + 375.0 mL	--	1.74	3.04
N-PMF-1.5	6.5 g	9.25 g	0 g	187.5 + 562.5 mL	--	1.83	3.37
H-/ P-PMF-0.5	6.5 g	9.25 g	30 g	62.5 + 187.5 mL	9.8	1.74	3.41
H-/ P-PMF-1	6.5 g	9.25 g	30 g	125.0 + 375.0 mL	9.8	1.98	3.48
H-/ P-PMF-1.5	6.5 g	9.25 g	30 g	187.5 + 562.5 mL	9.8	2.05	3.61

^apH of the pure Ludox® HS-40 solution.; ^bpH of the dispersion ultrapure water, oxalic acid and Ludox® HS-40 solution. ^cpH of the final reaction mixture after 24 h at 100 °C under reflux.

2.2.1. Synthesis of N-PMF-1.0, N-PMF-0.5 and N-PMF-1.5

6.5 g (51.6 mmol) melamine (M) and 9.29 g (309.4 mmol) paraformaldehyde (F) were dispersed in ultrapure water (125 mL for N-PMF-1, 62.5 mL for N-PMF-0.5 and 187.5 mL for N-PMF-1.5) in a 1 L round bottom flask. The dispersion was stirred at 50 °C for 40 min. Subsequently, a solution of 1.0 g (11.1 mmol) oxalic acid in ultrapure water (375 mL for N-PMF-1, 187.5 mL for N-PMF-0.5 and 562.5 mL for N-PMF-1.5) was prepared and added to the reaction mixture. The resulting mixture was then stirred for 24 h at 100 °C under reflux. Afterwards, the resulting solid was transferred into a 1 L vessel with ultrapure water. For three times, this vessel was filled to a total volume of 1 L with ultrapure water and shaken for 24 h at room temperature. Subsequently the particles were decanted and freeze-dried.

2.2.2. *Synthesis of H-PMF and P-PMF samples*

The synthesis with the hard templating approach was carried out as recently published [5,6] with minor modifications.

In the first step of the synthesis of H-PMF-1 and P-PMF-1, 6.5 g (51.6 mmol) melamine (M) and 9.29 g (309.4 mmol) paraformaldehyde (F) were dispersed in 125 mL ultrapure water in a 1 L round bottom flask. The dispersion was stirred at 50 °C for 40 min. For H-PMF-1, a solution 1.0 g (11.1 mmol) oxalic acid in 375 mL ultrapure water was added to the reaction mixture. Then, a solution of 375 mL ultrapure water with 1.0 g (11.1 mmol) oxalic acid, and 30.0 g Ludox® HS-40 was prepared and then added to the reaction mixture.

The syntheses of H-PMF-0.5, and H-PMF-1.5 were modified from the synthesis described above by varying the volume of water used by a factor of 0.5 and 1.5, respectively. An overview of all reactants is presented in Table 7.1.

After the synthesis, the purification steps for H-PMF and P-PMF differed because for the P-PMF samples the templated was removed as well.

Purification of H-PMF samples: The sediment was transferred into a 1 L vessel with ultrapure water. For three times, this vessel was filled to a total volume of 1 L with ultrapure water and shaken for 24 h at r.t.. Subsequently, the particles were decanted and freeze-dried.

Purification of P-PMF samples: To obtain the porous P-PMF particles, the sediment of the respective reaction mixture was transferred into a 1 L vessel and filled with 1 M NaOH solution to remove the silica particles. The solution was shaken for 24 h and subsequently, the supernatant was discarded after sedimentation. The washing procedure with 1 M NaOH was repeated two more times. The particles were then transferred to a Spectra/Por™ 2 dialysis bag with 12 – 14 kDa molecular weight cut-off (Spectrum Chemical Mfg. Corp., New Brunswick, USA) and dialyzed with ultrapure water. The resulting particles were freeze-dried.

2.2.3 *Synthesis of $[\text{Cu}_4(\text{SO}_4)(\text{OH})_6]$*

The mineral brochantite $[\text{Cu}_4(\text{SO}_4)(\text{OH})_6]$ was synthesized as published by Dabinett et al. [32] for comparison with the formed surface precipitate.

2.3. Methods

Thermogravimetric analysis (TGA) was performed by using the device 1 Star System from Mettler Toledo, Gießen, Germany. The measurements were carried out with approximately 5 to 8 mg of the sample in a platinum crucible. The investigated temperature range was from 25 °C to 1000 °C with a heating rate of 10 °C/min, under air atmosphere at a flow rate of 40 mL/min.

Scanning electron microscopy (SEM) was carried out using a SEM Ultra Plus from Carl Zeiss Microscopy GmbH, Oberkochen, Germany. For this purpose, the samples were fixed with double-sided adhesive carbon tape on an aluminum pin sample tray and afterwards streamed

Adsorption vs. Surface Precipitation of Cu²⁺ onto Porous Poly(melamine-co-formaldehyde) Particles

with N₂ to obtain only a thin layer of particles. The samples were then sputtered with 3 nm of platinum using a Sputter Coater SCD050 from Leica Microsystems, Wetzlar, Germany before the investigation starts. The measurements were carried out with an acceleration voltage of 3 keV at different magnifications.

Transmission electron microscopy (TEM) was carried out using a Libra 120 device from Carl Zeiss Microscopy GmbH, Oberkochen, Germany. The acceleration voltage was 120 keV. The studied particles were dispersed in ultrapure water and dripped onto a carbon coated Cu mesh.

Particles sizes were analyzed using a Mastersizer 3000 (Malvern, Kassel Germany). The samples were dispersed with ultrasonic in ultrapure water (0.1 g/100 mL). The data was evaluated using the model "Polydisperse" and "OHD" (Particle RI: 1.5, Abs.: 0.1000 and Dispersant RI: 1.3300).

Particle size distribution measurements of the reaction mixture were performed by Zetasizer Nano ZS (Malvern, Kassel Germany). The dispersion Ludox-HS40, oxalic acid and ultra-pure water was prepared as stated in chapter 2.3.1 for each sample. After the preparation, the dispersion was stirred for 15 min before measurement. The samples were partly filtered with an 0.2 µm syringe filter (polyethylenesulfone). Data was evaluated using Particle RI: 1.5, Abs.: 0.1000 and Dispersant RI: 1.3300.

Nitrogen and CO₂ sorption measurements were performed using the Autosorb iQ MP from Quantachrome Instruments, Boynton Beach, USA. Samples were activated by degassing in vacuum (5×10^{-10} mbar) at 110 °C for 24 h. The nitrogen sorption measurements were performed at 77 K. The surface area was calculated in the relative pressure (p/p_0) range from 0.07 to 0.22 by BET method [33,34]. The pore size distribution (PSD) was analyzed by a QSDFT model fit for adsorption of N₂ onto carbon, considering spherical, cylindrical and slit pores. CO₂ sorption measurements were performed at 273 K.

Attenuated total reflection infrared spectroscopy (ATR-FTIR) measurements were performed using a Tensor 27 device equipped with a Platinum ATR module both from Bruker Corporation, Billerica, USA. All samples were measured in dry state with a resolution of 2 cm⁻¹ and with 50 scans. The acquired spectra were subjected to an atmospheric compensation to remove the rotation bands of water. Further, all spectra were normalized using the triazine ring-bending band at 812 cm⁻¹.

Inductively coupled plasma optical emission spectrometry (ICP-OES) (iCAP 7400 from Thermo Scientific) was used to determine the copper, sulfate and phosphate ions concentration in simulated water. Thus, 5 standards whereby both Cu and S had the following concentrations: Standard 1: 2500 mg/L, standard 2: 1250 mg/L, standard 3: 625 mg/L, standard 4: 312.5 mg/L, standard 5: 156.25 mg/L. Each standard contained 4 wt.% HNO₃. From the threefold measurement of all standards, a linear calibration curve was determined. To

Adsorption vs. Surface Precipitation of Cu²⁺ onto Porous Poly(melamine-co-formaldehyde) Particles

each sample (8 mL) was added 2 mL 20 % nitric acid prior to analysis. All samples have been measured three times. The given detection limits were calculated by the software Qtegra™ from Thermo Scientific, Waltham, USA. The detection limits in the measurement solutions were given with 0.01 mg/L Cu, and 0.01 mg/L for S.

UV/Vis spectroscopy was performed for the determination of nitrate and chloride concentrations. Therefore, the UV-Vis-spectrophotometer DR6000 (Hach Lange GmbH, Germany) was used together with the respective cuvette test kits (LCK 340 for nitrate and LCK 311 for chloride). The samples were processed as stated in the test kit manual.

Scanning electron microscope with energy-dispersive X-ray spectroscopy (SEM-EDX): The elemental mapping of the samples after adsorptions was carried out using a Phenom XL Workstation from Thermo Scientific (Waltham, USA) with an energy-dispersive X-ray spectroscopy detector (Silicon Drift Detector SDD, thermoelectrically cooled (LN₂free), 25 mm² detector active area). The samples were fixed on a double sided adhesive carbon tape on an aluminum pin sample tray. The measurements were carried out in high vacuum mode ($p = 0.1$ Pa) with an acceleration voltage of 10 keV at different magnifications.

pH measurement: The measurement of pH was carried out with the device SevenExcellence from Mettler Toledo (Gießen, Germany) at room temperature.

Centrifugation: The adsorber materials were separated from their supernatants by centrifugation with the device 5804 from Eppendorf (Leipzig, Germany) at room temperature and 10000 rpm.

Elemental analysis was carried out using a vario MICRO cube from the company Elementar, Langenselbold, Germany.

Powder X-ray diffraction (XRD): XRD patterns were recorded using a Bruker D8 Discover diffractometer (Bruker, Karlsruhe, Germany) with a Cu Twist tube ($\lambda = 0.154018$ nm, operating at 40 kV and 40 mA) in reflection mode with a zero-background silicon specimen holder. The diffraction patterns were recorded with a VÅNTEC-500 2D detector using a sample-to-detector distance of 149.8 mm. The pattern of each sample (from 10° to 65°) was measured in two steps (step 1: $\Theta = 5^\circ$, detector (middle) = 20°, $2\Theta = 25^\circ$; step 2: $\Theta = 12.5^\circ$, detector (middle) = 37.5°, $2\Theta = 50^\circ$) with a detection time of 30 min/step. The diffraction patterns were integrated, combined and then displayed as plot of the intensity as a function of 2Θ .

The reference reflexes were calculated from ICSD using POWD-12++.

Electron paramagnetic resonance (EPR) spectra (X-band) were recorded on an EMX-plus spectrometer (Bruker BioSpin, Billerica, MA, USA), equipped with the resonator ER 4119 HS-W1, and the variable temperature unit ER4141VT. The spectra were recorded at room temperature. Acquisition parameters were sweep width of 2000 G, microwave power of 2 mW, modulation frequency of 100 kHz, modulation amplitude of 10 G, time constant of 10.24

ms, conversion time of 40.96 ms, 16 scans, and 1024 data points. All spectra were normalized by the receiver gain and the quotient of sample mass and filling level.

2.4. Water treatment experiments

2.4.1. Adsorption experiments with copper(II) salt solutions

100 mg of the adsorber material was placed into a 50 mL centrifuge tube. Subsequently, 30 mL of the adsorptive solution of distinct concentration was added to every sample. If not stated differently, the pH of the samples was not adjusted. The samples were then magnetically stirred for 24 h at rt. Afterwards, the samples were centrifuged for 12 min at 10000 rpm. The supernatant of the samples after the adsorption and the initial concentrations of the adsorptive solutions were analyzed by ICP-OES. The pH of the solutions were determined.

2.4.2. Theoretical model

To determine the sorption efficiency of the PMF samples, the concentration of the adsorbed ions in equilibrium were detected by ICP-OES or UV/Vis spectroscopy. In equation (7.1), these concentrations were used for the calculation of the adsorption in percent. Thereby, c_0 is the concentration of the respective ion in the initial solution and c_{eq} is the concentration after reaching equilibrium.

$$\text{adsorption (\%)} = 100\% \cdot \frac{c_0 - c_{eq}}{c_0} \quad (7.1)$$

The respective sorption capacity q_{eq} in equilibrium was calculated as follows:

$$q_{eq} = \frac{(c_0 - c_{eq}) \cdot V_L}{m_A} \quad (7.2)$$

V_L is referring to the given volume of the adsorptive solution and m_A to the mass of the sorbent material used in the experiment.

To model the adsorption process, the Langmuir (Eq. 7.3) [35] and the Dubinin-Radushkevich isotherm models (Eq. 7.4 – 7.6) [36] were chosen. In general, non-linear equations were applied for the fitting, as linearization is known to change dependent and independent variables as well as transforming potential errors in unpredictable manner by e.g. logarithms [37–39]. The fitting was carried out in Origin 2022, using the Levenberg-Marquardt algorithm until $\chi \leq 10^{-9}$ or χ no longer changed.

Langmuir model:

$$q_{eq} = \frac{Q_m \cdot K_L \cdot c_{eq}}{1 + K_L \cdot c_{eq}} \quad (7.3)$$

K_L thereby represents the Langmuir equilibrium constant and Q_m the maximum adsorption capacity [40–42].

Dubinin-Radushkevich model:

$$q_{eq} = Q_m \times \exp(-\beta_{DR} \times \varepsilon^2) \quad (7.4)$$

Q_m refers to the maximum adsorption capacity, β_{DR} is the activity coefficient and ε is the adsorption potential [40–42]. As pointed out by Zhou, the adsorption potential can be exchanged with $\varepsilon = RT \times \ln\left(1 + \frac{1}{c_{eq}}\right)$, when two necessities are met: First, using a mol/L concentration for modelling is mandatory, second, it is only possible for values of c_{eq} that are several orders of magnitudes smaller than c_s . With that, equation 7.6 is obtained, which was used for modelling.

$$q_{eq} = Q_m \times \exp\left(-\beta_{DR} \times \left(RT \times \ln\left(1 + \frac{1}{c_{eq}}\right)\right)^2\right) \quad (7.5)$$

Via equation 7.6, the mean free energy of adsorption can be calculated [40–42].

$$E_{ads,DR} = \frac{1}{\sqrt{2 \times \beta_{DR}}} \quad (7.6)$$

For the surface precipitation step, a combination of the Langmuir isotherm and a sigmoidal Boltzmann equation (Eq. 7.7) [43] was used. The background for this is presented in section 3.2.3. For modelling, the Langmuir parameters were fitted first, then inserted as constants into this equation:

$$q_{eq} = Q_{m,L} + \frac{\left(\frac{Q_{m,L} \cdot K_L \cdot c_{eq}}{1 + K_L \cdot c_{eq}} - Q_{m,B}\right)}{1 + \exp\left(\frac{c_{eq} - c_P}{dc}\right)} \quad (7.7)$$

3. Results and discussion

The aim of our study is the investigation of the occurring adsorption equilibria of solved heavy metal ions and their respective anions in the presence of poly(melamine-co-formaldehyde) (PMF). Therefore, we prepared PMF particles in a dispersion polymerization in water. We synthesized different PMF particles by firstly using three different amounts of water as dispersant and secondly by application of a hard templating approach to the synthesis with SiO₂ nanospheres. Three non-templated N-PMF particles were compared to the three respective templated counterparts, which yielded highly porous PMF particles after etching with NaOH (P-PMF). By contrasting the porosity and morphology of the prepared particles, we have drawn conclusions about the particle and pore formation mechanism.

In batch adsorption experiments with solutions of different copper(II) salts, we analyzed competing equilibria of adsorption and surface precipitation of Cu²⁺ in dependence of the surface and pore morphology. Furthermore, we introduce a new mathematical model for the

two competing processes in one equation. This is in detail investigated and strongly supported by EPR spectroscopy and XRD analyses.

3.1. Synthesis and characterization of the PMF particles

The chemical structure of the PMF particles was analyzed by ATR-FTIR, EA, and TGA. The PMF structure was confirmed by the typical bands in ATR-FTIR spectra (compare Figure S1–S3) [1,44,45] and characteristic elemental composition, derived from EA (see Table S1). In TGA measurements (see Figure S4 – S6), the decomposition steps of PMF resin agree with literature [46–48]. In WAXS measurements, all samples showed a broad amorphous peak (Figure S11). A detailed evaluation of the ATR-FTIR, TGA, and EA measurements can be seen in the SI in the respective sections.

As the pore formation and achieved pore system is decisive for the adsorption characteristic later on, we first evaluated the hard templating and template removal process by TGA measurements, while the obtained pore structure itself was analyzed by N₂ and CO₂ sorption as well as electron microscopy.

From TGA, the residual mass of the H-PMF particles at 1000 °C shows the inclusion of SiO₂ NPs into the resin, with residual masses of 39 wt.% for H-PMF-0.5 and 55 wt.% for both H-PMF-1.0 and H-PMF-1.5, respectively (see Figure S4). Since the added amount of SiO₂ NPs to the reaction mixture was for all three samples constant, less SiO₂ NPs for H-PMF-0.5 were incorporated. In contrast, N-PMF and P-PMF samples showed no residual mass. Thus, both the hard templating process and the removal of the template by NaOH etching were successful.

To investigate the formed pore structure and potential differences between the nine samples, N₂ and CO₂ sorption experiments were conducted (see Figure 7.1 and Table 7.2).

All H-PMF samples featured a type II isotherm indicating a mainly non-porous character [33,34] with an insignificant amount of unordered mesopores, matching the low specific BET surface areas below 70 m²/g. In the H-PMF samples, unordered mesopores could be present due to aggregated silica template particles (see Table 7.2), which is in agreement with literature [6,49,50]. After template removal, the P-PMF samples exhibited N₂ sorption isotherms with the type IV (H1) character resulting in a mesoporous pore structure [33,34] with a defined pore size and a well accessible and connected pore system. The pore size distribution features a relatively narrow peak for pore diameters of approximately 17 nm, matching the diameter of used silica template nanoparticles (12 nm) [49]. Furthermore, the results are in very good agreement with previous hard templating experiments with silica/PMF materials [2,5,6,9]. P-PMF-1.0 with a specific surface area of 421 m²/g possess the highest obtained surface area and therefore represents the optimum amount of water used for synthesis. In comparison, P-PMF-0.5 featured a significantly lower specific surface area 157

Adsorption vs. Surface Precipitation of Cu²⁺ onto Porous Poly(melamine-co-formaldehyde) Particles

m²/g showing the significant impact of the dispersant amount. Here, the amount of water added to the reaction mixture of P-PMF-0.5 was also leading to less incorporation of the SiO₂ NPs into the polymer matrix, shown in the TGA measurement (see Figure S5).

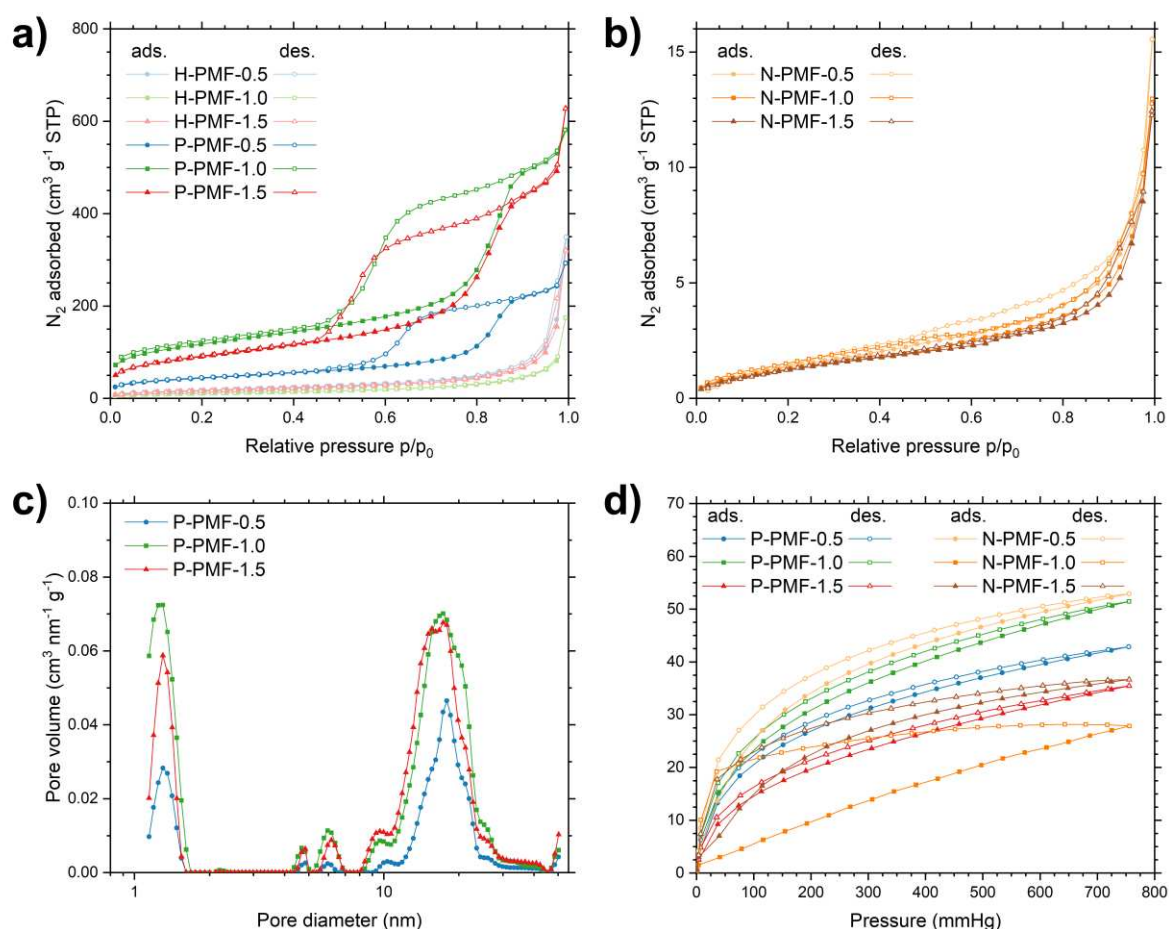


Figure 7.1. a) Nitrogen (N₂) de-/adsorption isotherms measured at 77 K for H-PMF and P-PMF samples, b) N₂ de-/adsorption isotherms measured at 77 K for N-PMF samples, c) Pore size distribution (PSD) analysis for the P-PMF samples, calculated from the adsorption branch by using QSDFT (quenched solid-state density functional theory) model for carbon with slit/cylindrical/sphere pores. d) Carbon dioxide (CO₂) de-/adsorption isotherms measured at 273 K for P-PMF and N-PMF samples. Carbon dioxide (CO₂) de-/adsorption isotherms measured at 273 K for H-PMF samples are shown in the SI. Data points in the adsorption and desorption branch of the isotherms are indicated by filled and empty symbols, respectively. P-PMF-0.5 is shown in dark blue with circles, H-PMF-0.5 in light blue with circles, H-PMF-1 in dark green with squares, H-PMF-1 in light green with squares, P-PMF-1.5 in red with triangles, H-PMF-1.5 in pink with triangles, N-PMF-0.5 in yellow with circles, N-PMF-1 in orange with squares, and N-PMF-1.5 in brown with triangles.

In contrast to the templated samples, the pure N-PMF samples featured a completely non-porous structure based on the N₂ sorption curves (see Figure 7.1b). As expected, specific surface areas below 10 m²/g were achieved for all N-PMF samples, which is why a templating process was applied to obtain the P-PMF samples. Additionally, the N-PMF and P-PMF samples were further investigated with CO₂ sorption measurements to get a deeper understanding of

Adsorption vs. Surface Precipitation of Cu²⁺ onto Porous Poly(melamine-co-formaldehyde) Particles

the pore structure and accessible functional groups for the water treatment applications. From all six investigated N-PMF and P-PMF samples, N-PMF-0.5 and P-PMF-1.0 featured the highest CO₂ adsorption with 2.36 mmol/g and 2.11 mmol/g, respectively, which is comparable to various triazine-based frameworks [51,52] and would present a potential starting point for CO₂ storage applications. All samples exhibited a bent curve progression with a small hysteresis except for N-PMF-1.0. N-PMF-1.0 possessed a linear adsorption branch and a huge hysteresis, which is why a different pore structure for N-PMF-1.0 can be expected. In general, all samples showed high CO₂ uptake indicating ultramicropores in the PMF particles and a high affinity for CO₂ due to the high amount of nitrogen functionalities in the polymer.

Table 7.2. Surface area (S_{BET}), pore volume (PV), micro pore volume (MPV) and CO₂ uptake of the PMF samples.

Sample code	S_{BET} ($\text{m}^2 \text{g}^{-1}$) ^[a]	PV ($\text{cm}^3 \text{g}^{-1}$) ^[b]	MPV ($\text{cm}^3 \text{g}^{-1}$) ^[c]	CO ₂ uptake (mmol g^{-1})
H-PMF-0.5	67	0.20	0.02	n.a.
P-PMF-0.5	157	0.36	0.06	1.91
N-PMF-0.5	6	n.a.	n.a.	2.36
H-PMF-1.0	41	0.10	0.01	n.a.
P-PMF-1.0	421	0.79	0.16	2.11
N-PMF-1.0	5	n.a.	n.a.	1.24
H-PMF-1.5	62	0.18	0.02	n.a.
P-PMF-1.5	328	0.72	0.12	1.58
N-PMF-1.5	5	n.a.	n.a.	1.64

^[a]Surface area calculated from N₂ adsorption isotherm using BET equation. ^[b]Pore volume (PV) calculated from N₂ uptake at $p/p_0 = 0.95$. ^[c]Micro pore volume (MPV) calculated from N₂ uptake at $p/p_0 = 0.10$. ^[d]CO₂ uptake calculated for 273 K and 1 bar.

To assess visually the pore system, electron microscopic investigations with SEM and TEM imaging of the samples in native state as well as of thin sections were conducted (Figure 7.2, Figure S7 – S9). The analysis of H-PMF samples furthermore enabled assumptions about the particle formation mechanism. An overview of a larger amount of the thin section sample with more particles is given in the SI in Figure S7 – S9.

From SEM imaging of H- and P-PMF samples, it is visible in that uniform spherical particles were formed, which are loosely aggregated due to the drying process. From respective size measurement of 45 particles, P-PMF-0.5 particles show a mean particle size of 588 ± 81 nm, P-PMF-1.0 a mean size of 361 ± 51 nm and P-PMF-1.5 a mean size of 266 ± 58 nm. Furthermore, from SEM and TEM imaging it is visible that the particle size of the corresponding H- and P-PMF particles are matching, whereas when increasing the dispersant amount in the synthesis procedure, the mean particle size decreases. In general, the templated H- and P-PMF particles are not showing significant coalescence but a uniform particle diameter.

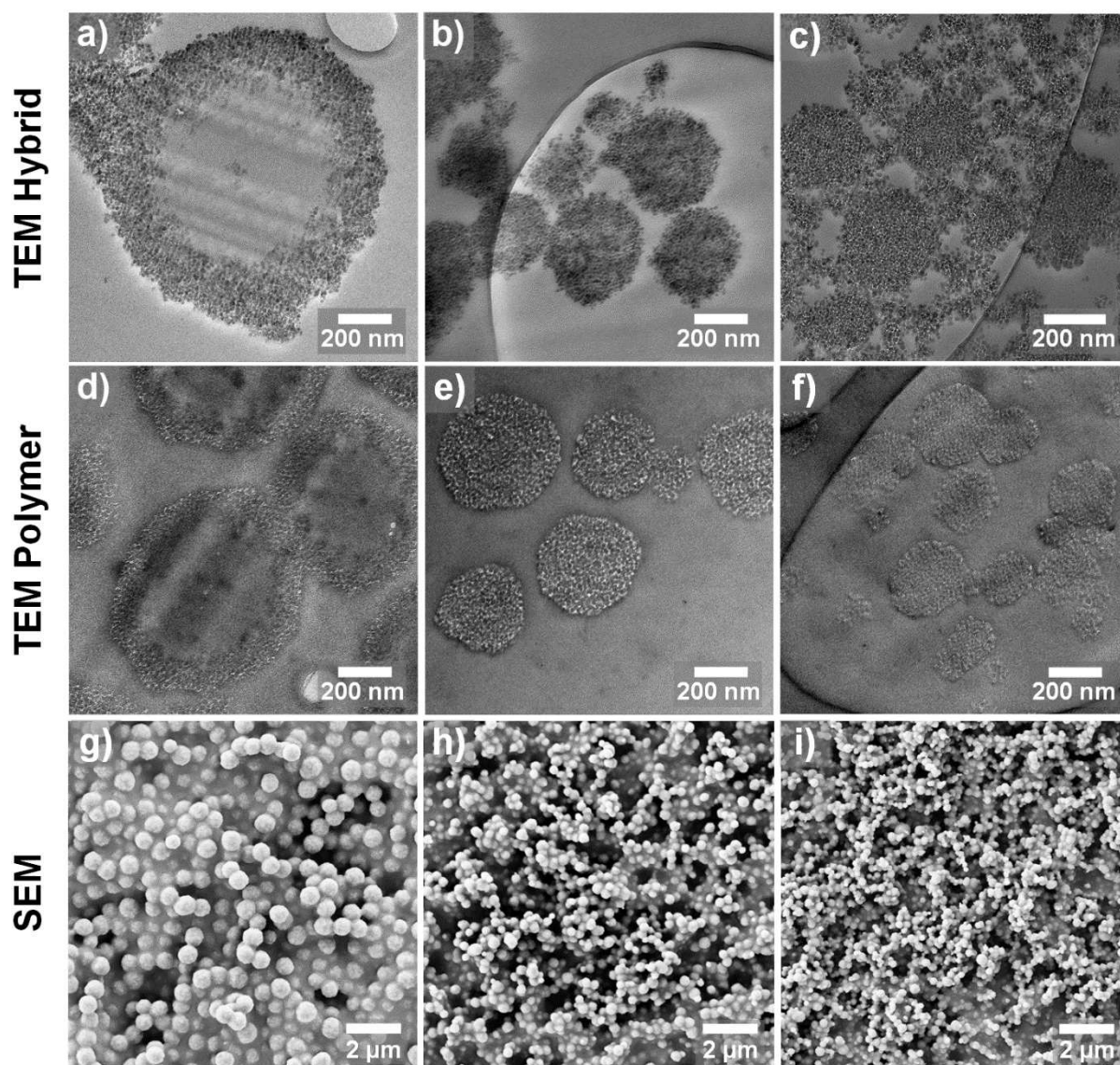


Figure 7.2. TEM imaging of thin sections of a) H-PMF-0.5, b) H-PMF-1.0, c) H-PMF-1.5, d) P-PMF-0.5, e) P-PMF-1.0, and f) P-PMF-1.5. g) SEM image of P-PMF-0.5, h) SEM image of P-PMF-1.0, and i) SEM image of P-PMF-1.5. Overview images of the H-PMF thin sections are given in Figure S7 – S9.

In the TEM thin sections of H-PMF-1.5 and H-PMF-1.0, we found that the particles are completely permeated with SiO_2 NPs across the entire cross-section of the particles. In contrast, the particles from H-PMF-0.5 visibly consist of three parts: In the middle, a core can be seen with several singly in PMF embedded SiO_2 NPs with a size of approximately 100 nm. Then, a shell of PMF resin without included silica is apparent, which is between 250 to 350 nm thick. On the outside, a shell made from PMF with incorporated SiO_2 NPs again can be seen. This is indicating that three differing steps in the particle formation of H-PMF-0.5 are occurring as it can be seen widely over the ultra-thin section sample. The formation of the pure PMF shell is leading to the incorporation of less SiO_2 NPs as seen from the TGA analysis and subsequently lower specific surface area seen from BET method. This PMF shell formation is

probably due to the significantly increased concentration of PMF precursor molecules, but further experiments are needed to clarify the driving force for the particle formation in detail.

The electron microscopy also supports the assumption that the SiO_2 NPs act as Pickering-like stabilizers at the interface between the hydrophobic resin and water [53,54], which prevent the coalescence of the particles in the synthesis effectively and contribute significantly to the formation of uniformly grown particles.

The N-PMF samples are showing a completely different morphology (see Figure 7.3). Here, the samples consist of intergrown, spherical particles whose size is in the micrometer range. It is visible that the size of the spherical primary particles decreases with increasing water amount from N-PMF-0.5 to N-PMF-1.5. This leads to the conclusion that the N-PMF particles formed spherical particles of the hydrophobic PMF resin to minimize the surface interaction to the continuous water phase, which do coalesce unjust upon contact in the progressing synthesis. The size of the primary particles in the aggregates is also strongly varying.

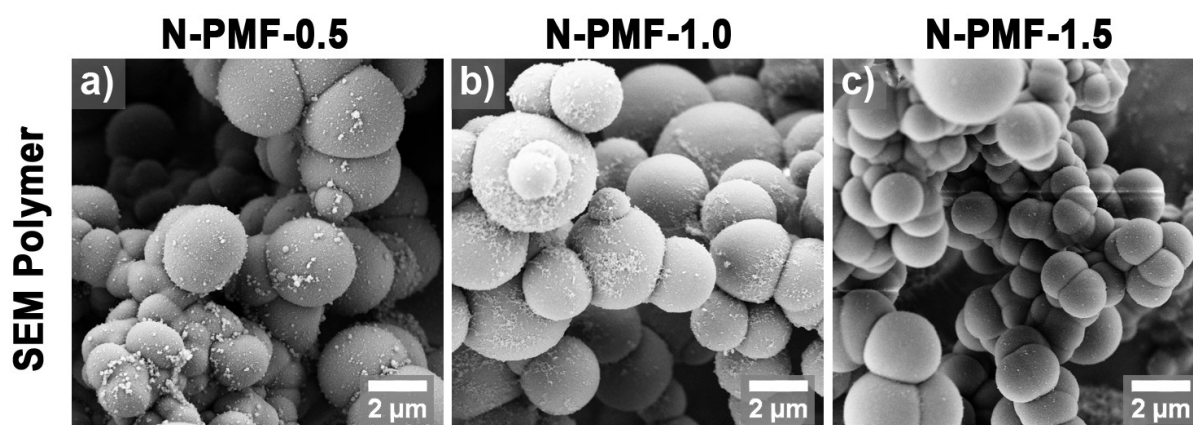


Figure 7.3. a) SEM image of N-PMF-0.5, b) SEM image of N-PMF-1.0, and c) SEM image of N-PMF-1.5.

3.2. Cu^{2+} uptake experiments

To investigate the adsorption process and distinguish the different pathways involved, we conducted batch adsorption experiments with three different copper(II) salts (CuSO_4 , $\text{Cu}(\text{NO}_3)_2$, and CuCl_2). We decided to investigate the adsorption of Cu^{2+} because of its paramagnetic properties, enabling the examination of the samples with EPR spectroscopy to determine the coordination environment of the metal ion after adsorption. After the initial adsorption experiments, the adsorbent samples of all experiments were separated from the supernatant, rinsed with ultrapure water and dried. Subsequently, the samples were then especially analyzed with WAXS, SEM-EDX and EPR spectroscopy to gain insights into the adsorption and precipitation mechanism.

We decided to test the three templated, porous samples and one non-templated sample (N-PMF-1.5) for a comparison of three different pore systems versus the only ultramicro-

Adsorption vs. Surface Precipitation of Cu^{2+} onto Porous Poly(melamine-co-formaldehyde) Particles

porous sample N-PMF-1.5. With this, we want to understand the dependence of the separation process on the adsorbent porosity.

3.2.1. Adsorption experiments with CuSO_4 solution

First, we chose to investigate the adsorption from CuSO_4 solutions with the samples as the divalent sulfate presented possibilities for an increased cooperative adsorption mechanism together with Cu^{2+} ions. The adsorption experiments were conducted with at 25 °C with a stirring time of 24 hours enabling diffusion into the pores of the P-PMF samples for equilibration (see Figure 7.4a and b).

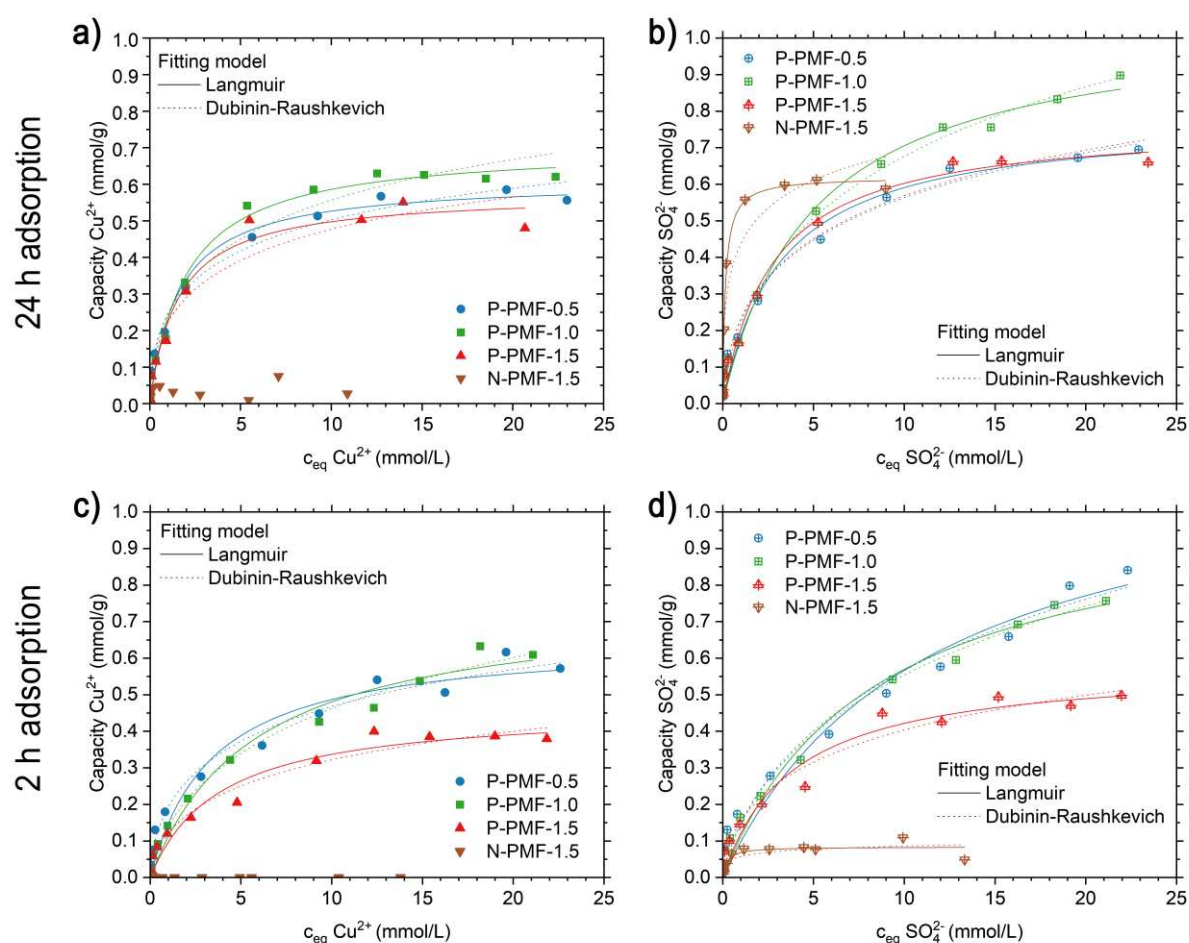


Figure 7.4. a) and b) Adsorption isotherms of a) Cu^{2+} and b) SO_4^{2-} onto P-PMF samples and N-PMF-1.5 from experiments with CuSO_4 solution after 24 h adsorption. c) and d) Adsorption isotherms of c) Cu^{2+} and d) SO_4^{2-} onto P-PMF samples and N-PMF-1.5 from adsorption experiments with CuSO_4 solution after 2 h adsorption. Data points for Cu^{2+} are displayed as filled squares and for SO_4^{2-} as crossed squares. Data points and isotherms for P-PMF-0.5 are shown in blue with circles, for P-PMF-1.0 in green with squares, for P-PMF-1.5 in red with triangles, and for N-PMF-1.5 in brown with triangles. The respective Langmuir isotherm fits are presented as solid lines and the Dubinin-Radushkevich isotherm as dotted lines of the corresponding color. The respective fitting parameters are displayed in Table S2. pH values before and after adsorption are presented in Figure S13.

From the adsorption isotherms of Cu^{2+} and SO_4^{2-} , a higher uptake of sulfate ions than Cu^{2+} ions was achieved for all P-PMF samples, which is indicating higher affinity for sulfate adsorption. The plateau for the Cu^{2+} uptake is relatively similar for the three P-PMF- samples and lies approximately between 0.5 mmol/g (for P-PMF-1.5) and 0.6 mmol/g (for P-PMF-1.0). The achieved capacities for sulfate adsorption for P-PMF-0.5 and P-PMF-1.5 are very similar with values around 0.65 mmol/g, while P-PMF-1.0 achieved an uptake up to 0.9 mmol/g and still increases its uptake slightly over the tested concentrations. In contrast, N-PMF-1.5 shows a steep uptake of sulfate ions, reaching its plateau around $q_{\text{eq}} = 0.6$ at initial sulfate concentrations of approximately $c_0 = 2$ mmol/L. The adsorption of Cu^{2+} ions is insignificant with values around 0.05 mmol/g or below. It is also visible that initially the uptake of Cu^{2+} is relatively steep up to an initial concentration of 0.5 mmol/L whereas this value decreases with further increasing Cu^{2+} concentration. Here, the adsorption of sulfate and Cu^{2+} ions is potentially competitive, which leads to the displacements of Cu^{2+} ions from adsorption sites.

The adsorptions isotherms were fitted using the Langmuir and the Dubinin-Radushkevich models (Fitting parameters given in Table S2). In general, very good fits are seen for both isotherms, whereby Dubinin-Radushkevich in most cases has a higher correlation, seen from the coefficient of determination, R^2 . The derived maximum adsorption capacities from the Langmuir model are consistent with the leveling of the experimental values, whereas for Dubinin-Radushkevich, Q_m values seem slightly overestimated. Nonetheless, from the activity coefficient β_{DR} the mean free energy of adsorption $E_{\text{Ads,DR}}$ can be derived (see Eq. 7.6). Here, sulfate is showing higher $E_{\text{Ads,DR}}$ values, lying between 10.6 to 9.9 kJ/mol, than for Cu, which range from 9.5 to 8.5 kJ/mol.

For N-PMF-1.5, only the sulfate isotherm was yielding meaningful fits in terms of the standard errors given for the respective parameters. The energy of adsorption for sulfate from the Dubinin-Radushkevich plot is showing a significantly higher value with 13.4 kJ/mol than for the P-PMF samples, indicating a high affinity of N-PMF-1.5 for sulfate.

As the uptake of Cu^{2+} and sulfate ions onto the porous P-PMF samples are relatively similar, we chose to further analyze the adsorbent materials to gain insight in the nature of adsorption. Therefore, the adsorbent samples were subsequently rinsed with ultrapure water and dried. We chose SEM-EDX elemental mapping to determine whether adsorption occurred over the entire sample surface and whether adsorption of Cu^{2+} and sulfate occurred for example locally separated. The elemental mapping of the P-PMF samples was conducted from experiments with initially 15.7 mmol/L Cu^{2+} , which is in the plateau region for the P-PMF samples (see Figure 7.5b-k). Here, the mapping showed a significant amount of Cu-rich, needle-like structures. In contrast, S was detected among the whole samples surfaces with only insignificant fluctuation among the sample. For N-PMF-1.5, the highest concentration was

Adsorption vs. Surface Precipitation of Cu^{2+} onto Porous Poly(melamine-co-formaldehyde) Particles

analyzed ($c_0 = 11.8 \text{ mmol/L}$), which showed a homogeneous distribution of both, Cu and S, whereby Cu is distinctly less occurring (Figure S18).

From subsequent WAXS measurements, we found that the Cu-rich, needle-like structures were crystalline in the samples at initial concentrations of $15.7 \text{ mmol/L Cu}^{2+}$ (Figure 7.5a). The crystalline species was assigned to $[\text{Cu}_4(\text{SO}_4)(\text{OH})_6]$, a non-water-soluble hydroxide species, which is found surface precipitation process. This precipitation is induced by the PMF resin that releases hydroxide ions from the protonation of its high amount of amino groups. This can be also seen from the equilibrium pH values after adsorption (Figure S12). Interestingly, Cu^{2+} is precipitated as a cluster together with sulfate instead of the pure $\text{Cu}(\text{OH})_2$ species. To see, from which concentration crystalline precipitate occurred, WAXS measurements along the P-PMF-1.0 isotherm were conducted as this sample showed the highest uptake. These WAXS measurements showed that crystalline species were also detectable at concentrations as low as $0.4 \text{ mmol/L Cu}^{2+}$, which means that precipitation is beginning at extremely low concentrations (see Figure S20). It is noteworthy that the crystalline species found at 0.4 mmol/L was assigned to $[\text{Cu}_4(\text{SO}_4)(\text{OH})_6(\text{H}_2\text{O})]$. At $1.6 \text{ mmol/L Cu}^{2+}$, crystalline reflexes of both $[\text{Cu}_4(\text{SO}_4)(\text{OH})_6]$ and $[\text{Cu}_4(\text{SO}_4)(\text{OH})_6(\text{H}_2\text{O})]$ were detectable, showing the transition to $[\text{Cu}_4(\text{SO}_4)(\text{OH})_6]$ for higher concentrations.

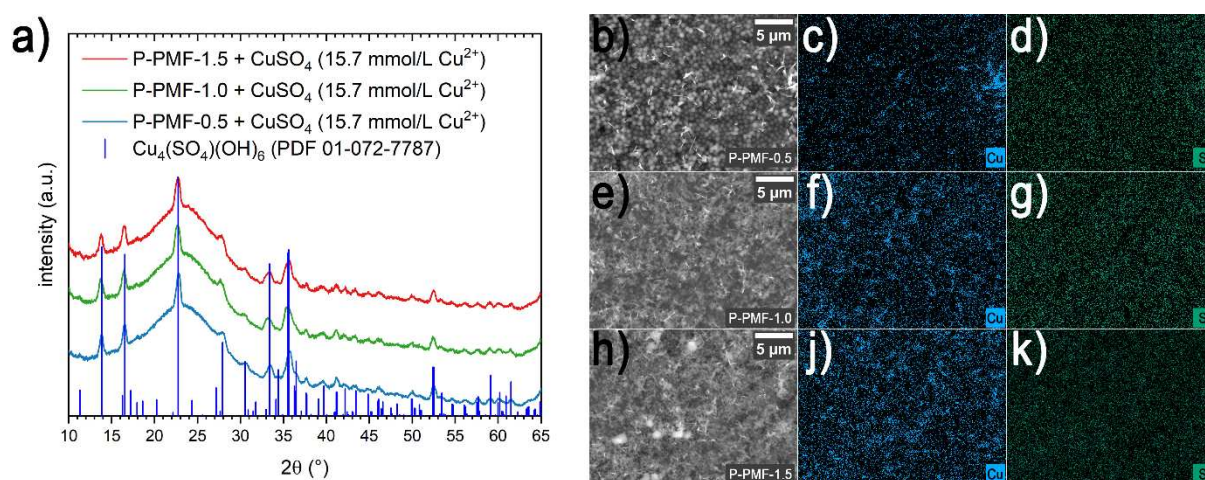


Figure 7.5. a) WAXS diffractogram of P-PMF samples after adsorption experiments with CuSO_4 solution ($c_0 = 15.7 \text{ mmol/L Cu}^{2+}$) and equilibration time of 24 h shown together with the reference reflexes of the identified $\text{Cu}_4(\text{SO}_4)(\text{OH})_6$ species [55]. P-PMF-0.5 is shown in blue, P-PMF-1.0 in green and P-PMF-1.5 in red. b) – k) SEM-EDX images of the P-PMF samples after adsorption (CuSO_4 , $c_0 = 15.7 \text{ mmol/L Cu}^{2+}$) with b) SEM image of P-PMF-0.5 after adsorption with the respective elemental mapping for c) Cu and d) S, e) SEM image of P-PMF-1.0 after adsorption with the respective elemental mapping for f) Cu and g) S, and h) SEM image of P-PMF-1.5 after adsorption with the respective elemental mapping for j) Cu and k) S.

The WAXS measurement of the non-templated N-PMF-1.5 sample showed no crystalline reflexes (see Figure S18), which is in accordance with the mapping from SEM-EDX. We can

conclude that porosity and specific surface area are decisive for the precipitation reaction and the achieved uptake.

As the porosity and specific surface area is significantly influencing the Cu^{2+} precipitation as seen by the comparison from N-PMF-1.5 to the different P-PMF particles, we analyzed the pore structure of the P-PMF adsorbent samples after the Cu^{2+} and sulfate uptake by N_2 sorption (see Figure S19). It can be seen that the specific surface area is not reduced by the precipitate indicating that the precipitation is taking place outside of the particles, not blocking the pore system. These findings are further supported by EFTEM analysis of thin sections of the P-PMF-0.5 sample as example after adsorption (Figure S19), which show that Cu is only found outside the particles as clusters in crystalline structures.

EPR is a powerful tool for investigating the immediate environment of paramagnetic Cu^{2+} species. Figure 7.6 shows EPR spectra of PMF samples after adsorption experiments with CuSO_4 solutions of different concentrations. The results indicate the presence of Cu^{2+} ions in the PMF samples. The amount of Cu^{2+} ions in the N-PMF sample is greater than in the P-PMF samples for both concentrations. For reasons of comparability, we synthesized brochantite, $\text{Cu}_4(\text{SO}_4)(\text{OH})_6$, by a known method [32]. In EPR spectroscopy, solid $\text{Cu}_4(\text{SO}_4)(\text{OH})_6$ does not show any EPR signal in stark contrast to solid CuSO_4 , which was used for the adsorption experiments (Figure S21). The signals in Figure 7.6 are exclusively attributed to Cu^{2+} ions immobilized by chelation. The spectra shown in Figure 7.6 have anisotropic shape characteristic of monomeric Cu^{2+} ions in axial symmetry. The four lines in the parallel region arise from the hyperfine coupling of the electron spin ($S=1/2$) of the copper nucleus with its nuclear spin ($I=3/2$). The analysis of the spectra results in $g_{\text{p||}} = 2.30$ and $A_{\text{p||}} = 15$ mT for N-PMF-0.5. For the P-PMF samples, the values depend on the initial concentration of the Cu ions: $g_{\text{p||}} = 2.30$ and $A_{\text{p||}} = 15$ mT for 0.16 mmol/l and $g_{\text{p||}} = 2.35$ and $A_{\text{p||}} = 13$ mT for 15.7 mmol/l. The frozen hexaaqua complex of Cu^{2+} is known to have $g_{\text{p||}} = 2.40$, $A_{\text{p||}} = 11.4$ mT [56]. Differences in $g_{\text{p||}}$ and $A_{\text{p||}}$ arise from chelate complex formation with different numbers of oxygen- and nitrogen containing functional groups [57]. Here, lower $g_{\text{p||}}$ values correspond to a higher number of chelating amino groups. However, the lower intensities of the P-PMF sample's signals are arising from a lower amount of Cu^{2+} , which is bound via coordinative interactions as onto the N-PMF-1.5 sample. Potentially only the Cu^{2+} ions, which are bonded the strongest are not expelled from the adsorption sites. From the EPR spectra in general we can conclude that only a part of the Cu^{2+} species immobilized onto the P-PMF samples is assumed to be chelated by amino groups.

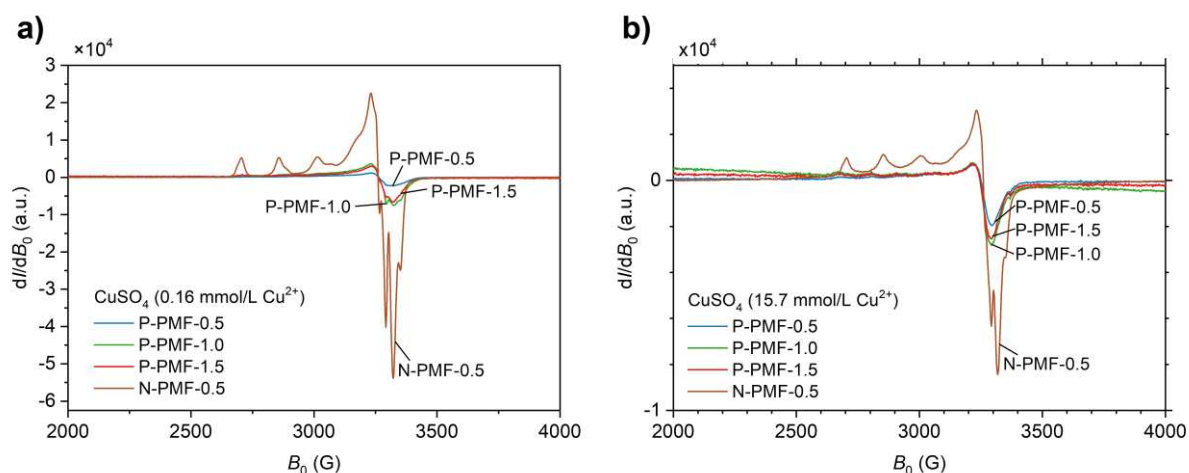


Figure 7.6. EPR spectra of the PMF samples after adsorption experiments with CuSO_4 solution containing a) 0.16 mmol/L Cu^{2+} and b) 15.7 mmol/L Cu^{2+} . P-PMF-0.5 is shown in blue, P-PMF-1.0 in green, P-PMF-1.5 in red, and N-PMF-1.5 is shown in brown.

To investigate the dynamics of precipitation, adsorption experiments with CuSO_4 solution were repeated with a decreased adsorption time of only 2 hours (see Figure 7.4c and d). Firstly, the general Cu^{2+} uptake of all P-PMF samples is in a similar range as for 24 h, indicating that the precipitation reaction and equilibration is taking place quite rapidly. While the uptake of both Cu^{2+} and sulfate is unchanged for P-PMF-1.0, P-PMF-0.5 exhibits an increased uptake of both and P-PMF-1.5 shows a decreased uptake. This trend is explainable, as the pores of P-PMF-0.5 are not reaching as deep into the particles, while P-PMF-1.0 and P-PMF-1.5 are completely permeated throughout their diameter. Hence, diffusion is facilitated for P-PMF-0.5. In the case of P-PMF-0.5, a later decrease of the Cu^{2+} and sulfate uptake may take place, as a partial dissolution of the precipitate is possible when the pH is equilibrating in the duration of 24 h.

The greatest differences can be seen by N-PMF-1.5, as its maximum adsorption capacity for sulfate (determined by the Langmuir fit) is only 0.1 mmol/g, indicating that equilibrium cannot be attained within 2 h although adsorption is localized on the outer particle surface.

From the dried adsorbent samples ($c_0 = 15.7$ mmol/L Cu^{2+}), crystalline reflexes of $\text{Cu}_4(\text{SO}_4)(\text{OH})_6$ were again detectable for all P-PMF samples (Figure S22). SEM-EDX analysis supports these findings (see Figure S22). After adsorption experiments with $c_0 = 1.57$ mmol/L, no significant reflexes were measurable. For N-PMF-1.5, no crystalline reflexes can be seen and in SEM-EDX elemental mapping, a homogeneous distribution of S was achieved. Cu was not detectable.

3.2.2. Adsorption experiments with $\text{Cu}(\text{NO}_3)_2$ solution

After we investigated the precipitation taking place in the presence of the divalent anion sulfate, further experiments with monovalent anions were conducted. As the first anion, nitrate was chosen and subsequently, adsorption experiments with $\text{Cu}(\text{NO}_3)_2$ solution were

conducted. From the respective isotherms of Cu^{2+} and NO_3^- ions, N-PMF showed a similar performance as for CuSO_4 solutions with a high uptake of anions and an insignificant uptake of Cu^{2+} . In strong contrast, we found a step-wise uptake of the P-PMF samples, which is dependent on the initial concentration of $\text{Cu}(\text{NO}_3)_2$ and the respectively attained equilibrium concentration (Figure 7.7). For Cu^{2+} , a first plateau of all samples extends from 0.4 mmol/L to approximately 2.5 mmol/L Cu^{2+} . After the subsequent uptake step (until Cu^{2+} equilibrium concentrations of up to 10 mmol/L), the second plateau is attained, whereby the value of the plateau is dependent on the sample. In the isotherm of NO_3^- , similar trends can be seen (Figure 7.7b), whereby the differences in the value for the first plateau as well as the concentration it spans varies more visible among the three P-PMF samples. A slight decrease of Cu^{2+} uptake can be seen in the range of the first plateau with increasing concentration. This is caused by the competition between Cu^{2+} complexation by non-protonated amines vs. the protonation of amines to enable ionic interaction towards NO_3^- ions.

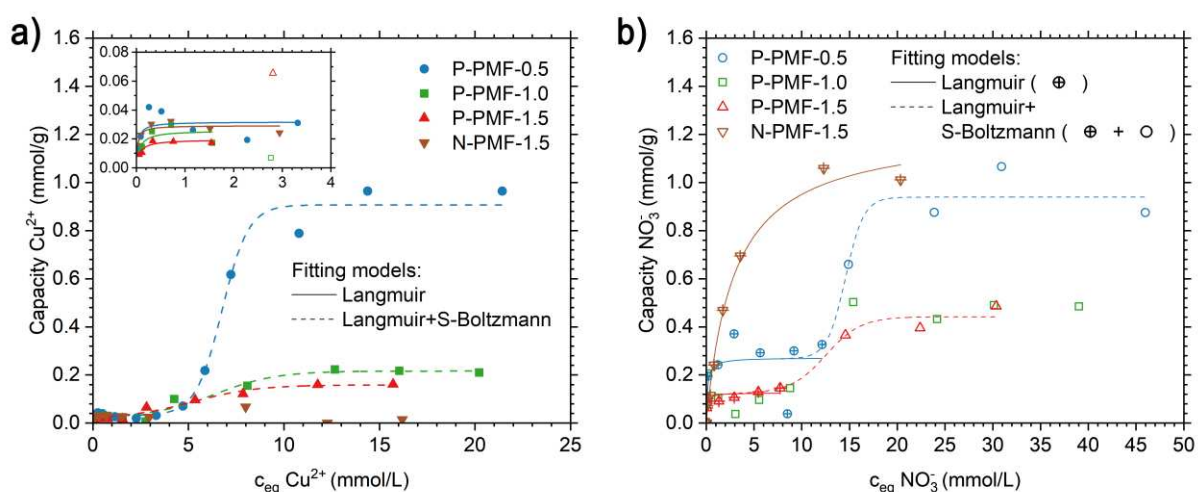


Figure 7.7. a) and b) adsorption isotherms of a) Cu^{2+} and b) NO_3^- onto P-PMF samples and N-PMF-1.5 from experiments with $\text{Cu}(\text{NO}_3)_2$ solution after 24 h adsorption. The inset in a) shows the respective data points for the lower concentration region and the respective Langmuir fitting. In general, data points for Cu^{2+} are displayed as filled symbols, whereas open symbols in the inset represent data points that were not included in the Langmuir fit but shown for clarity. In b), data points for NO_3^- are shown as open symbols, whereas the additionally crossed symbols were used for the Langmuir fitting. The Langmuir isotherms are shown as solid lines for both diagrams. The combined Langmuir/sigmoidal Boltzmann fit is shown as dashed line and all data points were used for this fit in both cases. Data points and isotherms for P-PMF-0.5 are shown in blue with circles, for P-PMF-1.0 in green with squares, for P-PMF-1.5 in red with triangles, and for N-PMF-1.5 in brown with triangles. The respective fitting parameters are displayed in Table 7.3. pH values before and after adsorption are presented in Figure S16.

This multi-step process seen by the porous samples cannot be modelled by e.g. the Langmuir isotherm. Therefore, we only used the respective points of the first uptake step and plateau into consideration for the fitting. The respective fits can be seen in the inset of Figure 7.7a or as enlarged version in Figure S14 and the fitting parameters are shown in Table 7.3.

Adsorption vs. Surface Precipitation of Cu^{2+} onto Porous Poly(melamine-co-formaldehyde) Particles

The achieved adsorption capacities show that nitrate is significantly more adsorbed onto the P-PMF samples, which strongly resembles the adsorption performance seen from N-PMF-1.5, although less uptake of nitrate is seen for P-PMF samples.

Table 7.3. Fitting parameters for Langmuir (L) isotherm fits for the adsorption of Cu^{2+} and NO_3^- ions from $\text{Cu}(\text{NO}_3)_2$ solution in the low-concentration region after 24 hours equilibrium time (Figure 7.7), respectively. Q_m thereby is the maximum sorption capacity, K_L is the Langmuir equilibrium constant R^2 (COD) is the coefficient of determination for the respective fit. For all parameters, the corresponding standard error from the fit is given.

Sample & Time	Model	Ion	Q_m mmol/g	K_L L/mmol	R^2 (COD)
P-PMF-0.5	L	Cu^{2+}	0.032 ± 0.005	31.44 ± 35.72	0.313
		NO_3^-	0.271 ± 0.047	7.54 ± 8.41	0.483
P-PMF-1.0	L	Cu^{2+}	0.026 ± 0.005	15.12 ± 13.9	0.574
P-PMF-1.5	L	Cu^{2+}	0.02 ± 0.002	14.92 ± 5.64	0.869
		NO_3^-	0.125 ± 0.014	10.74 ± 6.3	0.765
N-PMF-1.5	L	Cu^{2+}	0.029 ± 0.002	39.98 ± 20.18	0.703
		NO_3^-	1.227 ± 0.059	0.34 ± 0.05	0.989

To fully understand the underlying mechanic of the stepwise Cu^{2+} and NO_3^- uptake, we analyzed the adsorbents after the adsorption experiments, again with subsequent thorough rinsing with ultrapure water and drying to prevent crystallization from leftover supernatant. At concentrations of 15.7 mmol/L Cu^{2+} , crystalline reflexes are apparent, which can be attributed to $\text{Cu}_2(\text{NO}_3)(\text{OH})_3$ species (Figure 7.8). SEM-EDX mapping supported the findings as Cu was localized at spots of plate-like crystals apparent in the respective SEM images (Figure 7.8). In contrast, from adsorbents from initial Cu^{2+} concentration of 1.6 mmol/L, no crystalline reflexes were visible in WAXS diffractograms (see Figure S22).

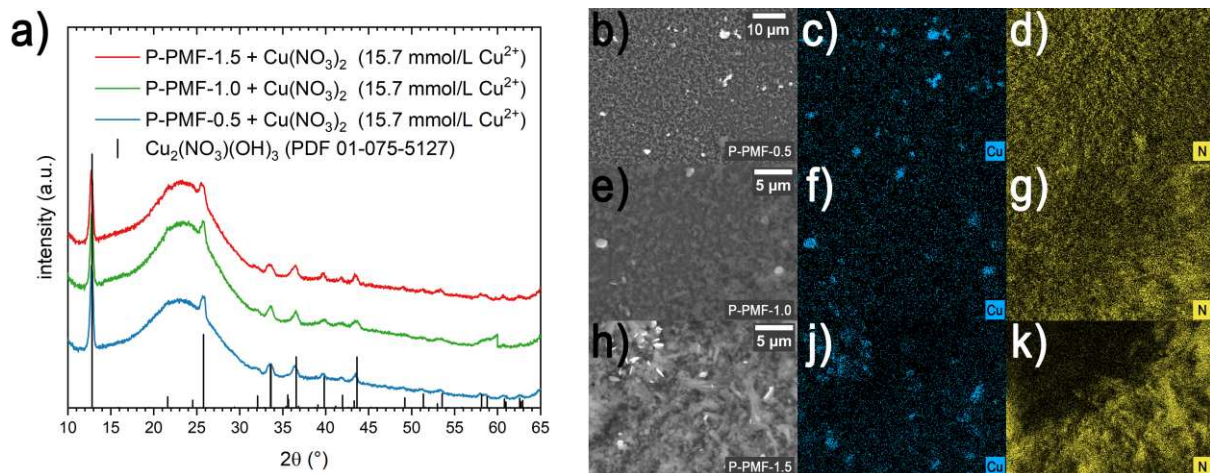


Figure 7.8. a) WAXS diffractogram of P-PMF samples after adsorption experiments with $\text{Cu}(\text{NO}_3)_2$ solution ($c_0 = 15.7$ mmol/L Cu^{2+}) and the reference reflexes of the identified $\text{Cu}_2(\text{NO}_3)(\text{OH})_3$ species [58]. P-PMF-0.5 is shown in blue, P-PMF-1.0 in green and P-PMF-1.5 in red. b) – k) SEM-EDX images of the

P-PMF samples after adsorption ($\text{Cu}(\text{NO}_3)_2$, $c_0 = 15.7 \text{ mmol/L Cu}^{2+}$) with b) SEM image of P-PMF-0.5 after adsorption with the respective elemental mapping for c) Cu and d) N, e) SEM image of P-PMF-1.0 after adsorption with the respective elemental mapping for f) Cu and g) N, and h) SEM image of P-PMF-1.5 after adsorption with the respective elemental mapping for j) Cu and k) N.

WAXS measurements of respective P-PMF-0.5 adsorbents from $\text{Cu}(\text{NO}_3)_2$ solution with initial concentrations of Cu^{2+} between 1.6 mmol/L and 15.7 mmol/L showed that crystalline reflexes were apparent from concentrations of 9.4 mmol/L and above (Figure 7.9). This coincides with the start of the second Cu^{2+} uptake step as well as the second uptake step of NO_3^- ions. Therefore, the use of Langmuir for the concentrations of $3.9 \text{ mmol/L Cu}^{2+}$ and below is justified.

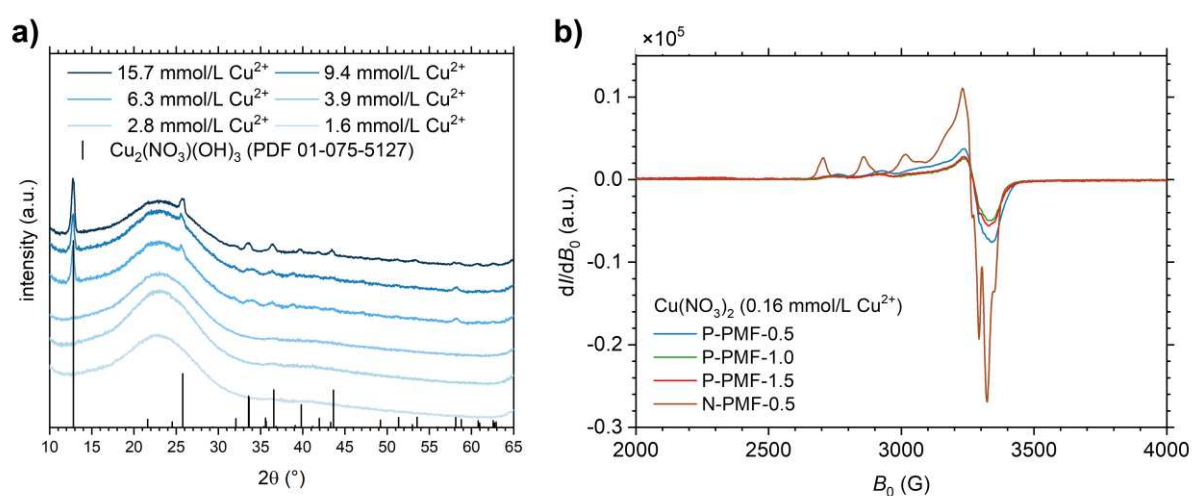


Figure 7.9. a) WAXS diffractogram of P-PMF-0.5 after adsorption experiments with $\text{Cu}(\text{NO}_3)_2$ solution at different concentrations (equilibration time 24 h) shown together with the reference reflexes of $\text{Cu}_2(\text{NO}_3)(\text{OH})_3$ (black) [58]. The diffractograms are presented in darker colors of blue for higher concentrations of Cu^{2+} . b) EPR spectra of the PMF samples after adsorption experiments with $\text{Cu}(\text{NO}_3)_2$ solution containing $0.16 \text{ mmol/L Cu}^{2+}$. P-PMF-0.5 is shown in blue, P-PMF-1.0 in green, P-PMF-1.5 in red, and N-PMF-1.5 is shown in brown.

The EPR spectra of PMF samples after adsorptions experiments with $\text{Cu}(\text{NO}_3)_2$ solutions plotted in Figure 7.9b also show the presence of chelated Cu^{2+} ions. As in the case of copper sulfate, the spectrum of N-PMF shows the greatest signal intensity, and has the same values of $g_{\text{pII}} = 2.30$ and $A_{\text{pII}} = 15 \text{ mT}$. In contrast, values of $g_{\text{pII}} = 2.26$ and $A_{\text{pII}} = 16 \text{ mT}$ were extracted from the spectra of the P-PMF samples. The decrease in g_{pII} is assumed to arise from an increasing number of chelating amino groups. From the spectra of P-PMF samples after adsorptions experiments with 1.6 or $15.7 \text{ mmol/L Cu}^{2+}$ from $\text{Cu}(\text{NO}_3)_2$ solution also show that only a very small part of the respective Cu^{2+} is immobilized on the surface via chelation, which is detectable via EPR (Figure S25 and S26). In contrast, N-PMF-1.5 shows distinct signals with higher intensity, thus larger number of chelated Cu^{2+} samples even at high concentrations although the total uptake is lower than for P-PMF samples.

3.2.3. Mathematical modelling of the surface precipitation

From these experiments, it can be concluded that the two-step uptake of both ions is directly linked to the two different processes of adsorption and surface precipitation. The achieved adsorption isotherms of the P-PMF samples cannot be modeled by most adsorption isotherms easily. Sposito reported that the modelling of surface precipitation should be possible by simple addition of two isotherm model terms [13]. This alone causes the equation to be split between at least two definition regions. This happens because most isotherm models are not defined at concentration values below zero, which is necessary to shift the onset, for example, by subtracting a constant from c_{eq} . Therefore, a split equation for the two regions is necessary. Nevertheless, a larger problem is that most adsorption isotherms are not designed for a three-dimensional deposition process, which surface precipitation is. The best example represents the Langmuir isotherm, physically based a monolayer adsorption onto energetically homogeneous adsorption sites. Even some seemingly more suitable examples as the Freundlich isotherm assume a multilayer adsorption, which is controlled by the energetic differences of the individual adsorption sites. However, precipitation is dependent on e.g. the local concentration of hydroxide ions and their diffusion to the vicinity of the adsorbent interface, which cannot be derived easily and which are not accessibly by energy differences or rate constants even deployed by present isotherm models. Despite the Brunauer-Emmett-Teller isotherm was designed for a multilayer process in gas adsorption [59] and which has been modified and applied for the use in aqueous separation processes [60], it did not yield meaningful fit for our adsorption data. Another plot method designed to distinguish between adsorption and surface precipitation, the surface mole-ratio method proposed by Wei et al. [61], is not resulting in conclusive results (Figure S35 – 37). The different competing equilibria underlying the adsorption, which comprise of the chelation of a metal ion, electrostatic interaction with its respective anion, the protonation of amines and the hydroxide precipitation of both ions in a certain ratio, prevents clear presentation as a single ratio.

As sigmoidal equations are commonly used for phase transition reactions [43,62,63], we chose a sigmoidal Boltzmann equation for the modeling of the second uptake step (Eq. 7.8) [43].

$$q_{eq} = Q_{m,B} + \frac{(q_1 - Q_{m,B})}{1 + \exp\left(\frac{c_{eq} - c_P}{dc}\right)} \quad (7.8)$$

Here, the parameters q_1 represents the value of the lower equilibrium uptake while $Q_{m,B}$ is the upper uptake value for this Boltzmann equation. c_P refers to the inflection point of the curve and dc describes the slope factor of the uptake step. As the lower equilibrium capacity coincides with the plateau of the Langmuir isotherm model (Eq. 7.3), q_1 was exchanged for the Langmuir equation, leading to Equation 7.9. For the modelling of the two-step process, the obtained parameters from the Langmuir fit were included in the fit as constants. For the

Adsorption vs. Surface Precipitation of Cu²⁺ onto Porous Poly(melamine-co-formaldehyde) Particles

modelling of the two-step process, the obtained parameters from the Langmuir fit were included in the fit as constants.

Combined Langmuir-sigmoidal Boltzmann equation:

$$q_{eq} = Q_{m,L} + \frac{\left(\frac{Q_{m,L} \cdot K_L \cdot c_{eq}}{1 + K_L \cdot c_{eq}} - Q_{m,B} \right)}{1 + \exp\left(\frac{c_{eq} - c_P}{dc}\right)} \quad (7.9)$$

In general, the combined model showed very good correlation with the data (Figure 7.7 and Table 7.4). The plateaus of all three P-PMF samples are described well by the respective fits. Here, a clear trend can be seen for the inflection point as its values increases from 5.3 mmol/L (P-PMF-1.5) to 6.8 mmol/L (P-PMF-0.5). Thus, the uptake step is shifted to higher concentrations for P-PMF-0.5 with its significantly differing pore system. Furthermore, the slope characteristics of the graphs, given by dc , are showing that P-PMF-0.5 shows the steepest uptake, while P-PMF-1.0 and P-PMF-1.5 are exhibiting a flat rise. Moreover, while P-PMF-1.0 and P-PMF-1.5 are showing plateaus for the surface precipitation around 0.21 mmol/g and 0.16 mmol/g, respectively, the uptake of P-PMF-0.5 levels significantly higher at 0.91 mmol/g. A similar performance can be seen for the uptake of NO₃⁻ ions, with P-PMF-0.5 having the lowest dc value as well as the highest plateau in comparison to P-PMF-1.5. Unfortunately, P-PMF-1.0 did not yield a meaningful Langmuir fit as no distinct plateau was visible that can be modeled, therefore no combined modeling was possible. Although the combined fit can be derived without the data from a previous Langmuir fit, the standard errors of the parameters are above the respective parameter values.

Table 7.4. Fitting parameters for combined Langmuir and sigmoidal Boltzmann isotherm (L-sB) fits for the adsorption of Cu²⁺ and NO₃⁻ ions from Cu(NO₃)₂ solution after 24 hours equilibrium time (Figure 7.7), respectively. Q_m thereby is the maximum sorption capacity from sigmoidal Boltzmann. c_P represents the inflection point of the phase change and dc the slope factor. R^2 (COD) is the coefficient of determination for the respective fit. In the fitting, Langmuir parameters were from the previous fit in low concentrations are used as constants to prevent over-parametrization. For all parameters, the corresponding standard error from the fit is given.

Sample & Time	Model	Ion	Q_m mmol/g	c_P mmol/L	dc L/mmol	R^2 (COD)
P-PMF-0.5	L-sB	Cu ²⁺	0.91 ± 0.03	6.76 ± 0.14	0.69 ± 0.12	0.989
		NO ₃ ⁻	0.94 ± 0.06	14.58 ± 0.59	0.95 ± 0.74	0.934
P-PMF-1.0	L-sB	Cu ²⁺	0.22 ± 0.01	6.42 ± 0.70	1.58 ± 0.43	0.963
P-PMF-1.5	L-sB	Cu ²⁺	0.16 ± 0.01	5.26 ± 0.55	1.67 ± 0.35	0.970
		NO ₃ ⁻	0.44 ± 0.02	12.53 ± 1.10	1.83 ± 0.74	0.972

*Parameters from low-concentration Langmuir fit were used as constants.

The results from the combined Langmuir and sigmoidal Boltzmann model can be explained by the higher release of hydroxide ions by P-PMF-1.5 from its less deep pore system,

Adsorption vs. Surface Precipitation of Cu^{2+} onto Porous Poly(melamine-co-formaldehyde) Particles

while P-PMF-1.0 and P-PMF-1.5 are showing similar characteristics because of the increased transportation length of hydroxide to the outer surface. Comparing the respective P-PMF-0.5 and P-PMF-1.5 isotherms for Cu^{2+} and NO_3^- , it is noteworthy that the onset of the second uptake step coincides with the stoichiometry of the initial $\text{Cu}(\text{NO}_3)_2$, beginning at Cu^{2+} concentrations around $c_{\text{eq}} = 5 \text{ mmol/L}$ and at NO_3^- concentrations of $c_{\text{eq}} = 10 \text{ mmol/L}$. Therefore, the isotherms show perfect accordance.

3.2.4. Adsorption experiments with CuCl_2 solution

As second monovalent anion, Cl^- was chosen (Figure 7.10). The adsorption experiments greatly resemble the experiments with $\text{Cu}(\text{NO}_3)_2$ solution, showing almost no uptake of Cu^{2+} by N-PMF-1.5, while Cl^- is bound to a high amount. The P-PMF samples are showing again two uptake steps with respective plateaus, which lie approximately at 0.6 mmol/g for P-PMF-1.0, at 0.35 mmol/g for P-PMF-0.5 and at 0.3 mmol/g for P-PMF-1.5. In the low-concentration region of the isotherm (see Figure 7.10a inset or Figure S16), a modelling with Langmuir is possible (Table 7.5).

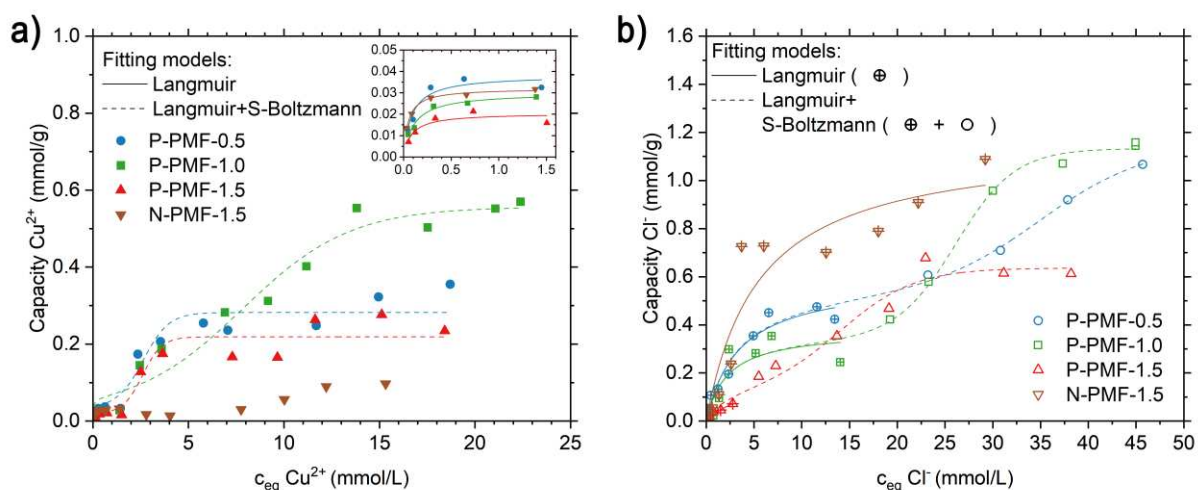


Figure 7.10. a) and b) adsorption isotherms of a) Cu^{2+} and b) Cl^- onto P-PMF samples and N-PMF-1.5 from experiments with CuCl_2 solution after 24 h adsorption. The inset in a) shows the respective data points for the lower concentration region with the respective Langmuir isotherm for these data points. Here, data points for Cu^{2+} are displayed as filled symbols. In b), data points for Cl^- are shown as open symbols, whereas the additionally crossed symbols were used for the Langmuir fitting. The Langmuir isotherms are shown as solid lines for both diagrams. The combined Langmuir/sigmoidal Boltzmann fit is shown as dashed line and all data points were used for this fit. Data points and isotherms for P-PMF-0.5 are shown in blue with circles, for P-PMF-1.0 in green with squares, for P-PMF-1.5 in red with triangles, and for N-PMF-1.5 in brown with triangles. The respective fitting parameters are displayed in Table 7.5. pH values before and after adsorption are presented in Figure S18.

The rinsed and dried P-PMF adsorbent samples from experiments with initial concentrations of Cu^{2+} above 1.6 mmol/L showed no crystalline reflexes in WAXS measurements (see Figure S23), indicating that surface precipitation is taking place at values above the first plateau. The application of the before-mentioned combined fitting model of

Adsorption vs. Surface Precipitation of Cu²⁺ onto Porous Poly(melamine-co-formaldehyde) Particles

Langmuir and sigmoidal Boltzmann is leading to very good fits in terms of R² values especially for P-PMF-0.5 and P-PMF-1.5 (see Table 7.5). P-PMF-1.0 is showing a significantly more stretched curve progression in comparison to both other porous samples, but with increased plateau values reaching 0.56 mmol/g. Here, P-PMF-1.0 exhibited a slope factor of 2.8 L/mmol, which is more than the four or fivefold of the dc values of P-PMF-0.5 and P-PMF-1.5, respectively. Interestingly, P-PMF-1.0 shows a very pronounced adsorption plateau in the Cl⁻ uptake as well as P-PMF-0.5. The plateau of P-PMF-1.5 is not easily identifiable, matching the samples low Cu²⁺ uptake, followed by a nearly linear uptake until its second plateau is reached at 0.64 mmol/g. The second plateau of P-PMF-1.0 is also very well visible with a value of 1.1 mmol/g Cl⁻. When comparing the respective plateaus of Cu²⁺ and Cl⁻, a discrepancy of the onset of the second step is visible. As the first Cl⁻ plateau is located in a concentration range in that the second Cu²⁺ uptake step is taking place, this means that mainly a conversion of adsorbed Cl⁻ ions into the co-precipitate occurs.

Table 7.5. Fitting parameters for Langmuir (L) and combined Langmuir and sigmoidal Boltzmann (L-sB) isotherm fits for the adsorption of Cu²⁺ and Cl⁻ ions from CuCl₂ solution after 24 hours equilibrium time (Figure 7.10). Q_m thereby is the maximum sorption capacity, K_L is the Langmuir equilibrium constant. c_p represents the medium concentration of the phase change and dc the slope factor, which are both derived from the combined Langmuir and sigmoidal Boltzmann fit. R² (COD) is the coefficient of determination for the respective fit. For all parameters, the corresponding standard error from the fit is given.

Sample & Time	Model	Ion	Q _m mmol/g	K _L L/mmol	c _p mmol/L	dc L/mmol	R ² (COD)
P-PMF-0.5	L	Cu ²⁺	0.038 ± 0.003	11.78 ± 4.39	--	--	0.908
		Cl ⁻	0.591 ± 0.065	0.29 ± 0.09	--	--	0.956
P-PMF-1.0	L	Cu ²⁺	0.030 ± 0.002	9.31 ± 1.88	--	--	0.971
		Cl ⁻	0.378 ± 0.097	0.45 ± 0.34	--	--	0.786
P-PMF-1.5	L	Cu ²⁺	0.020 ± 0.003	12.07 ± 6.63	--	--	0.804
		Cl ⁻	0.176 ± 0.17	0.25 ± 0.35	--	--	0.870
N-PMF-1.5	L	Cu ²⁺	0.032 ± 0.001	21.14 ± 1.87	--	--	0.993
		Cl ⁻	1.164 ± 0.157	0.182 ± 0.08	--	--	0.905
P-PMF-0.5	L-sB*	Cu ²⁺	0.28 ± 0.02	--	2.65 ± 0.38	0.67 ± 0.30	0.917
		Cl ⁻	1.15 ± 0.10	--	35.32 ± 2.63	5.62 ± 1.52	0.990
P-PMF-1.0	L-sB*	Cu ²⁺	0.56 ± 0.03	--	7.87 ± 0.69	2.80 ± 0.46	0.967
		Cl ⁻	1.13 ± 0.04	--	26.19 ± 0.96	3.10 ± 0.70	0.985
P-PMF-1.5	L-sB*	Cu ²⁺	0.22 ± 0.01	--	2.60 ± 0.00	0.51 ± 0.29	0.897
		Cl ⁻	0.64 ± 0.03	--	14.39 ± 1.24	3.87 ± 0.78	0.976

*Parameters from low-concentration Langmuir fit were used as constants.

From WAXS analyses of the P-PMF-0.5 over the initial concentration range of 1.6 mmol/L to 15.7 mmol/L Cu²⁺ as example for the adsorption process (Figure S26), it can be seen that

adsorption without formation of crystalline precipitate occurs up to $c_0 = 1.6$ mmol/L. Afterwards, crystalline reflexes of the precipitated $\text{Cu}_2\text{Cl}(\text{OH})_4$ are apparent.

Interestingly, the Cu^{2+} uptake curve from P-PMF-1.0 featured slight elements of a second plateau located between approximately 5 mmol/L to 10 mmol/L. Here, the precipitation of a second species was suspected. From WAXS measurements over the concentration range of 1.6 mmol/L to 15.7 mmol/L Cu^{2+} , this was ruled out. However, as this region is also the end of the first plateau and subsequent onset for the second Cl^- uptake step, it is logical that this may influence the Cu^{2+} uptake further, leading to this pseudo-plateau. This effect and coinciding location with the first Cl^- plateau can also be seen, although less pronounced, from P-PMF-0.5.

The experiments with CuCl_2 also results in chelate complexes as experimentally verified by EPR spectroscopy (Figure S29–S30). Almost the same values for g_{pII} and A_{pII} were found as for experiments with copper nitrate: $g_{\text{pII}} = 2.24$ and $A_{\text{pII}} = 16$ mT for the P-PMF samples as well as $g_{\text{pII}} = 2.29$ and $A_{\text{pII}} = 16$ mT for N-PMF-1.5. In higher concentrations of Cu^{2+} , distinct peaks of higher intensity are again seen for N-PMF-1.5 although the total uptake of Cu^{2+} is less than for all P-PMF samples. This supports the conclusion that almost all Cu^{2+} ions are immobilized via surface precipitation instead of chelation onto P-PMF particles.

3.3. Mechanism for Cu^{2+} and Anion Removal

PMF with its nitrogen functionalities is able to undergo different pathways for the removal of pollutants. As presented from the various adsorption experiments, the involved equilibria and reactions are non-trivial and are heavily influencing each other. A simplified overview is given in Figure 7.11. The first equilibrium present in the adsorption experiments is the protonation of the amino functionalities of the PMF which is either consuming protons released by solvation of the metal ion or is releasing hydroxide ions directly from dissociating water molecules. When not protonated, the amino functionalities are able to coordinate the metal ion, forming chelate complexes whose stability is determined by the number of amines involved and the respective metal ion. The third equilibria consists of the adsorption of anions towards the protonated amines. The latter two equilibria hereby describe the processes, which are assigned to the adsorption. In contrast, a high local concentration of hydroxide ions leads to the precipitation of hydrolysable metal ions at the adsorbent interface. Here, especially the specific surface area is adding towards the release of hydroxide ions into solution, while the depth of the underlying pore structure is heavily affecting the time needed for the ions to reach the outer interface of the particles. Also, the hydroxide-release is strongly dependent of the strength of interaction with anions as this is adding to protonation of amines.

In contrast to monovalent ions, no distinctly separate uptake step in the uptake isotherm for CuSO_4 in the lower concentration region can be seen. As sulfate ions possess a more

negative charge [64] at the tested pH than chloride or nitrate, it is more strongly interacting with the protonated amines of the resin by electrostatic forces. Shifting the adsorption/desorption equilibrium of sulfate onto protonated amines towards adsorption, this would also cause a shift in the protonation equilibrium of the amines towards more protonation, all in all adding to faster release of hydroxide ions into the solution accelerating general precipitation. This leads to precipitation of the $\text{Cu}_4(\text{SO}_4)(\text{OH})_6$ species even at very low concentrations and thereby superimposition with the adsorption step.

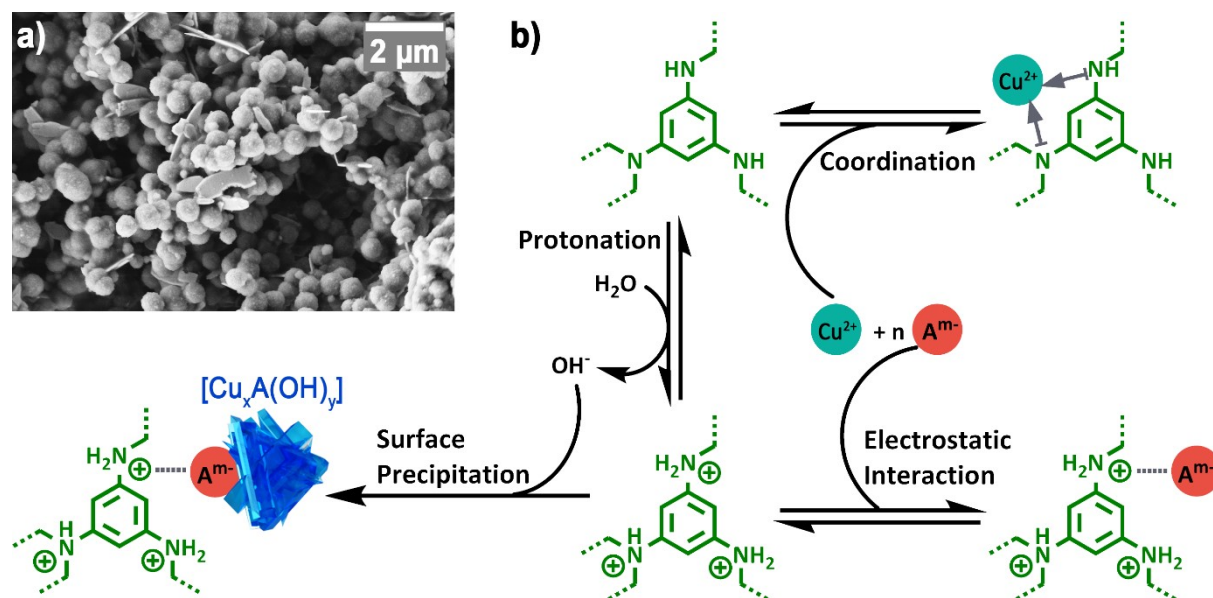


Figure 7.11. a) SEM image of crystalline $\text{Cu}_4(\text{SO}_4)(\text{OH})_6$ surface precipitate on P-PMF particles and b) Potential equilibria and reactions present in adsorption experiments with dissolved Cu^{2+} and anions (A^{m-}) which are leading to the removal of the respective ions by either surface precipitation yielding crystalline $[\text{Cu}_x\text{A}(\text{OH})_y]$ (left-hand side) or adsorption by electrostatic interaction or coordination (right-hand side).

3.4. Investigation of other heavy metal salts

To give an exemplary overview for occurrence of surface precipitation with other metal ions, experiments with $\text{Al}_2(\text{SO}_4)_3$, $\text{Cr}_2(\text{SO}_4)_3$, MnSO_4 , FeSO_4 , CoSO_4 , NiSO_4 , ZnSO_4 , CdSO_4 , and $\text{Pb}(\text{NO}_3)_2$ were performed, each with an initial metal ion concentration of 1000 mg/L for the respective metal ion. As P-PMF-1.0 and P-PMF-0.5 exhibited the highest adsorption in all experiments, they were chosen as adsorbent. The samples were analyzed for their adsorption capacity (Figure S33 and S34) and the respective adsorbent materials after the experiment was investigated with WAXS measurements (Figure S32).

Although all these metal ions are well hydrolysable, therefore theoretically prone to be precipitated as hydroxides, only $\text{Fe}^{2+/3+}$, Pb^{2+} , and Cd^{2+} is forming crystalline precipitates. Here, air-oxidized Fe^{3+} is forming FeOOH crystals, whereas Pb^{2+} and Cd^{2+} are forming respective precipitates with carbonate ions as $\text{Pb}_3(\text{CO}_3)_2(\text{OH})_2$ and CdCO_3 . Here, carbonate has increased interaction with the ions Cd^{2+} and Pb^{2+} as it represents a soft base in terms of HSAB principle,

whereas the hard Fe^{3+} ion is interacting better with a hard base like O^{2-} [65–67]. After $\text{Fe}^{2+/3+}$, Cr^{3+} showed the highest uptake, although no crystalline structures were detectable, meaning that adsorption is the main process responsible.

However, this shows that the apparent uptake of metal ions by adsorbents is possible by both, adsorption processes and surface precipitation, and is not as closely linked to their respective hydrolyzability as in contrast metal ions as zinc or manganese should show increased uptake and detectable crystalline precipitate.

4. *Conclusions*

Our author team showed the synthesis of highly porous PMF particles, synthesized by utilizing a facile and ecofriendly polymerization with SiO_2 hard templating in water. The obtained particles were comprehensively analyzed, showing their outstanding porosity with BET surface areas with up to $421 \text{ m}^2/\text{g}$. The particles have been compared to the unporous particles synthesized without the hard templating approach. This contrast in material properties was then used to investigate in-depth the uptake of the heavy metal ion Cu^{2+} as exemplary pollutant. Here, we uncovered strong dependence first of the Cu^{2+} uptake on the respective anion in solution but more interestingly on the pore structure of the PMF particles. The uptake process was a combination of an adsorption process and a surface precipitation by hydroxide ions, which can either, be mainly overlapping (as for $\text{CuSO}_{4(\text{aq})}$) or a distinctly visible two-step process (as for monovalent anions Cl^- or NO_3^-). Especially the differing pore structure of the three porous P-PMF samples showed differing influences on the dynamic of the uptake steps. We mathematically modeled the processes with a new adsorption isotherm, based on the Langmuir model for the adsorption part and a sigmoidal Boltzmann equation covering the surface precipitation.

Our investigation implies that both adsorptions and surface precipitation can partake in the separation process of metal ions as well as their respective anions. Therefore, it is crucial to clarify, which reaction is taking place in separation processes, as this massively influences the applicability in a larger scale. Furthermore, as the uptake of a pollutant can be a distinct two-step (or theoretically any multistep) process, it is strongly beneficial to evaluate the background as this enables the optimization of both, the adsorbent material as well as the experimental setup to maximize the achieved uptake capacity by taking advantage of both processes. Our proposed combination of the Langmuir model with the sigmoidal Boltzmann equation as isotherm showed its worth by deriving the slope and inflection point of the second uptake step, which can help for the testing and optimization of materials. Up to this point, the current adsorption models were found to be inadequate as they are either inapplicable because of their definition gaps or by losing their physical meaning. Prospectively, our isotherm model could also help for the synthesis of hybrid materials, which utilize either

adsorption or precipitation for the modification as the processing parameters can be derived from a simple isotherm investigation. With this knowledge, differing materials can then be obtained by favoring specifically one uptake mechanism by choosing the correct synthesis parameters.

Acknowledgments

The authors thank Eileen Schierz for conduction of the elemental analysis, Uta Reuter for the preparation of the thin sections.

Author Contributions

Konstantin B.L. Borchert: Conceptualization, methodology, validation, formal analysis, investigation, data curation, writing-original draft preparation, writing - review & editing, visualization. **Christine Steinbach:** Investigation, validation, writing - review & editing. **Berthold Reis:** Investigation, validation, writing - review & editing. **Uwe Lappan:** Investigation, validation, writing - review & editing. **Niklas Gerlach:** Investigation, validation, writing - review & editing. **Martin Mayer:** Conceptualization, methodology, writing - review & editing. **Simona Schwarz:** Resources, writing - review & editing, supervision, project administration, funding acquisition. **Dana Schwarz:** Conceptualization, methodology, resources, writing - review & editing, visualization, supervision, project administration, funding acquisition.

Funding

This work was supported by the German Federal Ministry of Education and Research [grant number 01DJ18010].

References

- [1] D. Schwarz, J. Weber, *Macromol. Mater. Eng.* 300 (2015) 531–541.
- [2] D. Schwarz, J. Weber, *Journal of colloid and interface science* 498 (2017) 335–342.
- [3] Y. Wang, Y. Xie, Y. Zhang, S. Tang, C. Guo, J. Wu, R. Lau, *Chemical Engineering Research and Design* 114 (2016) 258–267.
- [4] A. Deryło-Marczewska, J. Goworek, W. Zgrajka, *Langmuir the ACS journal of surfaces and colloids* 17 (2001) 6518–6523.
- [5] D. Schwarz, J. Weber, *Polymer* 155 (2018) 83–88.
- [6] K.B.L. Borchert, C. Steinbach, B. Reis, N. Gerlach, P. Zimmermann, S. Schwarz, D. Schwarz, *Molecules (Basel, Switzerland)* 26 (2021).
- [7] G. Ming, H. Duan, X. Meng, G. Sun, W. Sun, Y. Liu, L. Lucia, *Chemical Engineering Journal* 288 (2016) 745–757.
- [8] M.X. Tan, Y.N. Sum, J.Y. Ying, Y. Zhang, *Energy Environ. Sci.* 6 (2013) 3254.
- [9] D. Schwarz, J. Weber, *Langmuir the ACS journal of surfaces and colloids* 31 (2015) 8436–8445.
- [10] Y. Wu, Y. Li, L. Qin, F. Yang, D. Wu, *Journal of materials chemistry. B* 1 (2013) 204–212.
- [11] M. Mende, D. Schwarz, C. Steinbach, R. Boldt, S. Schwarz, *Materials (Basel, Switzerland)* 11 (2018).
- [12] J. Weißpflog, A. Gündel, D. Vehlow, C. Steinbach, M. Müller, R. Boldt, S. Schwarz, D. Schwarz, *Molecules (Basel, Switzerland)* 25 (2020).
- [13] G. Sposito, in: J.A. Davis, K.F. Hayes (Eds.), *Geochemical Processes at Mineral Surfaces*, American Chemical Society, Washington D.C., 1987, pp. 217–228.

Adsorption vs. Surface Precipitation of Cu²⁺ onto Porous Poly(melamine-co-formaldehyde) Particles

- [14] K.P. Ananthapadmanabhan, P. Somasundaran, *Colloids and Surfaces* 13 (1985) 151–167.
- [15] A. Godelitsas, J.M. Astilleros, in: G. Ferraris, M. Prieto, H. Stoll (Eds.), *Ion Partitioning in Ambient-Temperature Aqueous Systems*, Mineralogical Society of Great Britain & Ireland, London, 2011, pp. 289–324.
- [16] S.E. Fendorf, D.L. Sparks, M. Fendorf, R. Gronsky, *Journal of colloid and interface science* 148 (1992) 295–298.
- [17] F. Raji, M. Ejtemaei, A.V. Nguyen, *Applied Surface Science* 529 (2020) 147128.
- [18] R. Shyam, J.K. Puri, H. Kaur, R. Amutha, A. Kapila, *Journal of Molecular Liquids* 178 (2013) 31–36.
- [19] C. Dai, Y. Hu, *Environmental science & technology* 49 (2015) 292–300.
- [20] R.O. James, T.W. Healy, *Journal of colloid and interface science* 40 (1972) 53–64.
- [21] K. Müller, H. Foerstendorf, V. Brendler, A. Rossberg, K. Stolze, A. Gröschel, *Chemical Geology* 357 (2013) 75–84.
- [22] X. MO, M.G. SIEBECKER, W. GOU, L. LI, W. LI, *Pedosphere* 31 (2021) 11–27.
- [23] D.G. Strawn, *Soil Systems* 5 (2021) 13.
- [24] N. van Groeningen, B. Glück, I. Christl, R. Kretzschmar, *Environmental science. Processes & impacts* 22 (2020) 1654–1665.
- [25] T. Suzuki, M. Okita, S. Kakoyama, M. Niinae, H. Nakata, H. Fujii, Y. Tasaka, *Journal of hazardous materials* 338 (2017) 482–490.
- [26] R. Meng, T. Chen, Y. Zhang, W. Lu, Y. Liu, T. Lu, Y. Liu, H. Wang, *RSC Adv.* 8 (2018) 21480–21494.
- [27] J. Wei, L. Duan, J. Wei, E. Hoffmann, Y. Song, X. Meng, *Journal of environmental sciences (China)* 101 (2021) 135–144.
- [28] M. Luo, C. Huang, F. Chen, C. Chen, H. Li, *Journal of Dispersion Science and Technology* 42 (2021) 1710–1722.
- [29] L. Zhang, S. Tang, F. He, Y. Liu, W. Mao, Y. Guan, *Chemical Engineering Journal* 378 (2019) 122215.
- [30] A.V. Khramenkova, D.N. Ariskina, O.E. Polozhentsev, I.I. Lyatun, D.M. Kuznetsov, E.A. Yatsenko, *Composite Interfaces* 2017 (2022) 1–19.
- [31] A.R. wassel, M.E. El-Naggar, K. Shoueir, *Journal of Environmental Chemical Engineering* 8 (2020) 104175.
- [32] T.R. Dabinett, D. Humberstone, P. Leverett, P.A. Williams, *Pure and Applied Chemistry* 80 (2008) 1317–1323.
- [33] K.S.W. Sing, *Pure & Applied Chemistry* 54 (1982) 2201–2218.
- [34] M. Thommes, K. Kaneko, A.V. Neimark, J.P. Olivier, F. Rodriguez-Reinoso, J. Rouquerol, K.S.W. Sing, *Pure and Applied Chemistry* 87 (2015) 1051–1069.
- [35] I. Langmuir, *J. Am. Chem. Soc.* 38 (1916) 2221–2295.
- [36] M.M. Dubinin, *Proceedings of the USSR Academy of Sciences* 55 (1947) 327–329.
- [37] J. Wang, X. Guo, *Chemosphere* 258 (2020) 127279.
- [38] T.A. Osmari, R. Gallon, M. Schwaab, E. Barbosa-Coutinho, J.B. Severo, J.C. Pinto, *Adsorption Science & Technology* 31 (2013) 433–458.
- [39] B. Subramanyam, A. Das, *Journal of environmental health science & engineering* 12 (2014) 92.
- [40] F. Togue Kamga, *Appl Water Sci* 9 (2019) 456.
- [41] K.Y. Foo, B.H. Hameed, *Chemical Engineering Journal* 156 (2010) 2–10.
- [42] M.A. Al-Ghouti, D.A. Da’ana, *Journal of hazardous materials* 393 (2020) 122383.
- [43] A.L. Navarro-Verdugo, F.M. Goycoolea, G. Romero-Meléndez, I. Higuera-Ciapara, W. Argüelles-Monal, *Soft Matter* 7 (2011) 5847.
- [44] G. Socrates, *Infrared and Raman characteristic group frequencies: Tables and charts*, 3rd ed., John Wiley & Sons LTD, Chichester [etc.], 2015.
- [45] A. Baraka, P.J. Hall, M.J. Heslop, *Reactive and Functional Polymers* 67 (2007) 585–600.
- [46] C. Devallencourt, J.M. Saiter, A. Fafet, E. Ubrich, *Thermochimica Acta* 259 (1995) 143–151.
- [47] D.J. Merline, S. Vukusic, A.A. Abdala, *Polym J* 45 (2013) 413–419.
- [48] S. Ullah, M.A. Bustam, M. Nadeem, M.Y. Naz, W.L. Tan, A.M. Shariff, *The Scientific World Journal* 2014 (2014) 1–6.
- [49] M. Kosmulski, *Surface Charging and Points of Zero Charge*, CRC Press, 2009.
- [50] I.A. Rahman, P. Vejayakumaran, C.S. Sipaut, J. Ismail, C.K. Chee, *Materials Chemistry and Physics* 114 (2009) 328–332.
- [51] K. Wang, H. Huang, D. Liu, C. Wang, J. Li, C. Zhong, *Environmental science & technology* 50 (2016) 4869–4876.
- [52] I.D. Wessely, A.M. Schade, S. Dey, A. Bhunia, A. Nuhnen, C. Janiak, S. Bräse, *Materials (Basel, Switzerland)* 14 (2021).
- [53] A. Lotierzo, S.A.F. Bon, *Polym. Chem.* 8 (2017) 5100–5111.
- [54] S.U. Pickering, *J. Chem. Soc., Trans.* 91 (1907) 2001–2021.

Adsorption vs. Surface Precipitation of Cu²⁺ onto Porous Poly(melamine-co-formaldehyde) Particles

- [55] S. Merlino, N. Perchiazzi, D. Franco, *ejm* 15 (2003) 267–275.
- [56] M. Łabanowska, E. Bidzińska, K. Dyrek, T. Fortuna, S. Pietrzyk, J. Rożnowski, R.P. Socha, *Starch - Stärke* 60 (2008) 134–145.
- [57] J. Peisach, W.E. Blumberg, *Archives of Biochemistry and Biophysics* 165 (1974) 691–708.
- [58] N.G. Chernorukov, Y.N. Mikhailov, A.V. Knyazev, A.S. Kanishcheva, E.N. Bulanov, *Russ. J. Inorg. Chem.* 50 (2005) 701–704.
- [59] S. Brunauer, P.H. Emmett, E. Teller, *J. Am. Chem. Soc.* 60 (1938) 309–319.
- [60] A. Ebadi, J.S. Soltan Mohammadzadeh, A. Khudiev, *Adsorption* 15 (2009) 65–73.
- [61] J. Wei, X. Meng, Y. Song, Q. Shi, X. Wen, G. Korfiatis, *Journal of hazardous materials* 397 (2020) 122781.
- [62] L. Bentea, M.A. Watzky, R.G. Finke, *J. Phys. Chem. C* 121 (2017) 5302–5312.
- [63] J.M. Pardal, S.S.M. Tavares, M.P. Cindra Fonseca, J.A. de Souza, A. Loureiro, E.P. Moura, *J Mater Sci* 45 (2010) 616–623.
- [64] J. Casas, F. Alvarez, L. Cifuentes, *Chemical Engineering Science* 55 (2000) 6223–6234.
- [65] R.G. Pearson, *J. Am. Chem. Soc.* 85 (1963) 3533–3539.
- [66] R.G. Pearson, *J. Chem. Educ.* 45 (1968) 581.
- [67] R.G. Pearson, *J. Chem. Educ.* 45 (1968) 643.

8. SiO₂ Nanospheres as Surfactant and Template in Aqueous Dispersion Polymerizations Yielding Nanoporous Resin Particles

This chapter is based on a submitted publication in *Journal of Colloid and Interface Science* **2023**, 1, 819.

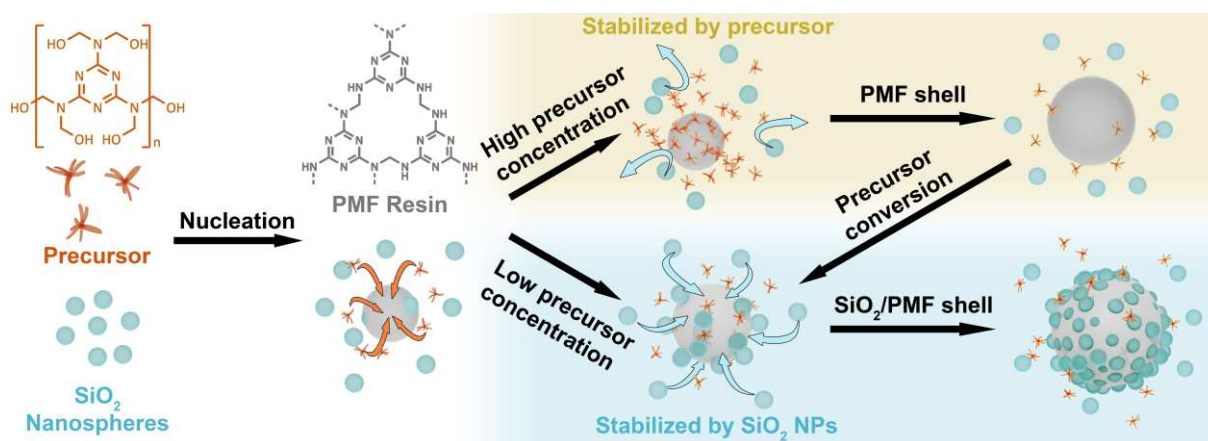
(DOI: 10.1016/j.jcis.2023.01.071)

By Konstantin B. L. Borchert, Niklas Gerlach, Christine Steinbach, Berthold Reis, Simona Schwarz* and Dana Schwarz*

Leibniz-Institut für Polymerforschung Dresden e.V., Hohe Str. 6, 01069 Dresden, Germany;

* Corresponding authors

Graphical Abstract



Abstract

Hypothesis: High nitrogen containing resins such as poly(melamine-co-formaldehyde) (PMF) are known for their very good adsorption properties. Until now, using an ecofriendly hard-templating approach with SiO₂ nanospheres in water for synthesis, only yielded either highly porous particles with diameters up to 1 μm or non-porous particles with diameters above 1 μm . Small particles cannot be used as fixed bed adsorbents in columns because of the very high pressure occurring.

Experiments: To yield particles with high porosity and larger diameters for the use as fixed bed adsorbent, we investigated the influence of several synthesis parameters on porosity and particle morphology.

Findings: From all variations, we proposed a mechanism for the complex interplay between the PMF prepolymer and resin species with SiO₂ nanoparticles acting both as Pickering-like surfactant and template particle. With this knowledge we were able to produce a suitable column material with high specific surface area up to 260 m²/g. We then proved the application of this material for dichromate separation from water in batch experiments,

yielding a maximum capacity of 138 mg/g. In column experiments, the contamination of 5 mg/L dichromate in water was reduced to drinking water safe levels for an influent volume equal to over 160 bed volumes.

1. *Introduction*

Highly porous materials are constantly under investigation because of their application in energy storage, catalysis and separation technologies, for which especially a suitable pore system and a high specific surface area are absolutely necessary [1–4]. The pore system is decisive for the mass transfer, which adds to processing speed, while the available specific surface area is accountable for the effectiveness of the process itself e.g. for the number of adsorption sites for separation applications [5–7]. Poly(melamine-co-formaldehyde) (PMF) is a highly functional polymer network consisting of aromatic triazine-rings and amino functionalities. These groups present interesting opportunities for the application as catalyst [8–10], in CO₂ storage [10–13] as well as adsorption processes in water treatment [14–19]. As PMF resin does not exhibit a well-accessible pore system, its specific surface area as bulk material is insignificant. In literature, different approaches were investigated to introduce porosity in the resin's network structure. One of the most common approaches is a solvothermal synthesis in dimethyl sulfoxide [12,16,18,20], which leads to a sulfur contamination and H₂S release as dimethyl sulfoxide decomposes at the temperatures used [10,12,18,20]. The sulfur contamination as well as the use of organic solvents and consumption of large amounts of energy for solvothermal syntheses diminish the applicability for e.g. water treatment as ecological application. To circumvent these problems, different approaches have been studied for a soft-templated synthesis in water or ethanol as solvent [17,21]. However, some of the synthesized polymers contain residual amounts of the surfactant as it e.g. can be seen from their color [17,21]. An approach to circumvent these problems is a dispersion polymerization in water utilizing a hard templating approach.

From previous studies with silica nanoparticles (SiO₂ NPs) as sacrificial template, we obtained highly porous PMF particles with specific surface areas up to 410 m²/g [14,15,19,22]. The spherical particles exhibited defined pore sizes, adjustable by the template diameter (12 or 22 nm), enabling viable mass transfer in adsorption applications [22]. However, until now the particle size of all samples was in the range of hundreds of nanometers, which does not allow an application in fixed bed adsorption applications due to high flow resistance. The used silica template, responsible for the high porosity, inevitably lead to the formation of sub-micron diameter particles. Without the template, particle diameters of several μ m can be obtained as shown by Wu et al. [23], which in turn are non-porous (by means of N₂ sorption). These opposing results lead us to the question if SiO₂ NPs were acting as colloidal nanoparticle surfactant as seen from Pickering emulsions [24], besides their structuring influence.

Therefore, we wanted to uncover the particle and pore formation mechanism in the dispersion polymerization process. In the current article, we present a detailed investigation of the particle formation and templating mechanism the system. The colloidal synthesis system comprises of water as dispersant, melamine and paraformaldehyde as monomers, the oligomeric PMF precursor forming here from, the silica particles as template and oxalic acid as catalyst.

Via systematic variation of single synthesis parameters, the particle formation and templating process is deduced. First, we investigated the influence of a differing reaction mixture on the formed particles by changing the amount of dispersant, of SiO₂ NPs as template and of the catalyst in single experimental series. Secondly, we changed the processing parameters such as stirring speed, polymerization temperature, and prepolymerization time. From these syntheses, different silica-PMF hybrid particles (H-PMF) and the subsequently etched, porous PMF particles (P-PMF) were obtained. We thoroughly studied especially the different particle morphologies and porosity in detail by N₂ sorption, particle size measurements and electron microscopy.

With the knowledge of the particle formation mechanism, we conducted a colloidal synthesis of multi- μm sized, porous P-PMF particles for application in fixed bed column adsorption. Subsequently, column adsorption experiments with dichromate solution are presented as proof of concept.

2. *Materials and methods*

2.1. Materials

For the synthesis of the PMF particles, melamine (Sigma-Aldrich, München, Germany, 99%), paraformaldehyde (Sigma-Aldrich, München, Germany, 95%), oxalic acid (Sigma-Aldrich, München, Germany, 99% and 98%, respectively), NaOH (Honeywell, Offenbach, Germany, $\geq 98\%$), Ludox® HS-40 (Sigma-Aldrich, München, Germany, 40 wt% in H₂O), were used as received without further purification. For all experiments and syntheses, ultrapure water purified by a Milli-Q Advantage A10® system (Millipore, Darmstadt, Germany) (total organic carbon = 5 ppb, resistivity of 18.2 M Ω ·cm) was used. For adsorption experiments, K₂Cr₂O₇ (> 99.8 %, p.a.) was used as received from Fluka (Honeywell) (Offenbach, Germany) without further purification. The embedding of the samples for TEM thin-sections was done using 1,2,3-propanetriol glycidyl ether, 2-Dodecenyl succinic anhydride, Methyl nadic anhydride, and 2,4,6-Tris(dimethylaminomethyl)phenol purchased from Serva Electrophoresis GmbH (Heidelberg, Germany). For the ICP-OES measurements, the following standards were used: 10,000 mg/L Cr in 10 wt.% HNO₃ (CPI International, Santa Rosa, CA, USA) and 9,993 mg/L K in HNO₃ (aq) (Tracecert, Sigma-Aldrich, Munich).

2.2. Methods

Scanning electron microscopy (SEM) was carried out using a SEM Ultra Plus from Carl Zeiss Microscopy GmbH, Oberkochen, Germany. For this purpose, the samples were fixed with double-sided adhesive carbon tape on an aluminum pin sample tray and afterwards streamed with N₂ to obtain only a thin layer of particles. The samples were then sputtered with 3 nm of platinum using a Sputter Coater SCD050 from Leica Microsystems, Wetzlar, Germany before the investigation starts. The measurements were carried out with an acceleration voltage of 3 keV at different magnifications.

Transmission electron microscopy (TEM) was carried out using a Libra 200 device from Carl Zeiss Microscopy GmbH, Oberkochen, Germany. The acceleration voltage was 200 keV. The studied particles were dispersed in ultrapure water and dripped onto a carbon coated Cu mesh (200 or 300 mesh). For measurements of energy-filtered TEM (EFTEM) investigations of ultrathin-sections, a Libra 120 device with an acceleration voltage of 120 keV was used (Carl Zeiss Microscopy GmbH, Oberkochen, Germany).

Preparations of ultrathin-sections: A few µg of the particles were embedded in a mixture of 80 µL Epon A (44.3 wt.% 1,2,3-propanetriol glycidyl ether; 55.7 wt.% 2-Dodecenyl succinic anhydride), 120 µL Epon B (51.3 wt.% 1,2,3-propanetriol glycidyl ether, 48.7 wt.% Methyl nadic anhydride), and 10 µL 2,4,6-Tris(dimethylaminomethyl)phenol. The mixture was transferred to a Beem® capsule (then heated to 60 °C for 48 h. Subsequently, the embedded samples were cut using the ultramicrotome EM UC6 (Leica Microsystems GmbH, Wetzlar, Germany).

Particles sizes were analyzed using a Mastersizer Microplus (Malvern, Kassel Germany). The samples were dispersed with ultrasonic in ultrapure water (0.1 g/100 mL). The data was evaluated using the model “Polydisperse” and “NFD” (Particle RI: 1.4564, Abs.: 0.0100 and Dispersant RI: 1.3300).

Nitrogen sorption measurements were performed using the Autosorb iQ MP from Quantachrome Instruments, Boynton Beach, USA. Samples were activated by degassing in vacuum (5×10^{-10} mbar) at 110 °C for 24 hours. The nitrogen sorption measurements were performed at 77 K. The surface area was calculated in the relative pressure (p/p_0) range from 0.07 to 0.22 by BET method [25]. The pore size distribution was derived by a QSDFT fit of the adsorption branch considering spherical, cylindrical and slit pores.

pH measurement: The measurement of pH was carried out with the device SevenMulti from Mettler Toledo (Gießen, Germany) at room temperature.

Dispersion stability analysis was carried out with the device LUMiSizer (LUM GmbH, Berlin, Germany) using a wavelength of 870 nm with relative centrifugal field (rcf) in the range of $5 \times g$ to $2300 \times g$ at 20 °C.

Centrifugation: The adsorber materials were separated from their supernatants by centrifugation with the device Sigma 3-18KS from Sigma Laborzentrifugen GmbH (Osterode, Germany) at room temperature and the respectively stated rpm.

Inductively coupled plasma optical emission spectrometry (ICP-OES) (iCAP 7400 from Thermo Scientific) was used to determine the chromium and potassium ion concentrations in simulated water. Thus, matrix-matched standards (4 wt.% HNO_{3(aq)}) were used with K and Cr in the following concentrations: 2000 mg/L, 1750 mg/L, 1500 mg/L, 1250 mg/L, 1000 mg/L, 750 mg/L, 500 mg/L, 250 mg/L, 100 mg/L, 50 mg/L, 25 mg/L, 10 mg/L, 5 mg/L, 1 mg/L, 0.1 mg/L. To each sample of 8 mL, 2 mL of 20 wt.% nitric acid was added prior to analysis. Each concentration was determined from threefold measurement. The limit of detection calculated by Qtegra™ software (Thermo Scientific, Waltham, MA, USA) were given with 0.1 mg/L for Cr and 0.5 mg/L for K.

2.3. Synthesis of the PMF particles

The PMF-Std particles were synthesized as recently published [14,15,22] with minor modifications of the dispersant amount and upscaling. First, 15.6 g (123.7 mmol) melamine (M) and 22.2 g (739.2 mmol) paraformaldehyde (F) were dispersed in 150 mL ultrapure water in a 1 L round bottom flask. The dispersion was stirred (500 rpm, 2 cm oval magnetic stirrer) at 50 °C for 40 minutes to form a precursor solution. A solution of 450 mL ultrapure water with 2.4 g (26.7 mmol) oxalic acid and 72.0 g Ludox® HS-40 was prepared and then added to the reaction mixture. The resulting mixture was stirred for 24 h at 100 °C under reflux. The amounts used for synthesis can also be seen in Table S1.

2.3.1. Synthesis of PMF-Std as standard

The PMF-Std particles were synthesized as recently published [14,15,22] with minor modifications. First, 15.6 g (123.7 mmol) melamine (M) and 22.2 g (739.2 mmol) paraformaldehyde (F) were dispersed in 150 mL ultrapure water in a 1 L round bottom flask. The dispersion was stirred (500 rpm, 2 cm oval magnetic stirrer) at 50 °C for 40 minutes to form a precursor solution. A solution of 450 mL ultrapure water with 2.4 g (26.7 mmol) oxalic acid and 72.0 g Ludox® HS-40 was prepared and then added to the reaction mixture. The resulting mixture was stirred for 24 h at 100 °C under reflux. The amounts used for synthesis can also be seen in Table S1.

2.3.2. Synthesis of PMF-Water

The PMF-Water-2 and PMF-Water-3 particles were synthesized analogous to PMF-Std, but the amounts of all reactants except the water as dispersant (in both steps) were divided by the factor 2 or 3, respectively, which corresponds to the suffix A of the samples. An overview of the synthesis parameters is given in Table 8.1. The amounts used for synthesis can also be seen in Table S1.

2.3.3. *Synthesis of PMF-SiO₂-B*

The PMF-SiO₂-B particles were synthesized analogous to PMF-Std as stated in the section 2.3.1. Here, the amount of Ludox® HS-40 was multiplied by the factor B with respect to PMF-Std, given by the samples' suffix -B. An overview of the synthesis parameters is given in Table 8.1. The amounts used for synthesis can also be seen in Table S1.

2.3.4. *Synthesis of PMF-Cat-C*

The PMF-Cat-C particles were synthesized analogous to PMF-Std as stated in the section 2.3.1. Here, the amount of oxalic acid as catalyst was multiplied by the factor C with respect to PMF-Std, given by the samples' suffix -C. An overview of the synthesis parameters is given in Table 8.1. The amounts used for synthesis can also be seen in Table S1.

2.3.5. *Synthesis of PMF-Stir-D*

The PMF-Stir-D particles were synthesized analogous to PMF-Std as stated in the section 2.3.1. Here, the stirring speed of the magnetic stirrer was varied as given by the respective suffix -D in rpm. The synthesis parameters are given in Table 8.1. The amounts used for synthesis can also be seen in Table S1.

2.3.6. *Synthesis of PMF-Temp-E*

The PMF-Temp-E particles were synthesized analogous to PMF-Std as stated in the section 2.3.1. Here, the reaction temperature after addition of the Ludox® HS-40 / oxalic acid dispersion of the final 24 h interval was modified. Here, the suffix -E corresponds to the temperature in °C. The first precursor formation step was not changed. For reaction temperatures below 50 °C, the precursor solution was first cooled to the desired temperature by a water bath before addition of the Ludox® HS-40 / oxalic acid dispersion. The reaction mixtures were then kept at the desired polymerization temperature for 24 h with stirring at 500 rpm using a 2 cm oval magnetic stirrer. A comparison of the reaction conditions can be seen in Table 8.1. The amounts used for synthesis can also be seen in Table S1.

2.3.7. *Synthesis of PMF-Time-F*

The PMF-Time-F particles were synthesized analogous to PMF-Std as stated in the section 2.3.1. Here, the time of the precursor formation at 50 °C (before addition of the silica/oxalic acid dispersion and subsequent heating to 100 °C) was varied as stated in Table 8.1. . The suffix -F describes the time in min held at 50 °C before the addition of template and precursor. This means, that e.g. PMF-Time-0 was synthesized in a one pot reaction with direct heating to 100 °C after addition of all reactants. The amounts used for synthesis can also be seen in Table S1.

SiO₂ Nanospheres as Surfactant and Template in Aqueous Dispersion Polymerizations Yielding Nanoporous Resin Particles

Table 8.1. Table of synthesis parameters of respective H-PMF and P-PMF particles with the corresponding sample codes. The used amounts for the reactants are displayed in Table S1.

Sample code	Oxalic acid ^a (mol%)	Dispersant amount of PMF-Std (%)	Mass share Ludox [®] HS-40 dispersion ^b (wt.%)	Stirring speed (rpm)	Reaction tempera- ture (°C)	Time for precursor formation (min)
PMF-Std	21.5	100	66	500	100	40
PMF-Cat-43	43.1	100	66	500	100	40
PMF-Cat-11	10.7	100	66	500	100	40
PMF-Water-2	21.5	200	66	500	100	40
PMF-Water-3	21.5	300	66	500	100	40
PMF-SiO₂-49	21.5	100	49	500	100	40
PMF- SiO₂-10	21.5	100	10	500	100	40
PMF- SiO₂-0	21.5	100	0	500	100	40
PMF-Stir-0	21.5	100	66	0	100	40
PMF-Stir-100	21.5	100	66	100	100	40
PMF-Stir-200	21.5	100	66	200	100	40
PMF-Stir-300	21.5	100	66	300	100	40
PMF-Stir-400	21.5	100	66	400	100	40
PMF-Temp-25	21.5	100	66	500	25	40
PMF-Temp-40	21.5	100	66	500	40	40
PMF-Temp-60	21.5	100	66	500	60	40
PMF-Temp-80	21.5	100	66	500	80	40
PMF-Temp-90	21.5	100	66	500	90	40
PMF-Time-0	21.5	100	66	500	100	0
PMF-Time-5	21.5	100	66	500	100	5
PMF-Time-10	21.5	100	66	500	100	10
PMF-Time-20	21.5	100	66	500	100	20
PMF-Time-30	21.5	100	66	500	100	30
PMF-Time-120	21.5	100	66	500	100	120

^aMolar ratio corresponding to melamine; ^bCalculated from mass of Ludox[®] HS-40 dispersion divided by total mass of melamine + paraformaldehyde + Ludox[®] HS-40.

2.3.8. Purification of the PMF samples

The PMF particles were processed in two possible ways, depending on whether the SiO₂/PMF hybrid particles (H-PMF) or the pure, porous PMF particles (P-PMF) were to be obtained after removal of the template.

Purification of H-PMF samples: The sediment was transferred into a 1 L vessel with ultrapure water. For three times this vessel was filled to a total volume of 1 L with ultrapure water and shaken for 24 hours at room temperature. Subsequently the particles sedimented and were decanted and freeze-dried. As these particles still contain the silica nanoparticles, these samples are called hybrid PMF (H-PMF) samples.

Purification of P-PMF samples: To obtain the pure PMF particles, the sediment of the reaction mixture was transferred into a 1 L vessel and filled with 1 M NaOH solution to remove the silica particles. The solution was shaken for 24 hours. The washing procedure with 1 M NaOH was repeated two more times. The particles were then transferred to a Spectra/Por™ 2 dialysis bag (Spectrum Chemical Mfg. Corp., New Brunswick, USA) and dialyzed with ultrapure water. The resulting particles were freeze-dried.

Centrifugal separation of P-PMF-Col: To obtain the P-PMF-Col particles, P-PMF-Time-0 particles were centrifuged in four repetitive steps, each with a centrifugation of differing duration at 395 rpm (corresponding to a relative centrifugal field of $30 \times g$) and subsequent redispersion. The first and second centrifugation were carried out for 25 min, the third centrifugation for 15 min and the last centrifugation for 5 min. After each centrifugation, the precipitate was separated from the supernatant, redispersed in ultrapure water for 15 min by ultrasonication in a bath. The last precipitate was named P-PMF-Col.

2.4. Water treatment experiments

2.4.1. Batch adsorption experiments with K₂Cr₂O₇ solution

For the kinetic and isotherm experiments, 0.03 g of the adsorbent material was placed into a 50 mL centrifuge tube. Subsequently, 30 mL of the adsorptive solution was added to every sample. The pH of the samples was not adjusted. The samples were then placed on a shaker at 250 rpm at 25 °C for the specified time. Subsequently, the samples were centrifuged once for 1 min at 10000 rpm (corresponding to a relative centrifugal field of $10509 \times g$) and one more time for 4 min at 10000 rpm to ensure complete separation of the supernatant from residual PMF. For the kinetic studies, adsorption experiments were conducted using an initial concentration of 100 mg/L Cr₂O₇²⁻ from K₂Cr₂O₇ at different shaking times ranging between 5 to 1440 min. For the adsorption isotherm, varying concentrations were tested for an adsorption time of 240 min. The supernatant of the samples after the adsorption and the initial concentrations of the adsorptive solutions were analyzed by ICP-OES. The pH of the solutions was determined.

2.4.2. Column adsorption experiments with K₂Cr₂O₇ solution

The column sorption experiments were carried out in a glass column (Omnifit®, Diba Industries, Danbury, USA) with a diameter of 6.6 mm and variable length of up to 12 cm. The column was closed on both sides with a glass frit and a PTFE membrane (pore size 10 µm). 100 mg of the particles were transferred to the column as dispersion in ultrapure water, while the column was fixed in vertical position. The column volume was then decreased until it was packed neatly and without any air inside. The resulting bed length was approximately 1.0 cm, which results in a column dead volume of 0.342 mL. The particles in the column were flushed with ultrapure water for 2 h with a flow rate of 0.5 mL/min. For the sorption experiment itself,

the K₂Cr₂O₇ solution with 5.2 mg/L Cr₂O₇²⁻ was fed continuously to the column by a peristaltic pump with a volume flow of 0.5 mL/min from a storage vessel. The adsorptive was flowing through the column from the bottom to the top to prevent diffusion effects and was then collected as eluate. Each sample taken consisted of 5 mL eluate collected within 10 minutes. The pH of each sample was determined and the concentration of Cr⁶⁺ and K⁺ ions was analyzed by ICP-OES. The data points were assigned to the mean time between the start and end time of the respective sample's collection. The achieved adsorption capacity Q_m was also calculated from the area below the retention curve in dependence of the eluate volume.

2.5. Theoretical model

To determine the sorption efficiency of the PMF samples, the concentration of the adsorbed Cr⁶⁺ in equilibrium were detected by ICP-OES. The obtained concentrations were used for the calculation of percentage adsorption (Eq. (8.1)). Hereby, c₀ is the concentration of the respective ion in the initial solution and c_{eq} is the concentration after reaching equilibrium.

$$\text{adsorption (\%)} = 100\% \times \frac{c_0 - c_{eq}}{c_0} \quad (8.1)$$

The respective sorption capacity q_{eq} in equilibrium was calculated as follows:

$$q_{eq} = \frac{(c_0 - c_{eq}) \times V_L}{m_A} \quad (8.2)$$

V_L refers to the given volume of the adsorptive solution and m_A to the mass of the sorbent material used in the experiment.

Different isotherm models can be applied to evaluate the adsorption process in detail. We chose to use non-linear isotherm equations for this, as linearization is changing dependent and independent variables. Furthermore, linearization transforms error values in unpredictable ways e.g. by application of logarithms [26–29].

The evaluation of the adsorption kinetics was modeled with the pseudo-first (Eq. (8.3)) [30] and pseudo-second order (Eq. (8.4)) [31] kinetic model. q_{eq,t} refers to the achieved adsorption capacity at the time t.

Pseudo-first order:

$$q_{eq,t} = Q_m(1 - \exp(K_1 \times t)) \quad (8.3)$$

Pseudo-second order:

$$q_{eq,t} = \frac{Q_m^2 \times K_2 \times t}{1 + Q_m \times K_2 \times t} \quad (8.4)$$

Here, Q_m describes the maximum adsorption capacity and K₁ and K₂ are the rate constants for the pseudo-first and pseudo-second order, respectively [29].

For evaluation of the adsorption in equilibrium over different initial concentrations, the Langmuir, Sips and Dubinin-Radushkevich equation was applied in fitting. The first model used is the Langmuir isotherm model [32], shown in Eq. (8.5). K_L refers to the Langmuir equilibrium constant and Q_m to the maximum adsorption capacity [33,34]. This equation was directly used in the fitting procedure.

$$q_{eq} = \frac{Q_m \times K_L \times c_{eq}}{1 + K_L \times c_{eq}} \quad (8.5)$$

The Sips model (Eq. (8.6)) [35] was chosen as it represents a combination of the Langmuir and Freundlich isotherm, extending the energetically homogeneous monolayer adsorption expressed by Langmuir with the energetically heterogeneous adsorption, possible also in multilayers expressed by the Freundlich model via its model exponent n [34].

$$q_{eq} = \frac{Q_m \times K_L \times c_{eq}^n}{1 + K_L \times c_{eq}^n} \quad (8.6)$$

The Dubinin-Radushkevich isotherm model [36] in its final non-linear form, which was used for fitting, can be seen in Eq. (8.10). In the original isotherm Eq. (8.7), ε represents the Polanyi potential while β_{DR} is the activity coefficient [33,34]. ε can also be expressed by Eq. (8.8) with c_s representing the solubility of the adsorbate.

$$q_{eq} = Q_m \times \exp(-\beta_{DR} \times \varepsilon^2) \quad (8.7)$$

$$\varepsilon = RT \times \ln\left(\frac{c_s}{c_{eq}}\right) \quad (8.8)$$

While c_s is not easily determinable, an exchange of the term inside the logarithm c_s/c_{eq} for the term $1 + 1/c_{eq}$ is favorable as pointed out by Zhou [37]. However, this exchange only leads to the same numerical solution with two strict requirements: First, c_{eq} needs to be much smaller than c_s . Second, this exchange requires the use of mol/L concentrations for the fitting. Both requirements were met in our modeling. With this, the following term for the Polanyi potential is obtained:

$$\varepsilon = RT \times \ln\left(1 + \frac{1}{c_{eq}}\right) \quad (8.9)$$

In Eq. (8.10), the final non-linear form of Dubinin-Radushkevich is shown, which was used for the fitting procedure.

$$q_{eq} = Q_m \times \exp\left(-\beta_{DR} \times \left(RT \times \ln\left(1 + \frac{1}{c_{eq}}\right)\right)^2\right) \quad (8.10)$$

β_{DR} as the activity coefficient is related via Eq. (8.11) to the mean free energy of adsorption $E_{ads,DR}$.

$$E_{\text{ads,DR}} = \frac{1}{\sqrt{2 \times \beta_{\text{DR}}}} \quad (8.11)$$

The column adsorption experiments were modelled via the Thomas model [38,39], the Bohart-Adams model [40,41] and the Yoon and Nelson model [42]. For that, the non-linear equations were used because of problems arising described above. All equations are based on the same type of sigmoidal function, whose general form is shown in Eq. (8.12) as the non-linear equation with c_e as effluent concentration, K as the respective model's rate constant and $E(t)$ as the model's exponent term depending on the time t . The exponential term $E(t)$ of each model differs as shown in Eq. (8.13) – (8.15) [43].

$$\frac{c_{\text{eq}}}{c_0} = \frac{1}{1 + \exp(K \times E(t))} \quad (8.12)$$

Bohart-Adams:

$$E = N_0 \times \frac{h}{u} - c_0 \times t \quad (8.13)$$

Thomas:

$$E = \frac{Q_m \times m_A}{v} - c_0 \times t \quad (8.14)$$

Yoon and Nelson:

$$E(t) = t_{0.5} - t \quad (8.15)$$

The generalized form in Equation 8.9 shows that, for the non-linear fit, the same fit will be achieved for all models as also pointed out by literature [43]. Only when linearization is applied, the respective change in dependent and independent variables as well as the unpredictable transformation of errors as well as weighting in terms of R^2 values by application of the logarithm will lead to a differing curve progression. However, from the different underlying exponential terms in the models, different parameters for the column kinetics can be determined. In the Bohart-Adams model, the constant h represents the bed length (1 cm), u is the superficial velocity cm/min and c_0 is the initial concentration (5.2 mg Cr₂O₇²⁻/L). Here, the rate constant K as well as the saturation capacity N_0 as mass per bed volume can be derived. The same parameters can be derived from the Thomas model with v being the flow rate (0.5 mL/min) and m_A being the mass of adsorbent. From the Yoon and Nelson model, the break through time $t_{0.5}$ can be derived as well as the models rate constant.

Another sigmoidal kinetics model that has been found in literature is the Weibull equation, shown in Eq. (8.16) [44] with the model parameters a and b .

$$\frac{c_e}{c_0} = 1 - \exp\left(-\left(\frac{t}{a}\right)^b\right) \quad (8.16)$$

All isotherm fittings were performed in Origin 2022 with orthogonal distance regression algorithm until $\chi \leq 10^{-9}$ or χ no longer changed. The reduced χ^2 value ($\chi^2_{red.}$) was used for evaluation of the correlation of the respective fits to the experimental data.

3. *Results and Discussion*

To investigate the templating process of PMF with SiO₂ NPs, syntheses with systematic variation of single parameters were carried out. In general, a dispersion polymerization of the monomers melamine and formaldehyde in water was used, with two steps: In the first heating step at 50 °C for 40 minutes, a precursor solution of oligomeric methylol melamine species is formed [15,19,45]. While melamine is only slightly soluble in hot water, the precursor species is highly hydrophilic [15,19]. In the second step, oxalic acid as catalyst is added and the temperature is increased to 100 °C, which starts the polycondensation reaction leading to the cross-linked, more hydrophobic PMF. Together with the catalyst, a dispersion of aqueous SiO₂ NPs is added to the reaction mixture as hard template. The formed SiO₂/PMF hybrid particles (hereafter H-PMF) can be etched with 1 M NaOH solution after the synthesis to obtain the mesoporous, pure PMF particles (hereafter P-PMF).

The main goal of this study was to obtain multi μ m-sized particles with high porosity and uniform morphology. To meet this goal, a deeper understanding of the complex multi-component system consisting of melamine, formaldehyde, the PMF-precursor, the PMF polymer and the silica template and water as dispersant is crucial. First, we must consider that the polymerization of the precursor to the PMF resin is mainly dependent on the catalyst concentration (H⁺) and the temperature. Second, the surface charge of the SiO₂ NPs and PMF precursor and resin species will greatly influence the interaction between both phases, therefore being decisive for the successful templating. Here, the SiO₂ surface charge is dependent from the pH value, as it is negatively charged only when pH is above its isoelectric point of approximately 2.0 [46–48]. In contrast, the PMF precursor as well as the PMF resin should be positively charged below a pH of around 7 due to their high amount of amino groups [14,23,49]. Third, the PMF precursor, which is hydrophilic, drastically increases its hydrophobicity by polymerization caused by elimination or transformation of hydrophilic groups and methylolamines to ether or methylene bridges. This in turn may inhibit its interaction with water as dispersant as well as the more hydrophilic silica.

To investigate the dependence of the above-mentioned parameters on the particle and pore formation, we chose one synthesis as starting point for subsequent variations (PMF-Std) as standard. In general, the varied parameters can be grouped into variation of the reaction mixture and variation of the synthesis process. To analyze the interaction with the dispersant, we included a synthesis with a higher amounts of water (PMF-Water), which partially resemble particles from our previous publications [14,22]. To test the considerations about

the polymerization speed, we modified the amount of catalyst in the reaction mixture (PMF-Cat) as well as changed the polymerization temperature (PMF-Temp). To evaluate the behavior of the SiO₂ NPs as template and potential Pickering surfactant, differing amounts of colloidal silica dispersions were used (PMF-SiO₂). The stirring speed was varied to analyze potential influence of a better homogenization of the reaction mixture and the input of differing amounts of kinetic energy (PMF-Stir). Lastly, we changed the duration of the prepolymerization step, which is decisive for the precursor and oligomer formation as a separate first step (PMF-Time).

3.1. PMF-Std

First, the morphology of the PMF-Std particles was thoroughly investigated in detail for a later comparison to the modified particles. SEM images show spherical particles of approximately 1 μm that are loosely aggregated because of the freeze-drying process for both the hybrid H-PMF particles as well as the etched P-PMF particles (see Figure 8.1b and c).

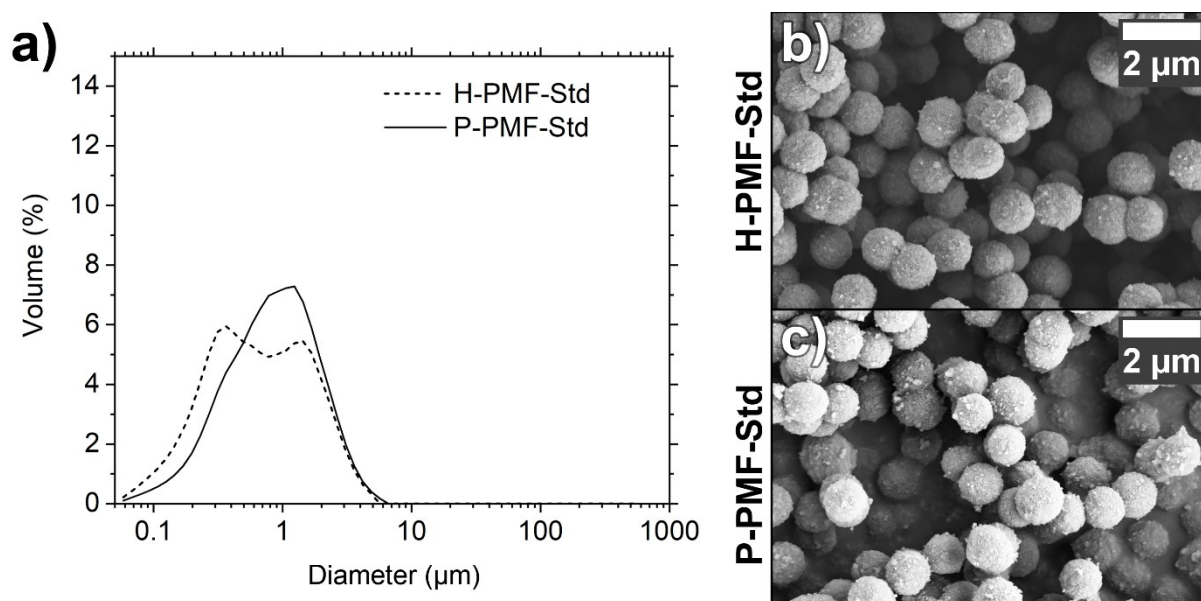


Figure 8.1. a) Particle size distribution of H-PMF-Std (dashed line) and P-PMF-Std (solid line), b) SEM image of H-PMF-Std, and c) SEM image of P-PMF-Std.

The particle diameter was determined by laser diffractometry (Figure 8.1a). Here, the unpurified H-PMF-Std sample shows a bimodal particle size distribution with two overlapping peaks at maxima of approximately 360 nm and 1.4 μm , respectively. The etched P-PMF-Std particles in comparison show a monomodal size distribution with a diameter maximum at approximately 1 μm . The second peak of the hybrid material around 1.4 μm therefore correlates with aggregates of several singular PMF particles with either SiO₂ NPs or other PMF particles while the small-diameter peak can be attributed to loose aggregates of left-over silica. Here, SiO₂ NP aggregation can be caused by the freeze-drying procedure. However, the

PMF particles are only weakly connected and not coalesced as it is visible from SEM (Figure 1b and c) and TEM images (Figure 8.2a and d). In the etching process, these connections are weakened while also SiO₂ NPs are removed from the particle surface which could have been a potential anchor or bridging point. Thereafter, a monomodal particle diameter is achieved that is perfectly matching the SEM images. However, no particle diameters of several μm can be obtained from this synthesis route.

To understand the particle formation and see in which time dimensions the reaction takes place, we *ex situ* investigated the particle size during synthesis (Figure S2). During the synthesis, the particle formation can be seen visually as the initially opaque reaction mixture (with added silica and catalyst) turns slightly turbid after 8.5 minutes with increasing intensity until at approximately 10 min the reaction mixture is completely white. Laser diffractometry measurements taken before the whitening of the reaction are not possible as the needed detector obscuration cannot be achieved for meaningful results. Even at 9 min, the needed detector obscuration cannot be matched. However, first measurements were possible at 11 min after template and catalyst addition. Here, a particle diameter between 300 and 500 nm can be seen. Already after 18 minutes, a particle diameter of 1 μm is reached, which stays constant until the reaction was finished. The broadening of the peak over the reaction time implies potentially formation of small amounts of SiO₂ NP aggregates, especially in the range below 100 nm. Furthermore, it shows that some particles are slowly further increase their diameter.

From TEM images from thin sections of embedded H-PMF-Std particles, the morphology of the nitrogen rich PMF resin and the silica nanoparticles can be seen as well as the porosity from the P-PMF-Std samples (Figure 8.2). With energy-filtered TEM (EFTEM) of the hybrid sample, it is visible that the particles are comprised of a core of several SiO₂ NPs, surrounded by a shell of PMF resin almost without any included silica. Outermost is a shell with SiO₂ NPs, which are embedded in the PMF resin. These findings indicate differing growing conditions over the formation time. As the single PMF particles all exhibit a monomodal diameter as well as a uniform morphology, it can be concluded that the particles are all growing simultaneously in the dispersion polymerization with three different growing steps.

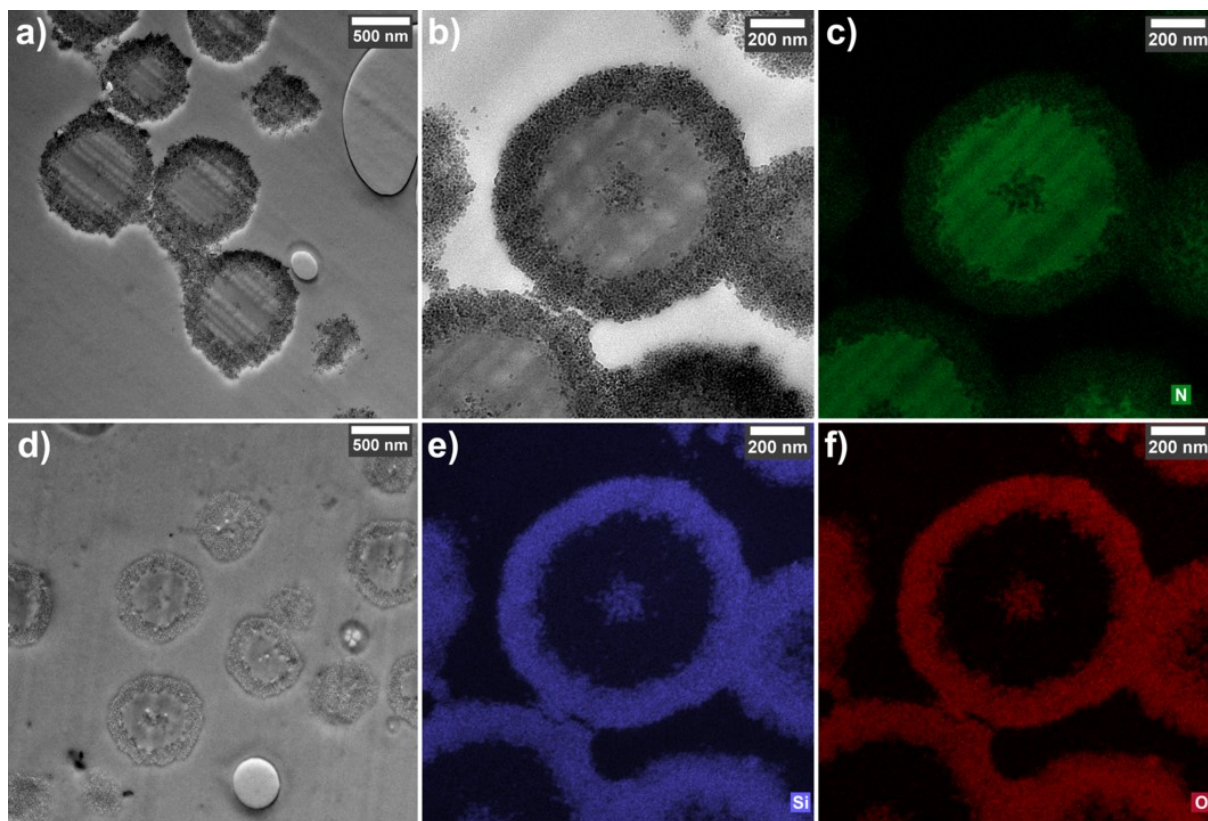


Figure 8.2. TEM images of ultrathin-sections of a) H-PMF-Std, and d) P-PMF-Std; b) TEM image of an ultrathin-section of H-PMF-Std with respective elemental maps for c) nitrogen, e) silicon, and f) oxygen from EFTEM measurements.

The formation of these kinds of particles can be well explained by a three-step mechanism that we propose at this point and further discuss and prove more deeply in the following sections. In short, the first step includes the nucleation of the PMF precursor molecules at the addition of the catalyst, seemingly facilitated by silica. This step yields the observed SiO₂/PMF core. In the second step, the particles grow a PMF shell, probably showing high colloidal stability up to a critical diameter as expected from a typical dispersion polymerization. Up to this point, the ongoing polymerization has two effects: On one hand, the growing PMF core increases its hydrophobicity by progressing cross-linking and elimination of free methylolamine groups. On the other hand, the initially high concentration of precursor molecules decreases. These molecules are hydrophilic and can also colloidally stabilize the growing particles by physical interactions with the resin. Therefore, it seems logical that the particles, which were stabilized by the low-molecular weight precursor in the first growing step, lose their colloidal stability in water at a certain diameter and certain precursor concentration. This in turn leads to step tree, in which silica acts as a colloidal stabilizer for the particles minimizing potential surface energy similarly to Pickering emulsions [24]. In order to be incorporated by the resin, the PMF structure must grow continuously and rapidly enough around the SiO₂ NPs, as the stabilization of these must be considered as continuous

equilibrium between attachment to and detachment from the PMF/water interface. The negative surface charge of the SiO₂ particles allows for a strong interaction towards the positively charged amino groups of the resin giving the particles a negatively charged and hydrophilic outer shell and ensuring colloidal stability. The effect of the silica's surface charge can still be seen from the streaming potential-vs.-pH curves of the negatively charged SiO₂/PMF hybrid particles, which our author team reported recently [14]. Here the respective isoelectric points of the hybrid particles were between pH of 3.7 to 4.8.

The N₂ sorption measurements (see Figure 8.3a, black curve) of the etched P-PMF-Std particles are typical for a well-connected pore system, recognizable by the type IV isotherm showing a parallel and steep hysteresis in the relative pressure range of $0.5 < p/p_0 < 0.85$ [50–52]. From a QSDFT fit of the adsorption branch, a main pore diameter around 17 nm was determined (see Figure 8.3b). P-PMF-Std reached a specific surface area of 271 m²/g and a total pore volume of 0.43 cm³/g.

The high specific surface area and pore volume of the sample as well as the occurrence of three distinct growth steps in the particle formation presents a viable starting point for the mechanistic investigation of the templating procedure.

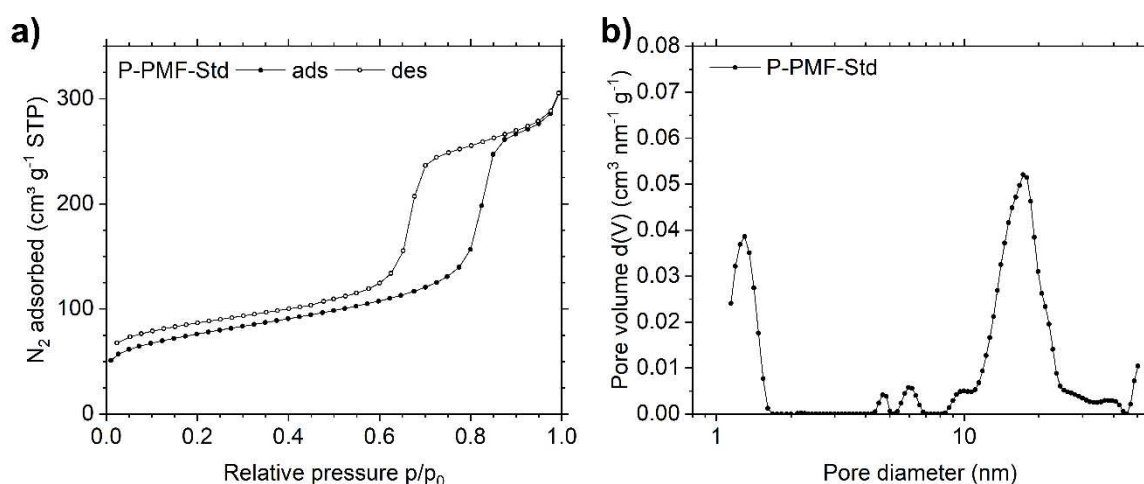


Figure 8.3. a) Nitrogen (N₂) de-/adsorption isotherm measured at 77 K for P-PMF-Std, b) Pore size distribution (PSD) analysis for the adsorption branch was calculated by using QSDFT (quenched solid-state density functional theory) model for nitrogen on carbon with slit/cylindrical/sphere pores. Data points in the adsorption and desorption branch of the isotherms are indicated by filled and empty symbols, respectively.

3.2. Influence of the reaction mixture composition

From the initial PMF-Std synthesis, three parameters were varied separately as there are the amount of water as dispersant, the amount of oxalic acid as catalyst and the amount of SiO₂ NPs as template.

3.2.1. Influence of the water amount

Doubling the amount of water in the reaction of P-PMF-Water-2 leads to uniform particles with diameters of around 400 nm (see Figure 8.4). Nitrogen sorption measurements are showing a high specific surface area (330 m²/g, see Figure S3 and Table S2) with a pore diameter matching the one of P-PMF-Std. This was also reported by similar preparation routes in previous publications [14,22]. However, TEM analysis of thin-sections of embedded particles show a homogeneous distribution of SiO₂ NPs over the complete particle diameter. This is in agreement for the distribution of pores in thin-sections of P-PMF-Water-2 (see Figure 8.4d – e). Here, no PMF shell is seen in the particles due to the significantly lower precursor concentration in the reaction mixture. Further increase of water as dispersant, as for PMF-Water-3, shows similar diameters to P-PMF-Water-2, although the size distribution is less uniform (Figure 8.4 and Figure S4 and S5).

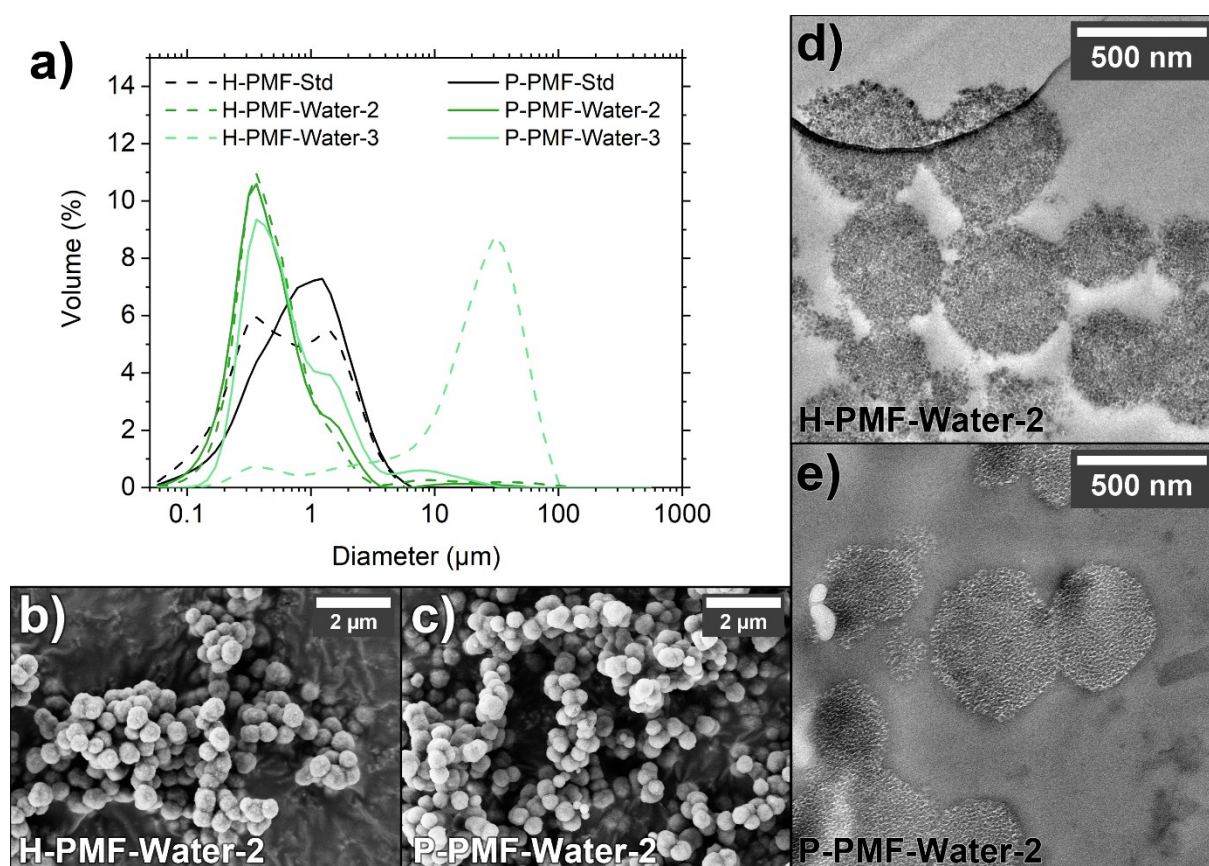


Figure 8.4. a) Particle size distribution of PMF-Water-2 (dark green), PMF-Water-3 (light green) and PMF-Std (black) with H-PMF samples shown as dashed lines and P-PMF samples as solid lines. b) – c) SEM image of b) H-PMF-Water-2 and c) P-PMF-Water-2. d) – e) TEM images of ultrathin-sections of d) H-PMF-Water-2 and e) P-PMF-Water-2. SEM and TEM images of PMF-Water-3 can be seen in Figure S4 – S9.

From TEM, the same internal morphology with incorporated SiO₂ can be seen for H- and P-PMF-Water-3 particles (Figure S6 – S9). Thus, the low initial concentration of PMF precursor, stabilization via SiO₂ as a Pickering surfactant takes place over the complete duration of the

particle formation. This leads to the inclusion of silica among the complete cross-section. Lowering the amount of water significantly further was not possible as this inevitably lead to an inhomogeneous reaction mixture.

3.2.2. Influence of the catalyst amount

To test the influence of the catalyst on the particle synthesis, half and double the amount of oxalic acid were used (standard was 21.5 mol%, referring to melamine). This corresponds to 10.7 mol% for PMF-Cat-11 with and 43.1 mol% PMF-Cat-43, respectively. From the particle size distribution, both P-PMF-Cat samples show a bimodal particle size distribution, which is well in agreement SEM images. The lower amount of oxalic acid as catalyst mainly leads to the formation of singular spherical particles of approximately 1.4 μm together with extremely small particles in the range of several hundred nm (Figure 8.5). From the SEM images of the H-PMF-Cat-11 particles (Figure S10), an extremely rough and uneven surface can be seen. So it seem logical that either these outgrowths on the surface are broken apart from the main particles or grew in dispersion and later on attached to the particle surface. Thus, these subunits or debris correspond to the first peak in the particle size distribution. In contrast, P-PMF-Cat-43 shows a main particle size around 6 μm . From SEM images it is apparent that these particles consist of uncontrollably coalesced primary particles, which merged at different times of the formation, as seen by differing degrees of coalescence.

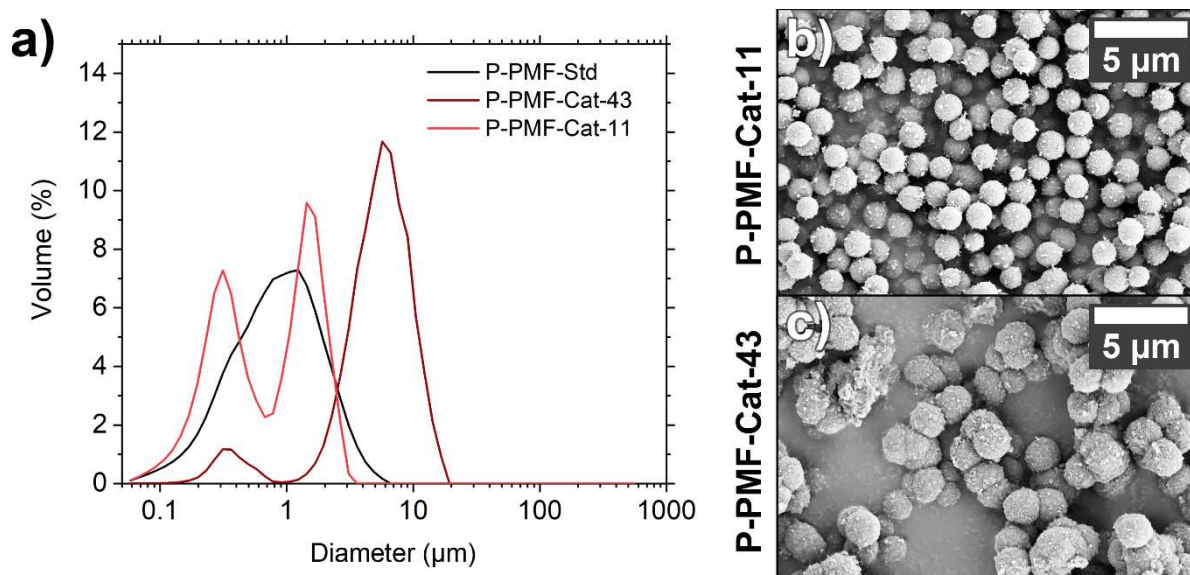


Figure 8.5. Particle size distribution of the sample from the a) P-PMF-Cat with P-PMF-Std is shown in black, P-PMF-Cat-43 in dark red, and P-PMF-Cat-11 in light red. b) SEM image of P-PMF-Cat-11, c) SEM image of P-PMF-Cat-43. The corresponding particle size distribution of the hybrid particles with SEM images can be seen in Figure S10.

The porosity analysis shows a slight decrease in specific surface area for P-PMF-Cat-43, whereas S_{BET} dropped significantly for P-PMF-Cat-11 (Figure S11 and Table 8.2). The main pore size of P-PMF-Cat-11 is slightly decreased, while P-PMF-Cat-43 exhibited an unchanged pore

SiO₂ Nanospheres as Surfactant and Template in Aqueous Dispersion Polymerizations Yielding Nanoporous Resin Particles

structure in comparison to P-PMF-Std. The shape of the hysteresis proves that the same kind of pore system is formed in all samples. Thus, as the type and size of pores is not changed, the lower specific surface area of P-PMF-Cat-11 as well as P-PMF-Cat-43 is caused by less inclusion of silica.

Table 8.2. Surface area (S_{BET}), pore volume (PV), and micro pore volume (MPV) of the P-PMF-Cat and P-PMF-SiO₂ samples.

Sample code	S_{BET} (m ² g ⁻¹) ^[a]	PV (cm ³ g ⁻¹) ^[b]	MPV (cm ³ g ⁻¹) ^[c]
P-PMF-Std	271	0.43	0.10
P-PMF-Cat-11	160	0.29	0.06
P-PMF-Cat-43	238	0.43	0.09
P-PMF-SiO ₂ -49	190	0.31	0.07
P-PMF-SiO ₂ -10	194	0.36	0.07
P-PMF-SiO ₂ -0	6	0.01	0

^[a]Surface area calculated from N₂ adsorption isotherm using BET equation. ^[b]Pore volume (PV) calculated from N₂ uptake at $p/p_0 = 0.95$. ^[c]Micro pore volume (MPV) calculated from N₂ uptake at $p/p_0 = 0.10$.

From this data, it is visible that the catalyst amount used for P-PMF-Std represents an optimum. A decrease in catalyst concentration leads to a slower growth of the particles. The same kind of outer sphere stabilization by SiO₂ NPs as Pickering surfactant is seen from the spherical shape of the particles. However, the lower polymerization speed leads to less entrapping of the SiO₂ NPs in the growing resin before their detachment from the interface.

A higher catalyst amount in contrast leads to a more rapid polymerization. As the SiO₂ NPs need a certain time for the attachment on the PMF/water interface, an acceleration of the polymerization leads to the fact that the surface is not saturated with SiO₂ NPs and thus is susceptible to coalescence by collisions. As the particle formation already occurs in less than 20 minutes as seen by the kinetic study of P-PMF-Std, an acceleration is unsuitable for the formation of uniform particles.

3.2.3. Template amount

In our recent publication, we showed that increasing the template amount leads to a more chaotic, unordered pore structure by inclusion of silica aggregates and also partial pore collapse when SiO₂ NPs exit the respective cavity before they are completely confined by polymerization. Furthermore, a higher amount of silica in the reaction mixture decreased the main particle diameter because of increased Pickering stabilization [14]. However, no experiments with less template were conducted before under these conditions, thus we included syntheses with 49 wt.% (P-PMF-SiO₂-49) and 10 wt.% (P-PMF-SiO₂-10) Ludox® HS-40 and one synthesis completely without silica (P-PMF-SiO₂-0).

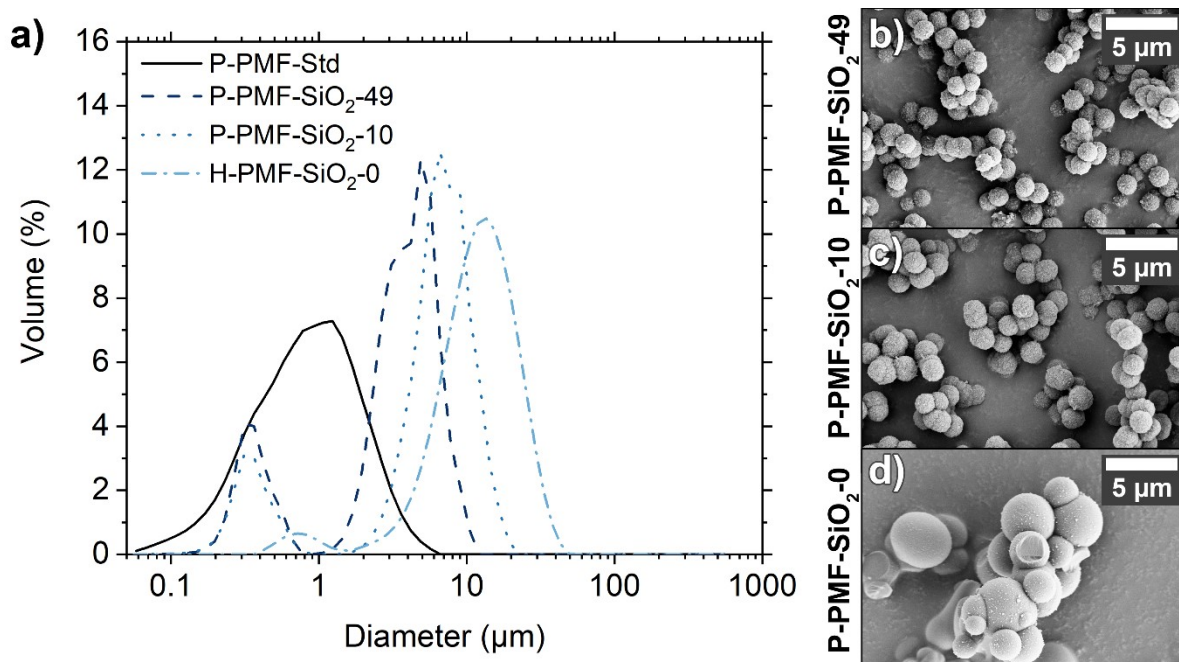


Figure 8.6. Particle size distribution of the sample from the a) P-PMF-SiO₂ series. P-PMF-Std is shown in black (solid line), P-PMF-SiO₂-49 in dark blue (dashed line), P-PMF-SiO₂-10 in medium blue (dotted line), and P-PMF-SiO₂-0 in light blue (dash-dot line). b) SEM image of P-PMF-SiO₂-49, c) SEM image of P-PMF-SiO₂-10, and d) SEM image of P-PMF-SiO₂-0. The corresponding particle size distribution and SEM images of the H-PMF-SiO₂ hybrid particles can be seen in Figure S12.

Particle size measurements (Figure 8.6) show that lowering the template amount significantly increases the particle diameter. A higher degree of coalescence is visible in SEM images, while the primary particle diameter only slightly changes.

As expected, a general decrease in specific surface area can be seen with lower template amounts in N₂ sorption, whereby an unporous character is shown by P-PMF-SiO₂-0 (Figure S13 and Table 8.2). Interestingly, both samples P-PMF-SiO₂-49 and P-PMF-SiO₂-10 exhibit a similar S_{BET} value and pore size, indicating that the SiO₂ inclusion of both samples reaches similar levels. This may show the high affinity of the SiO₂ NPs, as even low template amounts are included in the hybrid particles to a high degree.

3.3. Variation of the process parameters

Different synthesis process parameters were varied which are discussed in the following. Besides the polymerization temperature and precursor formation time, the stirring speed was tested as the simplest parameter. Here, we found that the stirring speed does not exhibit any significant influence on the synthesis. The results of the P-PMF-Stir series are therefore only presented in Section 2.5 in the supporting information.

3.3.1. Influence of polymerization temperature

By lowering the temperature of the second polymerization step, the polymerization velocity decreases. Furthermore, entropic processes are inhibited. As both particle size

distributions for the H-PMF-Temp samples as well as their etched counterpart show, the particle size of P-PMF-Temp-40 and P-PMF-Temp-25 significantly increased, while the particle diameter for the other samples is approximately in the same regime as PMF-Std (Figure 8.7). After etching, the particle diameters show a clear trend of increasing the main particle size with lowering the temperature.

SEM images of all etched (Figure 8.7) and hybrid particles (Figure S17 – S21) show that lowering the temperature for polymerization seemingly only has small influence on the diameter of the primary particles except for PMF-Temp-25 with significantly smaller primary particles. The primary particles show the typical spherical shape with diameters in the range of 1 μm or slightly lower. However, using a temperature of 40 $^{\circ}\text{C}$ or 25 $^{\circ}\text{C}$ leads to considerably more coalesced particles, which explains the peak in the multi- μm range in the particle size distribution of both samples. However, as the primary particle size is still around 1 μm , the silica still interacts with the PMF particles in terms of Pickering-like stabilization. Otherwise, the formed primary particles are of higher diameter as proven from experiments without SiO₂ NPs in the reaction mixture (PMF-SiO₂-0 in section 3.2.3).

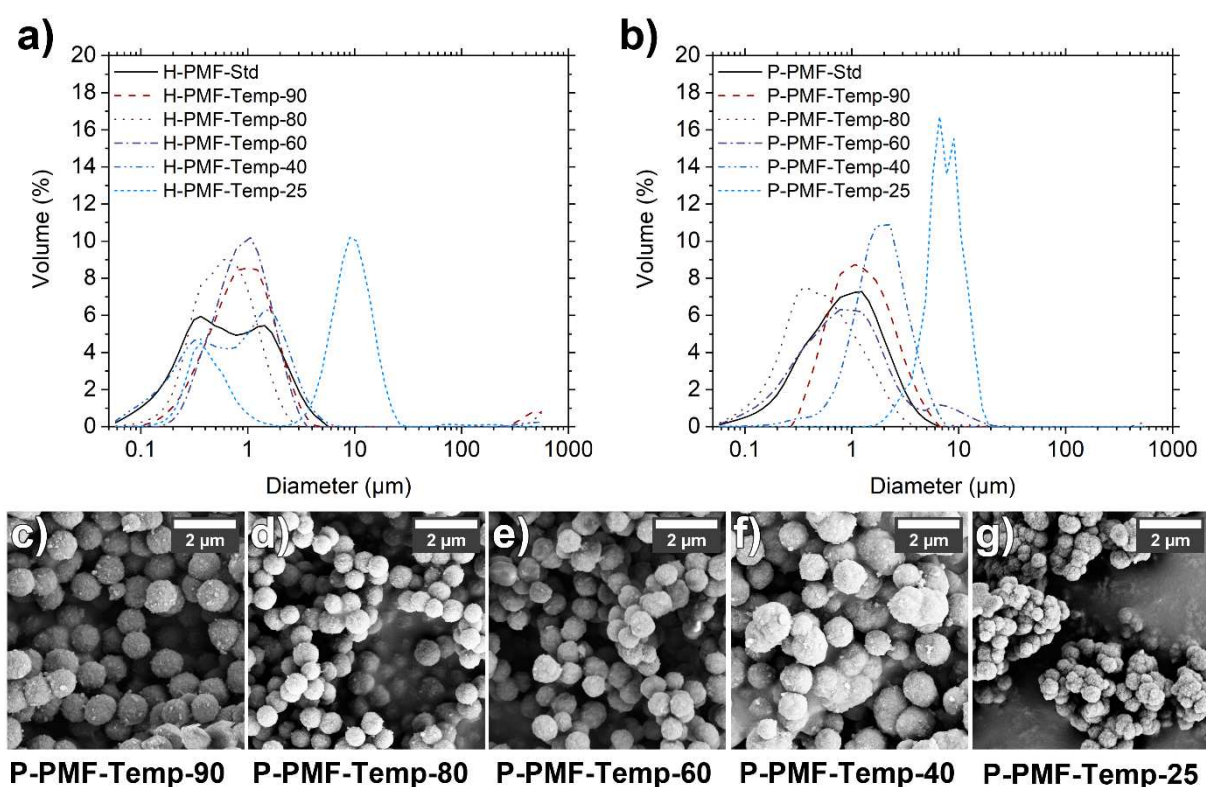


Figure 8.7. Particle size distribution of a) the H-PMF samples and b) the P-PMF samples (solid line) from the PMF-Temp series. P-PMF-Std is shown in black (solid line), P-PMF-Temp-90 in red (dashed line), P-PMF-Temp-80 in violet (dotted line), P-PMF-Temp-60 in dark blue (dash-dot line), P-PMF-Temp-40 in medium blue (dash-dot-dot line), and P-PMF-Temp-25 in light blue (short-dashed line). c) – g) SEM images of the P-PMF particles with c) P-PMF-Temp-90, d) P-PMF-Temp-80, e) P-PMF-Temp-60, f) P-PMF-Temp-40, and g) P-PMF-Temp-25.

When the polymerization temperature is changed, this significantly influences the porosity of the samples as seen from N₂ sorption experiments (Figure 8.8 and Table 8.3). Already at 90 °C, the specific surface area is decreased by 34%, at 60 °C the sample exhibits an unporous character. This directly correlates with a lower inclusion of SiO₂ NPs into the particle structure although the SEM images show that SiO₂ particles still interact with the outer surface.

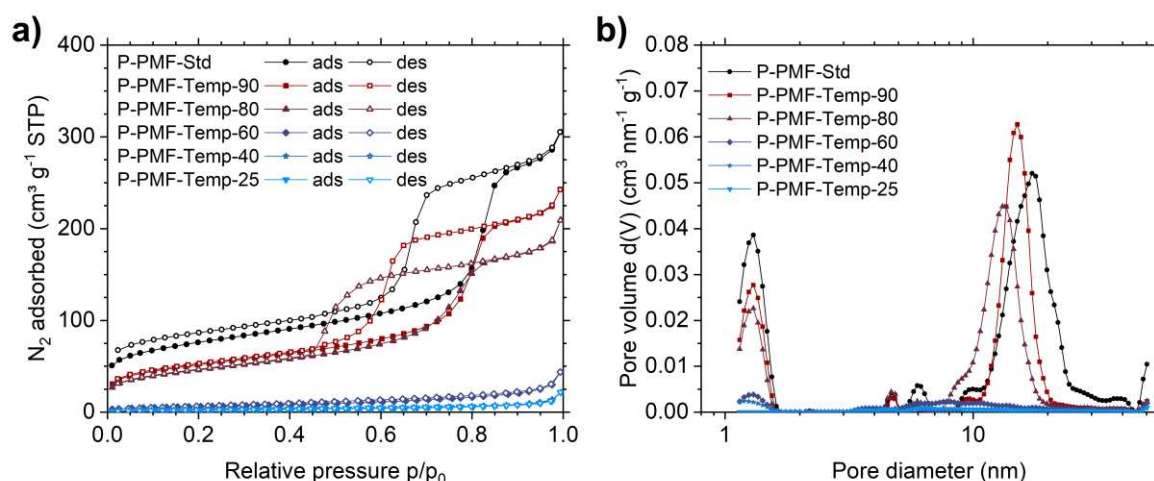


Figure 8.8. a) Nitrogen (N₂) de-/adsorption isotherms measured at 77 K for P-PMF-Temp samples, b) Pore size distribution (PSD) analysis for the adsorption branch was calculated by using QSDFT (quenched solid-state density functional theory) model for nitrogen on carbon with slit/cylindrical/sphere pores. Data points in the adsorption and desorption branch of the isotherms are indicated by filled and empty symbols, respectively. P-PMF-Std is shown in black as circles, P-PMF-Temp-90 in red as squares, P-PMF-Temp-80 in violet as upwards triangles, P-PMF-Temp-60 in dark blue as diamonds, P-PMF-Temp-40 in medium blue as stars, and P-PMF-Temp-25 in light blue as downwards triangles.

In general, a higher polymerization temperature should increase the kinetic energy of the SiO₂ NPs, thus lead to higher exchange of surface-adhered silica particles, which in turn makes it less probable for them to be enclosed by resin. However, the results show a contrary trend. The only explanation for this behavior is that SiO₂ NPs are still adsorbed on the PMF/water interface to a certain degree, but the strength of the binding interaction is lowered with temperature. As the silica particles exchange water molecules from the PMF particle's surface to attach, increased temperature and thus entropy should facilitate the exchange. By lower temperatures, this weakened attachment of SiO₂ to the interface leads to a higher exchange rate of the particles with dispersion, while the lowered polymerization speed is further lowering silica inclusion rates before desorption of a template particle. The pore size distribution also shows a trend towards lower pore diameters and broader distribution in general. This is caused by collapse of partially formed pores after the SiO₂ particle leaves the cavitation. This is also in good agreement with the proposed mechanism. These experiments further indicate that the SiO₂ NPs are not covered with PMF resin while dispersed and before

SiO₂ Nanospheres as Surfactant and Template in Aqueous Dispersion Polymerizations Yielding Nanoporous Resin Particles

attachment to the particle outer surface. Otherwise, PMF-covered SiO₂ NPs would still be included in the particle structure as long as the polymerization of PMF is ongoing.

Table 8.3. Surface area (S_{BET}), pore volume (PV), and micro pore volume (MPV) of the P-PMF-Temp samples.

Sample code	S_{BET} (m ² g ⁻¹) ^[a]	PV (cm ³ g ⁻¹) ^[b]	MPV (cm ³ g ⁻¹) ^[c]
P-PMF-Std	271	0.43	0.10
P-PMF-Temp-90	185	0.34	0.07
P-PMF-Temp-80	161	0.28	0.06
P-PMF-Temp-60	23	0.04	0.01
P-PMF-Temp-40	8	0.02	0.00
P-PMF-Temp-25	10	0.02	0.00

^[a]Surface area calculated from N₂ adsorption isotherm using BET equation. ^[b]Pore volume (PV) calculated from N₂ uptake at $p/p_0 = 0.95$. ^[c]Micro pore volume (MPV) calculated from N₂ uptake at $p/p_0 = 0.10$.

When comparing with the lower catalyst amount, also yielding in a slower polymerization, it can be seen that the inclusion of silica in the P-PMF-Cat-10 sample is comparable with P-PMF-Temp-80. For both samples, the primary particle shape is retained while lower porosity is exhibited.

3.3.2. Influence of the precursor formation time

As melamine is almost insoluble in water with slightly increasing solubility when heated, the formation of the hydrophilic precursor species is decisive to both, the polymerization process in general as well as the stability of other colloidal components in the reaction mixture. Therefore we modified the initial time of 40 min in this series to 120 min as longer period as well as shorter periods down to a one-pot synthesis style with 0 min.

In the particle size distribution from the H-PMF-Time samples, a significant change can be seen (see Figure 8.9). All H-PMF-Time samples show a peak at 360 nm, similar to one of the maxima exhibited by H-PMF-Std. Apart from this peak, the differing precursor formation time greatly influences the other peak shown by the samples.

With a longer reaction time, H-PMF-Stir-120 presents a peak at approximately 2 μm . Shortening the precursor formation time leads to broadening of the main sub- μm peak. Herein, H-PMF-Time-30 and H-PMF-Time-20 both exhibit a peak shoulder at a diameter of 600 nm. While H-PMF-Time-30 is almost unimodal with this peak shoulder, H-PMF-Time-20 additionally exhibits two small, broad peaks at diameters of 8 μm and 60 μm , respectively. This trend of larger diameter particles with lower reaction times further continues: H-PMF-Time-10 presents two broad peaks at 9 μm and 50 μm , H-PMF-Time-5 one peak at 25 μm and finally H-PMF-Time-0 a large peak at 12 μm . When comparing to the particle size distribution of the hybrid particles to the respective P-PMF samples, the apparent peaks do

not shift significantly in diameter. However, a shift of the intensities occurs as small SiO₂ NP aggregates are removed from the sample and silica-bridged particles are separated.

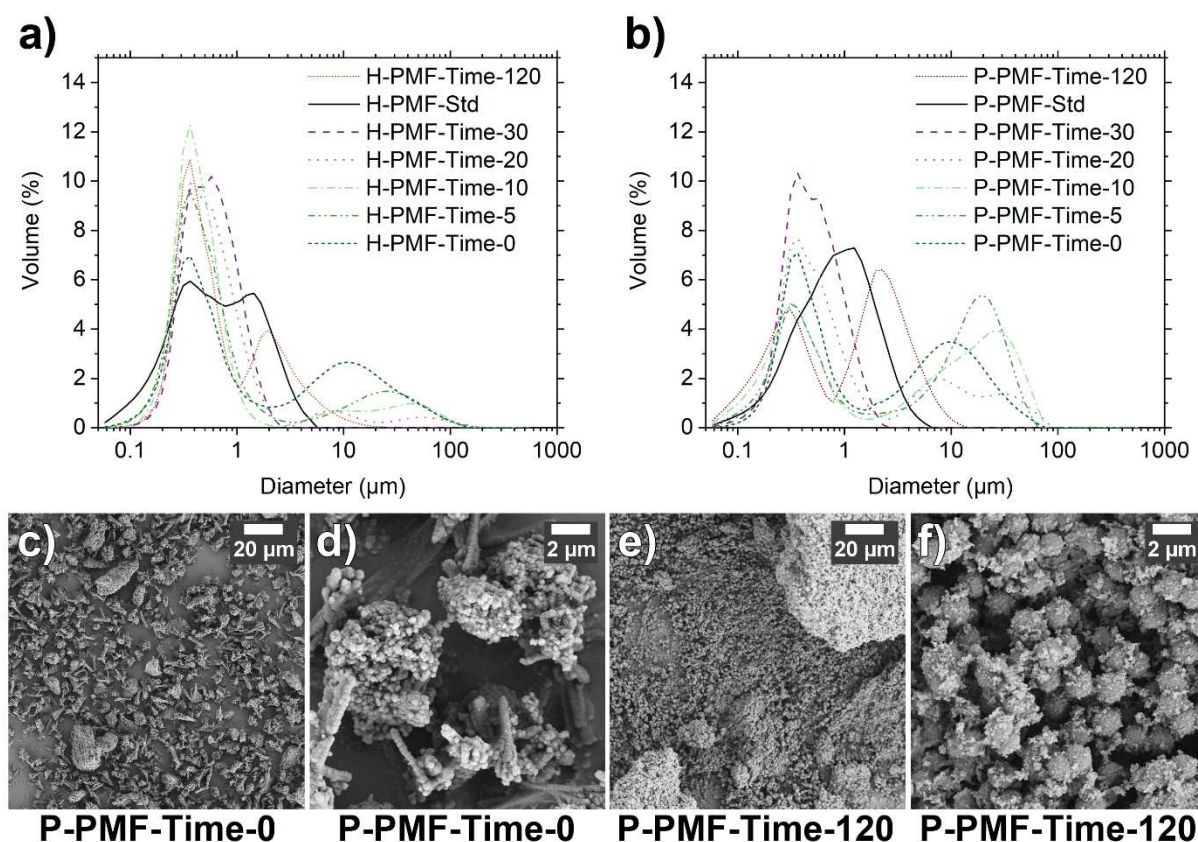


Figure 8.9. Particle size distribution of a) the H-PMF-Std and the H-PMF-Time samples and b) the respective P-PMF-Time samples after etching with NaOH. PMF-Std is shown in black (solid line), PMF-Time-120 in brown (short-dotted line), PMF-Time-30 in dark violet (dashed line), PMF-Time-20 in rose (dotted line), PMF-Time-10 in light green (dash-dot line), PMF-Time-5 in medium green (dash-dot-dot line) and PMF-Time-0 in dark green (short-dashed line). c) – f) SEM images of c) and d) P-PMF-Time-0, and of e) and f) P-PMF-Time-120. Images of all P-PMF-Time samples are presented in Figure S23.

Further insight in the particle formation can be gained by evaluating the shape of the particles by SEM imaging (see Figure 8.9 and Figure S23). In general, it is visible that the SEM images of the etched P-PMF-Time samples match the laser diffractometry measurements. In the images of the different samples, a drastic shift in morphology is noticeable. P-PMF-Time-30 show the closest optical match to the initial P-PMF-Std sample with uniform spherical particles. Seldom, coalescence of primary particles can be seen, potentially leading to the peak shoulder in the particle size distribution. A prolongation of the reaction time seemingly leads to rough particles, whose initial spherical shape is altered by outgrowths or pimples on the outer surface. Furthermore, coalescence of several particles are well visible leading to the 2 μm diameters measured. In the SEM images of P-PMF-Time-20, P-PMF-Time-10 and P-PMF-Time-5 largely varying particles of different dimensions can be

SiO₂ Nanospheres as Surfactant and Template in Aqueous Dispersion Polymerizations Yielding Nanoporous Resin Particles

seen. Besides the typical sub- μm spherical particles, spikey particles of several μm can be seen as well as much larger, coalesced aggregates thereof in the dimensions of tens of micrometers. P-PMF-Time-0 again shows a differing particle shape with a kind of branching, elongated primary elements (an image with medium magnification can be seen in Figure S22). The size and shape of the obtained particles is relatively similar.

To investigate if the templating of the particles was successful although large particle sizes were achieved, we measured the N₂ sorption isotherms (Table 8.4 and Figure S24). All samples show a very high porosity as it can be seen from the typical type IV isotherms. The achieved specific surface area of the P-PMF-Time particles all show values between 215 m²/g and 318 m²/g. Surprisingly, the particles synthesized with a precursor formation time with 10 min or less have only insignificantly decreased S_{BET} or even showed slightly higher values as presented by P-PMF-Time-20 (318 m²/g). The exhibited pore system is well-connected and accessible as it can be seen from the steep and parallel shape of the H1 hysteresis curve [50]. The derived pore size distribution shows that the pore diameter is slightly decreased by decreased pre-polymerization times. In contrast, P-PMF-Time-120 shows a significant decrease in specific surface area and a slight increase in its mean pore diameter. While P-PMF-Time-30 also shows a smaller specific surface area (215 m²/g), it fits in the trend of a decreased pore diameter shown by the other samples with decreased precursor formation time. These findings indicate that two different trends influence the templating process.

Table 8.4. Surface area (S_{BET}), pore volume (PV), and micro pore volume (MPV) of the PMF samples.

Sample code	S_{BET} (m ² g ⁻¹) ^[a]	PV (cm ³ g ⁻¹) ^[b]	MPV (cm ³ g ⁻¹) ^[c]
P-PMF-Std	271	0.43	0.10
P-PMF-Time-0	282	0.52	0.11
P-PMF-Time-5	258	0.47	0.10
P-PMF-Time-10	257	0.48	0.10
P-PMF-Time-20	318	0.58	0.12
P-PMF-Time-30	215	0.39	0.08
P-PMF-Time-120	232	0.41	0.09

^[a]Surface area calculated from N₂ adsorption isotherm using BET equation. ^[b]Pore volume (PV) calculated from N₂ uptake at $p/p_0 = 0.95$. ^[c]Micro pore volume (MPV) calculated from N₂ uptake at $p/p_0 = 0.10$.

In the PMF-Std synthesis and all other syntheses before, the kinetic influence that the first step may have, is completely eliminated from the particle formation as the time seems sufficient for a complete conversion of melamine to low-molecular precursor or oligomeric prepolymer species. The results point out that after 40 minutes the precursor is entirely formed from the added melamine and formaldehyde in terms of a low-molecular, monomeric or oligomeric species.

A significantly longer pre-polymerization time leads to propagation of these precursor oligomers, which in turn lead to increased coalescence and aggregation in the reaction mixture by decreased hydrophilicity. N₂ sorption supports these findings with larger pore sizes and significantly less specific surface area. However, the achieved shape of the particles is only slightly altered as the higher molecular weight precursors not show a differing behavior from ones with lower weight.

In contrast, with a decreased time before polymerization, melamine is not completely dissolved and cannot directly partake in the polymerization reaction. The dissolution of melamine and the subsequent transformation with formaldehyde now is the speed-determining step. Two main influences can be seen: First, the colloidal stability of the growing PMF particles can be achieved either by precursor molecules or SiO₂ NPs as explained before, depending on the precursor. Secondly, a high precursor concentration facilitates fast polymerization and a short growth time. This leads the formation of larger particles of non-spherical shapes as well as prolonged shapes. Nonetheless, when a precursor formation time between 5 to 20 minutes is used, part of the melamine is already converted while the rest is present in non-solubilized form. This leads to a more chaotic and inhomogeneous particle formation with significant differences in shape and size of the obtained particles even within a single synthesis. Herein, nucleation, particle growth and the two stabilization routes can occur at a statistical basis leading to heterogeneous growth.

Noteworthy, the one-pot synthesis with 0 min shows more uniformly shaped particles with larger diameters around 12 µm and still a high specific surface area. Thus, the non-dissolved melamine not irrevocably leads to a completely inhomogeneous reaction mixture and subsequent heterogeneous particle formation. Here, the resin formation is to full extend a two-step process with its preceding precursor formation from melamine and subsequent polymerization, which causes an initial Pickering stabilization via SiO₂ NPs and a direct conversion of freshly formed precursors to the PMF resin structure, as the polymerization is the faster process (see kinetics of PMF-Std at Figure S2). The occurrence of prolonged particle shapes up to the bouquet-shaped particles also indicates a strong entropic effect and a lower difference in potential surface energy between the particles and the dispersant as well as a growth-directing influence. Otherwise, spherical particles were strongly preferred if minimizing surface energy would be the main driving force in this special system.

3.4. Conclusion on the templating mechanism for PMF-Std

From our findings in N₂ sorption, electron microscopy, and TGA measurements, as well as from literature, including our previous publications [14,15,19,22,23,53], we can deduce a theory for the particle formation in the reaction system. The particle formation is extremely complex. Our starting point for the following theory is the appearance of the three distinct

morphologies of the H-PMF-Std particles. To obtain these homogeneous compartments in the particles as well as uniform particle sizes, the particle nucleation and subsequent growth need to be continuous and simultaneous.

Starting from melamine and paraformaldehyde in water, it is well known that an oligomeric MF precursor is formed at 50 °C [19,45]. These precursor molecules are hydrophilic in nature, as they comprise many terminal hydroxyl and amino groups.

With the addition of the catalyst and template to this precursor solution, a rapid polymerization of neighboring precursor molecules is occurring. When polymerized, the precursor species will quickly increase in hydrophobicity as the degree of cross-linking is enhanced by conversion of the hydrophilic end groups and with this, the aromatic character of the formed resin is predominant. From a certain point, with increasing molecule size and hydrophobicity, the forming resin polymer loses its colloidal stability in water as dispersant. At this point, potentially with similarities to the particle mechanism suggested by LaMer [54], this leads to spontaneous nucleation of small PMF polymer molecules together with several SiO₂ NPs, until the precursor concentration falls below a critical value.

Although the growth mechanism of resin particles is often described with analogies to the Stöber synthesis [55,56], the main particle growth in this system may not be aggregation-driven for the most part. The Stöber particle mechanism includes a rapid nucleation as first step with a subsequent growth by a homogenous aggregation of these nuclei to form particles. In a third step, leftover monomers are converted on the interphase of the formed particles [57,58]. However, the formation of two differing shells, the first without and the second with the inclusion of silica is only explainable by monomer-addition based growth with a switch in colloidal stabilization. When measuring the pH values of the reaction components, a pH of 7.4 was found for the MF precursor and 1.7 for the SiO₂/catalyst dispersion for PMF-Std. Nonetheless, directly after joining both components, the resulting pH value of the reaction mixture is 4.7. In that pH region, SiO₂ should exhibit a strong negative charge, while the PMF structure is positively charged, thus facilitating strong interaction between the two components from the beginning [46,47]. Thus, another parameter must change between the two shell growth steps, which only can be the precursor concentration of the system. This is supported by the findings of the PMF-SiO₂ series, showing that minimization of the PMF/water interface area by mediation of SiO₂ NPs (or precursor molecules) is the main driving force for the particle assembling.

Therefore, we conclude that the first shell growing step occurs with a stabilization of the hydrophobic PMF resin by the more hydrophilic precursor molecules as surfactant. Thus, the growth of a pure PMF shell occurs without interaction to and inclusion of silica. From later experiments regarding the polymerization speed (discussed in section 3.3.1), less inclusion of

SiO₂ Nanospheres as Surfactant and Template in Aqueous Dispersion Polymerizations Yielding Nanoporous Resin Particles

silica is especially seen with lower polymerization velocity. As that situation is illogical for the start of the particle growth, the stabilization is the last possible explanation.

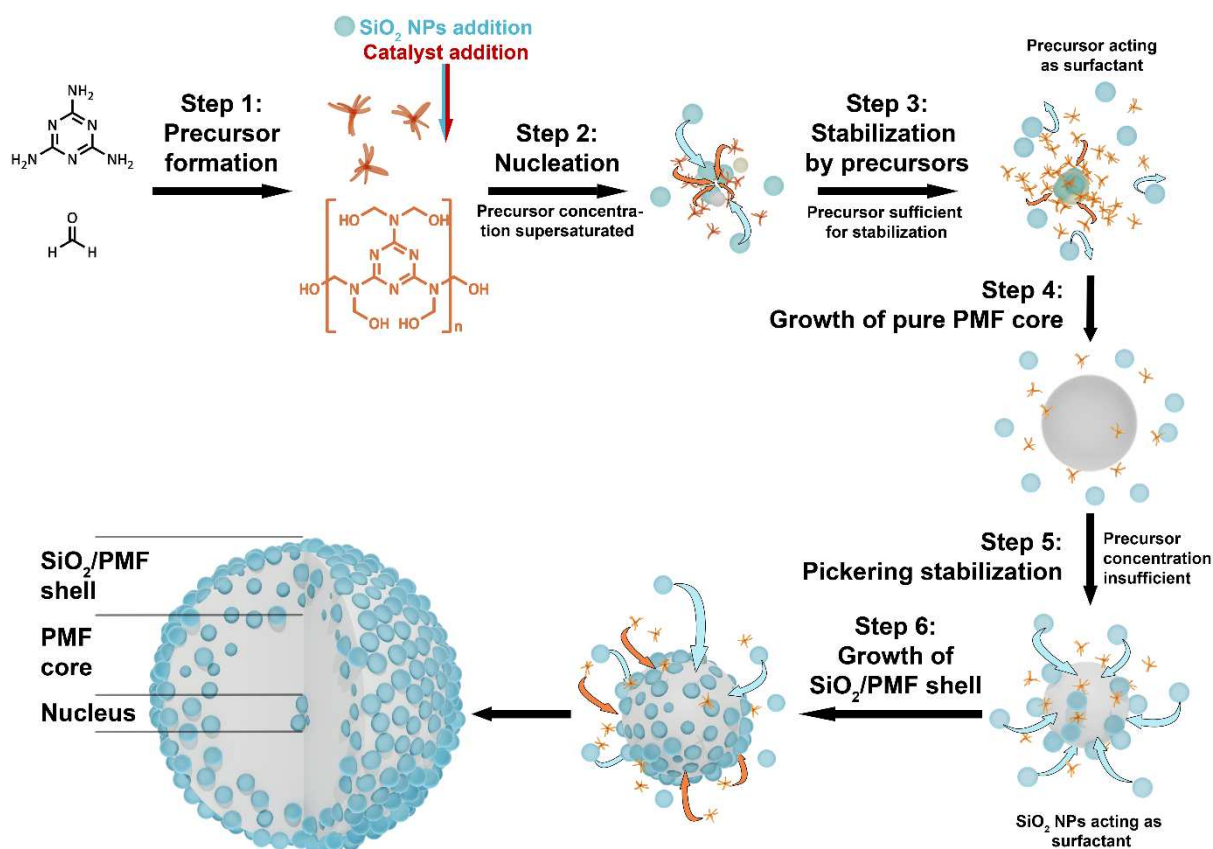


Figure 8.10. Schematic mechanism for the formation of templated, colloidal H-PMF particles. The oligomeric precursor molecules are shown as yellow stars, the formed PMF resin is shown in white and the SiO₂ NPs as blue spheres. Here, Step 1 needs sufficient time for the complete conversion of melamine and formaldehyde to the precursor species. Step 4 to 6, which include the interaction with SiO₂ NPs need ideally a reaction temperature of 100 °C, while decreasing the temperature will lead to a significantly decreased interaction between both.

This stabilization and respective particle growth continues until the precursor concentration decreases further, down to a certain concentration. Afterwards, silica acts as surfactant attaching to the PMF/water interface in terms of a Pickering surfactant [24,59] with their moderate hydrophilicity and simultaneous negative surface charge [46]. SiO₂ NPs can well interact with both the positively charged PMF particles and the water as dispersant, reducing the surface potential of the PMF/water interface, which leads to colloidal stabilization of the particles. With the progressing polymerization, the attached SiO₂ NPs are overgrown and included to form a homogenous PMF/SiO₂ hybrid shell, while remaining SiO₂ NPs from the dispersion can attach to the newly formed outer resin surface. Here, the polymerization speed is decisive for the timely inclusion before detachment.

In Figure 8.10, we summarized the mechanism for syntheses that include a separate step with sufficient time for complete precursor formation (step 1) and subsequent polymerization

at 100 °C (steps 2 – 6). In step 2, the number of nuclei formed is probably dependent of the amount of catalyst and precursor molecules. As we know from the synthesis with lower precursor concentrations (e.g. higher amount of dispersant) and similar systems reported recently [14], step 3 and 4 can be bypassed when the precursor concentration is insufficient for colloidal stability. Here, SiO₂ NPs stabilized the growing particles from the start of the dispersion polymerization.

3.4.1. Mechanistic conclusion for varied polymerization speed by catalyst or temperature

From the comparison of P-PMF-Std with PMF-Temp and PMF-Cat, a conclusion on the polymerization kinetics can be drawn. Our experiments showed lower template inclusion when the polymerization speed was decreased with catalyst amount or temperature. When increasing the polymerization speed e.g. by a higher catalyst amount, also less SiO₂ NPs are entrapped as template in the resin. Here, the time for the attachment of these NPs to the PMF/water interface is insufficient while the polymerization progresses.

Thus, the appearance of the non-templated PMF shell in PMF-Std is not caused by a too slow polymerization as sufficient catalyst, precursor macromonomers and temperature was used. Furthermore, this can also not be caused by a too rapid polymerization taking place, in which less SiO₂ NPs are entrapped. When this was the case, a lowering of the polymerization speed by either temperature or catalyst should have initially increased the silica uptake. This behavior cannot be seen from P-PMF-Cat-11, P-PMF-Temp-90 or P-PMF-Temp-80. In stark contrast, a significant drop in specific surface area can be seen for all samples. Thus, the absence of silica in this shell must be attributed to the stabilization effect of the precursor itself as the last remaining possibility.

3.4.2. Conclusion on kinetics of the two-step polymerization

We proved that the prepolymerization step to form low-molecular weight species from melamine and formaldehyde is the speed-limiting step in the network formation. When no prepolymerization is done before the 100 °C heating step, the colloidal stabilization mechanism is altered completely and is forcing SiO₂ NPs to act as Pickering surfactants from the start of the reaction. Nonetheless, the continuous formation of precursor molecules enables the inclusion of the adhered SiO₂ NPs, thus efficiently generating a pore structure after etching. By exploiting the prepolymerization step and using a one-pot synthesis route, relatively homogeneous bouquet-like particles can be obtained. From the prolonged particle shapes, a good colloidal stabilization can be deduced as minimization of the particle surface area was not a significant driving force.

3.5. Acquiring μm-sized porous PMF particles for adsorption application

P-PMF-Time-0 was chosen as most suitable sample as start to obtain uniform particles in the diameter range of several micrometers. This sample showed two distinct peaks in the

particle size distribution with also a very large share of particles with diameters around 10 μm . Furthermore, the sample showed unimpaired porosity with a specific surface area of 282 m^2/g . The bouquet-like shape of the particles also potentially prevents blockage of a column in later fixed bed experiments. As dispersions of PMF particles tend to exhibit strong rheopectic behavior. In vacuum filtration experiments with frits having sizes of POR2 to POR4, the frit is immediately blocked, which prevents even sub- μm sized PMF particles to pass through although the nominal pore diameters are two orders of magnitude larger. This behavior can be seen from various samples, not only the bouquet-like P-PMF-Time-0 particles. Therefore, centrifugation was chosen as it allows for facile size-dependent separation and also potentially sedimentation solely by gravity. Stability experiments with a solid concentration of 5 g particles per L at a relative centrifugal field of $30 \times g$ showed that a significant share of the particles sedimented in approximately 125 s for a cuvette length of approximately 20 mm (Figure S25).

Thus, centrifugation experiments were performed for the separation at $30 \times g$ with four repetitions of centrifugation and subsequent redispersion in 300 mL vessels. For the first and second centrifugation, 25 min were chosen, for the third centrifugation 15 min and for the fourth centrifugation 5 min. These centrifugation times showed a large percentage of residual sub- μm particles in the supernatant and an increasing share in the precipitate. After each step, redispersion was carried out by 15 min ultrasonication via bath. In the first centrifugation steps, a significantly longer duration was needed compared to the stability experiments because of the larger sample volumes and sedimentation path of the containers.

After the fourfold centrifugation, the share of the bouquet-like particles significantly increased and the peaks narrowed down in width (see Figure S26). The obtained sample after four centrifugation steps was named P-PMF-Col. From summation of the volumetric particle size distribution, it was found that initially 52 % of the particles were assigned to the peak with a particle size of 1.4 μm or less for P-PMF-Time-0. The sample P-PMF-Col decreased the share of particles with 1.4 μm or less down to 21 %, thus 79 % of the sample mass is assigned to the peak with a maximum diameter of 10 μm . Further centrifugation can clearly further shift the distribution in favor of larger particles but out of economic reasons no further separation was carried out.

The obtained particles showed an unimpaired specific surface area of 256 m^2/g (see Figure S27 and Table S4). Thus, the production of highly porous PMF particles for column adsorption application was successful.

To prove a reproducibility of the experiments, we have repeatedly synthesized P-PMF-Time-0 particles and subsequently centrifuged these in the same manner as done for the separation of P-PMF-Col. The respective samples were named P-PMF-Time-0-repeat and P-PMF-Col-repeat. Nitrogen sorption and particle size measurements (Figure S27–S28, Table

S4) show that only insignificant changes are occurring, thus, the results are very well reproducible. From the synthesis, the product is easily obtained in multi-gram scale.

3.6. Adsorption experiments with K₂Cr₂O₇ solution

Dichromate Cr₂O₇²⁻ ions pose severe risk to all lifeforms including aquatic organisms as well as non-aquatic organism and humans. Therefore our team chose to study the adsorption of Cr₂O₇²⁻ ions as we also wanted to continue to test PMF for the adsorption of anionic pollutants as sulfate and phosphate as recently reported by our author team [14]. The newly obtained P-PMF-Col particles were therefore applied in batch adsorption experiments, first in dependence of time to gain insights into the adsorption kinetics and then in dependence of the initial Cr₂O₇²⁻ concentration to determine the adsorption efficiency and physicochemical parameters. Afterwards we tested the adsorption in fixed bed column adsorption experiments as preliminary presentation for pass-through separation processes.

3.6.1. Kinetic batch adsorption

The kinetic adsorption experiments with $c_0 = 100$ mg/L Cr₂O₇²⁻ solution (Figure 8.11a) show a steep uptake of the samples at times of 5 min, whereby around 75% of the maximum experimental adsorption capacity is reached (at 480 min with 20.3 mg/g). After 240 min, the plateau area of the adsorption capacity is reached with 20 mg/g, only differing insignificantly afterwards. K⁺ showed no significant adsorption (see Figure S30).

Both the pseudo-first and pseudo-second order models rendered relatively similar correlation in terms of X^2_{red} values (Table S5). Here, a maximum adsorption capacity of 184 and 18.8 mg/g are fitted, well in agreement with the experimental data. The low contact time required to reach 75% of the maximum capacity indicates that the particles are a viable adsorption material for flow-through experiments.

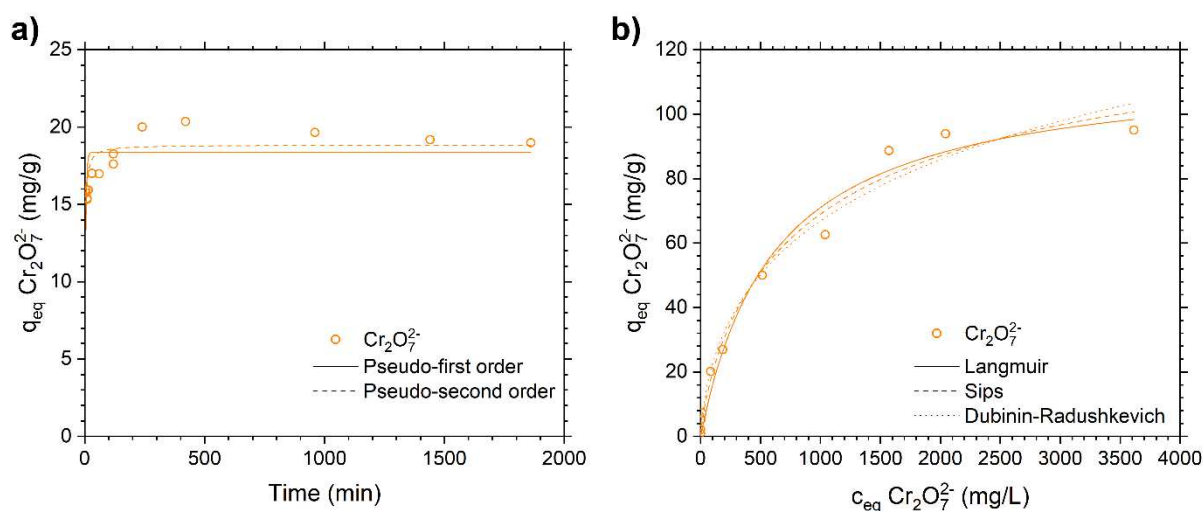


Figure 8.11. a) Time-dependent adsorption isotherm for $c_0 = 100$ mg/L Cr₂O₇²⁻ onto P-PMF-Time-Col with the corresponding Pseudo-first order (solid lines) and pseudo-second order (dashed lines). The

SiO₂ Nanospheres as Surfactant and Template in Aqueous Dispersion Polymerizations Yielding Nanoporous Resin Particles

corresponding pH values are displayed in Figure S29. The corresponding K⁺ adsorption is shown in Figure S30. The fitting parameters are displayed in Table S5. b) Sorption isotherm for Cr₂O₇²⁻ onto P-PMF-Col after 240 min equilibration time with the corresponding Langmuir (solid line), Sips (dashed line) and Dubinin-Radushkevich (dotted line) fits. The corresponding pH values are displayed in Figure S31 and K⁺ adsorption is presented in Figure S32. The fitting parameters are displayed in Table 8.5.

3.6.2. Batch adsorption isotherm

To determine the maximum adsorption capacity of the particles, the adsorption isotherm was studied at different concentrations (see Figure 8.11b). A contact time of 240 min was chosen to reach the plateau in adsorption capacity. As it can be seen, a plateau is approximated at concentrations of $c_{eq} = 1600$ mg/L Cr₂O₇²⁻ ions, achieving adsorption capacities close to 95 mg Cr₂O₇²⁻/g. In the low-concentration region up to $c_0 = 2.2$ mg/L, over 93% of adsorption can be seen, reducing the contamination over one order of magnitude.

Table 8.5. Fitting parameters for Langmuir, Sips and Dubinin-Radushkevich isotherm model for Cr₂O₇²⁻ adsorption from K₂Cr₂O₇ solution onto P-PMF-Col. Q_m thereby is the maximal sorption capacity and K is the Langmuir or Sips equilibrium constant, n is the Sips model exponent, β_{DR} is the activity coefficient for Dubinin-Radushkevich and $E_{Ads,DR}$ is the mean free energy of adsorption associated with the activity coefficient β_{DR} . For all parameters, the corresponding standard error from the fit is given.

Isotherm model	Q_m μmol/g	K_L (*)	n	β_{DR} $10^{-9} \text{ mol}^2/\text{J}^2$	$E_{Ads,DR}$ kJ/mol	X^2_{red}
Langmuir	115.3 ± 7.6	1.6 ± 0.3	--	--	--	28.831
Sips	137.6 ± 29.8	4.7 ± 3.3	0.78 ± 0.16	--	--	27.196
Dubinin-Radushkevich	190.4 ± 16.8	--	--	5.88 ± 0.56	9.22 ± 0.44	30.497

*Unit for parameter K_L from Langmuir fit is mL/mg and K_S from Sips fit (mL/mg)ⁿ.

Three isotherm equations were chosen to model the adsorption process, namely Langmuir, Sips and Dubinin-Radushkevich. The Sips model showed the highest correlation in terms of its X^2_{red} value, rendering an adsorption capacity of 138 mg/g. The Sips model exponent of 0.76, differing from unity, indicates energetically inhomogeneous adsorption. The Langmuir model showed a closer approximation for the plateau region, determining a monolayer capacity of 115 mg/g. The Dubinin-Radushkevich fit overestimates the maximum adsorption capacity greatly, but the initial slope of the isotherm, given by the activity coefficient β_{DR} is in good agreement with the experimental data. The mean free energy of adsorption $E_{Ads,DR}$, which is calculated from β_{DR} , shows a strong interaction of PMF with Cr₂O₇²⁻ ions with a value of 9.2 kJ/mol.

From SEM-EDX analysis of the particles after adsorption experiments with $c_0 = 2100$ mg/L, a homogeneous distribution of Cr across the sample surface is apparent (see Figure S33) supporting findings from both, Sips and Langmuir modelling.

When comparing the achieved adsorption capacities with literature (Table S6), the results are comparable to other synthetic adsorbents such as cationic metal organic frameworks [60]

or Fe- and ethylene diamine-functionalized silica [61]. PMF hereby surpasses different ion exchange materials as Lewatit® FO36 [62] or several bio-based materials [63–65]. However, some modified ion exchange resins achieve higher adsorption capacities [63,66,67]. Nonetheless, this presented PMF adsorbent here is the first applicable, highly porous PMF column material that is synthesized via ecofriendly dispersion polymerization in water as dispersant. Furthermore, as the PMF resin shows extremely good stability, the material can be reused and as already known from different publications is also applicable for the adsorption of various other adsorbents [14–18]. Thus, this material presents a great opportunity for further optimization.

3.6.3. Fixed bed column adsorption

As example for the application in flow-through water purification, one fixed bed adsorption experiment with P-PMF-Col was conducted (Figure 8.12). A small amount of 100 mg particles were slurry packed in a column, yielding in a bed height of 1 cm and with this a nominal bed volume of 0.342 mL. An initial concentration of 5.1 mg/L Cr₂O₇²⁻ was chosen for the influent, which corresponds to the 50fold of the limit value given by the World Health Organization (0.05 mg/L [68]) for chromium compounds with 2.45 mg Cr⁶⁺/L as ambitious goal. The experiment was carried out with a flow of 0.5 mL/min (corresponding to a superficial velocity of 1.46 cm/min).

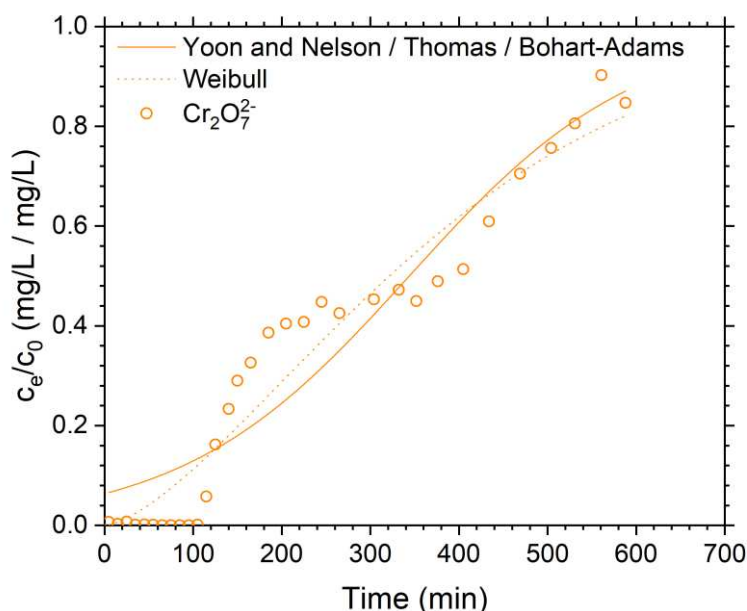


Figure 8.12. Results for the fixed bed adsorption experiment of Cr₂O₇²⁻ ions onto P-PMF-Col from K₂Cr₂O₇ solution. The corresponding exponential models (Bohart-Adams, Thomas and Yoon-Nelson) can be seen as solid line, while the Weibull model is shown as dotted line. The corresponding pH values are displayed in Figure S34. The adsorption of K⁺ is shown in Figure S35.

SiO₂ Nanospheres as Surfactant and Template in Aqueous Dispersion Polymerizations Yielding Nanoporous Resin Particles

Despite the high pollutant concentration, the high flow rate of 1.46 bed length per min and the low adsorbent amount of 100 mg, the column is able to achieve almost complete removal of Cr₂O₇²⁻ ions for 110 min, achieving drinking water quality for all samples with maximum c_e values being below 0.019 mg/L. This shows that the P-PMF-Col particles are able to efficiently adsorb Cr₂O₇²⁻ ions from solution over a viable amount of time. Calculated from the volume flow, the bed volume and the given time of 105 min, this means that the contamination in a water volume of over 160 times the bed volume is reduced to drinking water standards, set by the World Health Organization, although the contamination is 50fold higher.

However, between 115 min and 120 min, the breakthrough point with $c_e/c_0 = 0.1$ is reached with a steady increase in non-retained Cr₂O₇²⁻. From the area below the adsorption curve up to the end time of the experiment (588 min), a loading capacity of 8.59 mg Cr₂O₇²⁻/g adsorbent can be obtained (see Figure S36).

The breakthrough curve was modeled with the exponential equation, which represents the Bohart-Adams, Thomas and Yoon-Nelson model (Table 8.6). These models render the exact same fit in non-linear form because of their similar mathematical structure (Eq. (8.12)), but allow for the determination of different parameters for the column performance.

Table 8.6. Fitting parameters for the Thomas, Bohart-Adams, Yoon-Nelson and the Weibull model for Cr₂O₇²⁻ adsorption onto P-PMF-Col. Q_m thereby is the maximum adsorption capacity and K is the rate constant, N_0 is the saturation concentration per bed volume including bed voidage, $t_{0.5}$ is the breakthrough time of Yoon-Nelson, when half of the contamination is retained. a and b are parameters for the Weibull equation. For all parameters, the corresponding standard error from the fit is given.

Isotherm model	Q_m mg/g	K mL/(mg·min)	N_0 mg/mL	$t_{0.5}$ min	a min ⁻¹	b	$X^2_{red.}$
Thomas	8.95 ± 0.35	1.51 ± 0.00	--	--	--	--	0.00874
Bohart-Adams	--	1.51 ± 0.00	2.61 ± 0.10	--	--	--	0.00874
Yoon-Nelson	--	7.82 ± 0.00	--	344 ± 14	--	--	0.00874
Weibull	--	--	--	--	410 ± 16	1.52 ± 0.12	0.00544

From the Thomas model, a maximum adsorption capacity of 8.95 mg/g is predicted, which is in agreement with the experimental value although the models fit do not include a complete removal at the start of the experiment. The given saturation concentration from Bohart-Adams also predicts a similar adsorption performance as the N_0 value corresponds to a capacity of 2.61 mg/mL of bed volume including fractional bed voidage [43]. This means for 1 g P-PMF-Col (or 3.421 mL of bed volume), a capacity of 8.93 mg/g is determined. The Yoon-Nelson model calculates the inflection point of the symmetrical breakthrough $t_{0.5}$ for $c_e/c_0 = 0.5$, which is given with a value of 344 min. This is also close to the real time between 376 min to 405 min.

Nonetheless, the breakthrough point of this experiment cannot be fitted with these models as they underestimate the initial adsorption performance. This behavior was also reported in literature [44], whereby the Weibull equation was in significantly better agreement. Here, the breakthrough time was found to be 92 min for $c_e/c_0 = 0.1$, whereas the exponential models show a breakthrough at 63 min.

The results of this experiment show that the particles are in general applicable for flow-through water purification. The great differences between the adsorption capacities achieved in the batch isotherm experiments and the column sorption are very probably due to the high loading and the relatively low contact time for the adsorbent as the 1 cm column is passed by in less than 45 s. It is well-known that e.g. increasing the bed length is leading to significantly higher loading of the column material, as diffusion enhances the diffusion into the particles [69]. This experiment presents a successful proof of concept for the application of highly porous PMF particles from colloidal synthesis. Thus, with optimization of the column experiments, significantly higher efficiency is very likely to be achieved.

4. Conclusion

In this publication we have thoroughly analyzed the influence of various chemical and process parameters on the dispersion polymerization of hard-templated PMF particles. Our goal was to investigate the particle formation and templating mechanism from variation of the dispersant, template and catalyst amount, as well as process parameters as the stirring speed, polymerization temperature and the prepolymerization time. From the gained results, we elucidated the complex interplay of the single components in the reaction mixture. Especially from experiments with lower polymerization temperatures we found that the interaction between the forming PMF resin and the SiO₂ NPs is entropically driven. From experiments with a lower prepolymerization time as well as experiments with higher dispersant volume, we concluded that the colloidal stabilization route of the particles was decided by the precursor concentration. This was supported by syntheses of varied template amount and catalyst concentration. Thereafter, we were able to suppose a mechanism for the particle formation, extending previously assumed mechanisms from literature. Regarding the mechanism, we found that the particle formation follows a monomer growth mechanism, which is in contrast to previous publications. The particle synthesis was previously often described as Stöber-like mechanism via coating of the SiO₂ nanoparticles and subsequent aggregation due to hydrophobic effects [15]. Although previous results indicated this, that first step can be ruled out by our results for the investigated system. Instead, the SiO₂ nanoparticles act as both surfactant and template for the resin. Our investigation showed that this behavior can be switched to one of these effects or both via choice of suitable process parameters.

Our findings about the synthesis mechanism and switchable surfactant/template behavior can enable the tailored synthesis of other templated resin particles from e.g. phenolic or urea containing polymers.

Regarding the produced material, no synthetic route was known up to now for the colloidal preparation of PMF particles in the diameter range of several micrometer without impairing the templating and therefore the porosity considerably [14,15,22,23]. With the knowledge about the function of the SiO₂ NPs, we were able to produce bouquet-like particles with a diameter of approximately 10 µm and a specific surface area of 260 m²/g. The particles were proven to be easily reproducible and obtainable in multi-gram scale. In subsequent batch adsorption experiments with the extremely toxic oxyanion Cr₂O₇²⁻, we first showed that the maximum adsorption is achieved after 4 h, but 75% of the maximum is already adsorbed after just 5 min. The material yielded an adsorption capacity of 138 mg Cr₂O₇²⁻/g. In column experiments, we found that even under sub-optimal conditions, chromate contamination was reduced to drinking-water safe levels by at least two orders of magnitude. With this, a volume equal to 160 bed volumes was purified.

As colloidal syntheses are known to be scalable relatively well, the production scale may be extended further. As PMF resin is synthesized using inexpensive, high volume production chemicals as melamine, formaldehyde and silica, this method can be used easily in large scale. Furthermore, the chemical stability of the resin makes PMF a potential well-reusable adsorbent. From our proof of concept, optimization for the flow-through separation process may lead to the utilization of the complete batch adsorption capacity.

Acknowledgements

The authors want to thank Uta Reuter for the preparation of ultrathin-sections from embedded samples for TEM measurements.

Funding

This work was supported by the German Federal Ministry of Education and Research [grant number 01DJ18010].

Author Contributions

Konstantin B. L. Borchert: Conceptualization, methodology, validation, formal analysis, investigation, data curation, writing – original draft preparation, writing – review & editing, visualization. **Christine Steinbach:** Investigation, validation, writing – review & editing. **Berthold Reis:** Investigation, validation, writing – review & editing. **Niklas Gerlach:** Investigation, validation, writing – review & editing. **Simona Schwarz:** Resources, writing – review & editing, supervision, project administration, funding acquisition. **Dana Schwarz:** Resources, supervision, project administration, funding acquisition.

References

- [1] P. Kaur, J.T. Hupp, S.T. Nguyen, Porous Organic Polymers in Catalysis: Opportunities and Challenges, *ACS Catal.* 1 (2011) 819–835.
- [2] W. Lu, D. Yuan, D. Zhao, C.I. Schilling, O. Plietzsch, T. Muller, S. Bräse, J. Guenther, J. Blümel, R. Krishna, Z. Li, H.-C. Zhou, Porous Polymer Networks: Synthesis, Porosity, and Applications in Gas Storage/Separation, *Chem. Mater.* 22 (2010) 5964–5972.
- [3] A. Mohan, M.H. Al-Sayah, A. Ahmed, O.M. El-Kadri, Triazine-based porous organic polymers for reversible capture of iodine and utilization in antibacterial application, *Scientific reports* 12 (2022) 2638.
- [4] T. Zhang, G. Xing, W. Chen, L. Chen, Porous organic polymers: a promising platform for efficient photocatalysis, *Mater. Chem. Front.* 4 (2020) 332–353.
- [5] D. Wu, F. Xu, B. Sun, R. Fu, H. He, K. Matyjaszewski, Design and preparation of porous polymers, *Chemical reviews* 112 (2012) 3959–4015.
- [6] M. Seo, S. Kim, J. Oh, S.-J. Kim, M.A. Hillmyer, Hierarchically porous polymers from hyper-cross-linked block polymer precursors, *J. Am. Chem. Soc.* 137 (2015) 600–603.
- [7] J. Li, F.F. Cantwell, Intra-particle sorption rate and liquid chromatographic bandbroadening in porous polymer packings III. Diffusion in the polymer matrix as the cause of slow sorption, *Journal of Chromatography A* 726 (1996) 37–44.
- [8] M.X. Tan, L. Gu, N. Li, J.Y. Ying, Y. Zhang, Mesoporous poly-melamine-formaldehyde (mPMF) – a highly efficient catalyst for chemoselective acetalization of aldehydes, *Green Chem.* 15 (2013) 1127.
- [9] J. Yin, T. Zhang, E. Schulman, D. Liu, J. Meng, Hierarchical porous metallized poly-melamine-formaldehyde (PMF) as a low-cost and high-efficiency catalyst for cyclic carbonate synthesis from CO₂ and epoxides, *J. Mater. Chem. A* 6 (2018) 8441–8448.
- [10] T.Q. Bui, L.J. Konwar, A. Samikannu, D. Nikjoo, J.-P. Mikkola, Mesoporous Melamine-Formaldehyde Resins as Efficient Heterogeneous Catalysts for Continuous Synthesis of Cyclic Carbonates from Epoxides and Gaseous CO₂, *ACS Sustainable Chem. Eng.* 8 (2020) 12852–12869.
- [11] A. Wilke, J. Weber, Hierarchical nanoporous melamine resin sponges with tunable porosity—porosity analysis and CO₂ sorption properties, *J. Mater. Chem.* 21 (2011) 5226.
- [12] M.X. Tan, Y. Zhang, J.Y. Ying, Mesoporous poly(melamine-formaldehyde) solid sorbent for carbon dioxide capture, *ChemSusChem* 6 (2013) 1186–1190.
- [13] C. Duan, W. Zou, Z. Du, H. Li, C. Zhang, Fabrication of micro-mesopores in macroporous poly (formaldehyde-melamine) monoliths via reaction-induced phase separation in high internal phase emulsion template, *Polymer* 167 (2019) 78–84.
- [14] K.B.L. Borchert, C. Steinbach, B. Reis, N. Gerlach, P. Zimmermann, S. Schwarz, D. Schwarz, Mesoporous Poly(melamine-co-formaldehyde) Particles for Efficient and Selective Phosphate and Sulfate Removal, *Molecules (Basel, Switzerland)* 26 (2021).
- [15] D. Schwarz, J. Weber, Organic-solvent free synthesis of mesoporous and narrow-dispersed melamine resin particles for water treatment applications, *Polymer* 155 (2018) 83–88.
- [16] M.X. Tan, Y.N. Sum, J.Y. Ying, Y. Zhang, A mesoporous poly-melamine-formaldehyde polymer as a solid sorbent for toxic metal removal, *Energy Environ. Sci.* 6 (2013) 3254.
- [17] D. Schwarz, J. Weber, Synthesis of mesoporous poly(melamine-formaldehyde) particles by inverse emulsion polymerization, *Journal of colloid and interface science* 498 (2017) 335–342.
- [18] Y. Wang, Y. Xie, Y. Zhang, S. Tang, C. Guo, J. Wu, R. Lau, Anionic and cationic dyes adsorption on porous poly-melamine-formaldehyde polymer, *Chemical Engineering Research and Design* 114 (2016) 258–267.
- [19] D. Schwarz, J. Weber, Nanoporous Poly(Melamine Formaldehyde) Networks by Aqueous Dispersion Polycondensation-Synthesis and Adsorption Properties, *Macromol. Mater. Eng.* 300 (2015) 531–541.
- [20] G. Yang, H. Han, C. Du, Z. Luo, Y. Wang, Facile synthesis of melamine-based porous polymer networks and their application for removal of aqueous mercury ions, *Polymer* 51 (2010) 6193–6202.
- [21] K. Kailasam, Y.-S. Jun, P. Katekomol, J.D. Epping, W.H. Hong, A. Thomas, Mesoporous Melamine Resins by Soft Templating of Block-co-Polymer Mesophases, *Chem. Mater.* 22 (2010) 428–434.
- [22] K.B.L. Borchert, K.H. Carrasco, C. Steinbach, B. Reis, N. Gerlach, S. Schwarz, D. Schwarz, Tuning the Pore Structure of Templated Mesoporous Poly(melamine-co-formaldehyde) Particles toward Diclofenac Removal, *Journal of environmental management (in press)*.
- [23] Y. Wu, Y. Li, L. Qin, F. Yang, D. Wu, Monodispersed or narrow-dispersed melamine-formaldehyde resin polymer colloidal spheres: preparation, size-control, modification, bioconjugation and particle formation mechanism, *Journal of materials chemistry. B* 1 (2013) 204–212.
- [24] S.U. Pickering, CXCVI.—Emulsions, *J. Chem. Soc., Trans.* 91 (1907) 2001–2021.
- [25] S. Brunauer, P.H. Emmett, E. Teller, Adsorption of Gases in Multimolecular Layers, *J. Am. Chem. Soc.* 60 (1938) 309–319.

SiO₂ Nanospheres as Surfactant and Template in Aqueous Dispersion Polymerizations Yielding Nanoporous Resin Particles

- [26] T.A. Osmari, R. Gallon, M. Schwaab, E. Barbosa-Coutinho, J.B. Severo, J.C. Pinto, Statistical Analysis of Linear and Non-Linear Regression for the Estimation of Adsorption Isotherm Parameters, *Adsorption Science & Technology* 31 (2013) 433–458.
- [27] B. Subramanyam, A. Das, Linearised and non-linearised isotherm models optimization analysis by error functions and statistical means, *Journal of environmental health science & engineering* 12 (2014) 92.
- [28] J. Wang, X. Guo, Adsorption isotherm models: Classification, physical meaning, application and solving method, *Chemosphere* 258 (2020) 127279.
- [29] J. Wang, X. Guo, Adsorption kinetic models: Physical meanings, applications, and solving methods, *Journal of hazardous materials* 390 (2020) 122156.
- [30] S. Lagergren, About the Theory of So-Called Adsorption of Soluble Substances, *K. Sven. Vetenskapsakad. Handl.* 24 (1898) 1–39.
- [31] Y.S. Ho, D.A.J. Wase, C.F. Forster, Removal of lead ions from aqueous solution using sphagnum moss peat as adsorbent, *Water SA* 22 (1996) 219–224.
- [32] I. Langmuir, THE CONSTITUTION AND FUNDAMENTAL PROPERTIES OF SOLIDS AND LIQUIDS. PART I. SOLIDS, *J. Am. Chem. Soc.* 38 (1916) 2221–2295.
- [33] F. Togue Kamga, Modeling adsorption mechanism of paraquat onto Ayous (*Triplochiton scleroxylon*) wood sawdust, *Appl Water Sci* 9 (2019) 456.
- [34] K.Y. Foo, B.H. Hameed, Insights into the modeling of adsorption isotherm systems, *Chemical Engineering Journal* 156 (2010) 2–10.
- [35] R. Sips, On the Structure of a Catalyst Surface, *The Journal of Chemical Physics* 16 (1948) 490–495.
- [36] M.M. Dubinin, The Equation of the Characteristic Curve of Activated Charcoal, *Proceedings of the USSR Academy of Sciences* 55 (1947) 327–329.
- [37] X. Zhou, Correction to the calculation of Polanyi potential from Dubinin-Rudushkevich equation, *Journal of hazardous materials* 384 (2020) 121101.
- [38] H.C. Thomas, Chromatography: a problem in kinetics, *Annals of the New York Academy of Sciences* 49 (1948) 161–182.
- [39] H.C. Thomas, Heterogeneous Ion Exchange in a Flowing System, *J. Am. Chem. Soc.* 66 (1944) 1664–1666.
- [40] G.S. Bohart, E.Q. Adams, Some aspects of the behavior of charcoal with respect to chlorine, *Journal of the Franklin Institute* 189 (1920) 669.
- [41] N.R. Amundson, A Note on the Mathematics of Adsorption in Beds, *J. Phys. Chem.* 52 (1948) 1153–1157.
- [42] Y.H. Yoon, J.H. Nelson, Application of gas adsorption kinetics. I. A theoretical model for respirator cartridge service life, *American Industrial Hygiene Association journal* 45 (1984) 509–516.
- [43] K.H. Chu, Breakthrough curve analysis by simplistic models of fixed bed adsorption: In defense of the century-old Bohart-Adams model, *Chemical Engineering Journal* 380 (2020) 122513.
- [44] K.H. Chu, Fixed bed adsorption of chromium and the Weibull function, *Journal of Hazardous Materials Letters* 2 (2021) 100022.
- [45] J. Bentley, Organic film formers, in: *Paint and Surface Coatings*, Elsevier, 1999, pp. 19–90.
- [46] M. Kosmulski, *Surface Charging and Points of Zero Charge*, CRC Press, 2009.
- [47] S. Ortelli, A.L. Costa, P. Matteucci, M.R. Miller, M. Blosi, D. Gardini, S.A.M. Tofail, L. Tran, D. Tonelli, C.A. Poland, Silica modification of titania nanoparticles enhances photocatalytic production of reactive oxygen species without increasing toxicity potential in vitro, *RSC Adv.* 8 (2018) 40369–40377.
- [48] L.H. Allen, E. Matijević, Stability of colloidal silica, *Journal of colloid and interface science* 31 (1969) 287–296.
- [49] M. Kosmulski, The pH dependent surface charging and points of zero charge. IX. Update, *Advances in colloid and interface science* 296 (2021) 102519.
- [50] M. Thommes, K. Kaneko, A.V. Neimark, J.P. Olivier, F. Rodriguez-Reinoso, J. Rouquerol, K.S.W. Sing, Physisorption of gases, with special reference to the evaluation of surface area and pore size distribution (IUPAC Technical Report), *Pure and Applied Chemistry* 87 (2015) 1051–1069.
- [51] C. Schlumberger, M. Thommes, Characterization of Hierarchically Ordered Porous Materials by Physisorption and Mercury Porosimetry—A Tutorial Review, *Adv. Mater. Interfaces* 8 (2021) 2002181.
- [52] K.S.W. Sing, Reporting physisorption data for gas/solid systems: With special reference to the determination of surface area and porosity, *Pure & Applied Chemistry* 54 (1982) 2201–2218.
- [53] G. Ming, H. Duan, X. Meng, G. Sun, W. Sun, Y. Liu, L. Lucia, A novel fabrication of monodisperse melamine–formaldehyde resin microspheres to adsorb lead (II), *Chemical Engineering Journal* 288 (2016) 745–757.
- [54] V.K. LaMer, R.H. Dinegar, Theory, Production and Mechanism of Formation of Monodispersed Hydrosols, *J. Am. Chem. Soc.* 72 (1950) 4847–4854.
- [55] J. Choma, D. Jamioła, K. Augustynek, M. Marszewski, M. Gao, M. Jaroniec, New opportunities in Stöber synthesis: preparation of microporous and mesoporous carbon spheres, *J. Mater. Chem.* 22 (2012) 12636.

SiO₂ Nanospheres as Surfactant and Template in Aqueous Dispersion Polymerizations Yielding Nanoporous Resin Particles

- [56] J. Liu, S.Z. Qiao, H. Liu, J. Chen, A. Orpe, D. Zhao, G.Q.M. Lu, Extension of The Stöber Method to the Preparation of Monodisperse Resorcinol-Formaldehyde Resin Polymer and Carbon Spheres, *Angew. Chem.* 123 (2011) 6069–6073.
- [57] W. Stöber, A. Fink, E. Bohn, Controlled growth of monodisperse silica spheres in the micron size range, *Journal of colloid and interface science* 26 (1968) 62–69.
- [58] S. Li, Q. Wan, Z. Qin, Y. Fu, Y. Gu, Understanding Stöber silica's pore characteristics measured by gas adsorption, *Langmuir the ACS journal of surfaces and colloids* 31 (2015) 824–832.
- [59] A. Lotierzo, S.A.F. Bon, A mechanistic investigation of Pickering emulsion polymerization, *Polym. Chem.* 8 (2017) 5100–5111.
- [60] J.-J. Liu, J.-J. Fu, G.-J. Li, T. Liu, S.-B. Xia, F.-X. Cheng, A water-stable photochromic MOF with controllable iodine sorption and efficient removal of dichromate, *CrystEngComm* 23 (2021) 7628–7634.
- [61] T. Sangvanich, W. Ngamcherdtrakul, R. Lee, J. Morry, D. Castro, G.E. Fryxell, W. Yantasee, Nanoporous sorbent material as an oral phosphate binder and for aqueous phosphate, chromate, and arsenate removal, *Journal of nanomedicine & nanotechnology* 5 (2014).
- [62] L. Rafati, A.H. Mahvi, A.R. Asgari, S.S. Hosseini, Removal of chromium (VI) from aqueous solutions using Lewatit FO36 nano ion exchange resin, *Int. J. Environ. Sci. Technol.* 7 (2010) 147–156.
- [63] W.E. Marshall, L.H. Wartelle, Chromate (CrO₄(2-)) and copper (Cu²⁺) adsorption by dual-functional ion exchange resins made from agricultural by-products, *Water research* 40 (2006) 2541–2548.
- [64] W.E. Marshall, L.H. Wartelle, An anion exchange resin from soybean hulls, *J. Chem. Technol. Biotechnol.* 79 (2004) 1286–1292.
- [65] A.H.T.S.W. S. B. Lalvani, Chromium Adsorption by Lignin, *Energy Sources* 22 (2000) 45–56.
- [66] Y. Ren, Y. Han, X. Lei, C. Lu, J. Liu, G. Zhang, B. Zhang, Q. Zhang, A magnetic ion exchange resin with high efficiency of removing Cr (VI), *Colloids and Surfaces A: Physicochemical and Engineering Aspects* 604 (2020) 125279.
- [67] G. Stinchfield, J.F. Capitani, J. Regan, Bidentate and Monodentate Binding of Chromium (VI) on the Acid Scavenger Exchange Resin, MP-Carbonate, as a Function of pH, *Water Air Soil Pollut* 231 (2020) 1123.
- [68] Guidelines for drinking-water quality, World Health Organization, Geneva, 2017.
- [69] I.P. Verduzco-Navarro, N. Rios-Donato, C.F. Jasso-Gastinel, Á.d.J. Martínez-Gómez, E. Mendizábal, Removal of Cu(II) by Fixed-Bed Columns Using Alg-Ch and Alg-ChS Hydrogel Beads: Effect of Operating Conditions on the Mass Transfer Zone, *Polymers* 12 (2020).

9. Waterborne Phenolic, Triazine-Based Porous Polymer Particles for the Removal of Nickel, Cadmium, and Lead Ions

This chapter is based on a submitted publication in *JCIS Open* **2022**, 8, 100066.

(DOI: 10.1016/j.jciso.2022.100066)

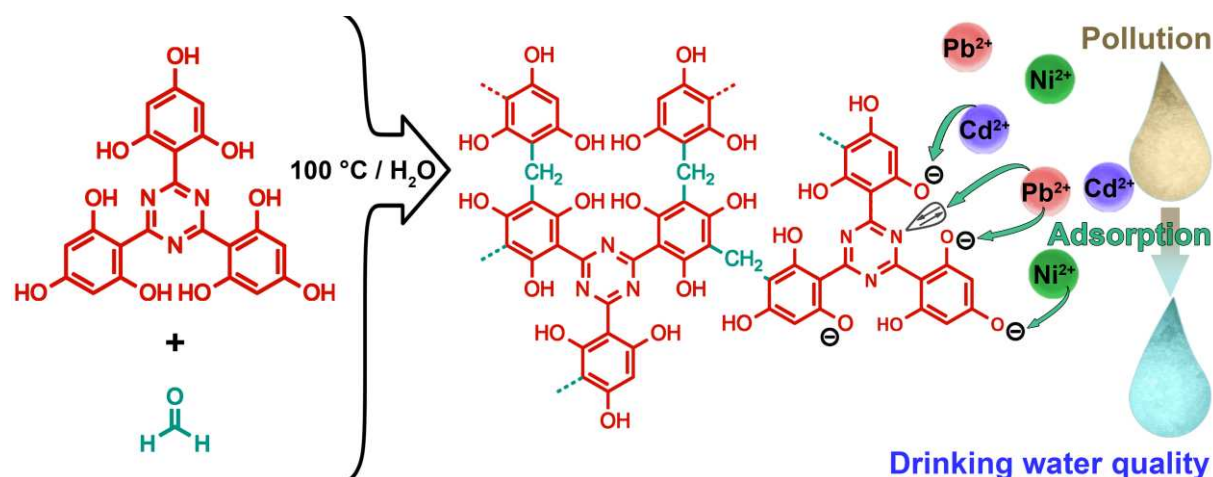
By Konstantin B. L. Borchert^a, Robert Frenzel^{a,b}, Niklas Gerlach^a, Berthold Reis^a, Christine Steinbach^a, Benjamin Kohn^a, Ulrich Scheler^a, Simona Schwarz^{a,*}, Dana Schwarz^{a,*}

^a Leibniz-Institut für Polymerforschung Dresden e.V., Hohe Str. 6, 01069 Dresden, Germany;

^b Technische Universität Chemnitz, Straße der Nationen 62, 09111 Chemnitz, Germany.

* Corresponding authors

Graphical Abstract



Abstract

Highly functional and also highly porous materials present great advantages for applications in energy storage, catalysis and separation processes that is why a continuous development of new materials can be seen. To create a material that combines the promising potential interactions of triazine-groups with the electrostatic or hydrogen bonding interactions of phenolic groups, a completely new polymeric resin was synthesized. From an eco-friendly dispersion polymerization in water, a copolymer network was obtained that includes nine hydroxyl groups and one s-triazine ring per repetition unit. The polymer forms highly porous particles with specific surface areas up to 531 m²/g and a negative streaming potential over a large pH range. The adsorption isotherms of Ni²⁺, Cd²⁺, and Pb²⁺ were studied in more detail achieving very good adsorption capacities (16 mg Ni²⁺/g, 24 mg Cd²⁺/g, and 90 mg Pb²⁺/g). Demonstrating excellent properties for adsorption applications. In further experiments with Pb²⁺, the adsorption was not impaired by present Fe^{2+/3+}, Mg²⁺, Ca²⁺, or K⁺

ions, proving selectivity of the material. Facile and quantitative desorption was possible using low volumes of aqueous HCl.

1. Introduction

Highly functional materials based on cross-linked polymer networks are gaining immense attention due to their high stability and the facile introduction of various functional groups into their structure [1,2]. Especially triazine-based network structures such as triazine-based covalent frameworks have been investigated for different applications as gas capture and separation [3–8], catalysis [9,10] and various energy storage related applications [11,12]. Rather less frequently, triazine-based organic polymers are also investigated for their adsorption properties for aqueous pollutants for water treatment applications [13–18] although these polymers show great potential for separation technologies. It is also known that the triazine moiety itself is available to undergo various additional interactions [19], thus enhancing the adsorption capacities as it was shown e.g. for Cu^{2+} [14]. Part of our author team recently showed the viability of poly(melamine-co-formaldehyde) that is also featuring a triazine moiety, for the removal of various pollutants such as oxyanions, and dyes and less frequently also heavy metal ions [16–18,20].

However, ion exchange resins are the material commonly used for the removal of aqueous pollutants as heavy metal ions at the moment [21–23]. Here, besides amino-functionalized resins [23–26], also phenolic resins are partially applied [27–31]. Ion exchange resins have various disadvantages as they tend to be expensive [32,33], partially lack a high removal efficiency [33] and are often synthesized using several organic solvents that partially neglects their ecological contribution. Using electrostatic interactions to achieve very good removal efficiency and high adsorption capacities for heavy metal ions is well-known from different polymeric or hybrid adsorbent materials with negatively charged groups such as hydroxyl, carboxyl, and phenolic groups [34–38].

Thus, the combination of negatively charged groups together with the before-mentioned enhancement from the triazine moieties presents a great potential for efficient adsorption of heavy metal ions in realistically low concentrations. Although the synthesis of these kind of polymers have seldom been reported [3,11,39], only Gómez-Ceballos et al. applied such material, a hyperbranched polymer network from oxidized lignin and cyanuric chloride, for heavy metal adsorption [39]. The monomers used by Nandi et al., comprised of an *s*-triazine ring with three moieties of resorcinol or phloroglucinol, were cross-linked with terephthalaldehyde and used solid electrolyte. The comprising functional hydroxyl and *s*-triazine groups pose a really viable starting point for the application as potential adsorbents [11].

The phloroglucinol-based monomer (shown in Figure 9.1) includes nine hydroxyl groups per *s*-triazine monomer that should enable strong interactions with metal ions. This monomer was also reported for its strong intermolecular hydrogen bonds of the hydroxyl proton to the *s*-triazine nitrogen [40], showing potential synergistic effects for adsorption interactions.

Nandi et al. showed the polymerization of this monomer to obtain a highly nanoporous and highly functional polymer particles that should also add to their adsorption efficiency. However, the synthesis of the monomer together with terephthalaldehyde as cross-linker uses harsh hydrothermal conditions in organic solvents such as dioxane, tetrahydrofuran and includes washing with dimethyl formamide. This partly diminishes a potential use for environmental applications. Therefore, we planned a more eco-friendly polymerization route (see Figure 9.2):

Here, we present the facile synthesis of a new copolymer with an extremely high number of phenolic groups in a triazine-based polymer. It can be obtained by an eco-friendly, catalyst-free dispersion polymerization with water as solvent. By variation of the amount of formaldehyde as cross-linker, particles with different porosities were achieved. We thoroughly characterized the obtained particles using N_2 and CO_2 adsorption, electron microscopy, ATR-FTIR, elemental analysis, and thermogravimetric analysis. As a colloidal approach was used for the preparation, the synthesis of the polymer is easily upscale able without impaired morphological or chemical properties. To demonstrate a potential application for the particles, adsorption isotherms with lead, cadmium, and nickel ions as pollutants in water were investigated.

2. *Materials and methods*

2.1. *Materials*

2.1.1. *Chemicals used for the synthesis*

Aluminum(III) chloride (anhydrous, $\geq 99\%$), cyanuric chloride (anhydrous, $\geq 99\%$), paraformaldehyde (F) ($\geq 95\%$), and phloroglucinol (1,3,5-trihydroxybenzene, $\geq 99\%$) were purchased from Sigma-Aldrich (Merck KGaA, Darmstadt, Germany). Anhydrous solvents dichloromethane (DCM) and diethyl ether (Et₂O) were purchased from Carl Roth (Karlsruhe, Germany). Hydrochloric acid (37 wt.%, Normapur) and ethanol (absolute, Normapur) were purchased from VWR International (Darmstadt, Germany). NaOH ($\geq 98\%$, p.a.) was purchased from Honeywell (Offenbach, Germany). All listed chemicals were used without further purification.

2.1.2. *ICP-OES standard solutions*

For the preparation of the elemental standards for ICP-OES analysis, the following standards were used: 9998 mg/L S in water (Sigma Aldrich, München, Germany), 10008 mg/L Pb in water (Sigma Aldrich, München, Germany), 10000 mg/L Ni in 2 mol/L HNO₃ (Bernd Kraft, Duisburg, Germany), and 10000 mg/L Cd in 2 mol/L HNO₃ (Bernd Kraft, Duisburg, Germany). For the screening experiments, the ICP multi-element standard solution IV (Merck KGaA, Certipur®) was used. Nitric acid (85 wt.%, Normapur) was used for preparing the matrix.

2.1.3. *Ultrapure water*

Waterborne Phenolic, Triazine-Based Porous Polymer Particles for the Removal of Nickel, Cadmium, and Lead Ions

As medium for adsorption experiments, reactions, and ICP-OES standards, ultrapure water purified by a Milli-Q Advantage A10[®] system (TOC 5 ppb, resistivity of 18.2 MΩ·cm at 25 °C) was used.

2.1.4. Chemicals used for the adsorption process

Cadmium(II) sulfate octahydrate (p.a.) and magnesium chloride (anhydrous, for synthesis) were purchased from Merck KGaA (Darmstadt, Germany). Lead(II) nitrate (99.999%), nickel(II) sulfate hexahydrate (≥ 98%), iron(II) chloride tetrahydrate (ReagentPlus[®]), potassium chloride (p.a.), and copper(II) chloride dihydrate (reagent grade) were purchased from Sigma-Aldrich (Merck KGaA, Darmstadt, Germany). Lead(II) chloride (98%) was purchased from Aldrich (Merck KGaA, Darmstadt, Germany). Calcium chloride (anhydrous, ≥ 94%) was purchased from Carl Roth (Karlsruhe, Germany). All listed chemicals were used without further purification.

2.2. Synthesis

2.2.1. Synthesis of 2,4,6-tris(2,4,6-trihydroxyphenyl)-1,3,5-triazine (3PT)

The synthesis of the monomer 2,4,6-tris(2,4,6-trihydroxyphenyl)-1,3,5-triazine (3PT) was carried out in a Friedel-Crafts arylation according to Conn and Eisler with some adjustments (Figure 9.1) [40]. The synthesis and handling of air and moisture sensitive chemicals was carried out under inert gas atmosphere (nitrogen) using common Schlenk techniques to prevent reactions with oxygen and water for example.

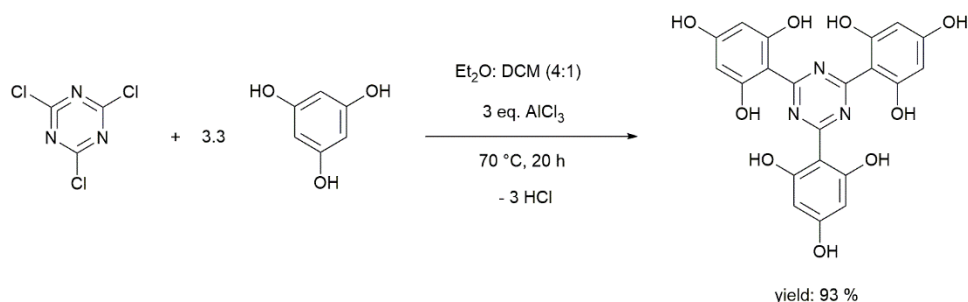


Figure 9.1. Synthesis of the monomer 3PT. [40]

Starting with a three-necked round bottom flask (1000 mL) with attached reflux condenser, dropping funnel and a stir bar, cyanuric chloride (8.29 g, 45.0 mmol, 1.0 eq.) and phloroglucinol (18.80 g, 149.1 mmol, 3.3 eq.) were added to the reaction vessel under inert gas counterflow. The solids were suspended in ether (300 mL) and DCM (100 mL). In a second round bottom flask (250 mL) AlCl_3 (17.80 g, 133.5 mmol, 2.96 eq.) was dissolved in ether (100 mL) at 0 °C. The rose-tinted AlCl_3 solution was transferred to a dropping funnel and slowly added to the ice-cooled suspension over the course of 30 min under intense stirring. The suspended solids dissolved in the mixture and a color change from pale yellow to a bright orange were observed. After the addition was completed, the reaction mixture was left for stirring until room temperature was reached. Subsequently, the mixture was heated to 70 °C

for 20 h under reflux. During this period, the solution changed color once again to a deep red. After the mixture reached room temperature again, ethanol (50 mL) was added. The orange precipitate was filtrated with a fritted glass (POR 4), washed thoroughly with ether, and finally dried at 100 °C for 24 h. For further purification, the crude product was suspended in hydrochloric acid (10 %, 300 mL). The suspension was centrifuged at 5000 rpm for 5 min. This purification procedure was repeated with HCl_(aq), ultrapure water, and ether. Finally, the solid was filtrated through a fritted glass (POR 3). Residual solvent was removed via vacuum drying at 100 °C for 48 h. The synthesis yielded in 19.0 g (41.8 mmol, corresponding to 93 % in relation to cyanuric chloride) bright orange powder.

Elemental analysis (*theoretical values given in brackets*): C₂₁H₁₅N₃O₉, C: 50.17 wt.% (55.64 wt.%), H: 4.22 wt.% (3.34 wt.%), N: 8.39 wt.% (9.27 wt.%). C/N-ratio (mol/mol): 6.97 (7.00).

¹H-NMR: δ = 5.90 ppm (s, 6H, aryl-H), 10.10 ppm (s_{br}, 3H, *p*-OH), 12.25 ppm (s_{br}, 6H, *o*-OH)

¹³C-NMR: δ = 95.69 ppm (3-aryl-C and 5-aryl-C), 98.95 ppm (1-aryl-C), 163.18 ppm (2-aryl-C and 6-aryl-C), 163.85 ppm (4-aryl-C), and 166.62 ppm (s-triazine-C).

2.2.2. Synthesis of Poly(3PT-co-formaldehyde) with 1 eq. 3PT to 3 eq. formaldehyde (P(3PT-F)-3)

In a round bottom flask (100 mL) equipped with a stirring bar and a reflux condenser, 3PT (0.7 g, 1.54 mmol, 1 eq.) and paraformaldehyde (F, 139.08 mg, 4.63 mmol, 3 eq.) were suspended in ultrapure water (12.5 mL). The mixture was heated to 50 °C for 40 min under constant stirring. Afterwards, 12.5 mL ultrapure water was added and the temperature was raised to 100 °C. After 24 h under reflux and constant stirring, the suspension changed color from bright orange to carmine. The solid was filtered off with a fritted glass (POR 4), washed with ultrapure water and ethanol, and dried at 100 °C for 24 h. For additional purification, the raw product was treated with hot ethanol in a Soxhlet extractor for 72 h. Subsequently, the solid was dried at 100 °C for 24 h in an oven and another 24 h at 100 °C in a vacuum drying oven.

2.2.3. Synthesis of P(3PT-F)-2, P(3PT-F)-4 and P(3PT-F)-3L

Reactions with an alternation of the amount of paraformaldehyde were carried out. The procedure followed the already described procedure for the synthesis of P(3PT-F)-3 in section 2.2.1. For P(3PT-F)-2 and P(3PT-F)-4, the amounts of formaldehyde used in the synthesis were varied.

For the upscaled synthesis of P(3PT-F)-3L, the amounts of 3PT, F and water as dispersant were multiplied to the 2.85-fold amounts with respect to P(3PT-F)-3. All used amounts are also stated in Table 9.1.

Waterborne Phenolic, Triazine-Based Porous Polymer Particles for the Removal of Nickel, Cadmium, and Lead Ions

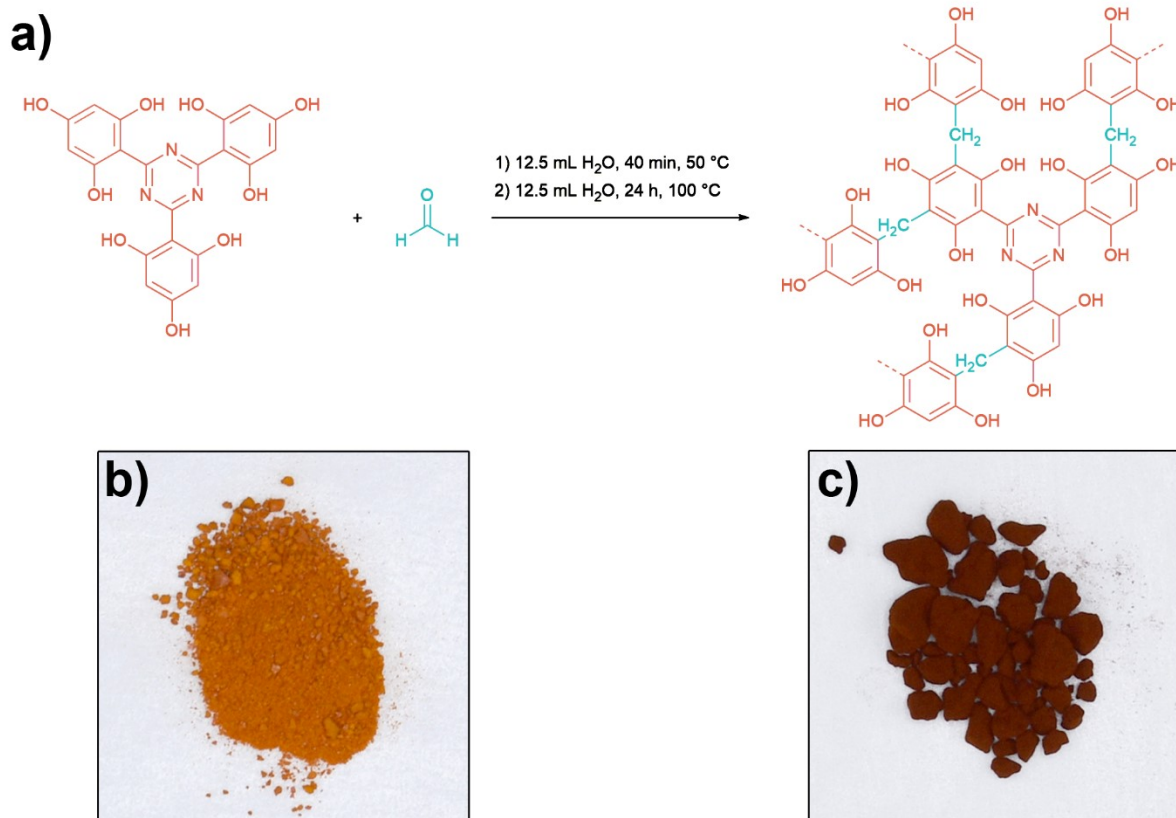


Figure 9.2. a) Reaction scheme of the synthesis of poly(3PT-co-formaldehyde) (P(3PT-F)), b) Image of 3PT powder, and c) image of P(3PT-F)-3L.

Table 9.1. Respective masses of the two monomers, 3PT and paraformaldehyde (F), and dispersant volumes used in the synthesis and variation of the equivalents of F for the products P(3PT-F)-2, P(3PT-F)-3, P(3PT-F)-4, and P(3PT-F)-3L.

Sample	Molar equivalents F:3PT	Mass 3PT in g	Mass F in mg	V water in mL
P(3PT-F)-2	2:1	0.7	93	12.5 + 12.5
P(3PT-F)-3	3:1	0.7	139	12.5 + 12.5
P(3PT-F)-4	4:1	0.7	185	12.5 + 12.5
P(3PT-F)-3L	3:1	2.0	400	35.5 + 35.5

2.3. Characterization

2.3.1. pH measurements

pH measurements were carried out with the device SevenExcellence pH/Ion/C/DO meter S975-K equipped with an InLab Expert Pro-2m-ISM electrode, both from Mettler Toledo, Gießen, Germany.

2.3.2. Scanning electron microscopy

Scanning electron microscopy (SEM) was performed to analyze the particles at nanometric scale (SEM Ultra plus, Carl Zeiss Microscopy GmbH, Oberkochen, Germany) using

a secondary electron detector (SE2). Before each analysis, the samples were attached to an aluminum pin sample tray with double-sided adhesive carbon tape and coated with 3 nm platinum to avoid electrostatic charging.

2.3.3. Thermogravimetric analysis

Thermogravimetric analysis (TG) was performed by using the device 1 Star System from Mettler Toledo Gießen, Germany. The measurements were carried out with approximately 5 – 7 mg of the respective sample in a platinum crucible. The investigated temperature range was from 30 °C to 1000 °C with a heating rate of 10 °C/min under air atmosphere and under N₂ atmosphere, with a flow rate of 40 mL/min.

2.3.4. Nitrogen sorption

Nitrogen sorption measurements were performed using the Autosorb iQ MP from Quantachrome Instruments. The samples were dried in a vacuum oven at 120 °C and activated by degassing in vacuum (5×10^{-10} mbar) at 100 °C for 24 h. Approximately 50 mg of the polymer particles was used for the measurement. The N₂ sorption measurements were performed at 77 K. The specific surface area S_{BET} was calculated using the multi-point Brunauer-Emmet-Teller method [41–43]. The pore size distribution (PSD) was determined by a fitting with a quenched-solid density functional theory model (QSDFT) for adsorption of N₂ to carbon including slit, sphere, and cylindrical pores.

2.3.5. Carbon dioxide sorption

Carbon dioxide sorption measurements were performed using the Autosorb iQ MP from Quantachrome Instruments. The samples were dried in a vacuum oven at 90 °C and activated by degassing in vacuum (5×10^{-10} mbar) at 100 °C for 24 h. Approximately 70 mg of the polymer particles was used for the measurement. The CO₂ sorption measurements were performed at 273 K.

2.3.6. Inductively coupled plasma optical emission spectrometry

Inductively Coupled Plasma Optical Emission Spectrometry (ICP-OES) (iCAP 7400 from Thermo Scientific) was used to determine the heavy metal ion concentrations in simulated and real water. Thus, eight matrix-matched, external standard solutions were used for calibration, containing the analyzed elements (Cr, Mn, Fe, Ni, Cu, Cd, Al, Pb, S) each in the same concentration (0.1 mg/L, 0.5 mg/L, 1 mg/L, 5 mg/L, 10 mg/L, 50 mg/L, 100 mg/L, or 500 mg/L, respectively). To each sample (8 mL), 2 mL 20% nitric acid was added prior to analysis. All samples were measured thrice.

2.3.7. UV-Vis spectroscopy

For the determination of the nitrate ion concentrations, the UV-Vis-spectrophotometer DR6000 (Hach Lange GmbH, Germany) was used with the associated Hach Lange cuvette test kits LCK 340 for nitrate (valid for a concentration range between 5 mg/L and 155 mg/L).

2.3.8. Attenuated total reflection infrared spectroscopy

Attenuated total reflection infrared spectroscopy (ATR-FTIR) measurements were performed using a Tensor 27 device equipped with a Platinum ATR module both from Bruker Corporation, Billerica, USA. All samples were measured in dry state with a resolution of 2 cm⁻¹ and with 100 scans under constant nitrogen flow to remove other atmospheric components. The acquired spectra were additionally subjected to an atmospheric compensation to remove the rotation bands of water.

2.3.9. Nuclear magnetic resonance

The monomer samples were dissolved in DMSO-d₆. ¹H- and ¹³C{¹H}-spectra were measured using an Avance III 500 MHz Bruker Biospin system (¹H-NMR at 500.30 MHz, ¹³C{¹H}-NMR at 125.80 MHz). Measurements were carried out at 20 °C and atmospheric pressure. The signals of the protons and carbon atoms of the solvent DMSO- d₆ was used as an internal standard ($\delta_{\text{H}} = 2.50$ ppm, $\delta_{\text{C}} = 39.52$ ppm).

CP-MAS solid-state NMR experiments have been performed on a Bruker Avance III 300 NMR spectrometer using a HF/X BL 4 mm MAS probe head with a sample spinning frequency of 8 kHz. Cross polarization was performed with a 2 ms contact time and 4 s repetition time a total of 16384 scans. The ¹³C chemical shift and Hartmann-Hahn match condition were adjusted with Adamantane and decoupling power was optimized with ¹³C₂ enriched Glycine.

2.3.10. Wide angle X-ray scattering (WAXS):

WAXS patterns were recorded using a Bruker D8 Discover diffractometer (Bruker, Karlsruhe, Germany) with a Cu Twist tube ($\lambda = 0.154018$ nm, operating at 40 kV and 40 mA) in reflection mode with a zero-background silicon specimen holder. The diffraction patterns were recorded with a VÅNTEC-500 2D detector using a sample-to-detector distance of 149.8 mm. The pattern of each sample (from 10° to 65°) was measured in two steps (step 1: $\Theta = 5^\circ$, detector (middle) = 20°, $2\Theta = 25^\circ$; step 2: $\Theta = 12.5^\circ$, detector (middle) = 37.5°, $2\Theta = 50^\circ$) with a detection time of 30 min/step. The diffraction patterns were integrated, combined, and then displayed as plot of the intensity as a function of 2Θ .

2.3.11. Particles size measurements

Particles sizes of the purified particles were analyzed using a Mastersizer Microplus (Malvern, Kassel Germany). For redispersion of the particles, 0.05 g of the sample was dispersed with ultrasonication in 10 mL ultrapure water. The resulting dispersion was then dropwise added to the measurement cell until the detector obscuration was between 13 to 20%. The data was evaluated using the model "Polydisperse", a particle refractive index (RI) of 1.5, absorbance of 0.01000 and a dispersant RI: 1.3300.

2.3.12. Streaming potential vs. pH measurements

Streaming potential vs. pH curves were measured to determine the surface charge of the particle in dependence of the pH. 0.1 g of the particles was redispersed using ultrasonication in 100 mL of ultrapure water. The resulting dispersion was characterized by titration to pH 9.0 from the initial pH of 3.5 with the particle charge detector Müttek PCD-04 from the company BTG Instruments GmbH, Wessling, Germany with 0.1 M NaOH, respectively

2.3.13. Scanning electron microscope with energy-dispersive X-ray spectroscopy

Scanning electron microscope with energy-dispersive X-ray spectroscopy (SEM-EDX): The elemental mapping of the samples after adsorptions was carried out using a Phenom XL Workstation from Thermo Scientific (Waltham, USA) with an energy-dispersive X-ray spectroscopy detector (Silicon Drift Detector SDD, thermoelectrically cooled (LN₂free), 25 mm² detector active area). The samples were fixed on a double-sided adhesive carbon tape on an aluminum pin sample tray. The measurements were carried out in low vacuum mode (p = 60 Pa) with an acceleration voltage of 10 keV at different magnifications.

2.3.14. Elemental analysis

Elemental analysis was carried out using a vario MICRO cube from the company Elementar, Langenselbold, Germany.

2.3.15. Centrifugation

The adsorbent material was separated from the supernatant by double centrifugation, each at 22,000 × g for 8 min at r.t. with the device 3-18KS from Sigma Laborzentrifugen (Osterode am Harz, Germany).

2.4. Batch adsorption experiments

For all adsorption experiments, stock solutions of the respective heavy metal salt were prepared in a 500 mL volumetric flask to achieve the desired concentrations. Therefore, the salts were dissolved in water. The pH of the resulting solutions was not adjusted. 30 mg of the polymer particles was placed into a 50 mL poly(propylene) centrifuge tube. Subsequently, 30 mL of the respective heavy metal salt solution was added. The samples were stirred for 24 h at 23 °C with a magnetic stirrer. After centrifugation, the pH of the supernatant was analyzed. 8 mL of the supernatant was taken and mixed with 2 mL of 20 wt.% nitric acid for ICP-OES analysis.

2.4.1. Adsorption experiments at varying pH₀

For experiments with varying pH₀ values, respective stock solutions of Pb(NO₃)₂ were adjusted in pH by dropwise addition of aqueous HNO₃ until the stated pH was achieved. The subsequent adsorption experiments were conducted as stated in section 2.4.

2.4.2. Selectivity experiments

For the selectivity experiments, a stock solution was prepared by dissolving 0.5 mmol of the following salts in 1L ultrapure water: PbCl₂, CuCl₂, FeCl₂, MgCl₂, CaCl₂, and KCl. The adsorption experiment was carried out as triplet according to the procedure stated in section 2.4.

2.4.3. Recycling experiments with HCl(aq)

To show the reusability, adsorption experiments with a Pb(NO₃)₂ solution of 100 mg/L Pb²⁺ was carried out as stated in section 2.4. After separation of the precipitate from the supernatant, the precipitate was rinsed twice with 2 mL of water. For desorption, 10 mL of 0.5 M aqueous HCl was added. The sample was shaken for 3 h and centrifuged afterwards. The supernatant was analyzed by ICP-OES to determine the amount desorbed. For the regeneration of the adsorbent, 10 mL 0.5 M HCl was again added to the samples with subsequent shaking for 3 h. Afterwards, a second adsorption was conducted with the sample in the same manner. The adsorption/desorption/adsorption experiment was conducted as duplet.

2.5. Calculation and theoretical models

The percentage adsorption of the samples in equilibrium was determined using Equation 9.1, whereby the initial concentrations c_0 and the equilibrium concentration c_{eq} were analyzed by ICP-OES:

$$\text{adsorption in \%} = 100\% \cdot \frac{c_0 - c_{eq}}{c_0} \quad (9.1)$$

The respective adsorption capacity q_{eq} was calculated as follows:

$$q_{eq} = \frac{(c_0 - c_{eq}) \cdot V_L}{m_A} \quad (9.2)$$

Here, V_L refers to the given volume of the adsorptive solution and m_A to the mass of the sorbent material used in the experiment. For desorption, the respective desorbed capacity was calculated as follows, whereby V_L is equal to the 10 mL which was used as solution volume for desorption and c_{eq} is the concentration of Pb²⁺ in solution after desorption:

$$q_{Des} = \frac{c_{eq} \cdot V_L}{m_A} \quad (9.3)$$

2.5.1. Isotherm models

To model the adsorption process mathematically, different isotherm models were fitted. We applied the non-linear models of the Langmuir [45], Sips [46] and Dubinin-Radushkevich [47] models as given in Equations 9.4 – 9.10.

Langmuir model:

$$q_{eq} = \frac{Q_m \cdot K_L \cdot c_{eq}}{1 + K_L \cdot c_{eq}} \quad (9.4)$$

Sips model:

$$q_{eq} = \frac{Q_m \cdot K_S \cdot c_{eq}^n}{1 + K_S \cdot c_{eq}^n} \quad (9.5)$$

K_L and K_S thereby represent the respective model equilibrium constants for Langmuir and Sips, Q_m the maximum adsorption capacity, n the Sips model exponent [48–50].

Dubinin-Radushkevich:

$$q_{eq} = Q_m \cdot \exp\left(-\beta_{DR} \cdot \left(RT \cdot \ln\left(1 + \frac{1}{c_{eq}}\right)\right)^2\right) \quad (9.6)$$

Equation 9.6 is the final non-linear form of the Dubinin-Radushkevich model that was used for fitting. It was modified in the following way. In Equation 9.7, the original form of the equation is displayed [47]. The Polanyi potential ε can further be expressed by Equation 9.8, whereby T is the given temperature and R the universal gas constant [48,49]. c_s refers to the saturation concentration. However, as the saturation concentration is not easily accessible for the given species in the present adsorption system, thus it cannot be modelled this way. As pointed out by Zhou [51], the term inside the logarithm can be exchanged for the same numerical solution as it is displayed in Equation 9.9 with two absolutely necessary requirements: First, the equilibrium concentrations needs to be much smaller than the saturation concentration ($c_{eq} \ll c_s$). Second, this substitution requires mol/L as unit for the concentration. In the end, the combination of Equation 9.7 and 9.9 leads to Equation 9.6 that was then applied in the modelling.

$$q_{eq} = Q_m \cdot \exp(-\beta_{DR} \cdot \varepsilon^2) \quad (9.7)$$

$$\varepsilon = RT \cdot \ln\left(\frac{c_s}{c_{eq}}\right) \quad (9.8)$$

$$\varepsilon = RT \cdot \ln\left(1 + \frac{1}{c_{eq}}\right) \quad (9.9)$$

With these requirements, the energy of adsorption $E_{ads,DR}$ can be expressed by the relation to the activity coefficient β_{DR} , as given in Equation 9.10.

$$E_{ads,DR} = \frac{1}{\sqrt{2 \cdot \beta_{DR}}} \quad (9.10)$$

In general, non-linear fitting was performed because linearization is changing dependent and independent variables and their errors in a numerically unpredictable way as pointed out by literature [52–54]. The fitting was performed in Origin 2022 with the Levenberg-Marquardt algorithm until X^2 reached a value below 10^{-9} and did not change further.

3. *Results and discussion*

Highly functional polymer networks that include both phenolic and triazine groups, are promising materials for the removal of heavy metal ions from aqueous solutions. To study this approach, we synthesized a copolymer that has not been reported in literature, until now. Herein, we used a monomer which consists of three phloroglucinol groups bound to an s-triazine ring (3PT), known from literature [40]. In a dispersion polymerization in water, 3PT was polymerized with different amounts of paraformaldehyde (F) yielding in nanoporous polymeric particles (P(3PT-F)). To investigate the polymerization and particle formation mechanism, the P(3PT-F) particles were characterized toward their chemical composition, pore morphology and particle size. As application-oriented proof of concept, we scaled up the colloidal synthesis. Finally, the adsorption isotherms for Ni^{2+} , Cd^{2+} , and Pb^{2+} were acquired over a wide concentration range to determine the adsorption capacity.

3.1. Synthesis and characterization of the polymer particles

The monomer used, 3PT, was synthesized by a Friedel-Crafts arylation using AlCl_3 as catalyst according to the procedure reported by Conn and Eisler with minor modifications to improve the consistency in the catalyst addition step [40]. NMR and ATR-FTIR (see Figure 9.6 and Figure S1 and S2) proved the identity of the bright orange powder and TGA measurements (see Figure S3) ensured the absence of residual aluminum species from the catalyst. In WAXS measurements, the monomer exhibited a strong but broad reflex at 26.6° and two minor, broad reflexes at 13.3° and 18.1° (see Figure S9).

To ensure the dissolution and homogenization of the educts at the first step (50°C , 40 min), before the polymerization is ensured in the second step (100°C , 24 h). We varied the equivalents of paraformaldehyde used as cross-linker respective to the 3PT monomer with molar ratios of 1:2 for P(3PT-F)-2, 1:3 for P(3PT-F)-3 and 1:4 for P(3PT-F)-4. We obtained powdered products with intense, dark red color. First, N_2 and CO_2 sorption experiments were conducted to investigate the porosity of the obtained polymers (see Figure 9.3 and Table 9.2). As it can be seen in the N_2 experiments, the samples P(3PT-F)-2, P(3PT-F)-3, and P(3PT-F)-4 exhibit a type IV(a) isotherm with H4 hysteresis loops [42,43,55].

This kind of isotherms is associated with materials incorporating both, micro- and mesopores. The uptake in the p/p_0 range below 0.1 show micropore condensation of N_2 while the hysteresis loop with the beginning at approximately $p/p_0 = 0.42$ is caused by the filling of the mesopores. The non-parallel shape of the hysteresis itself is due to a broad pore size distribution. The delayed adsorption and desorption here indicates pore blockage effects by broad variation in pore sizes and only partially filled macropores. The usage of three different cross-linker amounts affects the pore structure as it can be seen from variation in the specific surface area S_{BET} and the pore volume of the samples (see Table 9.2). From these three

samples, P(3PT-F)-3 shows the highest specific surface area with 493 m²/g. The use of less or more paraformaldehyde leads to a decrease of specific surface area that indicates an optimum at 3 equivalents in terms of cross-linking and the accessibility of the resulting pores especially in the microporous region. The pore size distribution (PSD) supports these findings (see Figure 9.3b). First, micropores with diameters below 2 nm can be seen for all samples. Additionally, two broad peaks are visible in the mesoporous region with maxima approximately at 3.2 nm and 6.5 nm. A very slight shift to lower diameters in the maxima can be seen from P(3PT-F)-2 to P(3PT-F)-4.

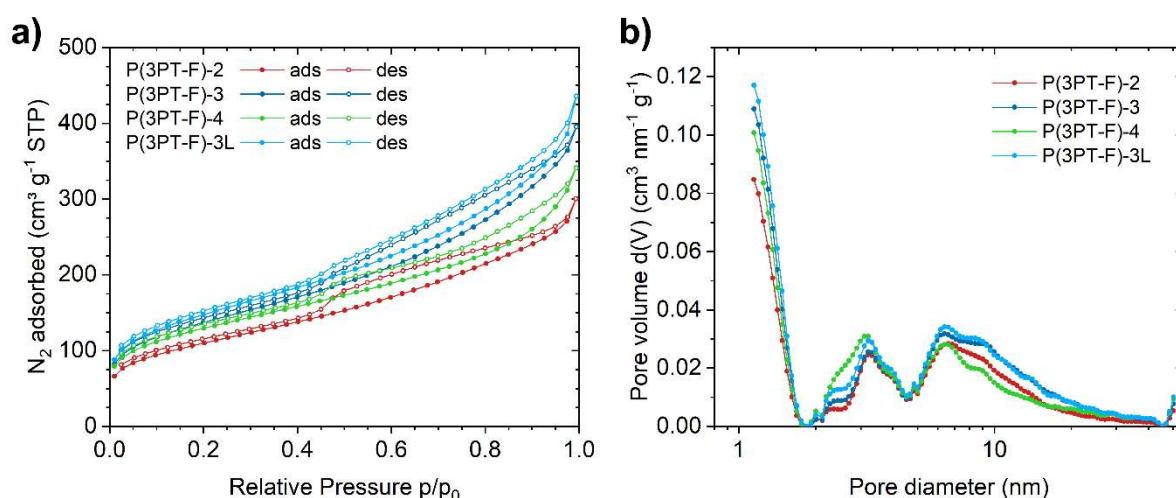


Figure 9.3. a) Nitrogen (N₂) sorption isotherms measured at 77 K for the P(3PT-F) samples, b) Pore size distribution (PSD) analysis for the P(3PT-F) samples, calculated from the adsorption branch by using QSDFT (quenched solid-state density functional theory) model for carbon with slit/cylindrical/sphere pores. Data points in the adsorption and desorption branch of the isotherms are indicated by filled and empty symbols, respectively. P(3PT-F)-2 is shown in red, P(3PT-F)-3 in dark blue, P(3PT-F)-4 in green, and P(3PT-F)-3L in light blue. Carbon dioxide (CO₂) sorption isotherms measured at 273 K are shown in Figure S5.

It is important to note that for the application in adsorption processes, two main points are crucial: First, micropores add greatly to the specific surface area that is important to maximize the potential uptake of pollutants by maximizing the amount of accessible adsorption sides of the material. Secondly, mesopores are necessary to enhance the diffusion and mass transfer in the adsorption to shorten the time needed to reach the maximum uptake that can be expressed by the pore volume given in Table 9.2. With this in mind, P(3PT-F)-3 showed the best results of the three materials in terms of both, specific surface area and pore volume. For this reason we decided to conduct an enlarged synthesis approach analogues to P(3PT-F)-3 for a subsequent application in adsorption experiments that was labeled P(3PT-F)-3L. P(3PT-F)-3L showed a nitrogen sorption isotherm and PSD very similar to the ones of sample P(3PT-F)-3. However, from the enlarged scale of the synthesis, a higher specific surface area (531 m²/g) and increased pore volume (0.56 cm³/g) was obtained. Potentially the

Waterborne Phenolic, Triazine-Based Porous Polymer Particles for the Removal of Nickel, Cadmium, and Lead Ions

altered heating of the bigger reaction flask could have resulted in a decrease in initial polymerization rate leading to overall higher pore accessibility and higher specific surface area. The sorption measurements with carbon dioxide (CO₂) at 273 K show bent isotherms with hysteresis loops and confirms ultramicroporosity for all the samples (see Figure S5).

Table 9.2. Surface area (S_{BET}), pore volume (PV), micro pore volume (MPV) and CO₂ uptake of the samples. Carbon dioxide (CO₂) sorption isotherms measured at 273 K are shown in Figure S5.

Sample code	S_{BET} ^[a] in m ² /g	PV ^[b] in cm ³ /g	MPV ^[c] in cm ³ /g
P(3PT-F)-2	395	0.40	0.15
P(3PT-F)-3	493	0.53	0.18
P(3PT-F)-4	464	0.45	0.17
P(3PT-F)-3L	531	0.56	0.20

^[a]Surface area calculated from N₂ adsorption isotherm using BET equation. ^[b]Pore volume (PV) calculated from N₂ uptake at $p/p_0 = 0.95$. ^[c]Micro pore volume (MPV) calculated from N₂ uptake at $p/p_0 = 0.10$.

In SEM images (Figure 9.4) it can be seen that particles in the micrometer range were obtained. The single particles also show a tendency towards formation of larger aggregates. In the case of P(3PT-F)-2 and P(3PT-F)-3. The particles of P(3PT-F)-2 show a polyhedral shape with smooth surfaces, while P(3PT-F)-3 exhibits a more flake-like surface morphology. In contrast, the particles of P(3PT-F)-4 are spherical with smooth surfaces again. P(3PT-F)-3L presents the same features and morphology as P(3PT-F)-3.

Noteworthy, when we analyzed P(3PT-F)-2, P(3PT-F)-3, and P(3PT-F)-4 before the purification step in the soxhlet apparatus, all samples exhibited a flake-like surface (see Figure S6 – S8). This indicates that the surface of P(3PT-F)-2 and P(3PT-F)-4 potentially still consisted of unreacted groups that were converted or eliminated by the purification step, thus forming a more smooth surface morphology afterwards. In contrast, the stoichiometry in the reaction mixture of P(3PT-F)-3 may lead to a more complete polymerization, thus retaining their initial morphology.

The particle size distribution after ultrasonication (Figure 9.4i) matches the particle sizes visible in SEM imaging. All samples exhibit one peak at diameters around 350 nm and a bigger one with diameters of several μm . This indicates that the visible, μm -sized aggregates although made up of smaller particles are rigidly connected, as it was not split by ultrasonication in a bath for 30 min. The non-upscaled samples are also exhibiting a small peak between 100 μm to 500 μm due to even larger aggregates. This peak is missing in the upscaled synthesis, probably caused by a decrease in particle collisions due to a differing rheological behavior.

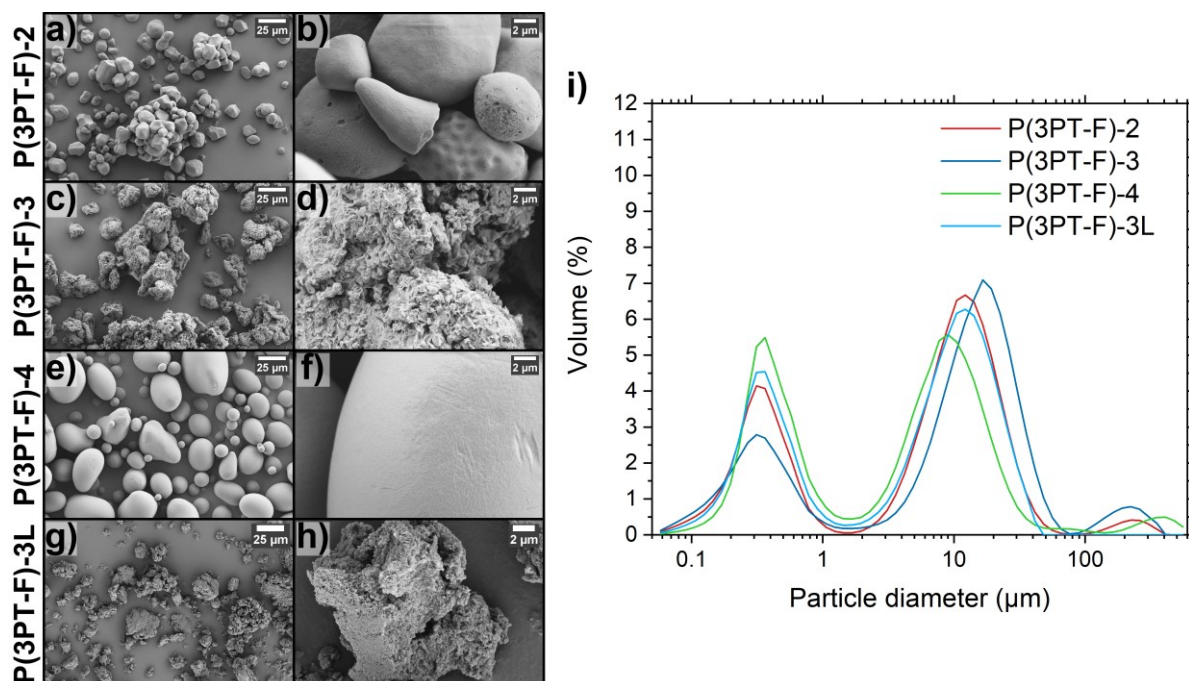


Figure 9.4. SEM images of a) and b) P(3PT-F)-2, c) and d) P(3PT-F)-3, e) and f) P(3PT-F)-4, g) and h) P(3PT-F)-3L and i) particle size distribution (volume) for the samples with P(3PT-F)-2 in red, P(3PT-F)-3 in dark blue, P(3PT-F)-4 in green, and P(3PT-F)-3L in light blue.

To characterize the network structure and chemical composition of the polymers, solid-state NMR spectroscopy, ATR-FTIR spectroscopy, WAXS measurements and thermogravimetric analysis were carried out. Understanding the methylene and ether cross-linking as well as possible tautomerism are especially important for the understanding of the polymer network and its reactivity.

In the $^{13}\text{C}\{^1\text{H}\}$ CP-MAS spectra (stack plot in Figure 9.5a), the methylene cross-linking is clearly observed as a broad peak around 10 – 30 ppm while the ether cross-linking is clearly observed as a broad peak around 50 – 70 ppm. Interpretation is obscured by peaks adjacent at 11 and 30 ppm for the methylene and 57 and 65 ppm for the ether, indicating multiple chemical environments with similar cross-linking maybe to tautomerized sub units.

With the high amount of heteroatoms in the aromatic sub structures, tautomerization of the hydroxyl group to a carbonyl group is visible. The corresponding carbonyl peak, expected around 206 ppm, is in fact greatly broadened, ranging from 180 – 220 ppm. While there are some differences, no clear identification of the potential tautomer is possible and both suggested tautomers (in ortho or para position to the triazine-linkage) are probable.

Figure 9.5 and Table S1 show the dominant peak positions and a suggested assignment. Peak 1 at 11 ppm is due to methyl carbon on the tautomerized, former aromatic ring. The peaks 2 and 3 at 20 and 30 ppm are assigned to the methylene type cross-linking in two different environments, while the peak 4 at 61 ppm corresponds to ether type cross-linking. The 5th peak at 100 ppm is caused by protonated aromatic carbon, whereas peak 6 at 109 is

assigned to aromatic carbon. Peak 7 at 167 ppm is due to phenol or azide aromatic carbon. Finally, the 8th peak at 197 ppm is assigned to the former aromatic carbon tautomerized to a carbonyl group. Figure 9.5b shows a proposed sub structure of the polymer network.

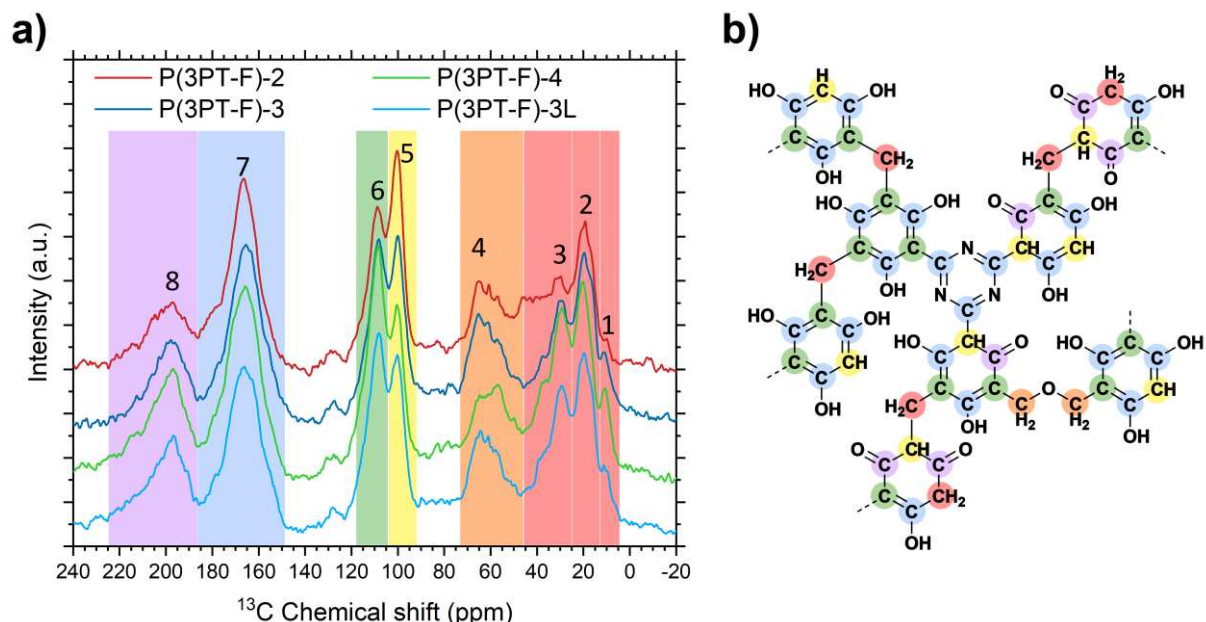


Figure 9.5. a) ^{13}C CP MAS NMR spectra for P(3PT-F)-2 (red line), P(3PT-F)-3 (dark blue line), P(3PT-F)-4 (green line) and P(3PT-F)-3L (light blue line) with peaks 1 – 8, described in detail in Table S1. The peaks are shaded according to the proposed assignments. b) Example chemical substructure of the polymer network. The colored highlights of the peaks 1 – 8 in a) correspond to the similarly highlighted carbon atoms in the chemical structure in b).

Though CP-MAS spectra are not quantitative, trends within a series of samples investigated under identical conditions can be derived. Analysis of the CPMAS spectra was done by deconvolving each spectrum into 8 peaks using DMFit software [44]. The broad peak at 62 ppm, due to the ether type moiety, was deconvolved as a single peak as the signal-to-noise does not allow apparent peaks to be resolved individually. The small signal around 127 ppm could potentially be a spinning side band and was not further analyzed. The relative content of the total integral for each peak is summarized in Table S1. Peaks 2 and 3 represent the methylene type cross-linking, while peak 4 represents the ether type cross-linking. Sample P(3PT-F)-3 shows a cross-linking ratio of 1.4:1 while the other three show a cross-linking ratio of 2:1. The linewidth in the ^{13}C CPMAS NMR spectra is considered to originate from inhomogeneous broadening, i.e. disorder in these materials.

The ATR-FTIR spectra are very similar despite the increase in formaldehyde equivalents. All spectra were normalized to the *s*-triazine bending mode at 820 cm^{-1} to ensure comparability. The very broad $\nu(\text{OH})$ mode is shifted towards a higher wavenumber (3390 cm^{-1}) when compared to the monomer 3PT (3340 cm^{-1}) presumably due to the inductive effect of methylene bridges. A further indicator for the network formation is the $\nu(\text{CH})$ mode at 2980

cm^{-1} originating from the methylene linkages. The band at 1705 cm^{-1} originating from the $\nu(\text{C=O})$ mode indicates, that the hydroxyl functionalities partially undergo the tautomerization to the carboxyl analogue in the network. Further observed modes are $\nu(\text{CN})$ at 1543 cm^{-1} , $\delta(\text{CH}_2)$ at 1435 cm^{-1} and $\nu(\text{C=C})$ at 1371 cm^{-1} and 1340 cm^{-1} that further support the formation of methylene bridges between the aromatic subunits. [11,56]

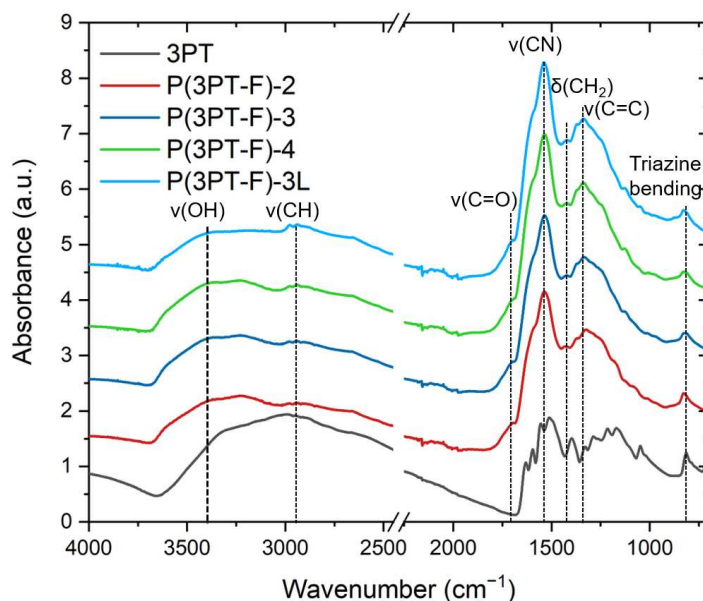


Figure 9.6. ATR-FTIR spectrum of 3PT (black), P(3PT-F)-2 (red), P(3PT-F)-3 (dark blue), P(3PT-F)-4 (green) and P(3PT-F)-3L (light blue) with the significant mode assignment and normalized to the s-triazine bending at 812 cm^{-1} for reasons of comparability.

From elemental analysis (see Table S2), a rough evaluation of the formaldehyde uptake per triazine and therefore cross-linking can be derived regarding the molar C/N ratio. The higher this value is, the more the sample is cross-linked. From direct comparison of P(3PT-F)-2, P(3PT-F)-3 and P(3PT-F)-4, it can be seen that the increased amount of paraformaldehyde also leading to a more cross-linked polymer.

From the TGA (see Figure S3 and S4), two main decomposition steps under air atmosphere can be seen (after physical dehydration up to 120°C): In the first step, approximately around 150°C , both the monomer and the polymer show a mass loss that potentially corresponds to chemical dehydration from the hydroxyl groups. Also, as it is known from Poly(melamine-co-formaldehyde) networks, formaldehyde could be eliminated from ether bonds or non-cross-linked hydroxymethyl groups [57–59]. In the second, steeper step, beginning approximately at 300°C , the complete decomposition of the network can be seen that is completed at 600°C . In general, the samples exhibit a very similar behavior. However, under nitrogen atmosphere, this second decomposition step is less steep and levels off at around 600°C ,

nearing a residual mass between 40 to 50 wt.%. Hereby, potentially only the hydroxyl groups are decomposed while the aromatic and triazine structure may be preserved to a high percentage.

In WAXS measurements of the P(3PT-F) samples (see Figure S9), a broad amorphous reflex with its maximum around 25.7° can be seen. This represents a shift towards lower 2θ values, with respect to the monomer due to increased grid spacing between the 3PT units by cross-linking. The strong broadening of the reflex represents also a greater variance in this distance. In general, all P(3PT-F) samples show the same kind of amorphous reflexes with no detectable shift in the values of peak maxima. To investigate the surface properties of the P(3PT-F)-3L particles, their surface charge was determined in a streaming potential vs. pH measurement (see Figure 9.7). It is visible that the particles exhibit a strong negative charge at between pH values of 3.5 and 9.0. This behavior is attributed to the hydroxyl groups of the polymer, easily deprotonated in water. This highly negative surface charge of the particles that is independent of the pH, grants a very good applicability of the particles for the adsorption of positively charged heavy metal ions.

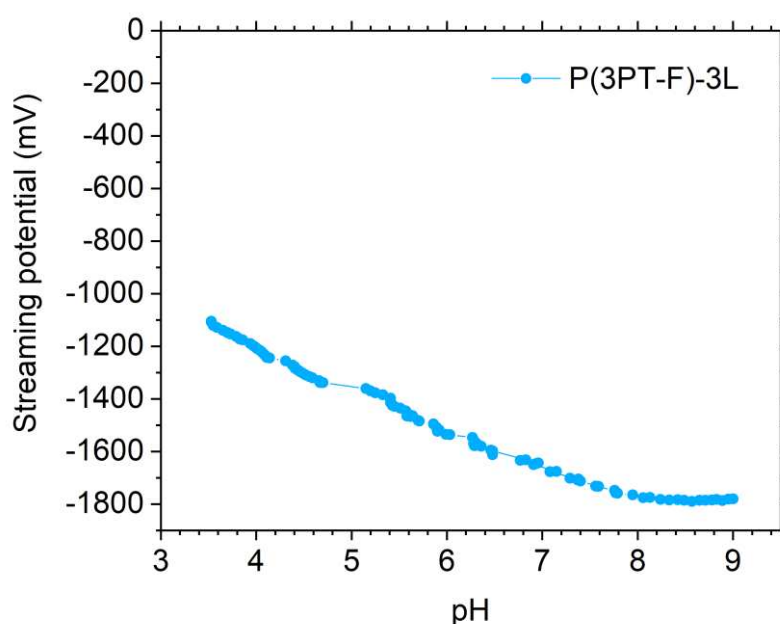


Figure 9.7. Streaming potential of P(3PT-F)-3L (light blue) over the pH range of 3.5 to 9.0.

3.2. Adsorption experiments with Ni^{2+} , Cd^{2+} , and Pb^{2+} onto P(3PT-F)-3L

For the adsorption study, P(3PT-F)-3L was used as adsorbent as it was easily producible in larger quantities and at the same time showing slightly better porosity. To demonstrate a potential application for the new polymer resin, adsorption experiments with lead, cadmium, and nickel ions as pollutants in water were investigated. Especially Pb^{2+} , Cd^{2+} , and Ni^{2+} pose a high risk to both, humans [60–73] and various aquatic species [64,74–77] in extremely low

concentrations. Therefore, we determined the adsorption isotherms of these elements over a broader concentration range to determine the efficiency in low concentrations as well as their capacity in high concentrations.

First, the transition metal ions Ni^{2+} and Cd^{2+} were tested with an adsorbent dose of 1 g/L (see Figure 9.8a and b and Table 9.3). It is well visible for both experiments that in the low-concentration region, almost 100% of the respective ions was adsorbed, therefore c_{eq} is decreased to almost 0. Here, for initial Ni^{2+} concentrations of up to 1.6 mg/L, drinking water quality (limit value of 0.07 mg Ni/L, WHO [63]) can be achieved after adsorption as the pollution is reduced by two orders of magnitude. For Cd^{2+} , an initial concentrations of up to 0.13 mg/L is reduced to 0.005 mg/L, almost reaching drinking water quality (limit value of 0.003 mg Cd/L, WHO [63]). For higher concentrations of Ni^{2+} , a maximum experimental uptake up to 15 mg/g was achieved. This value is supported by the Langmuir and Sips isotherm model, whereas the Dubinin-Radushkevich fit potentially overestimates the maximum achievable uptake. Here, the Sips model as combination of the Langmuir and Freundlich isotherm was found to best represent the adsorption process, calculating a maximum adsorption capacity of 15.7 mg/g (corresponding to 268 $\mu\text{mol Ni}^{2+}/\text{g}$). Although the adsorption capacity Q_m of the Dubinin-Radushkevich model is less accurate, its activity coefficient β_{DR} is probably relatively accurately representing the slope of the isotherm (see Figure S13). Here from, the mean free energy of adsorption $E_{\text{Ads,DR}}$ can be calculated via Eq. 9.9. It is visible that this energy is very high with a value of 17.3 kJ/mol leading to the assumption of a very strong interaction between the P(3PT-F)-3L particles and Ni^{2+} .

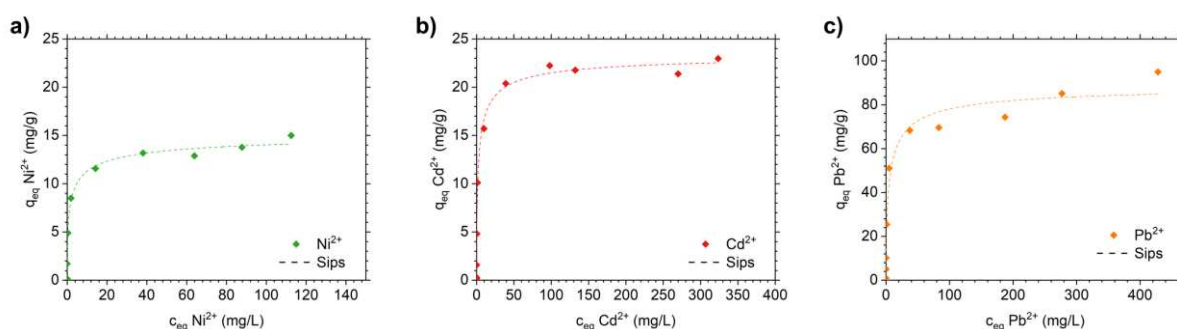


Figure 9.8. Adsorption isotherm of a) Ni^{2+} from NiSO_4 solution and b) Cd^{2+} from CdSO_4 solution, and c) Pb^{2+} from $\text{Pb}(\text{NO}_3)_2$ solution onto P(3PT-F)-3L with the respective fittings for the Sips isotherm model. The pH values before and after adsorption are displayed in Figure S10 – S12. A graphical fitting comparison can be seen in Figure S13 – S15.

Cd^{2+} exhibits a higher plateau experimentally at 23 mg/g, also supported by the fitting with the Langmuir and Sips equations (Figure 9.8b and S14). The Sips model, presenting the highest correlation, determines a maximum adsorption capacity of 23.6 mg/g (corresponding to 211 $\mu\text{mol/g}$) (see Table 9.3). This plateau is almost reached with an initial concentration of 50 mg/L Cd^{2+} , due to the extremely high affinity exhibited by the particles towards Cd^{2+} ,

Waterborne Phenolic, Triazine-Based Porous Polymer Particles for the Removal of Nickel, Cadmium, and Lead Ions

represented also from the high $E_{\text{Ads,DR}}$ value of 17.2 kJ/mol determined by the Dubinin-Radushkevich fit.

Pb^{2+} as a main group element showed the highest adsorption capacity with a plateau at around 90 mg/g (see Figure 9.8c and S15). Nonetheless, it showed an extremely steep rise in the adsorption isotherm in the low concentration region. Up to an initial concentration of 1 mg/L, drinking water quality is achieved after adsorption (limit value of 0.01 mg Pb/L, WHO [63]). In general, a decrease in Pb^{2+} concentration of one order of magnitude or even above for initial concentrations of 50 mg/L were determined that shows the efficient attainment of the maximum adsorption capacity for this material. The adsorption capacity is given with 89.8 mg/g (corresponding to 433 $\mu\text{mol/g}$) from the Sips fitting that shows a higher molar uptake of Pb^{2+} than the other investigated metal ions. In contrast to Ni^{2+} and Cd^{2+} , Pb^{2+} readily forms hydroxyl species like $[\text{Pb}(\text{OH})]^+$ and $[\text{Pb}_4(\text{OH})_4]^{4+}$ [78] that require less adsorption sites per Pb^{2+} ion, therefore contributing towards the significantly higher uptake of Pb^{2+} . This may also result in a slightly lower adsorption energy (15.8 kJ/mol), when compared to Ni^{2+} and Cd^{2+} , but with still represents a very strong interaction between Pb^{2+} and P(3PT-F)-3L in general.

Table 9.3. Fitting parameters for Langmuir, Sips and Dubinin–Radushkevich isotherm models for adsorption of Ni^{2+} and Cd^{2+} onto P(3PT-F)-3L. Q_m thereby is the maximum adsorption capacity, K is the equilibrium constant of Langmuir or Sips, n is the Sips model exponent, and β_{DR} represents the activity coefficient related to the mean free energy of adsorption $E_{\text{Ads,DR}}$. R^2 is the coefficient of determination (COD) for the respective fits. For all parameters, the corresponding standard error given from the fit are displayed. The respective graphical fitting comparison can be seen in Figure S13 – S15. The fitting for Dubinin-Radushkevich was conducted with concentration in mol/L.

Ion	Model	Q_m (mg/g)	K (*)	n	β_{DR} ($10^{-9} \text{ mol}^2/\text{J}^2$)	$E_{\text{Ads,DR}}$ (kJ/mol)	R^2 (COD)
Ni^{2+}	Langmuir	13.5 ± 0.5	1.2 ± 0.36	--	--	--	0.966
	Sips	15.7 ± 1.1	0.79 ± 0.16	0.51 ± 0.08	--	--	0.991
	Dubinin–Radushkevich	22.2 ± 1.4	--	--	1.67 ± 0.17	17.3 ± 0.9	0.978
Cd^{2+}	Langmuir	21.7 ± 0.6	0.63 ± 0.13	--	--	--	0.986
	Sips	23.6 ± 0.8	0.57 ± 0.06	0.62 ± 0.06	--	--	0.996
	Dubinin–Radushkevich	34.8 ± 2.4	--	--	1.70 ± 0.19	17.2 ± 1.0	0.970
Pb^{2+}	Langmuir	81.1 ± 3.3	0.33 ± 0.09	--	--	--	0.970
	Sips	89.8 ± 7.4	0.34 ± 0.07	0.65 ± 0.14	--	--	0.978
	Dubinin–Radushkevich	149.3 ± 13.8	--	--	1.99 ± 0.24	15.8 ± 1.0	0.963

* Unit of K for Langmuir model is L/mg and for Sips model (L/mg) ^{n} .

To gain further information about the nature of the adsorption process, the loaded adsorbent material was also analyzed by SEM-EDX after the adsorption experiments where the plateau of adsorption capacity was reached (see Table S3 and Figure S16 – S21). The

elemental surface composition derived from the EDX spectra were in the same range to the achieved adsorption capacities with 1.1 wt.% Ni²⁺, 9.8 wt.% Cd²⁺ and 14.7 wt.% Pb²⁺ (see Table S3). Here, the mass concentration of Cd²⁺ and Pb²⁺ on the surface is higher than the corresponding adsorption capacity, while Ni²⁺ show a slightly lower mass concentration than respective capacities. Therefore, we can conclude that Cd²⁺ and Pb²⁺ are probably adsorbed more to the outside of the particles while Ni²⁺ is taken up into the pore structure to a higher degree. Here, the significantly larger ionic radii of Pb²⁺ and Cd²⁺ compared to Ni²⁺ may inhibit entrance of the micropore structure [79].

In general, a homogeneous adsorption of all heavy metal ions over the visible adsorbent surface is apparent in the elemental mapping, validating the use of Langmuir and Langmuir-based isotherms such as the Sips model (Figure S16 – S21, it is noteworthy that the shadows in the mappings are mainly caused by the detector placement).

Comparing the achieved adsorption capacities to literature (Table S4 – S6), P(3PT-F)-3L is especially competitive for the adsorption of Cd²⁺ and Pb²⁺. Here, P(3PT-F)-3L shows capacities as high as commercially available resins or further modified resinous adsorbents. In the case of Pb²⁺, the new *s*-triazine-based phenolic adsorbent partially surpasses them. Thus, this first test of this newly synthesized polymer show a promising point for further development.

3.2.1. Selectivity, pH dependence and recyclability

To further analyze the adsorption mechanism and dependence on the solution pH or the presence of other ions, further experiments were conducted with Pb²⁺ as it showed the best adsorption capacity of the investigated contaminants.

The evaluation of the adsorption at differing pH₀ values gives information about the adsorption mechanism, therefore we conducted experiments with 100 mg/L Pb²⁺ at pH₀ values of 2.0, 3.0, and 4.0 besides the native pH of the solution that was 4.96 (Figure 9.9). Experiments with higher pH values were not conducted as partial hydrolysis of Pb²⁺ and subsequent precipitation is expected as shown in literature [80]. As expected from the adsorbents structure, the initial pH influences the adsorption performance of the P(3PT-F) sample. Lowering the pH, here leads to less adsorption of Pb²⁺. At pH₀ = 2.0, an adsorption capacity of only 22.5 mg/g is achieved that directly is attributed to less deprotonation of the adsorbent's hydroxyl groups, thus less active binding sites present for the adsorption. Furthermore, the formation of Pb²⁺ hydroxyl complexes is inhibited, further decreasing the adsorption capacity as discussed in the previous section [78]. Nonetheless, even at these harsh conditions, a third of the adsorption performance is retained. As Pb²⁺ is most often present in low amounts, the retention of this contaminant is possible even at this pH value but with overall lower capacity. At a pH₀ of 3.0, 78% of the original adsorption capacity is achieved, showing the viability of the adsorbent. In addition, municipal wastewater exhibits often pH

values close to neutral pH and even industrial wastewaters with high concentrations of metal ions seldom reach extremely low pH values [81–84].

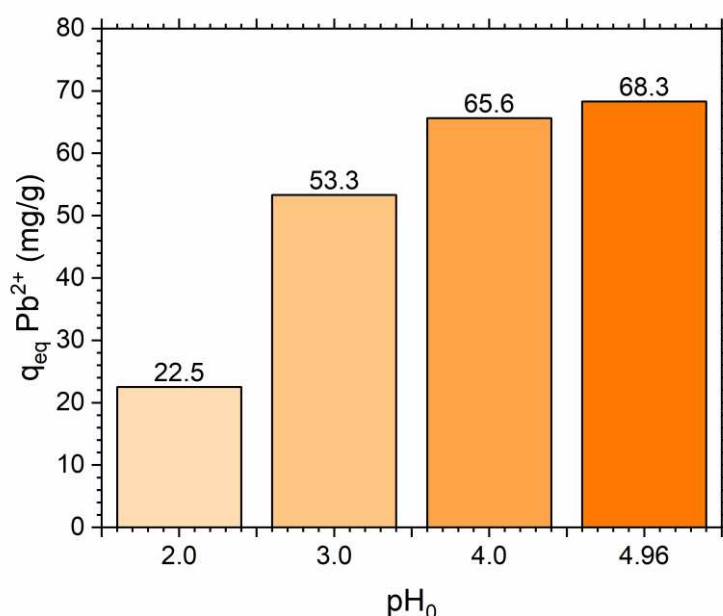


Figure 9.9. Adsorption capacity of P(3PT-F)-3L from experiments with a $\text{Pb}(\text{NO}_3)_2$ solution with $c_0 = 100$ mg/L Pb^{2+} at various pH_0 . The respective pH_{eq} values after adsorption are presented in Figure S22.

To gain information about possible competitive adsorption influences, a separate experiment, where Pb^{2+} was adsorbed in the presence of other abundantly present ions in wastewaters, was conducted. Here, the ions K^+ , Mg^{2+} , Ca^{2+} , Fe^{2+} and Cu^{2+} were chosen, each at a concentration of 0.5 mmol/L that is in the plateau region of the Pb^{2+} isotherm (corresponding to 100 mg/L Pb^{2+}) (Figure 9.10). Here, all ions were used as their respective chloride salt as chloride also represents the most abundant natural anion. It is visible, that the P(3PT-F)-3L sample showed extremely strong adsorption of Cu^{2+} as well as Pb^{2+} that is not impaired by the presence of K^+ , Mg^{2+} , Ca^{2+} and Fe^{2+} ions. Although the adsorption of Cu^{2+} is preferred over Pb^{2+} by means of molarity, the effective loading of Pb^{2+} is higher than Cu^{2+} (Figure 9.10b). Often, Cu^{2+} is also regarded as harmful [85,86], thus separation via adsorption by P(3PT-F)-3L can be considered a benefit. To add to this, ions as Ca^{2+} , Mg^{2+} , Fe^{2+} , K^+ and Cl^- that occur more often in both municipal and industrial wastewaters than Cu^{2+} , only are adsorbed in a negligible amount. This shows that the interaction of P(3PT-F) towards metal ions, especially Pb^{2+} , is selective and not attributable only to the charge of the respectively adsorbed ions.

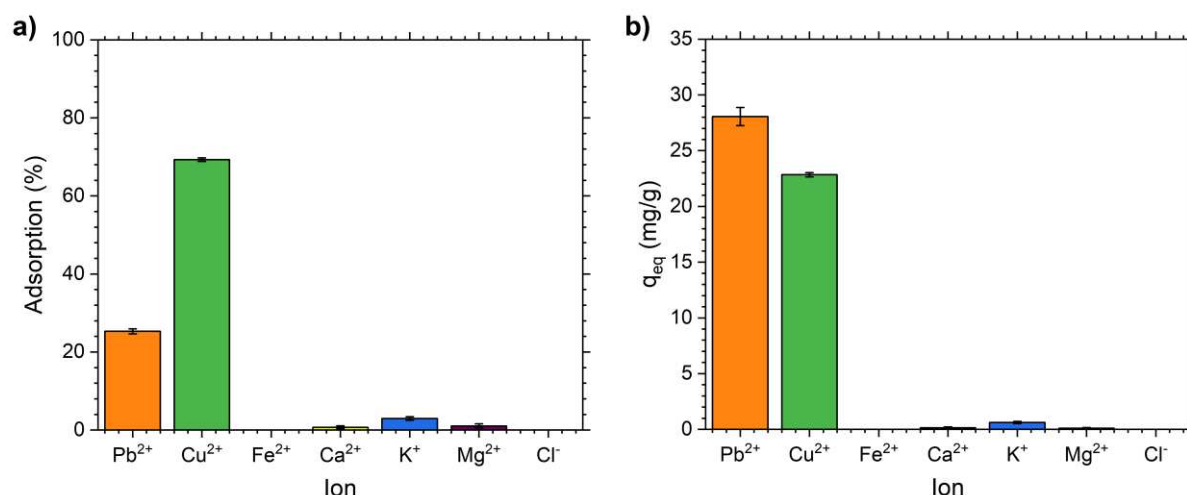


Figure 9.10. a) Percentage adsorption and b) adsorption capacity of P(3PT-F)-3L from the selectivity experiments with a solution containing 0.5 mmol of Pb²⁺ (103.6 mg/L), Cu²⁺ (31.8 mg/L), Fe²⁺ (27.9 mg/L), Ca²⁺ (20.0 mg/L), K⁺ (19.6 mg/L), Mg²⁺ (12.2 mg/L), and the respective anion Cl⁻ of all ions with c_{0,Cl⁻} = 3 mmol/L (212.7 mg/L). The experiment was conducted as triplet with respective standard deviation in both percentage adsorption and capacity shown as vertical bars. The pH₀ before adsorption was 4.01 and pH_{eq} after adsorption 3.02.

To show that P(3PT-F) is reusable, we included an experiment as proof of principle, in which the material first adsorbed Pb²⁺ from a 30 mL Pb(NO₃)₂ solution containing 100 mg/L Pb²⁺ for 24 h. Subsequently, we desorbed the loaded Pb²⁺ with 10 mL 0.5 M aqueous HCl (see Figure 9.11).

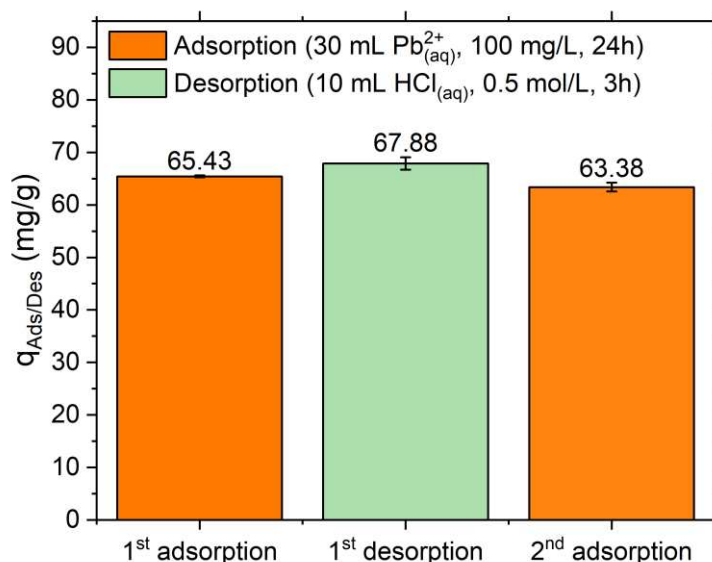


Figure 9.11. Adsorbed (orange) and desorbed (green) capacity of Pb²⁺ from respective adsorption/desorption experiments of P(3PT-F)-3L. The error bars correspond to the standard deviation from duplets. Adsorption was carried out with 30 mL Pb(NO₃)₂ solution containing 100 mg/L Pb²⁺ with an equilibration time of 24 h. Desorption was carried out using 10 mL 0.5 M HCl solution for 3 h equilibration time. The capacity of Pb²⁺ that was ad-/desorbed, was calculated with respect to the total amount of Pb²⁺ in the respective 30 mL or 10 mL. The initial pH₀ of the adsorption experiments was 5.1 and pH_{eq} after adsorption was 3.3 for both times.

From the experiments, it is visible that the desorption step can be regarded as quantitative as the desorbed amount and the adsorbed amount are basically equal with the deviation likely to result from the multiple centrifugation and washing steps. The adsorption achieved during the second cycle leads to a very similar capacity as the first one, proving excellent reusability of the material. Here, for desorption only a third of the volume was used when comparing with the adsorptive solution as well as less time with 3 h for desorption vs. 24 h for adsorption. Further, this demonstrates that desorption can be done with plain HCl circumventing the use of organic chelating agents such as ethylenediaminetetraacetic acid.

The adsorption experiments at differing pH_0 as well as the selectivity evaluation and the successful desorption via HCl also directly provide viable insight into the adsorption mechanism. It is apparent that the adsorption significantly depends on the deprotonation of the hydroxyl functionalities that increases with pH. However, selectivity experiments prove that adsorption is not solely dependent on the charge of the ions, we conclude that the s-triazine moiety facilitates the adsorption of Pb^{2+} and Cu^{2+} that are both well known for their coordinative chemistry [87]. Furthermore, iron ions that are prone to oxidize about the duration of the experiment, and thus should exhibit a positive charge of +III, are not adsorbed in considerable amounts. Therefore, the triazine moiety increases the interaction towards the tested ions, enhancing the adsorption.

4. Conclusions

We presented the successful preparation of a previously unknown polymer for the application in heavy metal ion removal. In a facile dispersion polymerization using water as dispersant, a highly nanoporous polymer with specific surface areas up to $531 \text{ m}^2/\text{g}$ were obtained. We thoroughly characterized its chemical composition elemental analysis and FTIR spectroscopy. The morphology and physicochemical properties of the material were evaluated in detail using electron microscopy, N_2 and CO_2 adsorption as well as particle size and streaming potential vs. pH measurements. With a successful upscaling, material for batch adsorption experiments was obtained in a more detailed investigation, the adsorption isotherms for Ni^{2+} , Cd^{2+} , and Pb^{2+} were determined. Here, maximum adsorption capacities of $16 \text{ mg Ni}^{2+}/\text{g}$, $24 \text{ mg Cd}^{2+}/\text{g}$, and $90 \text{ mg Pb}^{2+}/\text{g}$ were attained. In realistically low concentrations, the heavy metal contamination was reduced by up to two orders of magnitude, thus achieving drinking water quality in these experiments. The high amount of hydroxyl and triazine functionalities of the polymer is enabling a very strong interaction with metal ions in terms of ionic interactions as well as coordinative bonds. In general, a very steep uptake in the adsorption isotherms was observed, also represented by the very high mean free energy of adsorption, calculated by fittings with the Dubinin-Radushkevich model. Our study shows that the polymer is especially viable because of its high affinity towards the

analyzed metal ions leading to a high uptake already in low concentrations of the contaminants. Furthermore, our adsorbent shows outstanding capacities for the adsorption of Cd^{2+} and Pb^{2+} . Although the adsorption capacity decreases at lower pH_0 values, we could show that even at harsh conditions of $\text{pH}_0 = 2$, 33% of the capacity is retained, while for $\text{pH}_0 = 3.0$, 78% of the initial capacity can be achieved. From selectivity experiments, it was found that the abundant, significantly less toxic ions Ca^{2+} , Mg^{2+} , Fe^{2+} , K^+ and Cl^- did not interfere, while the less common Cu^{2+} showed significant adsorption. Herein, Pb^{2+} still showed the highest adsorption capacity in terms of mass contaminant per mass adsorbent. With a short recycling experiment, we proved that desorption can be carried out easily using 0.5 M HCl in a low volume and at significantly less time than the adsorption (3 h vs. 24 h). Reusing the adsorbent a second time yielded in an unimpaired adsorption capacity for Pb^{2+} .

Overall, this could lead to further development of this new material and can exhibit an impact on the treatment of water to achieve safety in terms of drinking water quality demanded by the WHO.

Acknowledgments

The authors want to thank Eileen Schierz for the conduction of the elemental analysis.

Funding

This work was supported by the German Federal Ministry of Education and Research [grant number 01DJ18010].

References

1. J. Huang, S.R. Turner, Hypercrosslinked Polymers: A Review, *Polymer Reviews* 58 (2018) 1–41.
2. C. Wang, C. Li, E.R.C. Rutledge, S. Che, J. Lee, A.J. Kalin, C. Zhang, H.-C. Zhou, Z.-H. Guo, L. Fang, Aromatic porous polymer network membranes for organic solvent nanofiltration under extreme conditions, *J. Mater. Chem. A* 8 (2020) 15891–15899.
3. S. Nandi, U. Werner-Zwanziger, R. Vaidhyanathan, A triazine–resorcinol based porous polymer with polar pores and exceptional surface hydrophobicity showing CO_2 uptake under humid conditions, *J. Mater. Chem. A* 3 (2015) 21116–21122.
4. S. Nandi, J. Rother, D. Chakraborty, R. Maity, U. Werner-Zwanziger, R. Vaidhyanathan, Exceptionally stable Bakelite-type polymers for efficient pre-combustion CO_2 capture and H_2 purification, *J. Mater. Chem. A* 5 (2017) 8431–8439.
5. M. Saleh, S.B. Baek, H.M. Lee, K.S. Kim, Triazine-Based Microporous Polymers for Selective Adsorption of CO_2 , *J. Phys. Chem. C* 119 (2015) 5395–5402.
6. J. Gu, P. Shao, L. Luo, Y. Wang, T. Zhao, C. Yang, P. Chen, F. Liu, Microporous triazine-based ionic hyper-crosslinked polymers for efficient and selective separation of $\text{H}_2\text{S}/\text{CH}_4/\text{N}_2$, *Separation and Purification Technology* 285 (2022) 120377.
7. K. Wang, H. Huang, D. Liu, C. Wang, J. Li, C. Zhong, Covalent Triazine-Based Frameworks with Ultramicropores and High Nitrogen Contents for Highly Selective CO_2 Capture, *Environmental science & technology* 50 (2016) 4869–4876.
8. I.D. Wessely, A.M. Schade, S. Dey, A. Bhunia, A. Nuhnen, C. Janiak, S. Bräse, Covalent Triazine Frameworks Based on the First Pseudo-Octahedral Hexanitrile Monomer via Nitrile Trimerization: Synthesis, Porosity, and CO_2 Gas Sorption Properties, *Materials (Basel, Switzerland)* 14 (2021).

Waterborne Phenolic, Triazine-Based Porous Polymer Particles for the Removal of Nickel, Cadmium, and Lead Ions

9. N. Nouruzi, M. Dinari, N. Mokhtari, B. Gholipour, S. Rostamnia, S. Khaksar, R. Boluki, Porous triazine polymer: A novel catalyst for the three-component reaction, *Appl Organomet Chem* 34 (2020) 153.
10. D. Mullangi, S. Nandi, S. Shalini, S. Sreedhala, C.P. Vinod, R. Vaidhyanathan, Pd loaded amphiphilic COF as catalyst for multi-fold Heck reactions, C-C couplings and CO oxidation, *Scientific reports* 5 (2015) 10876.
11. S. Nandi, V.M. Dhavale, S. Shalini, U. Werner-Zwanziger, H. Singh, S. Kurungot, R. Vaidhyanathan, Lithium-Assisted Proton Conduction at 150 °C in a Microporous Triazine-Phenol Polymer, *Adv. Mater. Interfaces* 2 (2015) 1500301.
12. Y. Wang, J. Xiao, H. Wang, T.C. Zhang, S. Yuan, N-Doped Porous Carbon Derived from Solvent-Free Synthesis of Cross-Linked Triazine Polymers for Simultaneously Achieving CO₂ Capture and Supercapacitors, *Chemistry (Weinheim an der Bergstrasse, Germany)* 27 (2021) 7908–7914.
13. R. Peng, G. Chen, F. Zhou, R. Man, J. Huang, Catalyst-free synthesis of triazine-based porous organic polymers for Hg²⁺ adsorptive removal from aqueous solution, *Chemical Engineering Journal* 371 (2019) 260–266.
14. Y. He, Q. Liu, F. Liu, C. Huang, C. Peng, Q. Yang, H. Wang, J. Hu, H. Liu, Porous organic polymer bifunctionalized with triazine and thiophene groups as a novel adsorbent for removing Cu (II), *Microporous and Mesoporous Materials* 233 (2016) 10–15.
15. N. Mokhtari, M. Dinari, O. Rahmadian, Novel porous organic triazine-based polyimide with high nitrogen levels for highly efficient removal of Ni(II) from aqueous solution, *Polym. Int.* 68 (2019) 1178–1185.
16. K.B.L. Borchert, C. Steinbach, B. Reis, N. Gerlach, P. Zimmermann, S. Schwarz, D. Schwarz, Mesoporous Poly(melamine-co-formaldehyde) Particles for Efficient and Selective Phosphate and Sulfate Removal, *Molecules (Basel, Switzerland)* 26 (2021) 6615.
17. D. Schwarz, J. Weber, Organic-solvent free synthesis of mesoporous and narrow-dispersed melamine resin particles for water treatment applications, *Polymer* 155 (2018) 83–88.
18. D. Schwarz, J. Weber, Synthesis of mesoporous poly(melamine-formaldehyde) particles by inverse emulsion polymerization, *Journal of colloid and interface science* 498 (2017) 335–342.
19. T.J. Mooibroek, P. Gamez, The s-triazine ring, a remarkable unit to generate supramolecular interactions, *Inorganica Chimica Acta* 360 (2007) 381–404.
20. H. Shan, S. Li, Z. Yang, X. Zhang, Y. Zhuang, Q. Zhu, Di Cai, P. Qin, J. Baeyens, Triazine-based N-rich porous covalent organic polymer for the effective detection and removal of Hg (II) from an aqueous solution, *Chemical Engineering Journal* 426 (2021) 130757.
21. F. Fu, Q. Wang, Removal of heavy metal ions from wastewaters: a review, *Journal of environmental management* 92 (2011) 407–418.
22. E.O. Skogley, A. Dobermann, Synthetic Ion-Exchange Resins: Soil and Environmental Studies, *J. environ. qual.* 25 (1996) 13–24.
23. T.A. Kurniawan, G.Y.S. Chan, W.-H. Lo, S. Babel, Physico-chemical treatment techniques for wastewater laden with heavy metals, *Chemical Engineering Journal* 118 (2006) 83–98.
24. S.K. Sahni, R. van Bennekom, J. Reedijk, A spectral study of transition-metal complexes on a chelating ion-exchange resin containing aminophosphonic acid groups, *Polyhedron* 4 (1985) 1643–1658.
25. D.S. Stefan, I. Meghea, Mechanism of simultaneous removal of Ca²⁺, Ni²⁺, Pb²⁺ and Al³⁺ ions from aqueous solutions using Purolite® S930 ion exchange resin, *Comptes Rendus Chimie* 17 (2014) 496–502.
26. B. Alyüz, S. Veli, Kinetics and equilibrium studies for the removal of nickel and zinc from aqueous solutions by ion exchange resins, *Journal of hazardous materials* 167 (2009) 482–488.
27. H.P. Gregor, J.I. Bregman, Studies on ion-exchange resins. IV. Selectivity coefficients of various cation exchangers towards univalent cations, *Journal of Colloid Science* 6 (1951) 323–347.
28. S.K. Samanta, B.M. Misra, Ion Exchange Selectivity of a Resorcinol-Formaldehyde Polycondensate Resin for Cesium In Relation to other Alkali Metal Ions, *Solvent Extraction and Ion Exchange* 13 (1995) 575–589.
29. R. Verma, P.K. Maji, S. Sarkar, Detailed investigation of effective trace Cr(VI) removal mechanism by anion exchange resin with phenol-formaldehyde matrix, *Journal of Industrial and Engineering Chemistry* 188 (2022) 276.
30. S.A. Shady, Selectivity of cesium from fission radionuclides using resorcinol-formaldehyde and zirconyl-molybdopyrophosphate as ion-exchangers, *Journal of hazardous materials* 167 (2009) 947–952.
31. V.I. Gorshkov, V.A. Ivanov, I.V. Staina, Selectivity of phenol-formaldehyde resins and separation of rare alkali metals, *Reactive and Functional Polymers* 38 (1998) 157–176.
32. A.N. Nikoloski, K.-L. Ang, Review of the Application of Ion Exchange Resins for the Recovery of Platinum-Group Metals From Hydrochloric Acid Solutions, *Mineral Processing and Extractive Metallurgy Review* 35 (2014) 369–389.

Waterborne Phenolic, Triazine-Based Porous Polymer Particles for the Removal of Nickel, Cadmium, and Lead Ions

33. I.B. Rae, S. Pap, D. Svobodova, S.W. Gibb, Comparison of sustainable biosorbents and ion-exchange resins to remove Sr^{2+} from simulant nuclear wastewater: Batch, dynamic and mechanism studies, *The Science of the total environment* 650 (2019) 2411–2422.
34. N. Astrini, L. Anah, H.R. Haryadi, Adsorption of Heavy Metal Ion from Aqueous Solution by Using Cellulose Based Hydrogel Composite, *Macromol. Symp.* 353 (2015) 191–197.
35. X. Gao, C. Guo, J. Hao, Z. Zhao, H. Long, M. Li, Adsorption of heavy metal ions by sodium alginate based adsorbent-a review and new perspectives, *International journal of biological macromolecules* 164 (2020) 4423–4434.
36. Y. Ge, Z. Li, Application of Lignin and Its Derivatives in Adsorption of Heavy Metal Ions in Water: A Review, *ACS Sustainable Chem. Eng.* 6 (2018) 7181–7192.
37. M. Ochi, J. Ida, T. Matsuyama, H. Yamamoto, Thermoresponsive-interpenetrating polymer network hydrogels for heavy metal ion recovery, *J. Appl. Polym. Sci.* 135 (2018) 46701.
38. L.A. Shah, M. Khan, R. Javed, M. Sayed, M.S. Khan, A. Khan, M. Ullah, Superabsorbent polymer hydrogels with good thermal and mechanical properties for removal of selected heavy metal ions, *Journal of Cleaner Production* 201 (2018) 78–87.
39. V. Gómez-Ceballos, A. García-Córdoba, Z. Zapata-Benabithé, J. Velásquez, G. Quintana, Preparation of hyperbranched polymers from oxidized lignin modified with triazine for removal of heavy metals, *Polymer Degradation and Stability* 179 (2020) 109271.
40. G. Conn, S. Eisler, Synthesis and intramolecular hydrogen bonding networks of 2,4,6-tri(o-hydroxyaryl)-1,3,5-triazines, *Organic letters* 13 (2011) 5080–5083.
41. S. Brunauer, P.H. Emmett, E. Teller, Adsorption of Gases in Multimolecular Layers, *J. Am. Chem. Soc.* 60 (1938) 309–319.
42. M. Thommes, K. Kaneko, A.V. Neimark, J.P. Olivier, F. Rodriguez-Reinoso, J. Rouquerol, K.S.W. Sing, Physisorption of gases, with special reference to the evaluation of surface area and pore size distribution (IUPAC Technical Report), *Pure and Applied Chemistry* 87 (2015) 1051–1069.
43. K.S.W. Sing, Reporting physisorption data for gas/solid systems: With special reference to the determination of surface area and porosity, *Pure & Applied Chemistry* 54 (1982) 2201–2218.
44. D. Massiot, F. Fayon, M. Capron, I. King, S. Le Calvé, B. Alonso, J.-O. Durand, B. Bujoli, Z. Gan, G. Hoatson, Modelling one- and two-dimensional solid-state NMR spectra, *Magn. Reson. Chem.* 40 (2002) 70–76.
45. I. Langmuir, The Constitution And Fundamental Properties Of Solids And Liquids. Part I. Solids, *J. Am. Chem. Soc.* 38 (1916) 2221–2295.
46. R. Sips, On the Structure of a Catalyst Surface, *The Journal of Chemical Physics* 16 (1948) 490–495.
47. M.M. Dubinin, The Equation of the Characteristic Curve of Activated Charcoal, *Proceedings of the USSR Academy of Sciences* 55 (1947) 327–329.
48. F. Togue Kamga, Modeling adsorption mechanism of paraquat onto Ayous (*Triplochiton scleroxylon*) wood sawdust, *Appl Water Sci* 9 (2019) 456.
49. K.Y. Foo, B.H. Hameed, Insights into the modeling of adsorption isotherm systems, *Chemical Engineering Journal* 156 (2010) 2–10.
50. M.A. Al-Ghouti, D.A. Da'ana, Guidelines for the use and interpretation of adsorption isotherm models: A review, *Journal of hazardous materials* 393 (2020) 122383.
51. X. Zhou, Correction to the calculation of Polanyi potential from Dubinnin-Rudushkevich equation, *Journal of hazardous materials* 384 (2020) 121101.
52. T.A. Osmari, R. Gallon, M. Schwaab, E. Barbosa-Coutinho, J.B. Severo, J.C. Pinto, Statistical Analysis of Linear and Non-Linear Regression for the Estimation of Adsorption Isotherm Parameters, *Adsorption Science & Technology* 31 (2013) 433–458.
53. B. Subramanyam, A. Das, Linearised and non-linearised isotherm models optimization analysis by error functions and statistical means, *Journal of environmental health science & engineering* 12 (2014) 92.
54. J. Wang, X. Guo, Adsorption isotherm models: Classification, physical meaning, application and solving method, *Chemosphere* 258 (2020) 127279.
55. C. Schlumberger, M. Thommes, Characterization of Hierarchically Ordered Porous Materials by Physisorption and Mercury Porosimetry—A Tutorial Review, *Adv. Mater. Interfaces* 8 (2021) 2002181.
56. G. Socrates, Infrared and Raman characteristic group frequencies: Tables and charts, 3rd ed., John Wiley & Sons LTD, Chichester [etc.], 2015.
57. C. Devallencourt, J.M. Saiter, A. Fafet, E. Ubrich, Thermogravimetry/Fourier transform infrared coupling investigations to study the thermal stability of melamine formaldehyde resin, *Thermochimica Acta* 259 (1995) 143–151.
58. D.J. Merline, S. Vukusic, A.A. Abdala, Melamine formaldehyde: curing studies and reaction mechanism, *Polym J* 45 (2013) 413–419.

Waterborne Phenolic, Triazine-Based Porous Polymer Particles for the Removal of Nickel, Cadmium, and Lead Ions

59. S. Ullah, M.A. Bustam, M. Nadeem, M.Y. Naz, W.L. Tan, A.M. Shariff, Synthesis and thermal degradation studies of melamine formaldehyde resins, *TheScientificWorldJournal* 2014 (2014) 940502.
60. M. Jaishankar, T. Tseten, N. Anbalagan, B.B. Mathew, K.N. Beeregowda, Toxicity, mechanism and health effects of some heavy metals, *Interdisciplinary toxicology* 7 (2014) 60–72.
61. H.S. Kim, Y.J. Kim, Y.R. Seo, An Overview of Carcinogenic Heavy Metal: Molecular Toxicity Mechanism and Prevention, *Journal of cancer prevention* 20 (2015) 232–240.
62. United Nations Environment Programme, Chemical Branch, DTIE, Final Review of Scientific Information on Lead - Version of December 2010, 2010.
63. World Health Organization, Guidelines for drinking-water quality: First addendum to the third edition, volume 1 recommendations, Geneva, 2006.
64. H. Ali, E. Khan, Bioaccumulation of non-essential hazardous heavy metals and metalloids in freshwater fish. Risk to human health, *Environ Chem Lett* 16 (2018) 903–917.
65. Air quality guidelines for Europe, 2nd ed., WHO, Regional Office for Europe, Copenhagen, 2000.
66. E.M. Caravati, Medical toxicology, 3rd ed., Lippincott, Williams & Wilkins, Philadelphia, op. 2004.
67. L.M. Cleveland, M.L. Minter, K.A. Cobb, A.A. Scott, V.F. German, Lead hazards for pregnant women and children: part 1: immigrants and the poor shoulder most of the burden of lead exposure in this country. Part 1 of a two-part article details how exposure happens, whom it affects, and the harm it can do, *The American journal of nursing* 108 (2008) 40-9; quiz 50.
68. United Nations Environment Programme, Chemical Branch, DTIE, Final Review of Scientific Information on Lead - Version of December 2010, 2010.
69. J. Godt, F. Scheidig, C. Grosse-Siestrup, V. Esche, P. Brandenburg, A. Reich, D.A. Groneberg, The toxicity of cadmium and resulting hazards for human health, *Journal of occupational medicine and toxicology* (London, England) 1 (2006) 22.
70. A. Hartwig, Cadmium and cancer, *Metal ions in life sciences* 11 (2013) 491–507.
71. Seventh Annual Report on Carcinogens, *Environmental health perspectives* 102 (1994) 739.
72. K.K. Das, R.C. Reddy, I.B. Bagoji, S. Das, S. Bagali, L. Mullur, J.P. Khodnapur, M.S. Biradar, Primary concept of nickel toxicity - an overview, *Journal of basic and clinical physiology and pharmacology* 30 (2018) 141–152.
73. G. Genchi, A. Carocci, G. Lauria, M.S. Sinicropi, A. Catalano, Nickel: Human Health and Environmental Toxicology, *International journal of environmental research and public health* 17 (2020).
74. B.G. Church, P.A. van Sprang, M.J. Chowdhury, D.K. DeForest, Updated species sensitivity distribution evaluations for acute and chronic lead toxicity to saltwater aquatic life, *Environmental toxicology and chemistry* 36 (2017) 2974–2980.
75. T.I. Moiseenko, N.A. Gashkina, Biogeochemistry of Cadmium: Anthropogenic Dispersion, Bioaccumulation, and Ecotoxicity, *Geochem. Int.* 56 (2018) 798–811.
76. M.D. Pavlaki, M.J. Araújo, D.N. Cardoso, A.R.R. Silva, A. Cruz, S. Mendo, A.M.V.M. Soares, R. Calado, S. Loureiro, Ecotoxicity and genotoxicity of cadmium in different marine trophic levels, *Environmental pollution* (Barking, Essex 1987) 215 (2016) 203–212.
77. G. Pyle, P. Couture, Nickel, in: *Homeostasis and Toxicology of Essential Metals*, Elsevier, 2011, pp. 253–289.
78. B.C. Bunker, W.H. Casey, The Hydrolysis Products: Soluble Multi-cation Clusters, in: B.C. Bunker, W.H. Casey (Eds.), *The Aqueous Chemistry of Oxides*, Oxford University Press, 2016.
79. I. Persson, Hydrated metal ions in aqueous solution: How regular are their structures?, *Pure and Applied Chemistry* 82 (2010) 1901–1917.
80. M. Businelli, F. Casciari, D. Businelli, G. Gigliotti, Mechanisms of Pb (II) sorption and desorption at some clays and goethite-water interfaces, *Agronomie* 23 (2003) 219–225.
81. A. Alsulaili, B.Y. Al-Buloushi, M.F. Hamoda, Seasonal variation pattern of physicochemical and microbial parameters in a wastewater treatment plant, *DWT* 208 (2020) 244–260.
82. J. Wang, C.P. Huang, H.E. Allen, Predicting metals partitioning in wastewater treatment plant influents, *Water research* 40 (2006) 1333–1340.
83. T. Li, W. Dong, Q. Zhang, D. Xing, W. Ai, T. Liu, Phosphate removal from industrial wastewater through in-situ Fe²⁺ oxidation induced homogenous precipitation: Different oxidation approaches at wide-ranged pH, *Journal of environmental management* 255 (2020) 109849.
84. G. Macchi, M. Pagano, M. Santori, G. Tiravanti, Battery industry wastewater: Pb removal and produced sludge, *Water research* 27 (1993) 1511–1518.
85. V. Ochoa-Herrera, G. León, Q. Banihani, J.A. Field, R. Sierra-Alvarez, Toxicity of copper(II) ions to microorganisms in biological wastewater treatment systems, *The Science of the total environment* 412–413 (2011) 380–385.

Waterborne Phenolic, Triazine-Based Porous Polymer Particles for the Removal of Nickel, Cadmium, and Lead Ions

86. B. Fjällborg, G. Dave, Toxicity of copper in sewage sludge, *Environment International* 28 (2003) 761–769.
87. R.G. Pearson, Hard and Soft Acids and Bases, *J. Am. Chem. Soc.* 85 (1963) 3533–3539.

10. Conclusion and Outlook

The aim of this work is the synthesis of highly nanoporous resin particles that allow efficient adsorption of pollutants. By systematically varying synthesis parameters, starting from a known synthesis strategy, PMF particles could be obtained which were highly tunable both in their size and in the properties of their pore system. Very high specific surface areas of up to 420 m²/g were achieved, ordered pore systems with adjustable pore size (12 nm and 22 nm) and the intrinsic connecting channels between the spherical pores could be tailored in their diameter to obtain a particularly open or particularly closed pore system.

From the entirety of all variations, a particle formation and templating mechanism was derived, which could logically deduce and prove the complex interplay of the interactions between the different individual components of the reaction mixture. Here, it could be shown that SiO₂ NPs are not only included in the PMF resin in regard of a template, but can simultaneously shield the particle surface during polymerization as a Pickering-like surfactant. Via choice of suitable reaction parameters, the behavior of SiO₂ NPs as either template or surfactant can be selected and the other suppressed if needed.

The succeeding goal of the work was the preparation of particles with diameters of several micrometers without loss of porosity. Publications on colloidal PMF syntheses have so far only been able to obtain either uniform but nonporous particles of several micrometers in size, or highly porous particles with significantly smaller diameters by applying templating with SiO₂ NPs. This made a potential large-scale application as a flow-through fixed bed adsorber impossible. As part of the work on the particle formation mechanism, particles with a diameter of about 10 µm were obtained, which had a specific surface area of 280 m²/g. These were then used in a fixed-bed column adsorption experiment to separate extremely toxic Cr₂O₇²⁻. Here, drinking water quality was achieved in the adsorbent effluent despite the Cr⁶⁺ limit value in the influent being exceeded by a factor of 50 and a very low adsorbent mass being used.

The adsorption performance of PMF for pollutant removal of oxyanions, heavy metal ions, and pharmaceuticals, respectively, was demonstrated using samples that exhibited strong differences in the distinct pore system by varying single synthesis parameters. By changing the amount of template in the syntheses, PMF particles could be generated which should all nominally have the same pore diameter by using the same template size. However, a strong increase of the template amount led to the inclusion of single SiO₂ NPs as well as aggregates of several particles, which resulted on the one hand in the formation of larger pores but also in pore collapse due to the loss of the template before complete inclusion. Thus, when an optimum was exceeded, it was shown that a less ordered pore structure led to significantly broadened peaks in the pore size distribution.

In adsorption experiments with the oxyanions sulfate and phosphate, these less ordered pore systems recorded significantly higher adsorption capacities probably due to less pore

blocking effects by better accessibility. Here, exceptional capacities of 341 mg phosphate/g and 251 mg sulfate/g were achieved, exceeding the performance of commercial ion exchange resins by up to 2 and 1.5 times, respectively. In addition, separation of sulfate and phosphate ions from binary solutions was achieved, as sulfate ions could be selectively adsorbed by H-PMF particles.

To study the adsorption of more kinetically inhibited pharmaceutical molecules such as DCF, PMF particles were prepared using different commercial SiO₂ dispersions. The thereby varied template diameters or varied counter ions of the SiO₂ NPs resulted in very different pore systems, which differed in the accessibility of their pore systems and partly in the diameter of their pores. Surprisingly, significant changes were also found in microporosity and accessibility of these micropores by CO₂ sorption measurements. This variance in the distinct pore system makes the fabricated PMF particles ideal materials to identify the influence of the pore system on adsorption performance. In the experiments, it was recognized that the micropore volume directly correlates with the adsorption capacity for DCF. However, the accessibility of these micropores is also essential. Poor accessibility in the micropore region lead to decreased adsorption performance and was identified by different values for the micropore volume obtained via N₂ and CO₂ sorption. A similar effect of pore accessibility was seen in the mesoporous region. Here, a pore system with more connecting channels between the main cavities was found to have much higher removal rates in the low concentration range. This effect was attributed to the fact that narrow pore connecting channels lead to a blockage in the sense of a potential barrier by previously adsorbed molecules. This prevents the passage of further adsorptive molecules into the pore structure. The separation of pharmaceuticals is a particularly urgent issue due to their omnipresence and low effect concentration of these contaminants. In this work, an exceptionally good separation rate of DCF was obtained especially in the application-oriented low concentration range, as well as under realistic pH-neutral conditions. Since DCF is a model substance for other pharmaceuticals, this study implies a good applicability of PMF for the separation of further pharmaceuticals or other water polluting organic trace substances.

The separation of heavy metal ions by means of PMF was already partly known from the literature. However, solvothermal PMF was used, which was contaminated with up to 5 wt.% sulfur. Accordingly, the question arose as to the contribution of the impurity to the corresponding adsorption of Pb²⁺. In addition, the adsorption of heavy metal ions and, at the same time, the adsorption of anions also present had not been investigated so far. To further analyze the influence of the pore system, both non-templated (N-) and highly porous templated (P-) PMF particles were used to determine the removal efficiency from different copper(II) salt solutions. In this study, two effects were found for the separation of both Cu²⁺ ions and the corresponding anions: Adsorption via physical interaction and surface precipitation via released hydroxide ions. The non-porous N-PMF particles showed only

adsorption, with a much stronger affinity for the respective anion than for Cu^{2+} . In contrast, both adsorption and surface precipitation take place for uptake of Cu^{2+} and the respective anion onto P-PMF. For monovalent anions, this can even be seen in two separately occurring uptake steps for Cu^{2+} and the respective anion. This phenomenon was rarely studied in the literature, especially for organic adsorbents. From the results, a new isotherm model was developed which is suitable for the two-step separation process. Mathematical modeling with known adsorption isotherm models or published models for surface precipitation was not possible. In conclusion, it was shown that adsorption of anions via ionic interaction is strongly favored over coordination of Cu^{2+} , although Cu^{2+} is known to form strong chelate complexes.

The last part of the work focused on the synthesis of P(3PT-F), a novel, unknown resin polymer, which exhibits strongly modified adsorption properties due to hydroxyl groups, especially towards metal ions. An intrinsically highly nanoporous material was obtained by environmentally friendly dispersion polymerization in water analogous to the synthesis of PMF. Detailed structural and chemical characterization showed that the novel P(3PT-F) polymer exhibited extremely high negative surface charge in water, which is ideal for the separation of harmful metal ions. Furthermore, the synthesis was easily upscalable, which facilitates a potential application.

The P(3PT-F) sample was subsequently tested for the removal of the toxic and carcinogenic metal Ni^{2+} , Cd^{2+} and Pb^{2+} ions. Here, the particles showed very good separation rates especially in the realistically low concentration range. This is particularly important due to the very low effect concentration of potentially remaining heavy metal ions. In these concentrations, drinking water quality was achieved, showing the outstanding potential for water treatment applications. The adsorption capacities achieved with P(3PT-F) (e.g. 90 mg Pb^{2+} /g) were already in the range of commercially available materials such as ion exchange resins although no further material optimization was carried out yet. As a fundamental proof, the reusability of the material could be shown after adsorption of Pb^{2+} with respective uptake in the plateau region of the isotherm. Here, a smaller volume of dilute HCl solution was able to quantitatively desorb the Pb^{2+} ions completely, whereby only a 3 h were needed vs. 24 h used for the adsorption process. Using aqueous HCl also circumvented the use of organic chelators such as ethylenediaminetetraacetic acid. A subsequent adsorption experiment showed no significant reduction in the adsorption capacity achieved. With these findings, future optimization of the adsorbent material by parameter variation is likely to increase the adsorption efficiency of the material even further.

Overall, all the set objectives of the work have been achieved and it has been shown that mesoporous resin particles, especially with an s-triazine unit, can be excellently used for water purification. By understanding the adsorption and templating mechanism of PMF, a

foundation for tailored synthesis of the particles as well as their potential applicability has been laid for future work. For example, the polymerization of melamine and formaldehyde could be supplemented in future studies with another monomer such as 3PT, urea or thiourea to incorporate additional functional groups into the polymer. Advantageously, thiourea would introduce a thiocarbonyl group into the polymer in a controlled and environmentally friendly manner without doing so as an impurity resulting from the decomposition of dimethyl sulfoxide. This method could also be used to produce templated terpolymer particles, which would be particularly promising for the separation of well-chelatable heavy metals.

Further resin polymers could also be developed for the applied synthesis method. A fundamental proof here is the P(3PT-F) polymer, which could be synthesized in water, albeit without templating yet. The implementation of templating would increase the mass transfer within the polymer through additional mesopores. Furthermore, it would also be possible to develop this synthesis for other, triazine-based monomers that entail modified adsorption properties by incorporation of e.g. amino side chains, carboxylic groups or the like.

In the context of adsorption studies, pharmaceuticals in particular represent a very large potential for further investigation. Since PMF has only been tested twice so far for their separation and only four pharmaceuticals were investigated, there remains an immense choice for further tests. By the investigations within this work, PMF can be tuned for these applications in for example its pore size, in order to make an optimal separation possible of later examined organic trace contaminants.

In general, the methods shown here for adsorption outside of pollutant separation can also be used to recover resources that have already been consumed. An obvious example here would be the separation of phosphate ions from other oxyanions such as sulfate. Due to the increasing global demand for energy storage and thus lithium-based batteries, very large quantities of process waters containing sulfate and phosphate are produced. This results in a need for further research, especially from an economic point of view, to separate and recover the contained phosphorus. The increasing consumption of phosphorus due to its indispensable use in agriculture and due to the growing population of the world, makes phosphorus recycling already now an important research topic, which will accordingly gain further urgency in the coming decades. Through the results presented, two fundamental evidences have been obtained: Firstly, the separation of phosphate from mixed wastewater and, secondly, an applicability of PMF as a low-cost synthesizable, resistant adsorbent for flow-through filters. A next logical step would now be to demonstrate the separation of mixed sulfate and phosphate solutions via H-PMF or N-PMF particles suitable for a fixed bed column setup and to subsequently enrich and recover phosphate with high adsorption capacity via P-PMF.

By synthesizing the materials in water in an environmentally friendly way, the results of this work represent an important potential for the production of other highly functional and porous adsorbents, as the destruction of our environment by, for example, unnecessary consumption of organic solvents, large amounts of energy, or the use of non-renewable raw materials without possibilities of recovery will become an increasingly existential problem.

Contribution to Publications

The results and contents presented in chapters 5 – 9 are each based on a peer-reviewed, joint publication. The contributions of all authors are presented in detail below.

Mesoporous Poly(Melamine-co-Formaldehyde) Particles for Efficient and Selective Phosphate and Sulfate Removal

This chapter is based on the publication in *Molecules* **2021**, 26, 6615.

(DOI: 10.3390/molecules26216615)

Von Konstantin B. L. Borchert, Christine Steinbach, Berthold Reis, Niklas Gerlach, Philipp Zimmermann, Simona Schwarz, Dana Schwarz*

(* Corresponding authors)

I planned and largely carried out the synthesis of the P-PMF and H-PMF particles used. Under my guidance, Niklas Gerlach synthesized another part of the particles. I performed the entirety of the TEM measurements as well as most of the N₂ sorption measurements. Christine Steinbach performed part of the N₂ sorption measurements as well as the entirety of the CO₂ sorption measurements, and SEM, TGA, as well as particle size measurements. Marina Oelmann performed the streaming potential vs. pH measurements. Eileen Schierz and Roland Schulze performed the elemental analyses. I evaluated all measured results, and wrote the associated sections of the manuscript. Dana Schwarz and I prepared the corresponding graphs. Berthold Reis performed the ATR-FTIR measurements, evaluated them, prepared the associated graphs, and wrote the corresponding section of the manuscript.

The adsorption experiments of sulfate and phosphate ions were planned by Dana Schwarz and me. The adsorption experiments were mostly performed by Christine Steinbach and under her supervision to a further part by Niklas Gerlach. This also applies to the subsequent pH and ICP-OES measurements. The measured values were evaluated by me, I created the corresponding graphs and I wrote the corresponding part of the manuscript. The SEM-EDX measurements of the adsorbent after adsorption were performed by Philipp Zimmermann, as well as an evaluation of the measurements. I created the associated graphics and wrote the corresponding part of the manuscript.

I wrote the first draft of the manuscript (excluding ATR-FTIR). Dana Schwarz, Simona Schwarz, Philipp Zimmermann, Christine Steinbach, Berthold Reis, and I worked on editing, revising, and proofreading the manuscript. Simona Schwarz was responsible for providing resources, funding acquisition and project administration. Dana Schwarz was responsible for the technical supervision.

Tuning the Pore Structure of Templated Mesoporous Poly(melamine-co-formaldehyde) Particles toward Diclofenac Removal

This chapter is based on the publication in *Journal of Environmental Management* **2022**, 324, 116221.

(DOI: 10.1016/j.jenvman.2022.116221)

By Konstantin B. L. Borchert, Karina Haro Carrasco, Christine Steinbach, Berthold Reis, Niklas Gerlach, Martin Mayer*, Simona Schwarz*, Dana Schwarz*

(* Corresponding authors)

I planned and largely carried out the synthesis of the P-PMF and H-PMF particles used. Under my guidance, Niklas Gerlach synthesized another part of the particles. I performed the entirety of the TEM measurements as well as most of the N₂ sorption measurements. Christine Steinbach performed part of the N₂ sorption measurements as well as the entirety of the CO₂ sorption measurements, and SEM, TGA, as well as particle size measurements. Eileen Schierz performed the elemental analyses. I evaluated all measured results, wrote the associated sections of the manuscript, and prepared most of the corresponding graphics. Graphs for SEM, TEM as well as gas sorption were partially prepared by Dana Schwarz. Berthold Reis performed the ATR-FTIR measurements, evaluated them, prepared the associated graphs, and wrote the corresponding section of the manuscript.

The adsorption experiments of DCF were planned by myself and Dana Schwarz. The adsorption experiments were mostly performed by Karina Haro Carrasco and Christine Steinbach and to a lesser extent by Niklas Gerlach. This is also true for the pH measurements. The UV/VIS measurements of the adsorption isotherms after 24 were performed by Martin Mayer. The UV/VIS measurements of the time-dependent adsorption experiments were performed by Niklas Gerlach. The measured values were evaluated by me, I made the corresponding graphs and I wrote the corresponding part of the manuscript.

I wrote the first draft of the manuscript (excluding ATR-FTIR). All authors worked on editing, revising, and proofreading the manuscript. Simona Schwarz was responsible for providing resources, grant acquisition, and project administration. Dana Schwarz was responsible for technical supervision.

Adsorption vs. Surface Precipitation of Cu²⁺ onto Porous Poly(melamine-co-formaldehyde) Particles

This chapter is based on the publication in *Microporous and Mesoporous Materials* **2023**, 348, 112383.

(DOI: 10.1016/j.micromeso.2022.112383)

By Konstantin B. L. Borchert, Christine Steinbach, Berthold Reis, Uwe Lappan, Niklas Gerlach, Martin Mayer, Simona Schwarz*, Dana Schwarz*

(* Corresponding authors)

I planned and largely carried out the synthesis of the N-PMF, P-PMF and H-PMF particles used. Under my guidance, Niklas Gerlach synthesized another part of the particles. I performed the entirety of the TEM and WAXS measurements as well as most of the N₂ sorption measurements. Christine Steinbach performed part of the N₂ sorption measurements as well as the entirety of the CO₂ sorption measurements, and SEM, TGA, as well as particle size measurements. Eileen Schierz performed the elemental analyses. I performed the embedding of the samples and Uta Reuter prepared thin sections from them afterwards. I evaluated all measured results, wrote the corresponding sections of the manuscript and created most of the corresponding graphics. Graphs for SEM, TEM as well as gas sorption were partially prepared by Dana Schwarz. Berthold Reis performed the ATR-FTIR measurements, evaluated them, prepared the associated graphs, and wrote the corresponding section of the manuscript.

The adsorption experiments of DCF were planned by me. The adsorption experiments and UV/VIS, pH and ICP-OES measurements were performed by Christine Steinbach. The measured values were evaluated by me, I made the corresponding graphs and I wrote the corresponding part of the manuscript. The analysis of the adsorbent samples by WAXS, N₂ sorption measurements and EFTEM measurements was done by me. Corresponding graphs and text in the manuscript were prepared by me. The EPR investigations of the samples were performed by Uwe Lappan, he evaluated them, prepared corresponding graphics and wrote associated sections of the manuscript. Berthold Reis examined the samples with SEM-EDX and evaluated them. Corresponding graphics and text in the publication were created by me.

I prepared the first draft of the manuscript (excluding ATR-FTIR and EPR). All authors worked on editing, revising, and proofreading the manuscript. Simona Schwarz and Dana Schwarz were responsible for providing resources, grant acquisition, and project administration. Dana Schwarz was responsible for technical supervision.

SiO₂ Nanospheres as Surfactant and Template in Aqueous Dispersion Polymerizations Yielding Nanoporous Resin Particles

This chapter is based on the publication in the *Journal of Colloid and Interface Science* **2023**, *1*, 819.

(DOI: 10.1016/j.jcis.2023.01.071)

By Konstantin B. L. Borchert, Niklas Gerlach, Christine Steinbach, Berthold Reis, Simona Schwarz*, Dana Schwarz*

(* Corresponding authors)

I planned the synthesis of the P-PMF and H-PMF particles used. Niklas Gerlach synthesized all the particles. I performed the entirety of the TEM and EFTEM investigations as well as N₂ sorption measurements. Niklas Gerlach and I performed the particle size measurements. Christine Steinbach performed the SEM and TGA investigations. Eileen Schierz performed the elemental analyses. I performed the embedding of the samples and Uta Reuter prepared thin sections from them afterwards. I evaluated all measured results, wrote the associated sections of the manuscript, and prepared all graphs.

The adsorption experiments with K₂Cr₂O₇ solution were planned by me. The adsorption experiments and pH and ICP-OES measurements were performed by Niklas Gerlach. The measured values were evaluated by me, I made the corresponding graphs and I wrote the corresponding part of the manuscript. The analysis of the adsorbent samples by SEM-EDX was performed by Berthold Reis, who also evaluated them. Corresponding graphics and text in the publication were prepared by me.

I prepared the first draft of the manuscript. Niklas Gerlach, Christine Steinbach, Berthold Reis, Simona Schwarz, and I worked on editing, revising, and proofreading the manuscript. Simona Schwarz was responsible for providing resources, funding acquisition and project administration. Dana Schwarz was responsible for the technical supervision.

Waterborne Phenolic, Triazine-Based Porous Polymer Particles for the Removal of Nickel, Cadmium, and Lead Ions

This chapter is based on the publication in *JCIS Open* **2022**, 8, 100066.

(DOI: 10.1016/j.jciso.2022.100066)

By Konstantin B. L. Borchert, Robert Frenzel, Niklas Gerlach, Berthold Reis, Christine Steinbach, Benjamin Kohn, Ulrich Scheler, Simona Schwarz*, Dana Schwarz*

(* Corresponding authors)

I planned the synthesis of the monomer 3PT as well as the P(3PT-F) particles. The synthesis of the monomer was carried out by me. The synthesis of the P(3PT-F) particles was performed by Robert Frenzel under my guidance and supervision. I performed the entirety of the WAXS as well as part of the N₂ sorption measurements. Under my supervision, part of the N₂ sorption measurements were performed by Robert Frenzel. Christine Steinbach performed the entirety of the CO₂ sorption measurements, as well as SEM and TGA measurements. Niklas Gerlach performed the particle size measurements as well as the streaming potential vs. pH measurements. Eileen Schierz performed the elemental analyses. I evaluated all related results, prepared the graphs and wrote the corresponding parts of the manuscript. Berthold Reis performed the ATR-FTIR measurements, evaluated them, prepared the related graphs, and wrote the corresponding part of the manuscript. Benjamin Kohn and Ulrich Scheler performed the solid-state NMR studies of the P(3PT-F) samples, evaluated them, prepared the graphs and tables, and wrote the corresponding part of the manuscript.

The adsorption and desorption experiments were developed by me. The adsorption experiments were performed by Niklas Gerlach, as well as for the subsequent pH, ICP-OES and UV/VIS measurements. The measured values were evaluated by me, I created the corresponding graphs and I wrote the corresponding part of the manuscript. The SEM-EDX measurements of the adsorbent after adsorption were performed by Berthold Reis, as well as the evaluation of these measurements. I prepared the associated graphics and wrote the corresponding part of the manuscript.

I prepared the first draft of the manuscript (excluding ATR-FTIR and FK-NMR). All authors worked on editing, revising, and proofreading the manuscript. Simona Schwarz was responsible for providing resources, grant acquisition, and project administration. Dana Schwarz was responsible for the technical supervision.

Danksagung

Ich möchte mich herzlich bei allen bedanken, die mir während meiner Doktorarbeit mit ihrer fachlichen und tatkräftigen Unterstützung geholfen haben. Mein besonderer Dank gilt Prof. Dr. Andreas Fery für die Möglichkeit, diese Dissertation im Institut für Physikalische Chemie und Physik der Polymere am Leibniz-Institutes für Polymerforschung Dresden e.V. zu schreiben. Ihre wissenschaftliche Betreuung sowie Ihr fachlicher und organisatorischer Rat halfen mir sehr bei der Umsetzung meiner Forschungsziele.

Ich möchte ebenfalls meinem Zweitgutachter, Prof. Dr. Jens Weber, danken. Er hat mir nähergebracht, dass man Haarspalterei nicht mit Intelligenz verwechselt sollte.

Weiterhin möchte ich sehr herzlich Dr. Dana Schwarz danken für ihre fachliche Betreuung während ihrer Zeit am IPF sowie Dr. Simona Schwarz für die spätere Übernahme der Betreuung. Die Kenntnisse und Erfahrungen, welche ihr mit mir geteilt habt und der fortwährende Diskurs über Forschungsergebnisse und aktuelle Veröffentlichungen ermöglichten es mir, eine gewisse Eigenverantwortung im Rahmen meines Themengebietes zu erlangen, kreative Ansätze für aktuelle Probleme zu finden und die Darstellung und Klarheit meiner Ergebnisse zu steigern.

Weiterhin möchte ich den Personen meinen Dank aussprechen, welche tatkräftig an gemeinsamen Projekten und Veröffentlichungen mitgearbeitet haben und daran mitgewirkt haben, den unterschiedlichsten Phänomenen auf den Grund zu gehen. Dementsprechend möchte ich unter anderem Dr. Uwe Lappan, Uta Reuter, Dr. Petr Formanek, Philipp Zimmermann, Dr. Ulrich Scheler, Benjamin Kohn, und Dr. Regine Boldt, sowie den Kollegen meiner Arbeitsgruppe Martin Mayer, Karina Haro Carrasco, Egon Höfgen, Robert Frenzel und Rahma Boughanmi meinen Dank aussprechen. Ganz besonders möchte ich hier außerdem Christine Steinbach, Niklas Gerlach und Marina Oelmann für ihre andauernde Mitarbeit an der Umsetzung meiner Forschungsziele danken! Erst mit eurer Durchführung von Synthesen und Messungen wurde es möglich, einen tiefgreifenden Überblick über das Themengebiet zu erhalten. Vielen Dank für eure Zuverlässigkeit und auch besonders eure kurzfristige Mitarbeit in zeitkritischen Momenten! Generell bin ich dankbar für die angenehme Arbeitsatmosphäre mit allen Kollegen meiner Arbeitsgruppe und Abteilung!

Ich danke außerdem meinen Kommilitonen in der „Doktorandenmafia“ für die konstruktiven Diskussionen und erheiternden Gespräche, welche ich teilweise seit Beginn meiner Studienzeit genießen darf! Die gemeinsamen Mittagspausen dienten neben guten Unterhaltungen auch oft dem Austausch über Fachwissen und organisatorischen Gegebenheiten am IPF. Außerdem halfen sie immens bei einer Quervernetzung der einzelnen Arbeitsgruppen und dem Aufbau von Kooperationen. Speziell meinen Kommilitonen Berthold Reis, Christoph Horn, Patricia Flemming, Christian Mielke, Pauline Voigt, Carolin Bunk, Lisa Ehrlich, Simon Enders, Florian Schmidt und Mirjam Hofmaier gilt mein Dank für unsere Freundschaft, die mich auch in schwierigen Zeiten gestärkt hat. Außerdem habt ihr durch eure

Danksagung

kritische Sichtweise während des gemeinsamen Coffein-Konsums und Mittagessens den Ausdruck und die Darstellung meiner Ergebnisse maßgeblich verbessert und geschärft.

Meinen Eltern und dem Rest meiner Familie möchte ich dafür danken, dass sie mich seit jeher unterstützt haben und dass ich mich stets auf sie verlassen konnte.

Zuletzt möchte ich meiner Frau Dorothea Borchert von ganzem Herzen danken für ihr bedingungsloses Vertrauen und ihre unbändige Unterstützung! Danke, dass du an mich glaubst!

Appendix

The respective electronic Supporting Information of the publications, which form the basis of chapters 5 to 9, can be viewed on a CD enclosed with the dissertation.

References

- [1] World Water Assessment Programme, World Water Assessment., The United Nations World Water Development Report 3 Water in a Changing World (Two Vols.), Taylor and Francis, Hoboken, 2012.
- [2] S.L. Postel, G.C. Daily, P.R. Ehrlich, Human Appropriation of Renewable Fresh Water, *Science* 271 (1996) 785–788.
- [3] A.Y. Hoekstra, M.M. Mekonnen, The water footprint of humanity, *Proceedings of the National Academy of Sciences of the United States of America* 109 (2012) 3232–3237.
- [4] V. Kumar, R.D. Parihar, A. Sharma, P. Bakshi, G.P. Singh Sidhu, A.S. Bali, I. Karaouzas, R. Bhardwaj, A.K. Thukral, Y. Gyasi-Agyei, J. Rodrigo-Comino, Global evaluation of heavy metal content in surface water bodies: A meta-analysis using heavy metal pollution indices and multivariate statistical analyses, *Chemosphere* 236 (2019) 124364.
- [5] Q. Zhou, N. Yang, Y. Li, B. Ren, X. Ding, H. Bian, X. Yao, Total concentrations and sources of heavy metal pollution in global river and lake water bodies from 1972 to 2017, *Global Ecology and Conservation* 22 (2020) e00925.
- [6] United Nations Children’s Fund (UNICEF), World Health Organization, Progress on Household Drinking Water, Sanitation and Hygiene 2000-2017: Special Focus on Inequalities, United Nations Children’s Fund (UNICEF); World Health Organization, 2019.
- [7] F.A. Armah, S. Obiri, D.O. Yawson, E.E. Onumah, G.T. Yengoh, E.K.A. Afrifa, J.O. Odoi, Anthropogenic sources and environmentally relevant concentrations of heavy metals in surface water of a mining district in Ghana: a multivariate statistical approach, *Journal of environmental science and health. Part A, Toxic/hazardous substances & environmental engineering* 45 (2010) 1804–1813.
- [8] H. Ali, E. Khan, Bioaccumulation of non-essential hazardous heavy metals and metalloids in freshwater fish. Risk to human health, *Environ Chem Lett* 16 (2018) 903–917.
- [9] L.-C. Hsu, C.-Y. Huang, Y.-H. Chuang, H.-W. Chen, Y.-T. Chan, H.Y. Teah, T.-Y. Chen, C.-F. Chang, Y.-T. Liu, Y.-M. Tzou, Accumulation of heavy metals and trace elements in fluvial sediments received effluents from traditional and semiconductor industries, *Scientific reports* 6 (2016) 34250.
- [10] R. Islam, S. Kumar, J. Karmoker, M. Kamruzzaman, M.A. Rahman, N. Biswas, T.K.A. Tran, M.M. Rahman, Bioaccumulation and adverse effects of persistent organic pollutants (POPs) on ecosystems and human exposure: A review study on Bangladesh perspectives, *Environmental Technology & Innovation* 12 (2018) 115–131.
- [11] T.J. Mooibroek, P. Gamez, The s-triazine ring, a remarkable unit to generate supramolecular interactions, *Inorganica Chimica Acta* 360 (2007) 381–404.
- [12] D. Schwarz, J. Weber, Waterborne Colloidal Polymer/Silica Hybrid Dispersions and Their Assembly into Mesoporous Poly(melamine-formaldehyde) Xerogels, *Langmuir the ACS journal of surfaces and colloids* 31 (2015) 8436–8445.
- [13] D. Schwarz, J. Weber, Organic-solvent free synthesis of mesoporous and narrow-dispersed melamine resin particles for water treatment applications, *Polymer* 155 (2018) 83–88.
- [14] Y. Wang, Y. Xie, Y. Zhang, S. Tang, C. Guo, J. Wu, R. Lau, Anionic and cationic dyes adsorption on porous poly-melamine-formaldehyde polymer, *Chemical Engineering Research and Design* 114 (2016) 258–267.
- [15] D. Schwarz, J. Weber, Synthesis of mesoporous poly(melamine-formaldehyde) particles by inverse emulsion polymerization, *Journal of colloid and interface science* 498 (2017) 335–342.
- [16] A. Deryło-Marczewska, J. Goworek, W. Zgrajka, Studies of Melamine–Formaldehyde Resins by Sorption from Gas and Liquid Phases, *Langmuir the ACS journal of surfaces and colloids* 17 (2001) 6518–6523.
- [17] D. Schwarz, J. Weber, Organic-solvent free synthesis of mesoporous and narrow-dispersed melamine resin particles for water treatment applications, *Polymer* 155 (2018) 83–88.
- [18] M.X. Tan, Y.N. Sum, J.Y. Ying, Y. Zhang, A mesoporous poly-melamine-formaldehyde polymer as a solid sorbent for toxic metal removal, *Energy Environ. Sci.* 6 (2013) 3254.
- [19] G. Ming, H. Duan, X. Meng, G. Sun, W. Sun, Y. Liu, L. Lucia, A novel fabrication of monodisperse melamine–formaldehyde resin microspheres to adsorb lead (II), *Chemical Engineering Journal* 288 (2016) 745–757.

References

- [20] D. Schwarz, J. Weber, Nanoporous Poly(Melamine Formaldehyde) Networks by Aqueous Dispersion Polycondensation-Synthesis and Adsorption Properties, *Macromol. Mater. Eng.* 300 (2015) 531–541.
- [21] G. Yang, H. Han, C. Du, Z. Luo, Y. Wang, Facile synthesis of melamine-based porous polymer networks and their application for removal of aqueous mercury ions, *Polymer* 51 (2010) 6193–6202.
- [22] D. Schwarz, J. Weber, Synthesis of mesoporous poly(melamine-formaldehyde) particles by inverse emulsion polymerization, *Journal of colloid and interface science* 498 (2017) 335–342.
- [23] C. Du Fresne von Hohenesche, D.F. Schmidt, V. Schädler, Nanoporous Melamine-Formaldehyde Gels by Microemulsion Templating, *Chem. Mater.* 20 (2008) 6124–6129.
- [24] J. Briffa, E. Sinagra, R. Blundell, Heavy metal pollution in the environment and their toxicological effects on humans, *Heliyon* 6 (2020) e04691.
- [25] Ihsanullah, A. Abbas, A.M. Al-Amer, T. Laoui, M.J. Al-Marri, M.S. Nasser, M. Khraisheh, M.A. Atieh, Heavy metal removal from aqueous solution by advanced carbon nanotubes: Critical review of adsorption applications, *Separation and Purification Technology* 157 (2016) 141–161.
- [26] Y. Hashimoto, Y. Sekine, T. Otsushi, Atmospheric aluminum from human activities, *Atmospheric Environment. Part B. Urban Atmosphere* 26 (1992) 295–300.
- [27] M. Hutton, Sources of cadmium in the environment, *Ecotoxicology and Environmental Safety* 7 (1983) 9–24.
- [28] H.A. Naser, Assessment and management of heavy metal pollution in the marine environment of the Arabian Gulf: a review, *Marine pollution bulletin* 72 (2013) 6–13.
- [29] E.Z. Ochieng, J.O. Lalah, S.O. Wandiga, Analysis of heavy metals in water and surface sediment in five Rift Valley lakes in Kenya for assessment of recent increase in anthropogenic activities, *Bulletin of environmental contamination and toxicology* 79 (2007) 570–576.
- [30] M.C. Shinzato, R. Hypolito, Effect of disposal of aluminum recycling waste in soil and water bodies, *Environ Earth Sci* 75 (2016) 61.
- [31] L.M. Cleveland, M.L. Minter, K.A. Cobb, A.A. Scott, V.F. German, Lead hazards for pregnant women and children: part 1: immigrants and the poor shoulder most of the burden of lead exposure in this country. Part 1 of a two-part article details how exposure happens, whom it affects, and the harm it can do, *The American journal of nursing* 108 (2008) 40-9; quiz 50.
- [32] T.I. Moiseenko, N.A. Gashkina, Biogeochemistry of Cadmium: Anthropogenic Dispersion, Bioaccumulation, and Ecotoxicity, *Geochem. Int.* 56 (2018) 798–811.
- [33] M.D. Pavlaki, M.J. Araújo, D.N. Cardoso, A.R.R. Silva, A. Cruz, S. Mendo, A.M.V.M. Soares, R. Calado, S. Loureiro, Ecotoxicity and genotoxicity of cadmium in different marine trophic levels, *Environmental pollution (Barking, Essex 1987)* 215 (2016) 203–212.
- [34] B.O. Rosseland, T.D. Eldhuset, M. Staurnes, Environmental effects of aluminium, *Environmental geochemistry and health* 12 (1990) 17–27.
- [35] R.W. Gensemer, R.C. Playle, The Bioavailability and Toxicity of Aluminum in Aquatic Environments, *Critical Reviews in Environmental Science and Technology* 29 (1999) 315–450.
- [36] B.G. Church, P.A. van Sprang, M.J. Chowdhury, D.K. DeForest, Updated species sensitivity distribution evaluations for acute and chronic lead toxicity to saltwater aquatic life, *Environmental toxicology and chemistry* 36 (2017) 2974–2980.
- [37] M. Jaishankar, T. Tseten, N. Anbalagan, B.B. Mathew, K.N. Beeregowda, Toxicity, mechanism and health effects of some heavy metals, *Interdisciplinary toxicology* 7 (2014) 60–72.
- [38] J. Godt, F. Scheidig, C. Grosse-Siestrup, V. Esche, P. Brandenburg, A. Reich, D.A. Groneberg, The toxicity of cadmium and resulting hazards for human health, *Journal of occupational medicine and toxicology (London, England)* 1 (2006) 22.
- [39] A. Hartwig, Cadmium and cancer, *Metal ions in life sciences* 11 (2013) 491–507.
- [40] Air quality guidelines for Europe, 2nd ed., WHO, Regional Office for Europe, Copenhagen, 2000.
- [41] H. Ali, E. Khan, Bioaccumulation of non-essential hazardous heavy metals and metalloids in freshwater fish. Risk to human health, *Environ Chem Lett* 16 (2018) 903–917.
- [42] E.M. Caravati, Medical toxicology, 3rd ed., Lippincott, Williams & Wilkins, Philadelphia, op. 2004.
- [43] United Nations Environment Programme, Chemical Branch, DTIE, Final Review of Scientific Information on Lead - Version of December 2010, 2010.

References

- [44] H.S. Kim, Y.J. Kim, Y.R. Seo, An Overview of Carcinogenic Heavy Metal: Molecular Toxicity Mechanism and Prevention, *Journal of cancer prevention* 20 (2015) 232–240.
- [45] Guidelines for drinking-water quality, World Health Organization, Geneva, 2017.
- [46] Bundesministerin der Justiz und für Verbraucherschutz, Bundesministerin der Justiz und für Verbraucherschutz - Trinkwasserverordnung, Anlage 2 (zu § 6 Absatz 2): TrinkwV, 2019.
- [47] C.-Q. Liu, Y.-C. Lang, H. Satake, J. Wu, S.-L. Li, Identification of anthropogenic and natural inputs of sulfate and chloride into the karstic ground water of Guiyang, SW China: combined $\delta^{37}\text{Cl}$ and $\delta^{34}\text{S}$ approach, *Environmental science & technology* 42 (2008) 5421–5427.
- [48] H. Wang, Q. Zhang, Research Advances in Identifying Sulfate Contamination Sources of Water Environment by Using Stable Isotopes, *International journal of environmental research and public health* 16 (2019).
- [49] Z. Miao, K.C. Carroll, M.L. Brusseau, Characterization and quantification of groundwater sulfate sources at a mining site in an arid climate: The Monument Valley site in Arizona, USA, *Journal of hydrology* 504 (2013) 207–215.
- [50] K. Man, Z.M. Ma, X.J. Xu, Research on the Mechanism of Sulfate Pollution of Groundwater in Jiaozuo Area, *AMM* 665 (2014) 436–439.
- [51] C. Schaum (Ed.), *Phosphorus: Polluter and resource of the future removal and recovery from wastewater*, IWA Publishing, London, 2018.
- [52] M.M. Mekonnen, A.Y. Hoekstra, Global Anthropogenic Phosphorus Loads to Freshwater and Associated Grey Water Footprints and Water Pollution Levels: A High-Resolution Global Study, *Water Resour. Res.* 54 (2018) 345–358.
- [53] A.M. Farmer, Phosphate pollution: A global overview of the problem, in: C. Schaum (Ed.), *Phosphorus: Polluter and Resource of the Future – Removal and Recovery from Wastewater*, International Water Association, 2018, pp. 35–55.
- [54] C. Alewell, B. Ringeval, C. Ballabio, D.A. Robinson, P. Panagos, P. Borrelli, Global phosphorus shortage will be aggravated by soil erosion, *Nature communications* 11 (2020) 4546.
- [55] T. Fatima, A. Muntean, Sulfate attack in sewer pipes: Derivation of a concrete corrosion model via two-scale convergence, *Nonlinear Analysis: Real World Applications* 15 (2014) 326–344.
- [56] E.A. Katayev, Y.A. Ustynyuk, J.L. Sessler, Receptors for tetrahedral oxyanions, *Coordination Chemistry Reviews* 250 (2006) 3004–3037.
- [57] D.J. Soucek, A.J. Kennedy, Effects of hardness, chloride, and acclimation on the acute toxicity of sulfate to freshwater invertebrates, *Environmental toxicology and chemistry* 24 (2005) 1204–1210.
- [58] J.R. Elphick, M. Davies, G. Gilron, E.C. Canaria, B. Lo, H.C. Bailey, An aquatic toxicological evaluation of sulfate: the case for considering hardness as a modifying factor in setting water quality guidelines, *Environmental toxicology and chemistry* 30 (2011) 247–253.
- [59] Å.D. Austigard, K. Svendsen, K.K. Heldal, Hydrogen sulphide exposure in waste water treatment, *Journal of occupational medicine and toxicology (London, England)* 13 (2018).
- [60] L.P.M. Lamers, L.L. Govers, I.C.J.M. Janssen, J.J.M. Geurts, M.E.W. van der Welle, M.M. van Katwijk, T. van der Heide, J.G.M. Roelofs, A.J.P. Smolders, Sulfide as a soil phytotoxin-a review, *Frontiers in plant science* 4 (2013) 268.
- [61] S.P. Seitzinger, J.A. Harrison, E. Dumont, A.H.W. Beusen, A.F. Bouwman, Sources and delivery of carbon, nitrogen, and phosphorus to the coastal zone: An overview of Global Nutrient Export from Watersheds (NEWS) models and their application, *Global Biogeochem. Cycles* 19 (2005) n/a-n/a.
- [62] J.B. Sylvan, Q. Dortch, D.M. Nelson, A.F.M. Brown, W. Morrison, J.W. Ammerman, Phosphorus limits phytoplankton growth on the Louisiana shelf during the period of hypoxia formation, *Environmental science & technology* 40 (2006) 7548–7553.
- [63] D.W. Schindler, S.R. Carpenter, S.C. Chapra, R.E. Hecky, D.M. Orihel, Reducing Phosphorus to Curb Lake Eutrophication is a Success, *Environmental science & technology* 50 (2016) 8923–8929.
- [64] L. Horrigan, R.S. Lawrence, P. Walker, How sustainable agriculture can address the environmental and human health harms of industrial agriculture, *Environmental health perspectives* 110 (2002) 445–456.
- [65] Mineral commodity summaries 2021, Reston, VA, 2021.

References

- [66] D. Cordell, J.-O. Drangert, S. White, The story of phosphorus: Global food security and food for thought, *Global Environmental Change* 19 (2009) 292–305.
- [67] M.C. Chispim, M. Scholz, M.A. Nolasco, Phosphorus recovery from municipal wastewater treatment: Critical review of challenges and opportunities for developing countries, *Journal of environmental management* 248 (2019) 109268.
- [68] S. Petzet, B. Peplinski, P. Cornel, On wet chemical phosphorus recovery from sewage sludge ash by acidic or alkaline leaching and an optimized combination of both, *Water research* 46 (2012) 3769–3780.
- [69] K. Remmen, B. Müller, J. Köser, M. Wessling, T. Wintgens, Phosphorus recovery in an acidic environment using layer-by-layer modified membranes, *Journal of Membrane Science* 582 (2019) 254–263.
- [70] E.D. Roy, Phosphorus recovery and recycling with ecological engineering: A review, *Ecological Engineering* 98 (2017) 213–227.
- [71] A.R. Jupp, S. Beijer, G.C. Narain, W. Schipper, J.C. Slootweg, Phosphorus recovery and recycling - closing the loop, *Chemical Society reviews* 50 (2021) 87–101.
- [72] L. Kong, X. Hu, Z. Xie, X. Ren, J. Long, M. Su, Z. Diao, D. Chen, K. Shih, L.'a. Hou, Accelerated phosphorus recovery from aqueous solution onto decorated sewage sludge carbon, *Scientific reports* 8 (2018) 13421.
- [73] D. Tonini, H.G.M. Saveyn, D. Huygens, Environmental and health co-benefits for advanced phosphorus recovery, *Nat Sustain* 2 (2019) 1051–1061.
- [74] M. Atienza–Martínez, G. Gea, J. Arauzo, S.R.A. Kersten, A.M.J. Kootstra, Phosphorus recovery from sewage sludge char ash, *Biomass and Bioenergy* 65 (2014) 42–50.
- [75] X. Meng, Q. Huang, J. Xu, H. Gao, J. Yan, A review of phosphorus recovery from different thermal treatment products of sewage sludge, *Waste Dispos. Sustain. Energy* 1 (2019) 99–115.
- [76] M.C. Monea, C. Meyer, H. Steinmetz, H. Schönberger, A. Drenkova-Tuhtan, Phosphorus recovery from sewage sludge - phosphorus leaching behavior from aluminum-containing tertiary and anaerobically digested sludge, *Water science and technology a journal of the International Association on Water Pollution Research* 82 (2020) 1509–1522.
- [77] E. Yamasue, K. Matsubae, Phosphorus in Steelmaking Processes, in: H. Ohtake, S. Tsuneda (Eds.), *Phosphorus Recovery and Recycling*, Springer Singapore, Singapore, 2019, pp. 349–364.
- [78] T. Yamamoto, M. Nakamoto, Extraction of Phosphorus from Dephosphorization Slag, in: H. Ohtake, S. Tsuneda (Eds.), *Phosphorus Recovery and Recycling*, Springer Singapore, Singapore, 2019, pp. 339–347.
- [79] C.-M. Du, X. Gao, S. Ueda, S.-Y. Kitamura, Separation and recovery of phosphorus from steelmaking slag via a selective leaching–chemical precipitation process, *Hydrometallurgy* 189 (2019) 105109.
- [80] L. Lin, Y.-p. Bao, M. Wang, W. Jiang, H.-m. Zhou, Separation and Recovery of Phosphorus from P-bearing Steelmaking Slag, *J. Iron Steel Res. Int.* 21 (2014) 496–502.
- [81] N.-N. Lv, C.-M. Du, H. Kong, Y.-H. Yu, Leaching of Phosphorus from Quenched Steelmaking Slags with Different Composition, *Metals* 11 (2021) 1026.
- [82] Y. Kalmykova, K.K. Fedge, Phosphorus recovery from municipal solid waste incineration fly ash, *Waste management (New York, N.Y.)* 33 (2013) 1403–1410.
- [83] B.S. Rath, P.S. Kumar, D.-V.N. Vo, Critical review on hazardous pollutants in water environment: Occurrence, monitoring, fate, removal technologies and risk assessment, *The Science of the total environment* 797 (2021) 149134.
- [84] V.-H. Nguyen, S.M. Smith, K. Wantala, P. Kajitvichyanukul, Photocatalytic remediation of persistent organic pollutants (POPs): A review, *Arabian Journal of Chemistry* 13 (2020) 8309–8337.
- [85] T. aus der Beek, F.-A. Weber, A. Bergmann, S. Hickmann, I. Ebert, A. Hein, A. Küster, Pharmaceuticals in the environment—Global occurrences and perspectives, *Environmental toxicology and chemistry* 35 (2016) 823–835.
- [86] B. Gworek, M. Kijeńska, M. Zaborowska, J. Wrzosek, L. Tokarz, J. Chmielewski, Pharmaceuticals in aquatic environment. Fate and behaviour, ecotoxicology and risk assessment – A review, *Acta Poloniae Pharmaceutica - Drug Research* 76 (2019) 397–407.
- [87] A.J. Bamford, A. Monadjem, M.D. Anderson, A. Anthony, W.D. Borello, M. Bridgeford, P. Bridgeford, P. Hancock, B. Howells, J. Wakelin, I.C.W. Hardy, Trade-offs between specificity and regional generality in habitat association models: a case study of two species of African vulture, *Journal of Applied Ecology* 46 (2009) 852–860.

References

- [88] J.L. Oaks, M. Gilbert, M.Z. Virani, R.T. Watson, C.U. Meteyer, B.A. Rideout, H.L. Shivaprasad, S. Ahmed, M.J.I. Chaudhry, M. Arshad, S. Mahmood, A. Ali, A.A. Khan, Diclofenac residues as the cause of vulture population decline in Pakistan, *Nature* 427 (2004) 630–633.
- [89] G.E. Swan, R. Cuthbert, M. Quevedo, R.E. Green, D.J. Pain, P. Bartels, A.A. Cunningham, N. Duncan, A.A. Meharg, J.L. Oaks, J. Parry-Jones, S. Shultz, M.A. Taggart, G. Verdoorn, K. Wolter, Toxicity of diclofenac to Gyps vultures, *Biology letters* 2 (2006) 279–282.
- [90] V. Naidoo, K. Wolter, R. Cuthbert, N. Duncan, Veterinary diclofenac threatens Africa's endangered vulture species, *Regulatory toxicology and pharmacology RTP* 53 (2009) 205–208.
- [91] S. Joachim, R. Beaudouin, G. Daniele, A. Geffard, A. Bado-Nilles, C. Tebby, O. Palluel, O. Dedourge-Geffard, M. Fieu, M. Bonnard, M. Palos-Ladeiro, C. Turiès, E. Vulliet, V. David, P. Baudoin, A. James, S. Andres, J.M. Porcher, Effects of diclofenac on sentinel species and aquatic communities in semi-natural conditions, *Ecotoxicology and Environmental Safety* 211 (2021) 111812.
- [92] S. Schwarz, H. Schmieg, M. Scheurer, H.-R. Köhler, R. Triebkorn, Impact of the NSAID diclofenac on survival, development, behaviour and health of embryonic and juvenile stages of brown trout, *Salmo trutta f. fario*, *The Science of the total environment* 607-608 (2017) 1026–1036.
- [93] V.P. Panov, I.V. Zykova, S.A. Chekrenev, Heavy metals: The industry and environmental protection, *Fibre Chem* 40 (2008) 241–245.
- [94] J. Margot, L. Rossi, D.A. Barry, C. Holliger, A review of the fate of micropollutants in wastewater treatment plants, *WIREs Water* 2 (2015) 457–487.
- [95] A.D. Karathanasis, Lead Desorption and Remobilization Potential by Colloid Particles in Contaminated Sites, in: K.S. Sajwan, A.K. Alva, R.F. Keefer (Eds.), *Chemistry of Trace Elements in Fly Ash*, Springer US, Boston, MA, 2003, pp. 219–236.
- [96] C.A. Flemming, F.G. Ferris, T.J. Beveridge, G.W. Bailey, Remobilization of toxic heavy metals adsorbed to bacterial wall-clay composites, *Applied and environmental microbiology* 56 (1990) 3191–3203.
- [97] U. Förstner, Metal Transfer Between Solid and Aqueous Phases, in: U. Förstner, G.T.W. Wittmann (Eds.), *Metal Pollution in the Aquatic Environment*, Springer Berlin Heidelberg, Berlin, Heidelberg, 1981, pp. 197–270.
- [98] Y. Gao, A.T. Kan, M.B. Tomson, Critical evaluation of desorption phenomena of heavy metals from natural sediments, *Environmental science & technology* 37 (2003) 5566–5573.
- [99] K.J. Powell, P.L. Brown, R.H. Byrne, T. Gajda, G. Hefter, S. Sjöberg, H. Wanner, Chemical speciation of environmentally significant heavy metals with inorganic ligands. Part 1: The Hg^{2+} – Cl^- , OH^- , CO_3^{2-} , SO_4^{2-} , and PO_4^{3-} aqueous systems (IUPAC Technical Report), *Pure and Applied Chemistry* 77 (2005) 739–800.
- [100] K.S. Smith, L.S. Balistrieri, A.S. Todd, Using biotic ligand models to predict metal toxicity in mineralized systems, *Applied Geochemistry* 57 (2015) 55–72.
- [101] A. Sowmya, S. Meenakshi, Removal of nitrate and phosphate anions from aqueous solutions using strong base anion exchange resin, *Desalination and Water Treatment* 51 (2013) 7145–7156.
- [102] T. Nur, M.A.H. Jahir, P. Loganathan, T. Nguyen, S. Vigneswaran, J. Kandasamy, Phosphate removal from water using an iron oxide impregnated strong base anion exchange resin, *Journal of Industrial and Engineering Chemistry* 20 (2014) 1301–1307.
- [103] R. Bhande, P.K. Ghosh, Oxyanions Removal by Biological Processes: A Review, in: V.P. Singh, S. Yadav, R.N. Yadava (Eds.), *Water Quality Management*, Springer Singapore, Singapore, 2018, pp. 37–54.
- [104] C. Horn, S. Ihmann, F. Müller, D. Pospiech, K.B.L. Borchert, R. Hommel, K. Qin, K. Licha, P.J. Allertz, M. Drache, Design of Polymer-Embedded Heterogeneous Fenton Catalysts for the Conversion of Organic Trace Compounds, *Processes* 9 (2021) 942.
- [105] F.J. Beltrán, P. Pocostales, P. Alvarez, A. Oropesa, Diclofenac removal from water with ozone and activated carbon, *Journal of hazardous materials* 163 (2009) 768–776.
- [106] L.A. Pérez-Estrada, S. Malato, W. Gernjak, A. Agüera, E.M. Thurman, I. Ferrer, A.R. Fernández-Alba, Photo-fenton degradation of diclofenac: identification of main intermediates and degradation pathway, *Environmental science & technology* 39 (2005) 8300–8306.
- [107] N. Genç, E. Durna, E. Erkişi, Optimization of the adsorption of diclofenac by activated carbon and the acidic regeneration of spent activated carbon, *Water science and technology a journal of the International Association on Water Pollution Research* 83 (2021) 396–408.

References

- [108] J.R. de Andrade, M.F. Oliveira, M.G.C. da Silva, M.G.A. Vieira, Adsorption of Pharmaceuticals from Water and Wastewater Using Nonconventional Low-Cost Materials: A Review, *Ind. Eng. Chem. Res.* 57 (2018) 3103–3127.
- [109] Acid Mine Drainage, in: R. Lal (Ed.), *Encyclopedia of Soil Science*, Third Edition, CRC Press, 2017, pp. 6–10.
- [110] B. Huang, Z. Pan, X. Su, L. An, Recycling of lithium-ion batteries: Recent advances and perspectives, *Journal of Power Sources* 399 (2018) 274–286.
- [111] Y. Wang, N. An, L. Wen, L. Wang, X. Jiang, F. Hou, Y. Yin, J. Liang, Recent progress on the recycling technology of Li-ion batteries, *Journal of Energy Chemistry* 55 (2021) 391–419.
- [112] X. Zeng, J. Li, N. Singh, Recycling of Spent Lithium-Ion Battery: A Critical Review, *Critical Reviews in Environmental Science and Technology* 44 (2014) 1129–1165.
- [113] C.-A. Ghiorghita, K.B.L. Borchert, A.-L. Vasiliu, M.-M. Zaharia, D. Schwarz, M. Mihai, Porous thiourea-grafted-chitosan hydrogels: Synthesis and sorption of toxic metal ions from contaminated waters, *Colloids and Surfaces A: Physicochemical and Engineering Aspects* 607 (2020) 125504.
- [114] J. Weißpflog, A. Gündel, D. Vehlow, C. Steinbach, M. Müller, R. Boldt, S. Schwarz, D. Schwarz, Solubility and Selectivity Effects of the Anion on the Adsorption of Different Heavy Metal Ions onto Chitosan, *Molecules (Basel, Switzerland)* 25 (2020).
- [115] B. Reis, N. Gerlach, C. Steinbach, K. Haro Carrasco, M. Oelmann, S. Schwarz, M. Müller, D. Schwarz, A Complementary and Revised View on the N-Acylation of Chitosan with Hexanoyl Chloride, *Marine drugs* 19 (2021).
- [116] B. Reis, K.B.L. Borchert, M. Kafetzi, M. Müller, K.H. Carrasco, N. Gerlach, C. Steinbach, S. Schwarz, R. Boldt, S. Pispas, D. Schwarz, Ecofriendly Removal of Aluminum and Cadmium Sulfate Pollution by Adsorption on Hexanoyl-Modified Chitosan, *Polysaccharides* 3 (2022) 589–608.
- [117] N.A. Badawy, A.A. El-Bayaa, A.Y. Abdel-Aal, S.E. Garamon, Chromatographic separations and recovery of lead ions from a synthetic binary mixtures of some heavy metal using cation exchange resin, *Journal of hazardous materials* 166 (2009) 1266–1271.
- [118] X. Zhang, F. Chen, Facile Synthesis of Mesoporous Poly(melamine–formaldehyde) Solid Adsorbent in Ethylene Glycol, *Chem. Lett.* 45 (2016) 412–414.
- [119] T.C. Drage, A. Arenillas, K.M. Smith, C. Pevida, S. Piippo, C.E. Snape, Preparation of carbon dioxide adsorbents from the chemical activation of urea–formaldehyde and melamine–formaldehyde resins, *Fuel* 86 (2007) 22–31.
- [120] F. Yin, P. Peng, W. Mo, S. Chen, T. Xu, The preparation of a porous melamine–formaldehyde adsorbent grafted with polyethyleneimine and its CO₂ adsorption behavior, *New J. Chem.* 41 (2017) 5297–5304.
- [121] H. Zhou, S. Xu, H. Su, M. Wang, W. Qiao, L. Ling, D. Long, Facile preparation and ultra-microporous structure of melamine-resorcinol-formaldehyde polymeric microspheres, *Chemical communications (Cambridge, England)* 49 (2013) 3763–3765.
- [122] K.B.L. Borchert, C. Steinbach, B. Reis, N. Gerlach, P. Zimmermann, S. Schwarz, D. Schwarz, Mesoporous Poly(melamine-co-formaldehyde) Particles for Efficient and Selective Phosphate and Sulfate Removal, *Molecules (Basel, Switzerland)* 26 (2021) 6615.
- [123] Y. Wu, Y. Li, L. Qin, F. Yang, D. Wu, Monodispersed or narrow-dispersed melamine-formaldehyde resin polymer colloidal spheres: preparation, size-control, modification, bioconjugation and particle formation mechanism, *Journal of materials chemistry. B* 1 (2013) 204–212.
- [124] Y. Maitani, M. Kugo, M. Nakagaki, T. Nagai, Ionic size and behavior of diclofenac salts in water and ethanol/water mixtures by conductivity at 25 degrees C, *Journal of pharmaceutical sciences* 82 (1993) 1245–1249.
- [125] G. Conn, S. Eisler, Synthesis and intramolecular hydrogen bonding networks of 2,4,6-tri(o-hydroxyaryl)-1,3,5-triazines, *Organic letters* 13 (2011) 5080–5083.
- [126] S. Nandi, V.M. Dhavale, S. Shalini, U. Werner-Zwanziger, H. Singh, S. Kurungot, R. Vaidhyanathan, Lithium-Assisted Proton Conduction at 150 °C in a Microporous Triazine-Phenol Polymer, *Adv. Mater. Interfaces* 2 (2015) 1500301.
- [127] William F. Talbot, Manufacture of melamine-aldehyde condensation products.
- [128] H. Diem, G. Matthias, R.A. Wagner, Amino Resins, in: *Ullmann's Encyclopedia of Industrial Chemistry*, Wiley-VCH Verlag GmbH & Co. KGaA, Weinheim, Germany, 2000, p. 102.

References

- [129] J. Bentley, Organic film formers, in: *Paint and Surface Coatings*, Elsevier, 1999, pp. 19–90.
- [130] M. Dunky, P. Niemz, *Holzwerkstoffe und Leime: Technologie und Einflussfaktoren*, Springer Berlin Heidelberg; Imprint; Springer, Berlin, Heidelberg, 2002.
- [131] World Health Organization, Food, Agriculture Organization of the United Nations, Toxicological and health aspects of melamine and cyanuric acid report of a WHO expert meeting in collaboration with FAO, supported by Health Canada, Ottawa, Canada, 1-4 December 2008, World Health Organization, 2009.
- [132] J. Liebig, Ueber einige Stickstoff - Verbindungen, *Ann. Pharm.* 10 (1834) 1–47.
- [133] R.P. Dalal, D.S. Goldfarb, Melamine-related kidney stones and renal toxicity, *Nature reviews. Nephrology* 7 (2011) 267–274.
- [134] G.M.H. Swaen, Urolithiasis in children and exposure to melamine: A review of the epidemiological literature, *Toxicology Research and Application* 3 (2019) 239784731986160.
- [135] H. Wang, Z. Xin, Y. Li, Synthesis of Ureas from CO₂, in: X.-F. Wu, M. Beller (Eds.), *Chemical Transformations of Carbon Dioxide*, Springer International Publishing, Cham, 2018, pp. 177–202.
- [136] Herlinger, Hoffmann, Husemann, Istel, Kern, Krimm, Müller, Rinke, Schmitz-Josten, Schneider, Schulz, Spielberger, Wegler, Werner, V. Polyadditions- bzw. Polykondensationsprodukten von Carbonyl- und Thiocarbonylverbindungen (X), in: Herlinger, Hoffmann, Husemann, Istel, Kern, Krimm, Müller, Rinke, Schmitz-Josten, Schneider, Schulz, Spielberger, Wegler, Werner (Eds.), *Makromolekulare Stoffe*, Georg Thieme Verlag, Stuttgart, 1963.
- [137] D.J. Merline, S. Vukusic, A.A. Abdala, Melamine formaldehyde: curing studies and reaction mechanism, *Polym J* 45 (2013) 413–419.
- [138] S. Ullah, M.A. Bustam, M. Nadeem, M.Y. Naz, W.L. Tan, A.M. Shariff, Synthesis and Thermal Degradation Studies of Melamine Formaldehyde Resins, *The Scientific World Journal* 2014 (2014) 1–6.
- [139] M. Leskovšek, J. Kortnik, U. Stankovič Elesini, B. Šumiga, Characterisation of melamine formaldehyde microspheres synthesised with prolonged microencapsulated reaction time, *Journal of Polymer Engineering* 42 (2022) 288–297.
- [140] Herlinger, Hoffmann, Husemann, Istel, Kern, Krimm, Müller, Rinke, Schmitz-Josten, Schneider, Schulz, Spielberger, Wegler, Werner (Eds.), *Makromolekulare Stoffe*, Georg Thieme Verlag, Stuttgart, 1963.
- [141] I.A. Principe, A.J. Fletcher, Parametric study of factors affecting melamine-resorcinol-formaldehyde xerogels properties, *Materials Today Chemistry* 7 (2018) 5–14.
- [142] M. Thommes, K. Kaneko, A.V. Neimark, J.P. Olivier, F. Rodriguez-Reinoso, J. Rouquerol, K.S.W. Sing, Physisorption of gases, with special reference to the evaluation of surface area and pore size distribution (IUPAC Technical Report), *Pure and Applied Chemistry* 87 (2015) 1051–1069.
- [143] D. Schwarz, J. Weber, Nanoporous Poly(Melamine Formaldehyde) Networks by Aqueous Dispersion Polycondensation-Synthesis and Adsorption Properties, *Macromol. Mater. Eng.* 300 (2015) 531–541.
- [144] M. Heydari, N. Azizi, Z. Mirjafari, M.M. Hashemi, Magnetic mesoporous poly-melamine–formaldehyde: an efficient and recyclable catalyst for straightforward one-pot synthesis of imidazo[1,2-a]pyridines, *J IRAN CHEM SOC* 16 (2019) 2357–2363.
- [145] N.G. Khaligh, H. Gorjian, H. Fahim, S.J.J. Titinchi, Solid-phase synthesis of arylidene and alkylidene malonates, as versatile intermediates, catalyzed using mesoporous poly-melamine–formaldehyde as a nitrogen-rich porous organic polymer (POP), *Res Chem Intermed* 47 (2021) 3529–3536.
- [146] M.X. Tan, L. Gu, N. Li, J.Y. Ying, Y. Zhang, Mesoporous poly-melamine-formaldehyde (mPMF) – a highly efficient catalyst for chemoselective acetalization of aldehydes, *Green Chem.* 15 (2013) 1127.
- [147] D. Yang, P. Liu, N. Zhang, W. Wei, M. Yue, J. You, H. Wang, Mesoporous Poly(melamine-formaldehyde): A Green and Recyclable Heterogeneous Organocatalyst for the Synthesis of Benzoxazoles and Benzothiazoles Using Dioxxygen as Oxidant, *ChemCatChem* 6 (2014) 3434–3439.
- [148] R.A. Molla, M.A. Iqbal, K. Ghosh, A.S. Roy, K. Kamaluddin, S.M. Islam, Mesoporous poly-melamine-formaldehyde stabilized palladium nanoparticle (Pd@mPMF) catalyzed mono and double carbonylation of aryl halides with amines, *RSC Adv* 4 (2014) 48177–48190.
- [149] M. Li, Y. Zhang, X. Wang, W. Ahn, G. Jiang, K. Feng, G. Lui, Z. Chen, Gas Pickering Emulsion Templated Hollow Carbon for High Rate Performance Lithium Sulfur Batteries, *Adv. Funct. Mater.* 26 (2016) 8408–8417.

References

- [150] K. Jittmonkong, S. Roddecha, M. Sriariyanun, One-pot Synthesis of LiFePO₄ Nano-particles Entrapped in Mesoporous Melamine-Formaldehyde Matrix as the Promising Cathode Materials for the Next Generation Lithium Ion Batteries, *Materials Today: Proceedings* 17 (2019) 1284–1292.
- [151] C. Pevida, T.C. Drage, C.E. Snape, Silica-templated melamine–formaldehyde resin derived adsorbents for CO₂ capture, *Carbon* 46 (2008) 1464–1474.
- [152] D. Tiwari, C. Goel, H. Bhunia, P.K. Bajpai, Melamine-formaldehyde derived porous carbons for adsorption of CO₂ capture, *Journal of environmental management* 197 (2017) 415–427.
- [153] A.W. Adamson, A.P. Gast, *Physical chemistry of surfaces*, 6th ed., Wiley, New York, 1997.
- [154] C.W. Scheele, Chemical Observations and Experiments on Air and Fire, *The London Medical Journal* 1 (1781) 312–320.
- [155] A. Dąbrowski, Adsorption — from theory to practice, *Advances in Colloid and Interface Science* 93 (2001) 135–224.
- [156] W. Henry, III. Experiments on the quantity of gases absorbed by water, at different temperatures, and under different pressures, *Phil. Trans. R. Soc.* 93 (1803) 29–274.
- [157] H.M.F. Freundlich, *Kapillarchemie, Eine Darstellung der Chemie der Kolloide und verwandter Gebiete*, 1st ed., Akademische Verlagsgesellschaft, Leipzig, 1909.
- [158] H.M.F. Freundlich, Über die Adsorption in Lösungen., *Zeitschrift für Physikalische Chemie – Stöchiometrie und Verwandtschaftslehre* 57 (1907) 385–470.
- [159] I. Langmuir, THE CONSTITUTION AND FUNDAMENTAL PROPERTIES OF SOLIDS AND LIQUIDS. PART I. SOLIDS, *J. Am. Chem. Soc.* 38 (1916) 2221–2295.
- [160] C. Malara, G. Pierini, A. Viola, Commission of the European Communities. Directorate-General for Science, Research, Development, Correlation, Analysis and Prediction of Adsorption Equilibria: Final Report, Office for Official Publications of the European Communities, 1992.
- [161] R. Sips, On the Structure of a Catalyst Surface, *The Journal of Chemical Physics* 16 (1948) 490–495.
- [162] M.M. Dubinin, The Equation of the Characteristic Curve of Activated Charcoal, *Proceedings of the USSR Academy of Sciences* 55 (1947) 327–329.
- [163] F. London, M. Polanyi, Über die atomtheoretische Deutung der Adsorptionskräfte, *Naturwissenschaften* 18 (1930) 1099–1100.
- [164] M. Polanyi, The Potential Theory of Adsorption, *Science* 141 (1963) 1010–1013.
- [165] X. Zhou, Correction to the calculation of Polanyi potential from Dubinin-Rudushkevich equation, *Journal of hazardous materials* 384 (2020) 121101.
- [166] J.P. Hobson, Physical Adsorption of Nitrogen on Pyrex at Very Low Pressures, *The Journal of Chemical Physics* 34 (1961) 1850–1851.
- [167] M.A. Al-Ghouti, D.A. Da'ana, Guidelines for the use and interpretation of adsorption isotherm models: A review, *Journal of hazardous materials* 393 (2020) 122383.
- [168] K.Y. Foo, B.H. Hameed, Insights into the modeling of adsorption isotherm systems, *Chemical Engineering Journal* 156 (2010) 2–10.
- [169] G. Sposito, Distinguishing Adsorption from Surface Precipitation, in: J.A. Davis, K.F. Hayes (Eds.), *Geochemical Processes at Mineral Surfaces*, American Chemical Society, Washington D.C., 1987, pp. 217–228.
- [170] K.P. Ananthapadmanabhan, P. Somasundaran, Surface precipitation of inorganics and surfactants and its role in adsorption and flotation, *Colloids and Surfaces* 13 (1985) 151–167.
- [171] Y.S.R. Chen, J.N. Butler, W. Stumm, Kinetic study of phosphate reaction with aluminum oxide and kaolinite, *Environ. Sci. Technol.* 7 (1973) 327–332.
- [172] P. Rengasamy, J.M. Oades, Interaction of monomeric and polymeric species of metal ions with clay surfaces. III. Aluminium(III) and chromium(III), *Soil Res.* 16 (1978) 53.
- [173] R.O. James, T.W. Healy, Adsorption of hydrolyzable metal ions at the oxide—water interface. I. Co(II) adsorption on SiO₂ and TiO₂ as model systems, *Journal of colloid and interface science* 40 (1972) 42–52.
- [174] L. Li, R. Stanforth, Distinguishing Adsorption and Surface Precipitation of Phosphate on Goethite (alpha-FeOOH), *Journal of colloid and interface science* 230 (2000) 12–21.

References

- [175] A.G. Stack, R. Erni, N.D. Browning, W.H. Casey, Pyromorphite growth on lead-sulfide surfaces, *Environmental science & technology* 38 (2004) 5529–5534.
- [176] H.A. Thompson, G.A. Parks, G.E. Brown, Dynamic interactions of dissolution, surface adsorption, and precipitation in an aging cobalt(II)-clay-water system, *Geochimica et Cosmochimica Acta* 63 (1999) 1767–1779.
- [177] H.A. Thompson, Ambient-Temperature Synthesis, Evolution, and Characterization of Cobalt-Aluminum Hydrotalcite-Like Solids, *Clays and Clay Minerals* 47 (1999) 425–438.
- [178] Towle, Bargar, Brown, Parks, Surface Precipitation of Co(II)(aq) on Al₂O₃, *Journal of colloid and interface science* 187 (1997) 62–82.
- [179] J. Wei, X. Meng, Y. Song, Q. Shi, X. Wen, G. Korfiatis, Surface mole-ratio method to distinguish surface precipitation and adsorption on solid-liquid interface, *Journal of hazardous materials* 397 (2020) 122781.
- [180] L. Zhang, S. Tang, F. He, Y. Liu, W. Mao, Y. Guan, Highly efficient and selective capture of heavy metals by poly(acrylic acid) grafted chitosan and biochar composite for wastewater treatment, *Chemical Engineering Journal* 378 (2019) 122215.
- [181] J. Wei, L. Duan, J. Wei, E. Hoffmann, Y. Song, X. Meng, Lead removal from water using organic acrylic amine fiber (AAF) and inorganic-organic P-AAF, fixed bed filtration and surface precipitation, *Journal of environmental sciences (China)* 101 (2021) 135–144.
- [182] R. Meng, T. Chen, Y. Zhang, W. Lu, Y. Liu, T. Lu, Y. Liu, H. Wang, Development, modification, and application of low-cost and available biochar derived from corn straw for the removal of vanadium(v) from aqueous solution and real contaminated groundwater, *RSC Adv.* 8 (2018) 21480–21494.
- [183] M. Luo, C. Huang, F. Chen, C. Chen, H. Li, Removal of aqueous Cr(VI) using magnetic-gelatin supported on Brassica-straw biochar, *Journal of Dispersion Science and Technology* 42 (2021) 1710–1722.
- [184] K.S.W. Sing, Reporting physisorption data for gas/solid systems: With special reference to the determination of surface area and porosity, *Pure & Applied Chemistry* 54 (1982) 2201–2218.
- [185] D.W. Breck, *Zeolite molecular sieves: Structure, chemistry and use*, Wiley, 1974.
- [186] *Gas Separation Membranes: Polymeric and Inorganic*, 2015th ed., Springer International Publishing, Cham, 2015.
- [187] M. Thommes, K.A. Cychosz, A.V. Neimark, Advanced Physical Adsorption Characterization of Nanoporous Carbons, in: *Novel Carbon Adsorbents*, Elsevier, 2012, pp. 107–145.
- [188] C. Schlumberger, M. Thommes, Characterization of Hierarchically Ordered Porous Materials by Physisorption and Mercury Porosimetry—A Tutorial Review, *Adv. Mater. Interfaces* 8 (2021) 2002181.
- [189] J. Landers, G.Y. Gor, A.V. Neimark, Density functional theory methods for characterization of porous materials, *Colloids and Surfaces A: Physicochemical and Engineering Aspects* 437 (2013) 3–32.
- [190] M. Thommes, K.A. Cychosz, Physical adsorption characterization of nanoporous materials: progress and challenges, *Adsorption* 20 (2014) 233–250.
- [191] S. Brunauer, P.H. Emmett, E. Teller, Adsorption of Gases in Multimolecular Layers, *J. Am. Chem. Soc.* 60 (1938) 309–319.
- [192] S.W. Hell, J. Wichmann, Breaking the diffraction resolution limit by stimulated emission: stimulated-emission-depletion fluorescence microscopy, *Optics letters* 19 (1994) 780–782.
- [193] T.A. Klar, S.W. Hell, Subdiffraction resolution in far-field fluorescence microscopy, *Optics letters* 24 (1999) 954–956.
- [194] G. Cox, *Optical imaging techniques in cell biology*, 2017th ed., CRC Press - Taylor & Francis Group, Boca Raton, London, New York, 2017.
- [195] E. Abbe, Beiträge zur Theorie des Mikroskops und der mikroskopischen Wahrnehmung, *Archiv f. mikrosk. Anatomie* 9 (1873) 413–468.
- [196] L.E. Franken, K. Grünewald, E.J. Boekema, M.C.A. Stuart, A Technical Introduction to Transmission Electron Microscopy for Soft-Matter: Imaging, Possibilities, Choices, and Technical Developments, *Small (Weinheim an der Bergstrasse, Germany)* 16 (2020) e1906198.
- [197] E. Rutherford, LXXIX. The scattering of α and β particles by matter and the structure of the atom, *The London, Edinburgh, and Dublin Philosophical Magazine and Journal of Science* 21 (1911) 669–688.
- [198] D.B. Williams, C.B. Carter, *Transmission electron microscopy: A textbook for materials science*, Springer, New York, op. 2009.

References

- [199] C.C. Ahn (Ed.), *Transmission Electron Energy Loss Spectrometry in Materials Science and the EELS Atlas*, 2nd ed., Wiley-VCH, Weinheim, 2006.
- [200] K. Ohls, B. Bogdain, History of inductively coupled plasma atomic emission spectral analysis: from the beginning up to its coupling with mass spectrometry, *J. Anal. At. Spectrom.* 31 (2016) 22–31.
- [201] F. Caruso, S. Mantellato, M. Palacios, R.J. Flatt, ICP-OES method for the characterization of cement pore solutions and their modification by polycarboxylate-based superplasticizers, *Cement and Concrete Research* 91 (2017) 52–60.
- [202] S.R. Khan, B. Sharma, P.A. Chawla, R. Bhatia, Inductively Coupled Plasma Optical Emission Spectrometry (ICP-OES): a Powerful Analytical Technique for Elemental Analysis, *Food Anal. Methods* 15 (2022) 666–688.

Eidesstattliche Versicherung

Hiermit versichere ich, dass ich die vorliegende Arbeit ohne unzulässige Hilfe Dritter und ohne Benutzung anderer als der angegebenen Hilfsmittel angefertigt habe; die aus fremden Quellen direkt oder indirekt übernommenen Gedanken sind als solche kenntlich gemacht. Die Arbeit wurde bisher weder im Inland noch im Ausland in gleicher oder ähnlicher Form einer anderen Prüfungsbehörde vorgelegt.

Die vorliegende Arbeit wurde im Zeitraum vom Dezember 2018 bis September 2022 am Leibniz-Institut für Polymerforschung Dresden e. V. unter der Betreuung von Herrn Prof. Dr. Andreas Fery und mit fachlicher Unterstützung von Frau Dr. Dana Schwarz und Frau Dr. Simona Schwarz angefertigt.

Hiermit erkenne ich die Promotionsordnung der Fakultät Mathematik und Naturwissenschaften der Technischen Universität Dresden vom 23.02.2011 in der zuletzt geänderten Fassung vom 23.05.2018 an.

Datum, Unterschrift